

1998

Coherent neutral pion photoproduction on the deuteron

David G. Meekins

College of William & Mary - Arts & Sciences

Follow this and additional works at: <https://scholarworks.wm.edu/etd>



Part of the [Physics Commons](#)

Recommended Citation

Meekins, David G., "Coherent neutral pion photoproduction on the deuteron" (1998). *Dissertations, Theses, and Masters Projects*. Paper 1539623932.

<https://dx.doi.org/doi:10.21220/s2-2cvf-nc71>

This Dissertation is brought to you for free and open access by the Theses, Dissertations, & Master Projects at W&M ScholarWorks. It has been accepted for inclusion in Dissertations, Theses, and Masters Projects by an authorized administrator of W&M ScholarWorks. For more information, please contact scholarworks@wm.edu.

INFORMATION TO USERS

This manuscript has been reproduced from the microfilm master. UMI films the text directly from the original or copy submitted. Thus, some thesis and dissertation copies are in typewriter face, while others may be from any type of computer printer.

The quality of this reproduction is dependent upon the quality of the copy submitted. Broken or indistinct print, colored or poor quality illustrations and photographs, print bleedthrough, substandard margins, and improper alignment can adversely affect reproduction.

In the unlikely event that the author did not send UMI a complete manuscript and there are missing pages, these will be noted. Also, if unauthorized copyright material had to be removed, a note will indicate the deletion.

Oversize materials (e.g., maps, drawings, charts) are reproduced by sectioning the original, beginning at the upper left-hand corner and continuing from left to right in equal sections with small overlaps. Each original is also photographed in one exposure and is included in reduced form at the back of the book.

Photographs included in the original manuscript have been reproduced xerographically in this copy. Higher quality 6" x 9" black and white photographic prints are available for any photographs or illustrations appearing in this copy for an additional charge. Contact UMI directly to order.

UMI

A Bell & Howell Information Company
300 North Zeeb Road, Ann Arbor MI 48106-1346 USA
313/761-4700 800/521-0600

Coherent π^0 Photoproduction on the Deuteron

A Dissertation

Presented to

The Faculty of the Department of Physics
The College of William and Mary in Virginia

In Partial Fulfillment

Of the Requirements for the Degree of
Doctor of Philosophy

by

David G. Meekins

1998

UMI Number: 9920303

**Copyright 1999 by
Meekins, David George**

All rights reserved.

**UMI Microform 9920303
Copyright 1999, by UMI Company. All rights reserved.**

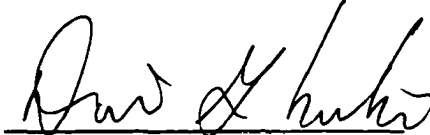
**This microform edition is protected against unauthorized
copying under Title 17, United States Code.**

UMI
300 North Zeeb Road
Ann Arbor, MI 48103

APPROVAL SHEET

This dissertation is submitted in partial fulfillment of
the requirements for the degree of

Doctor of Philosophy



David G. Meekins

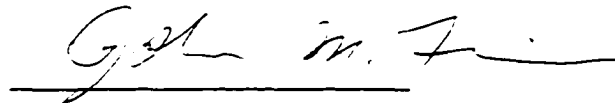
Approved, November 1998



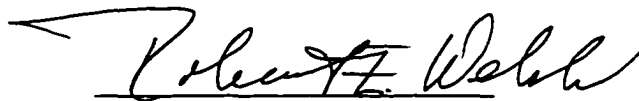
Roger D. Carlini



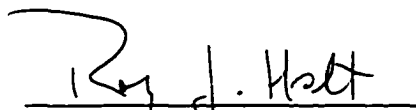
Carl E. Carlson



John M. Finn



Robert E. Welsh



Roy J. Holt

Department of Physics

University of Illinois, Urbana Champaign

Dedication

Dedicated with love and appreciation to my Family, especially Isobel.

Contents

1	Introduction	2
1.1	Overview and Physics Motivation	2
1.2	Notation and Definitions	6
2	Theoretical Discussion	10
2.1	General PQCD Treatment of Wide Angle Hadronic Processes	10
2.1.1	Wide Angle Hard Scattering in PQCD	11
2.1.2	Landshoff Scattering	13
2.1.3	Sudakov Suppression	14
2.2	Dimensional Scaling Laws	15
2.3	Reduced Nuclear Amplitudes	24
2.4	Meson Exchange Calculations	31
2.5	Applicability of PQCD to Hadronic Processes	34
2.5.1	QCD Sum Rules for $\gamma p \rightarrow \gamma p$	35
3	Experiment	39
3.1	Overview	39
3.2	Accelerator	40

3.3	Hall C Arc and Beamline	42
3.4	Beam Profile and Position Measurement	43
3.5	Beam Current Measurement	46
3.6	Hall C Beam Rastering System	52
3.7	Beam Energy Measurement	54
3.8	Hall C Bremsstrahlung Radiator	55
3.9	Hall C Cryogenic Target	56
3.9.1	The Hall C Scattering Chamber	57
3.9.2	Mechanical Aspects of the Hall C Cryogenic Target	60
3.9.3	Gas Handling System	65
3.9.4	Instrumentation and Control	66
3.9.5	Performance of the Hall C Cryogenic Target System	69
3.10	High Momentum Spectrometer	71
3.10.1	HMS Optical System	73
3.10.2	Commissioning and Calibrations of the HMS	76
3.10.3	HMS Acceptance	84
3.10.4	HMS Detector Package	89
3.11	Short Orbit Spectrometer	102
3.11.1	SOS Optical System	103
3.11.2	SOS Detector Package	107
3.12	Data Acquisition	117
3.12.1	Input Output Controllers	117
3.12.2	CODA Overview	119
3.13	Hardware Trigger	120
3.13.1	Hodoscope Trigger	120

3.13.2	Trigger Supervisor and 8LM	122
3.14	Dead Time Determination	124
3.14.1	Electronic dead time	125
3.14.2	Computer Dead Time	127
3.15	Hall C Analysis Software	128
3.15.1	General Event Analysis	128
3.15.2	HMS Specific Event Analysis	129
4	Event Reconstruction	131
4.1	Tracking	132
4.1.1	Tracking Efficiency	134
4.2	Time of Flight Measurement	136
4.3	Energy Loss in the scintillators	138
4.4	Particle Identification	141
4.4.1	Background Subtraction	147
4.5	Absorption of Deuterons	147
4.6	HMS Gate Valve	151
4.7	Effective Target Length	153
5	Experimental Cross Section	158
5.1	Endpoint Spectra	158
5.1.1	Subtraction of the Measured Background	159
5.1.2	Correction to the Radiator Out Spectra	164
5.1.3	Two Pion Background	166
5.1.4	Endpoint Fitting	168
5.2	Determination of the Cross Section	169

5.3	The Invariant Cross Section $\frac{d\sigma}{dt}$	174
5.4	Compton Background	174
5.5	Summary of Systematic Uncertainties	175
6	Results and Discussion	180
6.1	Asymptotic Scaling Laws	180
6.2	Reduced Nuclear Amplitudes	182
6.3	Comparison with Other Photoreactions	188
6.4	Conclusions	191
A	Bremsstrahlung Radiator	195
A.1	Hardware design aspects	195
A.1.1	Radiator foils and target mount	197
A.1.2	Water cooling system	198
A.1.3	Vacuum and motion components	202
A.2	Control subsystem for the Bremsstrahlung Radiator	203
A.3	Performance of the Bremsstrahlung Radiator	203
B	Bremsstrahlung Calculations	208
B.1	Bremsstrahlung Yield	209
B.1.1	Energy Loss Effects	210
B.1.2	Complete Bremsstrahlung Spectrum	213
B.2	Correction Function $C(E_\gamma)$	215
B.3	Calculated Yields	217
C	Derivation of Useful Expressions	220
C.1	Jacobian $\frac{d\Omega_{cm}}{dt}$	220

C.2	Center-of-Mass Three Momenta	221
C.3	Reconstructed Photon Energy E_γ	223
C.4	The Jacobian $\frac{d\Omega_{lab}}{d\Omega_{cm}}$	224
D	Kinematics	228

List of Tables

2.1	The measured s dependence of several processes and that predicted by the scaling laws.	19
3.1	Measurements of the beam energy in Hall C using three different techniques for single pass beam.	55
3.2	Characteristics of the Hall C scattering Chamber.	59
3.3	Critical dimensions of individual cryotarget cells used in the experiment. The thickness of the front window (on all cells) was $71 \pm 3 \mu\text{m}$	63
3.4	Results of target gas analysis performed at LLNL.	72
3.5	Densities of cryogenic target fluids. Errors reflect the uncertainty in target density from temperature, pressure, and localized boiling and the uncertainty of relative amounts of ortho and para hydrogen. Values in the table are from References [38] and [58].	72
3.6	Summary of the characteristics of the HMS magnets. The Focus directions are given for point-to-point tune only.	74
3.7	Summary of HMS performance characteristics [64].	75
3.8	Maximum power available for the SOS magnets. The maximum of 170 V for QS is only available with the power supply in overdrive.	103

3.9	Summary of SOS performance characteristics [64].	107
3.10	SOS hodoscope physical characteristics.	112
3.11	8LM logic table (\otimes implies logical AND and signals with bars on top refer to the logical not of the signal).	124
4.1	Summary of various lengths of materials, along the flight path of the recoil deuteron, found in the target and spectrometer. Composite materials have been separated into individual elements with weights other than 1.0. Note that the thickness of the deuterium (found only in the target) varies with the central angle of the HMS.	149
4.2	Measured transmission of deuterons in the HMS for two different central momentum settings. The cross sections $\frac{d\sigma}{d\Omega}$ are for the D(e,e'd) reaction one is from a measurement performed using the HMS and SOS without absorption corrections and the other is from a fit to world data. The measured transmission is calculated by taking the ratio of the measured cross section to the cross section determined from the fit.	151
4.3	Normalized yields for various kinematics and Y_{tar} cuts. The data indicate that the uncertainty in the normalized yield resulting from the Y_{tar} cuts is $\sim 1.5\%$. There errors indicated are statistical only.	156
5.1	Difference between single (E_{π}) and double pion ($E_{2\pi}$) production thresholds in the reconstructed photon energy, E_{γ} , at all kinematics. Note as the beam energy and deuteron center-of-mass increase, the difference between the single and double pion production thresholds falls. Thus, at higher energies it becomes more difficult to exclude the double pion production process.	167

5.2	Normalized yields from various regions of the endpoint spectra and various kinematical settings at $\theta_{cm} = 90^\circ$ (errors are statistical only). The 2- π region extends from $E_0 - 100$ MeV to the two-pion threshold $E_{2\pi}$ which are given in Table 5.1. The 1- π region extends from $E_{2\pi}$ to $E_0 - 10$ MeV. The full region covers the range $E_0 - 100 \leq E_\gamma \leq E_0 - 10$	168
5.3	Summary of systematic uncertainties in the measured cross section.	179
6.1	Center-of-mass differential cross sections for the process $\gamma d \rightarrow d\pi^0$ measured during Experiment E89-012. The errors given for the cross sections are the sums of the systematic and statistical uncertainties performed in quadrature. The photon energy \bar{E}_γ is used to determine kinematical quantities such as s and t and is obtained from the midpoint of the total photon energy region used in the analysis.	181
6.2	Overview of some of the world data for real photoprocesses. The invariant cross section $\frac{d\sigma}{dt}$ has been fit to the form As^{-n} for data with similar center-of-mass angles. The superscript \dagger indicates that the fit was given by the authors of the given reference.	192
A.1	Thickness data for copper foils making at given target positions in the radiator. The large error for the 8% foil stack is due to poor surface area data. Individual foils making up the complete stack for a given radiator thickness are separated for clarity.	198
A.2	Corrected yields for the process $\gamma p \rightarrow \pi^+ n$ for various foil stacks. The yield for 0.0 % thickness has been subtracted from all data points.	205

B.1	Calculated photon yields in $\gamma/1000 e^-$. The regions are described in the text above. All calculated yields are accurate to $\sim 3\%$ [56].	219
D.1	Table of kinematical settings used during the experiment. The beam energy is the incident electron beam energy. \tilde{E}_γ is the central photon energy. θ_{cm} is the center-of-mass angle of the scattered deuteron. θ_{HMS} and p_{HMS} are the angle and momentum settings of the HMS. s and t are the Mandelstam variables where t is the square of the momentum transferred to the deuteron.	228

List of Figures

1.1	Generic process $AB \rightarrow CD$. The four momentum and mass of particle i are p_i and m_i	7
1.2	Kinematics (in the center-of-mass frame) for the process $\gamma d \rightarrow d\pi^0$. The initial and final d momenta are labeled p_d and p'_d . $\theta_{\gamma d}$ is the scattering angle as measured by the spectrometer (in the laboratory frame). θ_{cm} is defined as the deuteron center-of-mass angle.	9
2.1	Hard elastic $\pi\pi$ scattering in PQCD with one single hard scattering occurring in a small region of space and time.	12
2.2	Landshoff elastic $\pi\pi$ scattering with two separate hard scatterings.	14
2.3	Example of a diagram for the process $\pi^+\pi^+ \rightarrow \pi^+\pi^+$, having multiple interactions among the constituents of the separate pions. This is the familiar Landshoff scattering picture described in Section 2.1.2.	17
2.4	Electromagnetic form factor of the proton in the PQCD picture.	19
2.5	Data for the process $pp \rightarrow pp$ are shown verses s . Data are from a compilation by Landshoff and Polkinghorn [16]. Figure taken from Reference [23]. The verticle axis is $\frac{d\sigma}{dt}$ in units of $\frac{b}{GeV^2}$. The horizontal axis is s in units of GeV^2	20

2.6	Data for the process $\gamma d \rightarrow d\pi^0$ at $\theta_{cm} = 90^\circ$. The data are from References [24] and [26].	22
2.7	Data for the process $\gamma d \rightarrow d\pi^0$ at $\theta_{cm} = 130^\circ$. The data are from Reference [24].	23
2.8	Various hadronic form factors multiplied by the PQCD predicted scaling behavior $(Q^2)^{n_H-1} F_H(Q^2)$ Figure taken from Reference [23].	25
2.9	Two different diagrams for elastic ed scattering.	27
2.10	Reduced form factor of the deuteron multiplied by its predicted scaling from Equation 2.19. Data are from References [34] and [35].	28
2.11	Data for the reaction $\gamma d \rightarrow pn$ for $\theta_{cm} = 90^\circ$. Data are from References [17, 18, 19] and [20]. The solid curve in the figure indicates the reduced nuclear amplitude prediction normalized to the $E_\gamma = 1.6$ GeV point. Figure courtesy of B. P. Terburg.	30
2.12	Three diagrams considered in the analysis of Imanishi <i>et al.</i> [24] for the process $\gamma d \rightarrow d\pi^0$. (a) and (b) show the single and double scattering terms. (c) depicts the dibaryon resonance term.	33
2.13	Various model calculations of the proton magnetic form factor G_M^p . The curves labeled hard are for a PQCD treatment of the form factor. The curves labeled soft are from calculations including only soft wave function effects. The figure is from Reference [28].	36
2.14	Angular dependence of Compton $\gamma p \rightarrow \gamma p$ data. Curves are from a model by Radyushkin [42]. The curves in the figure indicate the calculated angular dependence of the cross section for a given incident photon energy. Figure courtesy of A. Radyushkin [45].	38

3.1	Overview of CEBAF showing accelerator and three experimental endstations. The electron beam enters the accelerator at the injector and travels around the accelerator loop in a clockwise direction (if viewed from above).	40
3.2	Schematic diagram of the Hall C Arc and Beamline with major instrumentation shown. Positions shown are relative to the target center.	42
3.3	Diagram of the HARP beam profile monitor	44
3.4	Diagram of the HARP beam profile monitor scan. The three peaks come from a pass of each wire through the beam. Note that this scan was taken with improperly tuned beam.	45
3.5	Schematic view of a BPM.	46
3.6	Schematic diagram of the Unser beam current monitor. Figure courtesy of C. Armstrong.	49
3.7	V/F linearity test. The line in the figure is a least squares fit to the data.	50
3.8	Typical beam current monitor calibration run for the Unser monitor.	51
3.9	Beam raster pattern as seen by BCM 3H00A. Note the increased intensity at the edges and especially the corners of the spot. The pattern is off center (0,0) due to position offsets which have not been accounted for.	53
3.10	Scale drawing of the Hall C cryotarget. The scattering chamber has been removed from the figure for clarity.	58
3.11	Beam view of the Hall C scattering chamber. The Short Orbit Spectrometer and the High Momentum Spectrometer have been abbreviated as SOS and HMS, respectively. The external cryotarget apparatus is mounted on a rotating seal so that the target cells may be removed from the beam.	59
3.12	Scale drawing of a typical cryotarget loop. Beam is coming out of the picture. Only the longer cell (bottom cell) was used in the experiment.	62

3.13	Cross sectional view of a typical heat exchanger. Cold helium is piped through the fin-tubing. The target fluid is pumped through the screw type pump and over the outside of the fin-tubing.	62
3.14	Typical cell block and cells shown with the original 15 cm target cell installed on the bottom. The thickness of the front window (on all cells) was $71 \pm 3 \mu\text{m}$. Note that the outer part of the target cell was constructed of a beer can blank supplied by the Coors Brewing Company.	63
3.15	Close up view of the Hall C cryotarget target stack. Beam is to the right in the figure.	65
3.16	Data from the high power test of the 15 cm deuterium cell.	71
3.17	Scale drawing of the High Momentum Spectrometer (HMS) showing magnet carriage and detector hut.	73
3.18	Schematic view of the three positions available in the HMS collimator system. From left to right they are the sieve slit, the large collimator, and the small collimator. The thickness of each octagonal collimator is 2.5 inches. The thickness of the sieve slit is 1.0 inch.	76
3.19	Data from $C(e,e')$ scattering showing X vs. Y at the focal plane in the HMS. 78	
3.20	HMS sieve slit reconstruction. In this run the sieve slit is not centered on the central ray. This is evident from the ~ 5 mm offset (from 0,0) of the central hole in X_{slit} . The target quantities are projected forwards to the face of the sieve slit. Figure courtesy of G. Niculescu.	81
3.21	Schematic showing the slanted target positioned in the beam line. The position along the axis of the beam is determined from the vertical position of the target.	82
3.22	HMS δ dependence on Y_{tar} . δ is given in % and Y_{tar} is given in cm.	83

3.23	Reconstructed quantities as determined from the Monte Carlo model of the HMS for a 12 cm long target with $P_{central} = 4.0 \text{ GeV}$ and $\theta_{HMS} = 60^\circ$. Z_{rec} is given in cm, δ_{rec} is given in percent, and θ_{rec} and ϕ_{rec} are given in mrad.	87
3.24	Schematic of the HMS detector package as shown from the side. The z positions of the detectors relative to the focal plane are shown below each detector.	90
3.25	Schematic diagram of the wire layout for the HMS drift chambers. Note that X points in the dispersive direction. In the schematic on the right, the lines on the figure indicate the actual wire directions. The position information determined by the wires in a certain plane is perpendicular to that plane. Figure courtesy of C. Armstrong.	92
3.26	Schematic of a HMS drift chamber cell. Note that the sense wire is located in the center of the cell. Figure courtesy of G. Niculescu and D. Abbott. . .	93
3.27	Example drift time distribution for one of the planes in the HMS drift chambers. Units on the horizontal axis are in ns.	95
3.28	Example drift distance for one of the planes in the HMS drift chambers. Units on the horizontal axis are in cm.	96
3.29	Schematic diagram of a HMS hodoscope x, y pair of scintillators planes. Figure courtesy of C. Armstrong.	97
3.30	Schematic of electronic instrumentation for the HMS hodoscope. Specific electronics are discussed in later sections. Figure courtesy J. Arrington. . .	98

3.31	Schematic of the HMS lead glass shower calorimeter trigger electronics. The modules labeled NIM DISC are NIM output discriminator modules. The modules labeled with Σ are linear fan ins (signal amplitude adders). Figure courtesy J. Arrington.	100
3.32	Schematic diagram of the HMS Čerenkov detector. Figure courtesy J. Arrington.	101
3.33	Scale drawing of the SOS. Figure shows the central ray as a dot dashed line. Figure courtesy of K. Bailey, Argon National Lab.	104
3.34	Schematic view of the three positions available in the SOS collimator system.	105
3.35	Reconstructed Y_{tar} , Y and X at the face of the collimator, and X vs Y at the face of the collimator with the sieve slit in. Data are from C(e,e') scattering. Figure courtesy of C. Armstrong.	108
3.36	Schematic of the SOS detector package. Note that the figure does not show the Aerogel Čerenkov detector which was installed after the first phase of the experiment.	109
3.37	Cross sectional view of a SOS drift chamber.	110
3.38	Schematic diagram of the wire layout for a pair of planes in the SOS chambers.	110
3.39	Active area of the SOS drift chambers. The figure also shows the orientation of the wires for all planes.	111
3.40	Schematic views of the X planes in the SOS hodoscope.	113
3.41	Schematic views of the Y planes in the SOS hodoscope.	114
3.42	SOS Aerogel Čerenkov detector electronic instrumentation schematic. Figure courtesy J. Arrington.	116

3.43	Schematic of the General Hall C single arm trigger for the HMS or SOS. Figure courtesy of J. Arrington.	121
3.44	Trigger supervisor electronics schematic. Figure courtesy J. Arrington.	125
4.1	Sweet spots in the HMS hodoscope used to determine the tracking efficiency.	135
4.2	Calculated average energy loss, $\frac{dE}{dx}$, for deuterons and protons in a typical plastic scintillator. The solid curve depicts the energy loss of deuterons and the dashed curve is for protons.	140
4.3	Energy loss in the first layer of the HMS scintillators dE/dx at a momentum setting of 0.815 GeV. The deuteron peak is centered around 1100. For the purpose of clarity, the proton peak, centered ~ 450 with a long tail, has been reduced by a factor of 50.	142
4.4	Reconstructed mass spectrum for an example run with a beam energy of 0.845 GeV at $\theta_{cm} = 90^\circ$. The bulk proton mass peak has been cut from the figure for clarity.	144
4.5	Energy loss verses reconstructed mass in the first layer of the hodoscope for $\theta_{cm} = 90^\circ$ and $E_{beam} = 1.413$ GeV. Note that there is a clear separation between the proton and deuteron peaks in this phase space.	145
4.6	Reconstructed mass for $\theta_{cm} = 90^\circ$ at various beam energies (E_0). At higher incident beam energies and spectrometer momentums, the resolution of the reconstructed mass becomes worse. This is clearly indicated in the figure. The proton interaction tail also becomes more pronounced at higher energy.	146

4.7	Reconstructed mass for $E_0 = 2.245$ GeV beam $\theta_{cm} = 90^\circ$. The background, which is assumed to be protons interacting in the scintillators, under the deuteron mass peak is estimated as the sum of the shaded regions on either side of the peak.	148
4.8	Reconstructed target quantities projected forward to the face of the gate valve for a run with the valve present. The solid arc marks the approximate position of the edge of the gate valve. Note the decrease in event density on the left side of the valve.	152
4.9	Initial (left) and reconstructed (right) momentum from the Monte Carlo simulation including effects from the gate valve for the same kinematics described in Figure 4.8. The broad base of the plot on the right indicates poor momentum reconstruction for events undergoing multiple scattering in the gate valve.	154
4.10	Reconstructed momentum for simulated data with the gate valve present. Here cuts on the reconstructed target quantities are made to exclude the part of the acceptance with the valve. As is evident, the cuts are not 100% effective in removing events which passed through the valve.	155
4.11	Reconstructed Y at the target, Y_{tar} (in cm), for a typical run using a deuterium target with the radiator in and gate valve present. The total length of the target as seen by the spectrometer ranges between $\sim \pm 4$ cm. Note that cuts have been placed on Y_{tar} at ± 25 cm.	157

5.1	Typical endpoint spectrum from a deuterium radiator in run with an incident electron beam energy of 2.445 GeV, $\theta_{cm} = 90^\circ$, and a 6.02% copper radiator. Note that on the horizontal axis the beam energy has been subtracted from the reconstructed photon energy. The events with reconstructed photon energies higher than the endpoint ($E_\gamma - E_{beam} = 0$), which are assumed to be protons, were typically removed by background subtraction methods.	160
5.2	The same endpoint spectrum as that shown in Figure 5.1 with the estimated proton background overlaid in cross hatched style. Note that most of the events seen above the photon endpoint are removed by this subtraction. . .	161
5.3	Normalized yields from the $E_0 = 3.245$ GeV, $\theta_{cm} = 90^\circ$ setting. The solid circles are for runs with the 6.02% radiator in taken on the deuterium target. The solid squares indicate runs with no radiator taken on the deuterium target. The hydrogen target runs are depicted are triangles upward (downward) pointing for radiator in (out). The Errors shown are statistical only.	163
5.4	Total yield, Y_{tot} , spectrum for $E_0 = 1.413$ GeV and $\theta_{cm} = 90^\circ$ kinematics. The data show a clear endpoint at $E_\gamma - E_{beam} = 0$, where it is expected. . .	165
5.5	Endpoint spectrum for $E_0 = 1.413$ GeV and $\theta_{cm} = 90^\circ$. The solid curve in the figure is from a fit of the form shown in Equation 5.10. Errors shown are statistical only.	170
5.6	Endpoint spectrum for $E_0 = 2.445$ GeV and $\theta_{cm} = 90^\circ$. The solid curve in the figure is from a fit of the form shown in Equation 5.10. Errors shown are statistical only.	171

5.7	Endpoint spectrum for $E_0 = 3.245$ GeV and $\theta_{cm} = 90^\circ$. The solid curve in the figure is from a fit of the form shown in Equation 5.10. Errors shown are statistical only.	172
5.8	The ratio of the differential cross sections for Compton scattering to π^0 production on the proton, R_p . Data are from Reference [15].	176
6.1	Data shown as $s^{13} \frac{d\sigma}{dt}$ for $\theta_{cm} = 90^\circ$. The data are clearly inconsistent with the Constituent Counting Rule predictions. Errors shown include both statistical and systematic uncertainties.	183
6.2	Data for $\theta_{cm} = 136^\circ$ shown as $s^{13} \frac{d\sigma}{dt}$. The data are consistent with the Constituent Counting Rule predictions. Errors shown include both statistical and systematic uncertainties.	184
6.3	Data for the process $\gamma d \rightarrow d\pi^0$ shown as $f^2(\theta_{cm})$, which is described by the RNA analysis above, for $\theta_{cm} = 90^\circ$. Errors shown include both statistical and systematic uncertainties.	186
6.4	Data for the process $\gamma d \rightarrow d\pi^0$ from the present work shown as $f^2(\theta_{cm})$, which is described by the RNA analysis above, for $\theta_{cm} = 136^\circ$. Errors shown include both statistical and systematic uncertainties.	187
6.5	Center-of-mass differential cross sections for the process $\gamma d \rightarrow d\pi^0$ at both 136° and 90° shown as a function of t , the momentum transfer to the deuteron. The symbols in this figure have the same meaning as those in Figure 6.3. Errors shown include both statistical and systematic uncertainties.	189

6.6	Center-of-mass cross sections factored by the deuteron electric form factor $-t \cdot A(Q)$. $A(Q)$ was determined from a fit to the world data compiled from References [91, 92, 93, 94] and [95]. Errors shown include both statistical and systematic uncertainties.	190
A.1	Hall C bremsstrahlung radiator shown without the vacuum hardware. The target/heat sink, to which the copper foils are attached, and water lines can be seen at the bottom of the figure. The copper foils are not shown.	196
A.2	Downstream view of the bremsstrahlung radiator target mount/heat sink. View shows clamps, heat sink, and waterlines, which wrap around the back (upstream side) of the target.	199
A.3	Flow schematic for radiator water cooling system. Manual valves are denoted with the prefix MV. PS and FS are the symbols for pressure and flow switches.	200
A.4	Radiator GUI screen. (Figure is shown in greyscale. The actual GUI is in color.)	204
A.5	Data for $\gamma p \rightarrow \pi^+ n$ from radiator linearity test. The data are shown with the normalized yield from the radiator out case subtracted from the normalized yield for each radiator. Error bars are typically smaller than the point and are statistical only. Note that no cross sections were extracted from this data.	206
A.6	Data for $\gamma p \rightarrow \pi^+ n$ from the radiator linearity test normalized by the calculated photon flux.	207

B.1	Calculated electron energy distribution $W(E, E_0, Z, T)$ for a beam with an incident energy of $E_0 = 2445.0$ MeV passing through a copper radiator with a thickness of 6.02% radiation lengths.	212
B.2	Calculated distribution $I(E, E', Z, T)$ for an incident beam energy of 1413 MeV a 6.02% copper radiator and a beam energy spread of 0.1%.	214
B.3	Calculated bremsstrahlung spectra for an electron beam energy of 2445 MeV and a 6.02% copper radiator. The solid curve is a calculation using the thick code, and a similar calculation using the thin code is shown as the dashed curve.	216
B.4	The correction function $C(E_\gamma)$ for a 15 cm deuterium target, an incident electron beam energy of 2445 MeV, and a 6.02% copper radiator.	218
C.1	The two body process $AB \rightarrow CD$ in the center-of-mass. Note that θ_{AD} in the laboratory frame is the angle of the detected particle (d in the experiment) as seen by the spectrometer.	222
C.2	Kinematics of a general photoprocess in the laboratory frame.	223
C.3	General laboratory kinematics for a two-body process.	227

Acknowledgements

Many recent Ph.Ds. look back on their careers as graduate students remembering years of hardship and struggle. I am one of the few who was blessed with very happy times. This was due to the efforts of my colleagues, friends, and family all of whom I owe a debt I can never repay. As with all things that it is said that I have accomplished, this work would never exist without their help. The following is an inadequate attempt to express my appreciation to all who have helped me along my way. I sincerely apologize to those whom I forget to mention (due to my own faults) as I have no desire to ever forget.

I wish to thank my thesis advisor Roger Carlini for giving me the nearly unabated freedom to persue my interests in and around Hall C. Despite his busy schedule he always found time to provide whatever support and advice he could. Because of his efforts behind the scenes, I was able learn a great deal from my experiences at CEBAF (it will always be CEBAF to me). I am also greatfull to the Physics Department at the College of William and Mary for giving me a chance to learn about the things that interest me the most.

To my thesis committee, Roger Carlini, Carl Carlson, Mike Finn, Roy Holt, and Bob Welsh, I thank you all for taking the time to read my thesis and offer comments and for spending a pleasent November afternoon talking about physics.

My fellow students at William and Mary especially Marco Brown, John Goetz, Chris Hoff, Mike Seale, and Mike West, are good friends which I was saddened to part company with. I thank them for all of their help and encouragement over the long years.

I would like to express my deepest appreciation to Dr. Gerald Taylor of the James Madison University Physics Department. Dr. Taylor was not only my undergraduate research advisor, but a good friend who placed my education and well being above our work and whom I truly miss. I would also like to thank the entire faculty and staff of this department especially Dr. Don Chodrow who always seemed to be teaching some course right

when I needed it, every semester I was there. I remember my years and friends at Madison with fondness. To Steve Bowling, Pat Brady, Michelle Burt, Mark Freeman, Brad Graham, Heather Hough, Joe Howard, Kevin Kromer, Brian Powers, Bonnie Risinger, and Bryan Zimmerman, I thank you all for your encouragement and friendship.

I am greatfull to Roy Holt, for after all the experiment was his idea. I have learned a substantial amount of physics from talking with both Roy and Don Geesaman whom I also wish to thank. We had a number of interesting discussions and friendly meetings with each other and I am looking forward to the next time we can all work together.

I truly wish to thank the Accelerator Division at Thomas Jefferson National Accelerator Facility for all their hard work. CEBAF is truly a remarkable machine and without their hard work, experiments like ours (E89-012) would never succeed. I also thank the Physics Division for supporting me financially as well as in other ways. I also thank the E89-012 collaboration. There are just too many names to list here, but I know who you are and I thank you for all of your hard work.

To the Hall C staff, Roger Carlini, Keith Baker, Rolf Ent, Thia Keppel, Allison Lung, Dave Mack, Joe Mitchell, Steve Wood, Bill Vulcan, and Chen Yan. what can I say. Your doors were always open and I will not forget all of the help, trust, and advice (and work too) you have given me over the years. The opportunity to learn was always present even though I sometimes failed to take advantage of this.

The technical and engineering staff of Hall C, Joe Beaufait, Paul Brindza, Dan Brock, Mike Fowler, Steve Hickson, Mark Hoegerl, Paul Hood, Steve Knight, Steve Lassiter, and Jim Tacakus are rarely (in my opinion) given enough credit for the work they do. I have learned a great deal from them as well and I thank them for all of their efforts.

I would like to thank John Chamberlain, Jim Dahlberg, Eric Feldel, Mark Hoegerl, John Hollen, Jim Roerbauch, Joe van Dyke, for their help with the radiator design and

installation. I also thank Fraser Duncan and Steve Wood for their help developing the controls software for the radiator. I would also like to thank Steve Wood and David Abbott for their efforts on the data acquisition system for the Hall.

The Hall C Target Group labored for many years to get the first high power target working at the lab. We all became friends and I miss the days where all we had to do was work together. Joe Mitchell who provided fearless leadership through the many months of work was a source of inspiration and knowledge that I would not wish to have missed. The rest of us Fraser Duncan, Jim Dunne, Paul Hood, Ron ???, Mike Johnson, Steve Knight, Mark Hoegerl (my favorite welder) , and Bart Terberg, made a great team which I truly miss.

The team of graduate students involved in Hall C during the first eight experiments are great people who did a tremendous amount of work, many of whom are now good friends. Here especially, I know that I will omit people who were instrumental to the success of the experiment; to those I apologize in advance. I wish to thank the following students for their help and wish them all well in their future careers:

Chris Armstrong for the work on the beam current monitors and the incite into specifics of the thesis requirements.

John Arrington for all of the work on the analysis software and trigger, and all around hard work. Not to mention the help with the analysis.

Chris Bochna for his help with the analysis and work on the beam current monitors.

Jin Seok Cha for his work on the HMS optics.

Chris Cothran for his work on the HMS Čerenkov

Dipankar Dutta for the hard work commissioning the Hall and for working on the optics of the HMS.

Kenneth (redouble) Gustafson for his work on the target analysis.

Adrian Hoenecker for his work on the target and the information on $A(Q)$.

Gabriel Niculescu for his work on the HMS drift chambers, tracking software, HMS optics, and his help with the analysis.

Bart Terburg for help with the analysis and all of the target work need I say more.

Derek van Westrum for his work on the SOS Čerenkov and tracking procedure and for his help with the analysis.

I am very grateful for the friendship of John Arrington, Dipankar Dutta, Adrian Hoenecker, Gabriel Niculescu, Bart Terburg, and Bini Zilman. Working with people that you like and respect always makes the job more enjoyable. I am forever in debt to the lunch hockey gang too. That hour every day we spent on anything other than physics was truly a necessity.

To Bill Vulcan and Rolf Ent, friends like these are rare indeed and I have been blessed with their help, advice, and support throughout my time in Hall C. The conversations with Bill over the years have kept me focused on the important things (often having nothing to do with work) and assuaged my frustrations before I did anything really stupid. Rolf Ent, despite his efforts impose a contrary image, is truly one of the good guys. There are few people who sacrifice themselves for what they believe to be right consistently and in this Rolf has never erred. For this he has my deepest respect. Best of fortunes to always my friend. The following is just for you (R Ent, R Ent, R Ent, R Ent, R Ent, R Ent, R Ent, R Ent, R Ent, R Ent, R Ent, R Ent, R Ent, R Ent, R Ent, R Ent, and R Ent).

To my family, especially to my brother and my parents, I owe a debt I can never repay. My brother has been my best friend over the years and is still a constant companion if only in my thoughts. His support has always been there and for that I will always love him and try my best to provide the same support. It has been said that no one can understand the bond between a mother and her son, such is the case between my Mom and me. My love will never be enough to make up for the sacrifices she has made for me over my thirty years, thank you for everything. Every son should have a father like mine. His patience, understanding, wisdom, support and love have always been there. He is simply the best man I know and I aspire to be like him everyday. No matter what path I chose to follow he was always there for me. I can only hope to be half the father to my children as he is to me. Although I never say it enough I am thankful for everthing and I will always love you.

Finally, to my wife, nothing I can say will ever be enough to express my love and appreciation for all that you do. You are my best friend and confidant and I see in you everything that is most important. Isobel has sacrificed the most during my time as a grad student and has suffered my absences with nothing but support and encouragement. This work is as much her doing as mine as is everything that we do. I would simply be lost without you. My love is yours forever although that will never be long enough.

Abstract

The differential scattering cross section for the process $\gamma d \rightarrow d\pi^0$ was measured, as part of experiment E89-012 at Thomas Jefferson National Accelerator Facility. The experiment was performed in Hall C during the Spring of 1996 as the commissioning experiment for the Hall C cryogenic target. The High Momentum Spectrometer was used to detect the recoil deuteron and no effort was made to detect the π^0 or its decay photons. The differential cross section was measured at a number of incident photon energies between 0.8 GeV and 4.0 GeV for the center-of-mass angles of 90° and 136° . The data were found to disagree with both the constituent counting rule and reduced nuclear amplitude predictions. These are the first data at large deuteron center-of-mass angles for photon energies larger than 1.6 GeV.

Coherent π^0 Photoproduction on the Deuteron

Chapter 1

Introduction

1.1 Overview and Physics Motivation

Over the years, it has become standard practice to use traditional meson exchange theory to model nuclear reactions. These models use meson and baryon degrees of freedom in a local Lagrangian field theory and have met with a great deal of success in the low to moderate energy region ($< 1 \text{ GeV}$). Unfortunately, efforts to extend these calculations, which are constrained by lower energy data, to higher energies have met with difficulty. Perhaps, this is due to the higher energy and hence, shorter wavelength of the probe, which can resolve the substructure of the nucleon. This lack of success however, does not indicate that there is no possible model for nuclear interactions at higher energies.

Tremendous progress has been made in nuclear and particle physics in the last thirty years. Ever since inelastic electron proton scattering experiments first revealed the existence of subnucleonic degrees of freedom, there has been a flurry of theoretical and experimental activity. Six years after subnucleonic structure was seen, asymptotic freedom was discovered and led to the development of Quantum Chromodynamics (QCD) which is

widely believed to be the correct model of strong interactions today.

QCD incorporates quark and gluon degrees of freedom, which obey an exact SU(3) color symmetry, in a vector gauge field theory. Quarks (q) are point like spin-1/2 fermions that carry both electric charge and color, which is exchanged by eight spin-1 bicolored gluons (g). The nominal hadronic bound states are color singlet $q\bar{q}$ and qqq for mesons and baryons, respectively. However, the possibility of a qqq color octet and speculation of six quark states, and dibaryon resonances do exist. In actuality, the hadronic states mentioned previously are lowest order or valence states. The hadron is more properly expressed as a Fock state expansion. In the case of the nucleon, for example, the Fock state expansion may be written

$$|N\rangle = |qqq\rangle + |qqqg\rangle + |qqqq\bar{q}\rangle + \dots \quad (1.1)$$

In most models involving high momentum transfer, only the valence state is considered because effects from non valence states are suppressed. (See Section 2.1).

These states are bound together with gluons through quark-gluon couplings. In addition to the QCD quark gluon coupling (qg) (analogous to the QED photon electron coupling ($e\gamma$)), (ggg) and ($gggg$) couplings may also exist because gluons themselves carry color. Analogous to the ($e\gamma$) coupling, which has an effective strength α , the (qg) coupling has an effective strength α_s which is a function of the four-momentum transfer (q^μ) and is given by

$$\alpha_s(Q^2) = \frac{4\pi}{\left(11 - \frac{2n_f}{3}\right) \ln(Q^2/\Lambda^2)}, \quad (1.2)$$

where $Q^2 = -q^2$, n_f is the total number of quark flavors, and $\Lambda \approx 200 \pm 100$ MeV sets the scale of the interaction and must be determined from experiment [1].

There are two properties of QCD that make high momentum transfer (large Q^2) cal-

calculations tractable. First, and most important, QCD is an asymptotically free theory. This comes from the fact that at high Q^2 , the running coupling constant α_s , given in Equation 1.2, logarithmically vanishes allowing a perturbative expansion in α_s . The second feature is the existence of factorization theorems. The amplitude for a hard hadronic process may be factored into the product of a process-independent distribution amplitude, $\phi(Q, x)$ and a process-dependent hard amplitude $H(Q, x_i)$. This allows $H(Q, x_i)$, which contributes the bulk of the Q^2 dependence to the amplitude, and $\phi(Q, x)$ to be calculated separately.

These techniques, known as perturbative QCD (PQCD), have been successful in describing a number of high energy phenomena. Some believe that since QCD has relatively low mass scales ($\Lambda \sim 200 \text{ MeV} \sim 1/(\text{size of the nucleon})$) it should be applicable to intermediate energy (few GeV) nuclear processes. However, a rigorous first order PQCD calculation for even a simple process involves the calculation of over a million Feynman diagrams. Furthermore, at lower energies this perturbation expansion becomes invalid due to smaller momentum transfers (which are associated with lower energies) and hence, larger values of the coupling constant α_s . PQCD does however, provide models such as constituent counting rules and reduced nuclear amplitudes that should be applicable to high and perhaps even intermediate energy processes. Thus, measurement of exclusive nuclear processes in the intermediate energy region (few GeV) should provide critical tests of QCD in the space where the nonperturbative and perturbative regions meet.

In this intermediate region, effects which can often be ignored in the high energy region, such as “higher twists”, must be considered. These effects are corrections to the perturbative expansion and come, for example, from the non-zero mass of partons, “Landshoff” terms (described in Section 2.1.2), and the intrinsic transverse momentum in the hadronic wave function. This transverse momentum $k_{\perp} \sim 300 \text{ MeV}$ is neglected at high momentum transfer, where the assumption is made that the quarks in the hadron have momenta

parallel to the total hadron momentum. It has been argued that much of these effects could be suppressed at moderately high momentum transfer by higher powers of $1/Q^2$ [2]. This suppression could allow certain predictions of PQCD such as the scaling laws to become valid at lower energies and also provides a smooth transition from the perturbative to the nonperturbative regions.

For these reasons, it is interesting to study exclusive nuclear processes at energies of a few GeV. These processes shed light on the role of quarks and gluons in nuclear physics as well as their effects on hadronic wave functions in the nuclear medium. The simplest nucleus to model theoretically is the deuteron. It has long served as a test bed for new developments in both theory and experiment. The measurement of photo-processes in the intermediate energy region are made more tractable by the higher energy scales and continuous duty cycle available at new laboratories such as Thomas Jefferson National Accelerator Facility (TJNAF).

Photo-reactions on the deuteron have many distinct advantages over traditional lepton scattering and show more promise to reveal aspects of PQCD [3]. These processes can provide more momentum transfer to the individual nucleons before the sharp decrease in cross section makes measurement of these cross sections impractical. Further, because a photon can only couple to one quark in a hard scattering process, there are no first-order Landshoff terms to consider [4]. Given the above arguments, measurements of the process $\gamma d \rightarrow d\pi^0$ could provide interesting tests of the predictions stemming from PQCD.

As part of TJNAF experiment E89-012, the differential scattering cross section for the process $\gamma d \rightarrow d\pi^0$ was measured at deuteron center-of-mass angles ¹ of 90° and 136° for incident photon energies between 0.8 GeV and 4 GeV². The results from this part of

¹The deuteron center of mass angle is defined to be the angle between the ingoing and outgoing deuteron in the center-of-mass system.

²Note that the original intent of the experiment was to measure the the interaction at 90° and 135° .

the experiment will be presented here. The theory relevant to the study of the process is discussed in Chapter 1. Chapters 3 and 4 describe the experimental equipment and data analysis. In Chapter 5 the final steps to reach the measured cross section are shown. Finally, the results and comparison to theoretical models are presented in Chapter 6.

1.2 Notation and Definitions

The purpose of this section is to provide a general description of the notation used in the following chapters. Natural units, where $\hbar = c = 1$, and the Björken and Drell metric [5] are used throughout this work. For the process $\gamma d \rightarrow d\pi^0$, the four-momentum transfer squared to the deuteron, q^2 , is given by

$$q^2 = (p_f - p_i)^2 = (E_f - E_i)^2 - (\vec{p}_f - \vec{p}_i)^2 \quad (1.3)$$

where $p_f = (E_f, \vec{p}_f)$, $p_i = (E_i, \vec{p}_i)$, and \vec{p}_f , \vec{p}_i are the final and initial four momenta, energies and three momenta of the deuteron. The squared momentum transfer to the individual nucleons is also important and can be expressed roughly by

$$t_N \approx \left(\frac{p_f}{2} - \frac{p_i}{2} \right)^2 \quad (1.4)$$

where, it is assumed that each of the constituent nucleons in the deuteron carry half of its total momentum.

Consider the generic process $AB \rightarrow CD$ shown in Figure 1.1. The Mandelstam vari-

However, due to problems arising from the experimental equipment, the actual angles where measurements were performed were 90° and 136° .

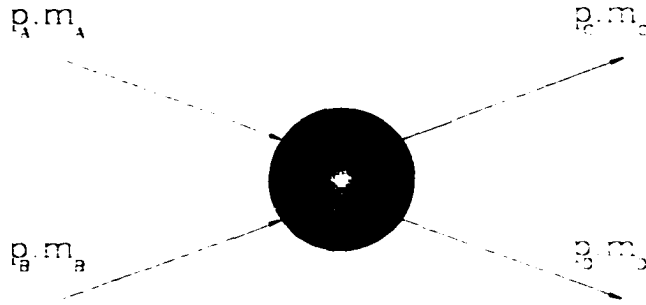


Figure 1.1: Generic process $AB \rightarrow CD$. The four momentum and mass of particle i are p_i and m_i .

ables for the process are defined by the following equations [6]:

$$\begin{aligned}
 s &= (p_A + p_B)^2 \\
 t &= (p_A - p_C)^2 \\
 u &= (p_A - p_D)^2.
 \end{aligned}
 \tag{1.5}$$

These variables are used extensively throughout this text.

The initial and final center-of-mass three momenta, \vec{p}_i and \vec{p}_f , can be expressed in terms of s and the particle masses as

$$|\vec{p}_i|^2 = \frac{[s - (m_A + m_B)^2][s - (m_A - m_B)^2]}{4s}
 \tag{1.6}$$

and

$$|\vec{p}_f|^2 = \frac{[s - (m_C + m_D)^2][s - (m_C - m_D)^2]}{4s}
 \tag{1.7}$$

These expressions are derived in Appendix C. Another useful quantity is the transverse

three momentum p_T which is simply

$$p_T^2 = \{\vec{p}_f \sin(\theta_{cm})\}^2 \quad (1.8)$$

In the high energy limit, p_T is often expressed as

$$\lim_{s \rightarrow \infty} p_T^2 \approx \frac{tu}{s}$$

In the intermediated energy region, Equation 1.8 is more correct and is used exclusively in this text.

For a given process with Feynman amplitude M , the center-of-mass differential cross section may be written as

$$\frac{d\sigma}{d\Omega_{cm}} = \frac{|\vec{p}_f|}{64\pi^2 s |\vec{p}_i|} |M|^2 \quad (1.9)$$

With the use of the Jacobian

$$\frac{d\Omega_{cm}}{dt} = \frac{\pi}{|\vec{p}_i| |\vec{p}_f|} \approx \frac{\pi}{s} \quad (1.10)$$

which is derived in Appendix C, Equation 1.9 may be written as

$$\frac{d\sigma}{d\Omega_{cm}} \frac{d\Omega_{cm}}{dt} = \frac{d\sigma}{dt} = \frac{|M|^2}{64\pi s |\vec{p}_i|^2} \quad (1.11)$$

The above relations will be referred to often in the following chapters. Figure 1.2 defines the center-of-mass scattering angle θ_{cm} and the laboratory angle (angle of d as detected by the spectrometer) for the process $\gamma d \rightarrow d\pi^0$,

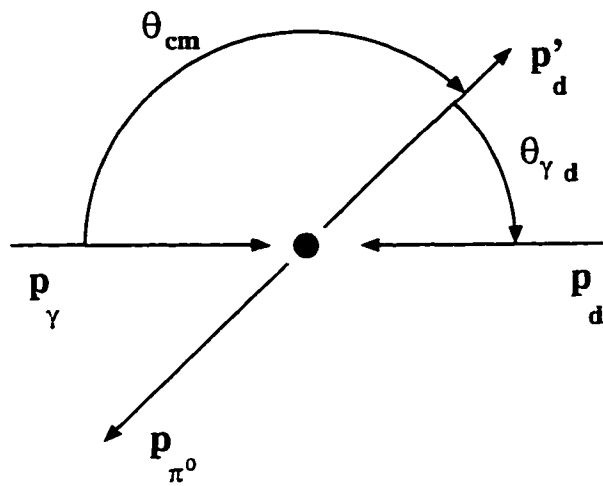


Figure 1.2: Kinematics (in the center-of-mass frame) for the process $\gamma d \rightarrow d\pi^0$. The initial and final d momenta are labeled p_d and p'_d . $\theta_{\gamma d}$ is the scattering angle as measured by the spectrometer (in the laboratory frame). θ_{cm} is defined as the deuteron center-of-mass angle.

Chapter 2

Theoretical Discussion

2.1 General PQCD Treatment of Wide Angle Hadronic Processes

Perturbative methods are most easily applied to hard hadronic processes. An excellent review of PQCD applied to exclusive processes is given by Lepage and Brodsky [7]. In this section, brief descriptions of “hard” scattering, “Landshoff” scattering and “Sudakov” suppression are given. These descriptions are not intended to be rigorous and only serve as an introduction to discussions in later sections. The formalism closely follows that developed by Yu. L. Dorkshitzer *et al.* [8].¹

¹It should also be noted that in wide angle scattering $s \sim t$ which is not the case for small angle scattering. For small angle processes, the substitution of t for s in the results obtained in this chapter can be made with surprising accuracy.

2.1.1 Wide Angle Hard Scattering in PQCD

It is instructive to first consider a PQCD description of wide angle elastic $\pi\pi$ scattering to simplify the notation and then extend the results to a general hadronic reaction. The z axis is defined to be parallel to the incoming pion momenta in the center-of-mass. The x, z plane is defined to be the scattering plane. Hence, the y axis is normal to the scattering plane. The interaction takes place over a short time interval, $\Delta t \sim 1/\sqrt{s}$ and in a small volume of space as shown in Figure 2.1. The quarks (q) and antiquarks (\bar{q}) in the initial and final state pions must all occupy this small region of space $|\Delta\vec{x}| \lesssim 1/\sqrt{s}$ in order for a hard interaction to take place. The differential cross section may be expressed by

$$\frac{d\sigma}{d\Omega} = P(p_1)P(p_2)P(p'_1)P(p'_2)\sigma_H \quad (2.1)$$

where $P(p_i)$ is the probability that the constituent q and \bar{q} in the pion with momentum p_i are within the required region of space, and σ_H describes the scattering of compact q, \bar{q} pairs. Since $1/\sqrt{s}$ is the only length scale available (for wide angle scattering $t \sim s$), σ_H must scale as $1/s$. Note that the wave functions for the pions are severely Lorentz contracted and thus the probability for the q and \bar{q} to be in an element of z space $|\Delta z| \lesssim 1/\sqrt{s}$ is roughly unity. Geometry may be used to determine the probability that they will occupy the region of space $|\Delta\vec{x}_\perp| \lesssim 1/\sqrt{s}$ is $P(p_i) \sim (1/\sqrt{s})^2$. Additional factors of $1/s$ are required for each constituent in the hadron with the exception of the first constituent which has the probability of unity to be close to itself in \vec{x}_\perp space. With the use of Equation 1.10 and Equation 2.1, the invariant cross section for elastic $\pi\pi$ scattering obeys the following relation.

$$\frac{d\sigma}{dt} \sim \left(\frac{1}{\sqrt{s}}\right)^2 \left(\frac{1}{\sqrt{s}}\right)^2 \left(\frac{1}{\sqrt{s}}\right)^2 \left(\frac{1}{\sqrt{s}}\right)^2 \frac{1}{s} \frac{1}{s} \sim \frac{1}{s^6}. \quad (2.2)$$

To generalize this result to the process $h_A h_B \rightarrow h_C h_D$, it is only necessary to consider the probability of the n_i constituents of hadron h_i to be in the element of space $|\Delta\vec{x}_\perp| \lesssim 1/\sqrt{s}$. Again, simple geometry gives $P(p_i) \sim (1/s)^{n_i-1}$. This gives the general result

$$\frac{d\sigma}{dt} \sim s^{2-(n_A+n_B+n_C+n_D)} \quad (2.3)$$

for large s . The above relation is known as the asymptotic scaling law or constituent counting rule and is discussed in detail in Section 2.2. It can be readily seen now why only valence Fock states were considered initially. Higher order states, with more constituents, will scale at large s , with higher powers of $1/s$ and thus, are suppressed.

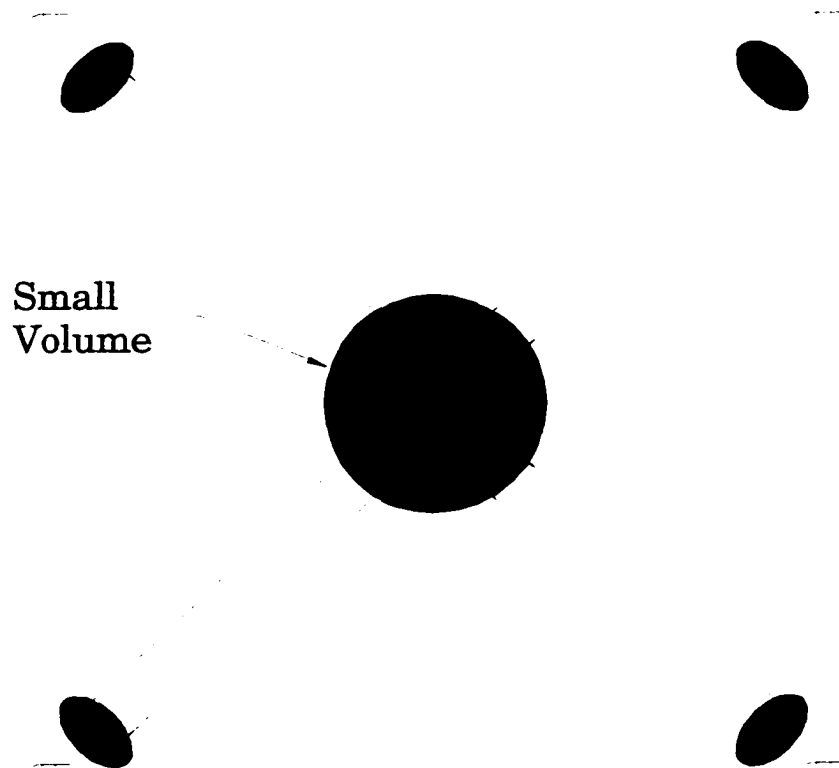


Figure 2.1: Hard elastic $\pi\pi$ scattering in PQCD with one single hard scattering occurring in a small region of space and time.

2.1.2 Landshoff Scattering

Landshoff scattering also takes place over a short time interval $\Delta t \sim 1/\sqrt{s}$, however, individual constituents scatter in separate regions of space. Consider once again elastic $\pi\pi$ scattering. The quark and antiquark scatter in a small z and x space $|\Delta x| \sim |\Delta z| \lesssim 1/\sqrt{s}$, but are only restricted in y space by the size of the pion wave function and the separation between the two scattering is given by b as shown in Figure 2.2. The cross section may now be expressed as

$$\frac{d\sigma}{d\Omega} = P(p_1)P(p_2)P(p'_1)P(p'_2)\sigma_H\Theta_y. \quad (2.4)$$

Here, $P(p_i)$ is the probability that the quarks occupy a small region of x space and is given by $P(p_i) \sim 1/\sqrt{s}$. The quantity σ_H still requires the $1/\sqrt{s}$ factor for the small x spacing, but in y there are two scatterings thus requiring a factor of $(1/\sqrt{s})^2$ therefore $\sigma_H \sim (1/\sqrt{s})^3$. The factor Θ_y describes the small angular region, out of the (x, z) plane, in which the scattering must take place, and is given by $\Theta_y \sim 1/\sqrt{s}$. For elastic $\pi\pi$ scattering the invariant cross section in the Landshoff picture is predicted to behave as

$$\frac{d\sigma}{dt} \sim \frac{1}{\sqrt{s}} \frac{1}{\sqrt{s}} \frac{1}{\sqrt{s}} \frac{1}{\sqrt{s}} \left(\frac{1}{\sqrt{s}}\right)^3 \frac{1}{\sqrt{s}} \frac{1}{s} = \frac{1}{s^5}. \quad (2.5)$$

This result may also be generalized for the process $h_A h_B \rightarrow h'_A h'_B$ with the restriction that there are n_A scatterings and $n_A \leq n_B$. The probabilities in Equation 2.4 generalize to $P(p_A) \sim (1/\sqrt{s})^{n_A-1}$. There are now n_A scattering “planes” hence, $\sigma_H \sim (1/\sqrt{s})^{1+n_A}$ and there must be $n_A - 1$ factors of Θ_y . The general result for Landshoff scattering is then

$$\frac{d\sigma}{dt} \sim \left(\frac{1}{s}\right)^{2n_A+n_B-1}. \quad (2.6)$$

Here as in the case for hard scattering, only the valence Fock states are used to describe the

hadrons.

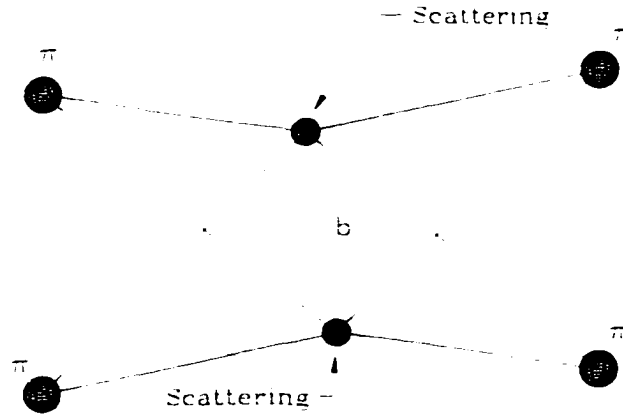


Figure 2.2: Landshoff elastic $\pi\pi$ scattering with two separate hard scatterings.

2.1.3 Sudakov Suppression

It is believed that the hard scattering region and the Landshoff region should be smoothly connected [2]. The individual scatterings in the Landshoff picture can vary in separation from a maximum of the diameter of the hadron down to $1/\sqrt{s}$. In the hard scattering picture, the hadronic wave function is completely compact and should be color neutral to very small sizes. In the Landshoff picture, this is not the case due to the possible large separation in y . It is therefore possible that the wave functions for the hadrons are not locally color neutral and so there is some probability for gluons to be present. This probability decreases with increasing energy (shorter distances), thereby suppressing Landshoff amplitudes. This suppression, known as Sudakov suppression, could allow scaling of the type in Equation 2.3 to dominate at lower energies than expected or to at least dampen the Landshoff terms such that they have the same scaling behavior for a given process [2]. More quantitative

discussions are given by Botts and Sterman [9] and by Sotiropoulos and Sterman [10].

2.2 Dimensional Scaling Laws

The dimensional scaling laws (also known as the asymptotic scaling laws and constituent counting rules) were first conceived by Brodsky and Farrar [11] and independently by Matveev, Muradyan and Tavheliidze [12]. Consider again the process $AB \rightarrow CD$ as shown in Figure 1.1. For this process, the scaling laws simply state that the asymptotic (large s) behavior of the invariant cross section at fixed center-of-mass scattering angle is given by

$$\frac{d\sigma}{dt}(AB \rightarrow CD) \sim s^{2-n} f(\theta_{cm}) \quad (2.7)$$

where $n = n_A + n_B + n_C + n_D$ is the total number of elementary fields (quark, lepton, photon, i.e., constituents) carrying a finite fraction of the momentum of particles A, B, C , and D , $f(\theta_{cm})$ is a function dependent only on the center-of-mass scattering angle θ_{cm} , and s is the standard Mandelstam variable given in Equations 1.5.

This result can be arrived at using simple dimensional analysis and by making a few assumptions following the example of Brodsky and Farrar [11]. If the conventional normalization $\langle p | p' \rangle = 2E\delta(p - p')$ (perhaps more commonly seen as $u^\dagger u = 2E$) is chosen, the Feynman amplitude M_n for the scattering of n free constituents has the dimension $[length]^{n-4}$. Note that the amplitude M_n has not yet been related to the amplitude, M , for the process $AB \rightarrow CD$ where the constituents are not free. For high energy processes (large s) and fixed t/s , the only length scale available is $1/\sqrt{s}$, implying that the amplitude M_n may be expressed as

$$M_n \sim \sqrt{s}^{4-n} g(\theta_{cm}) \quad (2.8)$$

where $g(\theta_{cm})$ is a function independent of s . Next it is assumed that each constituent must carry a finite fraction of the total momentum for each of the particles A, B, C, D and note that any integration over all possible momenta does not introduce any new powers of s . Hence, the amplitude for the process $AB \rightarrow CD, M$, where the constituents are bound, has the same scaling behavior in s as M_n , the amplitude for scattering the free constituents. From Equation 1.9, the center-of-mass differential cross section may be expressed as

$$\frac{d\sigma}{d\Omega_{cm}} = \frac{|\vec{p}_C|}{64\pi^2 s |\vec{p}_A|} |M|^2 \quad (2.9)$$

where \vec{p}_A and \vec{p}_C are the center-of-mass three momenta of particles A and C. Substituting p_A for p_i in Equation 1.11 gives

$$\frac{d\sigma}{dt} = \frac{|M|^2}{64\pi s |\vec{p}_A|^2}$$

Finally, by using Equation 1.6 and by noting that $|\vec{p}_A|$ may be written as

$$|\vec{p}_A|^2 = \frac{(s - (m_A + m_B)^2)(s - (m_A - m_B)^2)}{4s}. \quad (2.10)$$

For $s \gg m_i$, this gives

$$|\vec{p}_A|^2 \approx s/4,$$

which implies that the large s behavior of the invariant cross section obeys the relation

$$\frac{d\sigma}{dt} \propto \frac{|M|^2}{s^2}. \quad (2.11)$$

Combining this with Equation 2.8, the desired result of Equation 2.7 is trivially obtained.

The above is correct modulo logarithms in any renormalizable field theory, provided

the following assumptions hold:

1. Large momentum transfer interactions among the constituents in individual hadrons are asymptotically scale invariant.
2. Multiple scale invariant interactions among constituents of different hadrons (Landshoff terms) may be ignored. See Figure 2.3.
3. The hadrons are described by ground state wave functions which must be finite when the separation between quarks is zero and vanish for large separations.

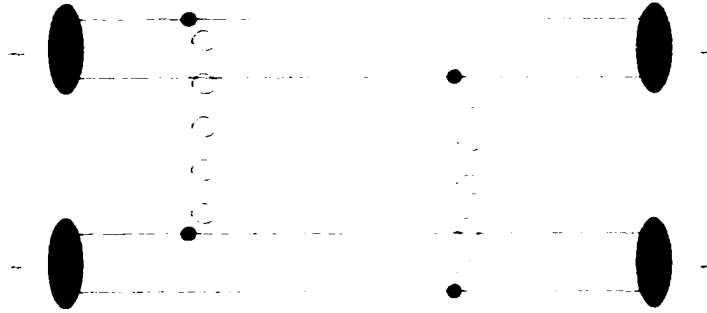


Figure 2.3: Example of a diagram for the process $\pi^+\pi^+ \rightarrow \pi^+\pi^+$, having multiple interactions among the constituents of the separate pions. This is the familiar Landshoff scattering picture described in Section 2.1.2.

The first two assumptions ensure that $M_n \sim (\sqrt{s})^{4-n}$ and remove contributions from Landshoff diagrams (known also as disconnected diagrams) like that shown in Figure 2.3. The last assumption limits the corrections from binding of the constituents in the hadron and from soft wave function effects. It also allows us to relate the hadronic amplitude, M , for the process $AB \rightarrow CD$, to the constituent amplitude, M_n , describing the analogous free constituent process. This can be seen by using the Bethe Salpeter formalism, where the hadronic amplitude is expressed in terms of the constituent amplitude as

$$M = \int \psi_H^\dagger \psi_H^\dagger M_n \psi_H \psi_H \prod_i^n d^4 k_i \quad (2.12)$$

where M_n is the n particle constituent amplitude from above, ψ_H is a hadronic wave function of the bound state and k_i is the momentum of constituent i . Because of the last assumption, the integrations over $d^4 k_i$ in equation 2.12 are convergent and it may be shown that M_n and M have the same behavior in s at large center-of-mass energies (large s).

The scaling laws can also be derived in terms of quark rescattering as described by Carlson [13]. Consider elastic ep scattering. An example of a lowest order PQCD diagram is shown in Figure 2.4 where a virtual photon with four-momentum q^μ strikes a quark in the nucleon. This quark then rescatters with other quarks in the nucleon via a hard gluon exchange. The scaling in q may be counted by noting the following:

- Each internal gluon propagator scales as $1/q^2$.
- Each internal fermion propagator scales as $1/q$.
- Each external quark line is given a Dirac spinor and thus scales as q if helicity is conserved.

The amplitude for this diagram scales as

$$M \sim q^4 \frac{1}{q^2} \left(\frac{1}{q}\right)^2 \left(\frac{1}{q^2}\right)^2 = q^{-4} \sim \sqrt{s}^{-4} \quad (2.13)$$

Equations 2.11 and 2.13 combine to give the simple scaling result of Equation 2.7.

The scaling laws seem to be successful in describing the fixed angle energy dependence of a number of processes. The comparisons with several processes such as $\gamma p \rightarrow \pi^+ n$ [14], $\gamma p \rightarrow \pi^0 p$ [15], $pp \rightarrow pp$ [16] and $\gamma d \rightarrow pn$ [20] are summarized in Table 2.1. Evidence

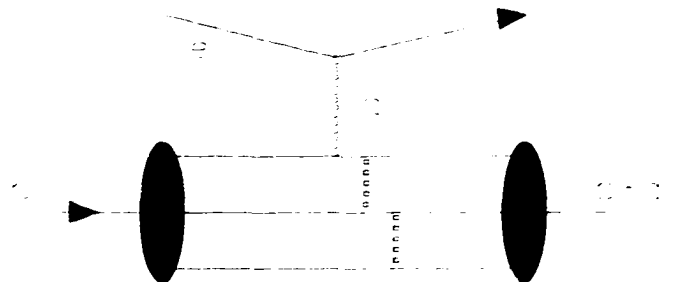


Figure 2.4: Electromagnetic form factor of the proton in the PQCD picture.

that the scaling laws do indeed give an accurate description of hadronic processes is perhaps most dramatically seen in the elastic pp scattering data shown in Figure 2.5. These data are consistent with scaling law predictions over a wide range of center-of-mass angles and energies. However, hadron helicity measurements performed on elastic pp scattering show that this helicity is not conserved [21]. Note that another prediction of asymptotic QCD is that hadron helicity is conserved in high energy processes [2]. Although such an analysis is difficult, it is believed that the non-zero hadron helicity measured in this reaction indicates that the reaction is dominated by Landshoff terms [22]. An interesting treatment of elastic pp scattering at near forward angles is given by Sotiropoulos and Sterman [10].

Process	θ_{cm}	Predicted s Dependence	Measured s Dependence	Energy Range
$\gamma p \rightarrow \pi^+ n$	90°	-7	-7.3 ± 0.4	$s \sim 1 \rightarrow 20 \text{ GeV}^2$
$\gamma p \rightarrow \gamma p$	45°	-6	-5.9 ± 0.3	$8 < s < 10 \text{ GeV}^2$
$\gamma p \rightarrow \pi^0 p$	90°	-7	-7.6 ± 0.3	$8 < s < 10 \text{ GeV}^2$
$pp \rightarrow pp$	$38^\circ < \theta_{cm} < 90^\circ$	-10	-9.7 ± 0.5	$s \sim 15 \rightarrow 60 \text{ GeV}^2$
$\gamma d \rightarrow pn$	90°	-11	-11.0 ± 0.2	$s \sim 10 \text{ GeV}^2$

Table 2.1: The measured s dependence of several processes and that predicted by the scaling laws.

The scaling observed (consistent with the asymptotic scaling law prediction) in these

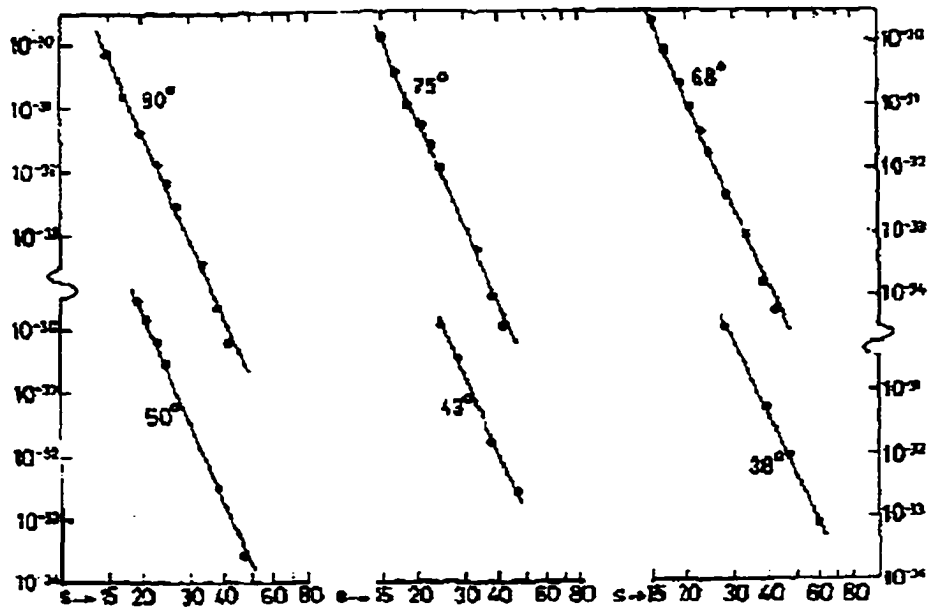


Figure 2.5: Data for the process $pp \rightarrow pp$ are shown versus s . Data are from a compilation by Landshoff and Polkinghorn [16]. Figure taken from Reference [23]. The vertical axis is $\frac{d\sigma}{dt}$ in units of $\frac{b}{\text{GeV}^2}$. The horizontal axis is s in units of GeV^2 .

hadronic reactions and the nuclear process $\gamma d \rightarrow pn$ at $\theta_{cm} = 90^\circ$ prompts the application of these scaling laws to $\gamma d \rightarrow d\pi^0$. For this process $n_d = 6$, $n_\gamma = 1$, and $n_{\pi^0} = 2$. The dimensional scaling laws (constituent counting rules) predict that the invariant cross section should obey the following relation

$$\frac{d\sigma}{dt} \sim s^{-13} f(\theta_{cm}), \quad (2.14)$$

where $n = 15$ has simply been inserted into Equation 2.7. Unfortunately, for this process, the highest energy data available with large deuteron center-of-mass scattering angles are from Imanishi *et al.* [24, 25], and a single unpublished measurement at $\theta_{cm} = 90^\circ$ from SLAC NE-17 [26]. These data extend only up to incident photon energies of ~ 1 GeV. The data are shown in Figures 2.6 and 2.7; note that the largest incident photon energies are of order of 1 GeV.

The dimensional scaling laws described above can also be used to model the q^2 behavior of hadronic electromagnetic form factors. For the process $eH \rightarrow eH$ the scaling laws predict

$$\frac{d\sigma}{dt}(eH \rightarrow eH) \sim s^{-2n_H} f(t/s). \quad (2.15)$$

Note that at large energy the ratio t/s is independent of energy because $t \sim s$ thus, $f(t/s)$ is dependent primarily on θ_{cm} at high energies and wide angles. The conventional definition of the spin averaged electromagnetic form factor indicates that the invariant cross section is given by

$$\frac{d\sigma}{dt}(eH \rightarrow eH) = \frac{4\pi\alpha^2 |F(t)|^2}{|t|^2} f(t/s) \quad (2.16)$$

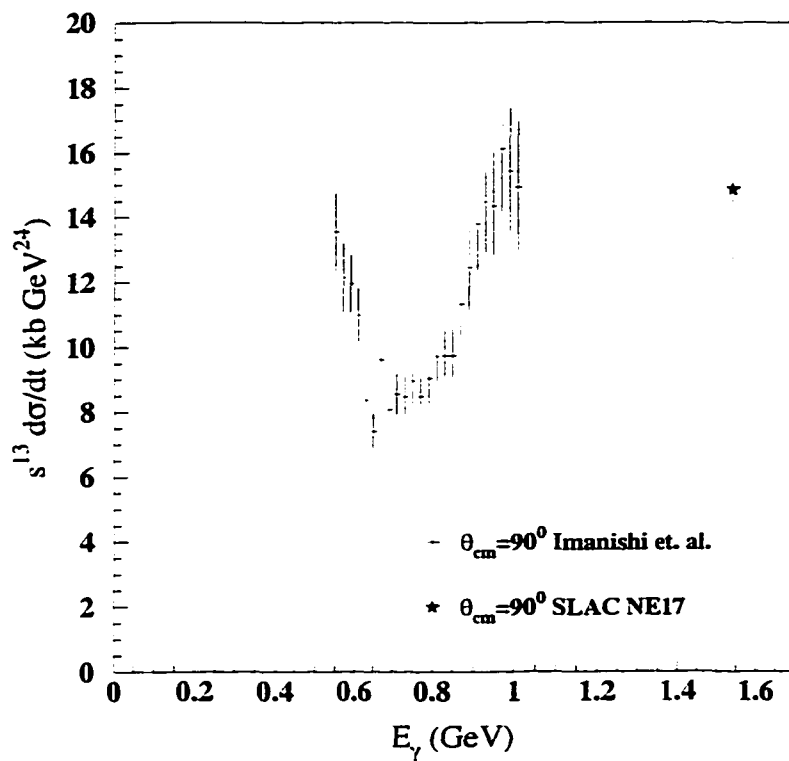


Figure 2.6: Data for the process $\gamma d \rightarrow d\pi^0$ at $\theta_{cm} = 90^\circ$. The data are from References [24] and [26].

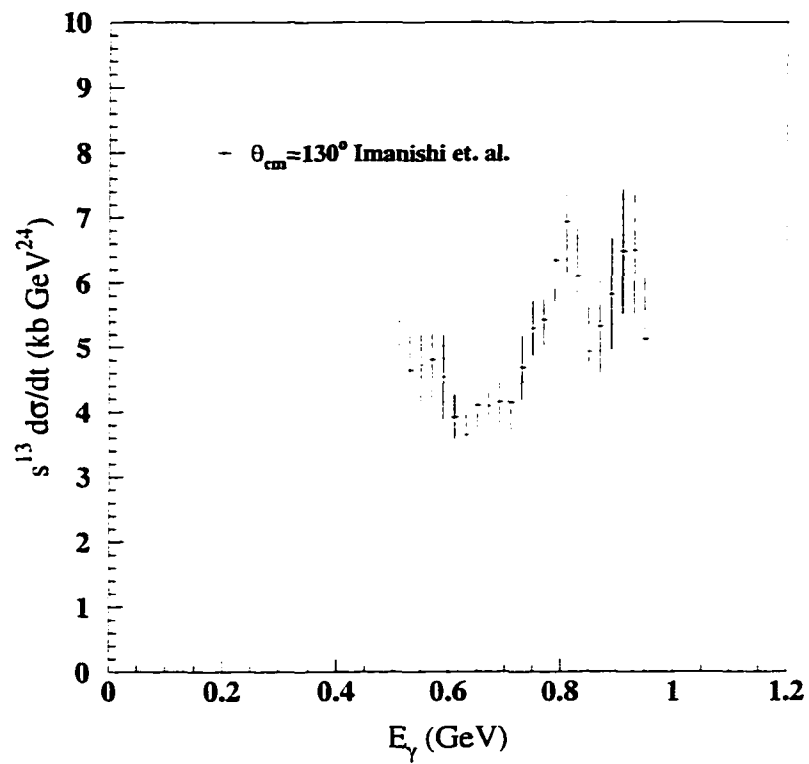


Figure 2.7: Data for the process $\gamma d \rightarrow d\pi^0$ at $\theta_{cm} = 130^\circ$. The data are from Reference [24].

Combining Equations 2.15 and 2.16 while keeping t/s fixed implies

$$|F(t)|^2 \sim t^{1-n_H}. \quad (2.17)$$

at large t .

Although there has been much controversy [27, 28, 29], which is discussed in Section 2.5, the data in Figure 2.8 seem to show that the dimensional scaling laws work well when describing the form factors of the pion and nucleons when $q^2 \approx (\text{few}) \text{ GeV}^2$. Note however, that scaling for the deuteron form factor (if indeed this form factor does scale) has not yet been reached². This may not be surprising when the momentum transfer to the individual nucleons in elastic electron deuteron scattering is compared to that of elastic electron proton scattering in the region of Q^2 where the nucleon form factors have been observed to scale. Even at the highest momentum transfers shown, the average momentum transfer to the individual nucleons is only $t_N^{ed} \approx -1 \text{ GeV}^2$ whereas in ep scattering the data do not start to scale until this same momentum transfer, $t_N^{ep} = q^2 \approx -4 \text{ GeV}^2$. The fact that the scaling laws cannot explain the deuteron form factor data, shown in Figure 2.8, led Brodsky and Chertok [30, 31] to develop the reduced form factor approach in an attempt to produce scaling at lower momentum transfers.

2.3 Reduced Nuclear Amplitudes

In the asymptotic scaling model, the deuteron is treated as a composite system of six quarks in a “bag” where constituent binding inside the nucleons is ignored (see Figure 2.9 (a)). If, however, the nucleons are allowed to retain their identity, the color selection rules of

²Recent preliminary results from TJNAF indicate that at higher energies the form factor does seem to scale with the predicted power of q (see Reference [32]).

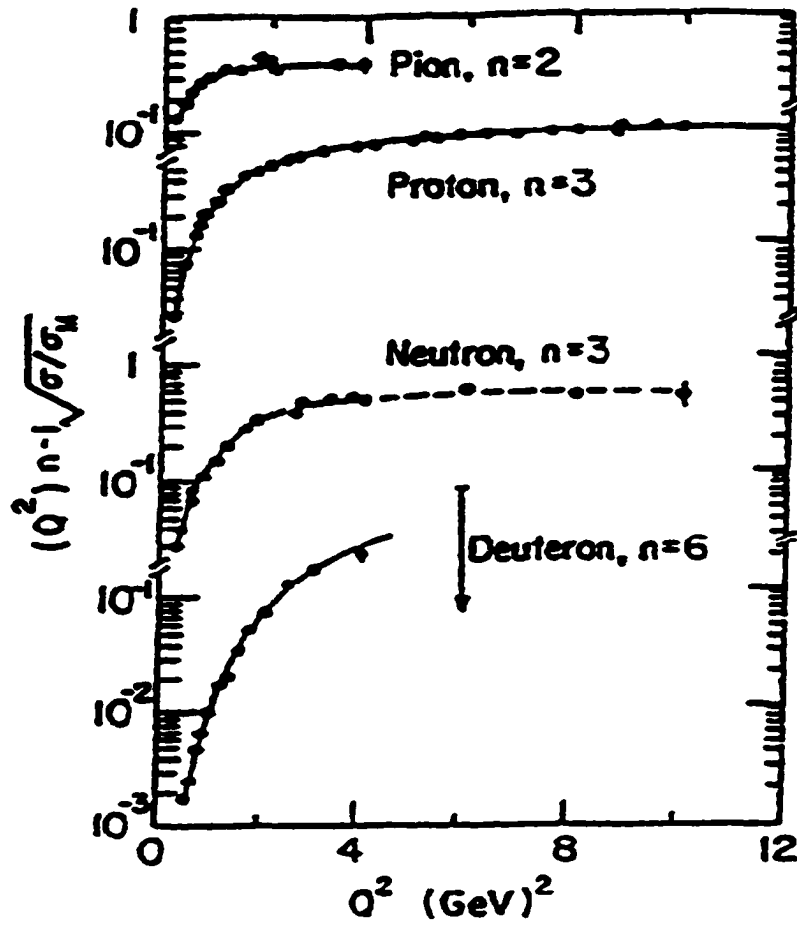


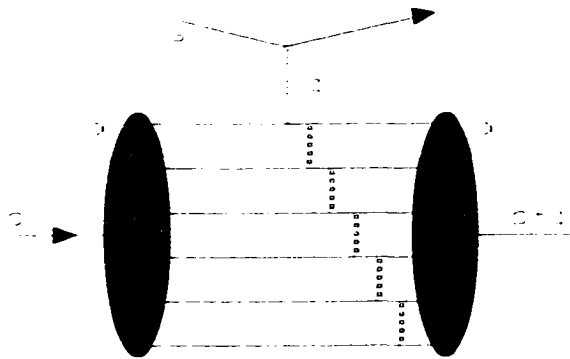
Figure 2.8: Various hadronic form factors multiplied by the PQCD predicted scaling behavior $(Q^2)^{n_H-1} F_H(Q^2)$ Figure taken from Reference [23].

SU(3) would be violated with a single gluon exchange between the color singlet nucleons. An interaction between the neutron and the proton must include a quark interchange, an example of which is shown in Figure 2.9 (b). Brodsky and Chertok, when considering the deuteron electromagnetic form factor, indicate that if the binding in the individual nucleon has a different mass scale than that of the interaction between the two nucleons then it is natural to try to separate two types of interactions. In this Section, a brief description is given of the reduced form factor developed by Brodsky and Chertok [?, 31] and later, of the general treatment of reduced nuclear amplitudes developed by Brodsky and Hiller [33].

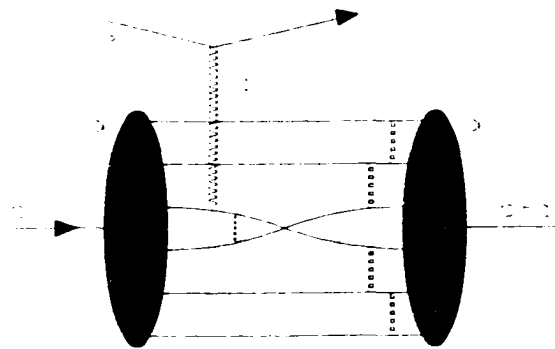
The principle of this theory is to remove the soft wave function effects from the hadronic amplitude (which are assumed to be contained in the hadronic form factor) by factoring out the hadronic form factors of those hadrons in the initial state. To see this more clearly, consider first the form factor for the deuteron. Following the prescription of Brodsky and Chertok, it is noted that the deuteron form factor $F_d(Q^2)$ is the probability amplitude for the deuteron to remain intact after absorbing four momentum q and where $Q^2 = -q^2$. If the binding of the nucleons to each other is neglected, the deuteron can be represented by two nucleons that each have half the total momentum of the deuteron. Hence, the deuteron form factor includes the probability that the nucleons remain intact after each absorbing $\sim \frac{1}{2}$ of the momentum transfer. This insight spawns the definition of the reduced form factor for the deuteron

$$f_d(Q^2) \equiv \frac{F_d(Q^2)}{F_p(Q^2/4) F_n(Q^2/4)} \quad (2.18)$$

where F_p and F_n are the familiar dipole form factors of the proton and neutron respectively. Any internal degrees of freedom of the nucleons are now removed from the measured form factor, by essentially reducing them to point-like spin-1/2 fermions. The reduced form factor still contains the probability that the scattered nucleons reform into the ground state



(a) Example of a diagram showing the six quark bag picture where binding is ignored



(b) Example of a diagram showing a quark interchange

Figure 2.9: Two different diagrams for elastic ed scattering.

of the deuteron and must (like the full form factor) be a decreasing function of q^2 . Brodsky and Chertok predict that the reduced deuteron form factor should behave (for large q) as

$$f_d(Q^2) \sim \frac{1}{Q^2 - m_0^2} \quad (2.19)$$

where $m_0^2 = 0.28 \text{ GeV}^2$ and comes from a fit to the pion form factor data. This is indeed an important prediction of QCD and implies that the reduced form factor of the deuteron has the same monopole Q^2 dependence as the meson form factor. The success of this approach is best summarized by a comparison of the reduced form factor in Equation 2.19 to data from References [34] and [35], as shown in Figure 2.10.

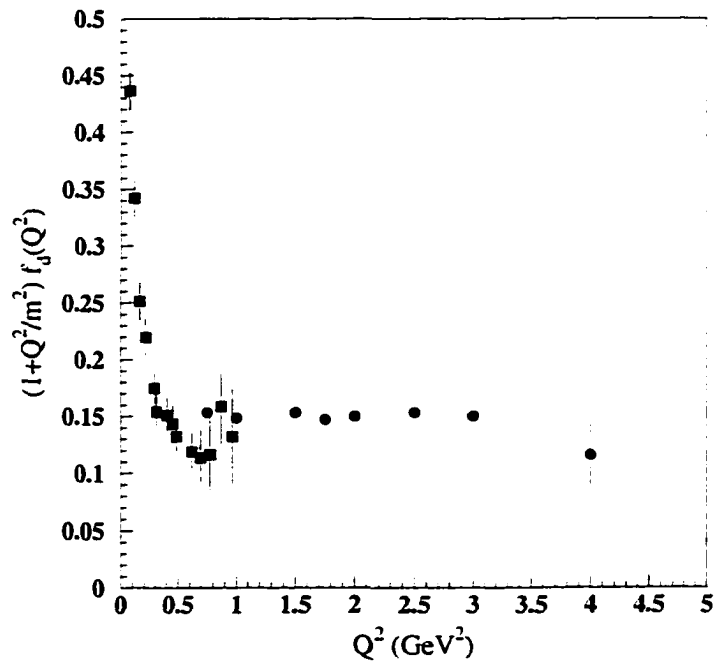


Figure 2.10: Reduced form factor of the deuteron multiplied by its predicted scaling from Equation 2.19. Data are from References [34] and [35].

The apparent success of this model led Brodsky and Hiller [33] to develop the general treatment of reduced nuclear amplitudes. In general, the reduced nuclear amplitude is defined as

$$m(s, t) = M(s, t) \left[\prod_{i=1}^A F_i(\hat{t}_i = q_i^2) \right]^{-1} \quad (2.20)$$

where A is the number of nucleons that are in both the initial and final states and q_i is the four momentum transfer to nucleon i . The large s fixed angle behavior of the reduced amplitude, $m(s, t)$, is predicted by the scaling laws (described in Equation 2.7) to be

$$m \sim p_T^{4-n} f(\theta_{cm}) \quad (2.21)$$

where p_T is the transverse momentum given in Equation 1.8 and $f(\theta_{cm})$ is a function that at most is only logarithmically dependent on s (note that $p_T \sim \sqrt{s}$ at high energies). Here, n is the number of elementary fields (leptons, photons ...) in the initial and final states with the exception that each nucleon has been reduced to one elementary field (constituent). Essentially, the effects of the composite nature of the nucleons involved in the process have been removed with their form factors.

Direct use of Equations 2.20, 2.21, and 1.9 gives for the center-of-mass cross section

$$\frac{d\sigma}{d\Omega} \sim \frac{|\vec{p}_f|}{64\pi^2 s |\vec{p}_i|} p_T^{(8-2n)} f^2(\theta_{cm}) \left[\prod_i^A F_i(q_i^2) \right]^2. \quad (2.22)$$

As an example, consider the process $\gamma d \rightarrow pn$. For this process, $n = 5$ and $A = 2$. Since binding has been neglected, the four momentum transferred to the neutron and proton may be written as

$$q_n^2 = \left(p_n - \frac{p_d}{2} \right)^2$$

and

$$q_p^2 = \left(p_p - \frac{p_d}{2}\right)^2.$$

by using the correct phase space factor, the center-of-mass cross section may be written

$$\frac{d\sigma}{d\Omega_{cm}} \sim \frac{1}{\sqrt{s(s - m_d^2)}} F_n^2(q_n^2) F_p^2(q_p^2) \frac{1}{p_T^2} f^2(\theta_{cm}).$$

Figure 2.11 shows that the data are inconsistent with the reduced nuclear amplitude prediction that $f^2(\theta_{cm})$ (shown as a dashed line) should have at most a logarithmic dependence on energy.

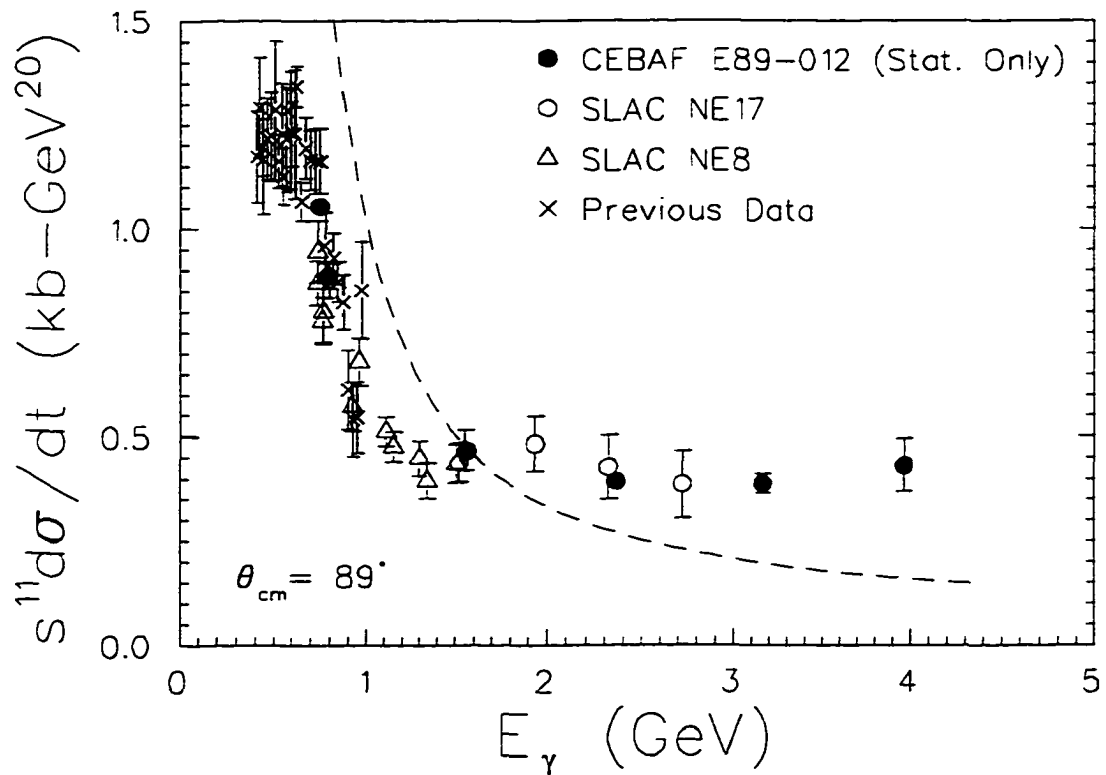


Figure 2.11: Data for the reaction $\gamma d \rightarrow pn$ for $\theta_{cm} = 90^\circ$. Data are from References [17, 18, 19] and [20]. The solid curve in the figure indicates the reduced nuclear amplitude prediction normalized to the $E_\gamma = 1.6$ GeV point. Figure courtesy of B. P. Terburg.

This partial success inspires the application of reduced nuclear amplitudes to the process $\gamma d \rightarrow d\pi^0$. The number of elementary fields in this case is 7; thus, the reduced amplitude is expected to scale as

$$m_{\gamma d \rightarrow d\pi^0} \sim p_T^{-3} f(\theta_{cm}).$$

With the proper phase space factor, the function $f(\theta_{cm})$ should behave at large s as

$$f^2(\theta_{cm}) \sim \frac{d\sigma}{d\Omega_{cm}} \left[F_n^2(q_n^2) F_p^2(q_p^2) \right]^{-1} p_T^6 \frac{s |\vec{p}_i|}{|\vec{p}_f|}$$

where q_n and q_p are given by

$$q_n^2 = q_p^2 = \left(\frac{p_f}{2} - \frac{p_i}{2} \right)^2.$$

Here p_f and p_i are the final and initial four momenta of the deuteron. The conventional dipole formula for the nucleon form factor will be used in the analysis and is given by

$$F_N(q_N^2) \propto \frac{1}{(1 - q_N^2 / (0.71 \text{ GeV}^2))^2}. \quad (2.23)$$

2.4 Meson Exchange Calculations

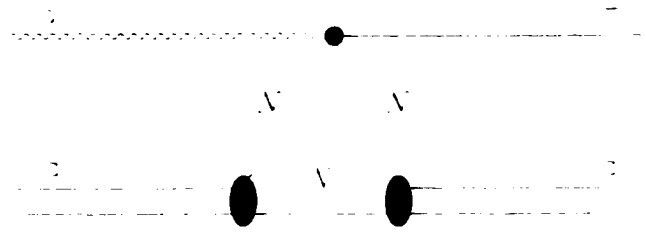
In addition to the predictions of the PQCD models mentioned above, there also exist numerous models that employ conventional meson exchange theory to describe the process $\gamma d \rightarrow d\pi^0$. Many of these models focus on the energy region near threshold and do not apply in the energy range above a few hundred MeV [36, 37, 38]. The models that describe the interaction above threshold accurately are still not considered appropriate in the energy

region above 1 GeV , and will only briefly be mentioned here.

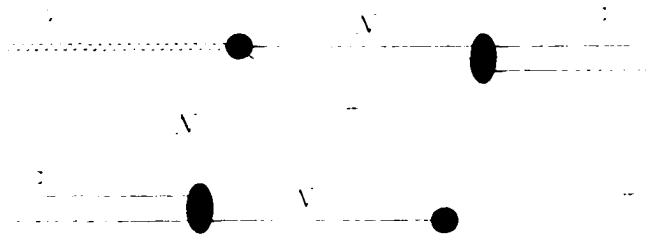
A model using Glauber multiple scattering theory and allowing for a possible dibaryon resonance term was developed by Imanishi *et al.* [24, 25] in an effort to describe experimental data gathered by the same collaboration. There are three basic terms, shown in Figure 2.12, considered in their treatment. The first two diagrams are the familiar single and double scattering graphs; the third is the dibaryon resonance diagram which was also included in their final analysis. Their model describes the data at large angles quite well for energies below $E_\gamma \approx 900 \text{ MeV}$, but predicts cross sections larger than those observed at higher energies.

The more recent model of Garcilaza and Moya de Guerra [39] does not include the controversial dibaryon resonance term. Both single and double scattering terms, shown in Figure (a) and (b), are used in a fully relativistic spectator-on-mass-shell prescription. A chiral Lagrangian, consistent with gauge invariance is used which includes contributions from the delta resonance and vector mesons ρ and ω . Unfortunately, this model also fails to accurately describe the data for energies above $E_\gamma = 800 \text{ MeV}$.

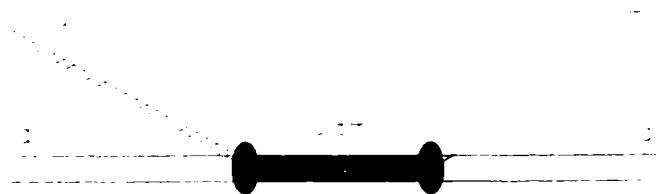
The failure of these models at high energy demonstrates the lack of understanding of the hadronic wave function at short distances. Some hope for understanding the process $\gamma d \rightarrow d\pi^0$ in terms of meson and baryon degrees of freedom comes from the model of Nagornyĭ *et al.* [40] for the photo disintegration of the deuteron. In their model, a Lorentz and gauge invariant field theory is used to avoid problems stemming from the lack of knowledge of the hadronic wave functions at short distances. This is done by calculating dNN vertices with meson and baryon degrees of freedom in the asymptotic limit. Their model for the process $\gamma d \rightarrow pn$ describes the data well and predicts the same scaling behavior that the asymptotic scaling laws do for $\theta_{cm} = 90^\circ$. Unfortunately, a calculation of this type for the process $\gamma d \rightarrow d\pi^0$ does not yet exist [41].



(a) Single scattering term



(b) Double scattering term



(c) Dibaryon resonance term

Figure 2.12: Three diagrams considered in the analysis of Imanishi *et al.* [24] for the process $\gamma d \rightarrow d\pi^0$. (a) and (b) show the single and double scattering terms. (c) depicts the dibaryon resonance term.

2.5 Applicability of PQCD to Hadronic Processes

The models described in Sections 2.2 and 2.3 are believed to be valid for large momentum transfer processes. There are two factors that must be considered when determining the applicability of PQCD. First is the relative contribution of nonperturbative effects. These effects should, at high Q^2 ($Q^2 = -q^2$ where q^μ is the four-momentum transfer), be suppressed by Sudakov effects (see Section 2.1.3). This suppression is not quantitatively well known however, due to our lack of knowledge of the hadronic wave function. The second is the validity of the perturbative expansion.

The PQCD expansion

$$a_0 + a_1\alpha_s(Q_{eff}^2) + a_2\alpha_s(Q_{eff}^2) + \dots$$

converges quickly for values of $Q_{eff} \gg \Lambda \sim 200 \text{ MeV}$ where Q_{eff} is the effective momentum transfer. The substitution for $Q_{eff} \rightarrow Q$ is more precise in the low Q limit and may be dropped in the high Q limit. For a large transverse momentum process, Q_{eff} is given by the momentum flow in the hard amplitude [2]. The ratio Q_{eff}/Q can vary depending on the x dependence of the distribution amplitude (where x is the fraction of the total hadronic momentum carried by a constituent). For more asymptotic distributions, $Q_{eff}/Q \approx 0.2$ but larger distributions can give a ratio a small 0.1. This causes serious problems for analysis of lower momentum transfer processes such as hadronic form factors at available Q^2 .

The difficulties in analyzing hadronic form factors using perturbative methods were highlighted by Isgur and Llewellyn Smith [?, 28, 29]. They note that in their analysis of pion and nucleon form factors, wave functions with large intrinsic transverse momentum, k_\perp , are needed to explain the data. The values of $\langle k_\perp^2 \rangle^{\frac{1}{2}}$ needed are such that a necessary

condition for PQCD to be valid, $Q \gg \langle k_{\perp}^2 \rangle^{\frac{1}{2}}$, no longer holds [2]³. More importantly, they show that, with more physical wave functions, conventional QCD sum rules predict nonperturbative contributions which are of the same order of magnitude as the data. Figure 2.13 shows a comparison of models using soft nonperturbative effects and those using PQCD with data for the proton magnetic form factor G_M^p . (Note that for all model calculations shown in the figure, the more physical wave functions with $\langle k_{\perp}^2 \rangle^{\frac{1}{2}} \approx 300 \text{ MeV}$ are used.) This analysis, although also uncertain due to our lack of knowledge of the hadronic wave function, brings into question the validity of PQCD at intermediate energies.

2.5.1 QCD Sum Rules for $\gamma p \rightarrow \gamma p$

A recent analysis of wide angle Compton scattering off the proton ($\gamma p \rightarrow \gamma p$) by Radyushkin [42, 43] also gives strong arguments for the dominance of soft effects in this intermediate energy range. In this model, Radyushkin suggests that the wide angle Compton amplitude is dominated by handbag diagrams which describe a single hard quark-photon vertex and a bag model for the remainder of the proton that can be described by nonforward double distributions by QCD sum rules. These distributions can, in turn, be related to the parton densities and nucleon form factors. This can be later simplified by ignoring the transverse part of the hard contribution such that the process can be described by the parton densities supplemented by a form factor type t dependence. While this model accounts for only $\sim 50\%$ of the amplitude of the $\gamma p \rightarrow \gamma p$ data, it correctly predicts the angular dependence as shown in Figure 2.14. The curves in the figure indicate the calculated angular dependence of the invariant cross section, $\frac{d\sigma}{dt}$, for the given incident photon energies. Shown

³Lepage and Brodsky [7] argue that asymptotic Q is such that $1 \gg (1-x) \gg m/Q$, where $(1-x)$ relates to the transverse momentum in the hadronic wave function, which is analogous to the condition $Q \gg \langle k_{\perp}^2 \rangle^{\frac{1}{2}} \gg m$.

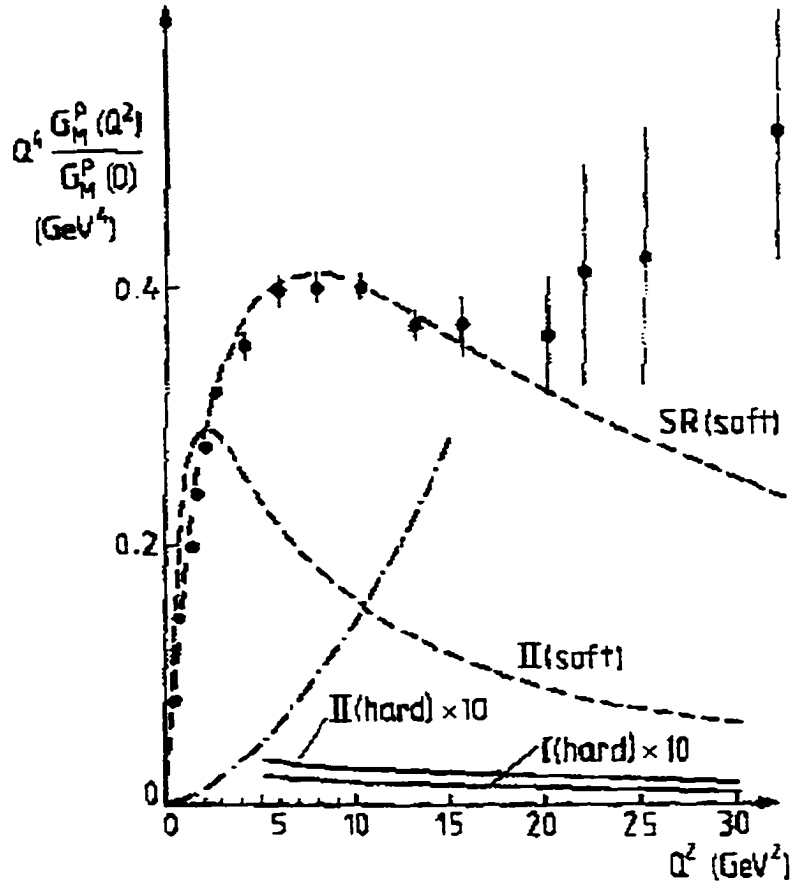


Figure 2.13: Various model calculations of the proton magnetic form factor G_M^p . The curves labeled hard are for a PQCD treatment of the form factor. The curves labeled soft are from calculations including only soft wave function effects. The figure is from Reference [28].

in this figure as $s^{-6} \frac{d\sigma}{dt}$, the curves intersect at a point near $\theta_{cm} = 60^\circ$ which is in good agreement with the data. Because the calculation predicts a dependence of the invariant cross section on s of the form $s^{-n(\theta_{cm})}$ (where the exponent $n(\theta_{cm})$ varies with the center-of-mass scattering angle), the curves for different photon energies separate as θ_{cm} deviates from $\cos(\theta_{cm}) \approx -0.6$. This feature (n having an angular dependence) is also seen in the data even though the calculated cross sections differ from the measured ones by roughly a factor of 2. This result is profound and in and of itself brings into question the predictions of the constituent counting rules and the application of PQCD in the intermediate region. A similar type of analysis is being considered for the $\gamma d \rightarrow pn$ reaction where the s dependence of the invariant cross section is also seen to vary with center-of-mass angle [44].

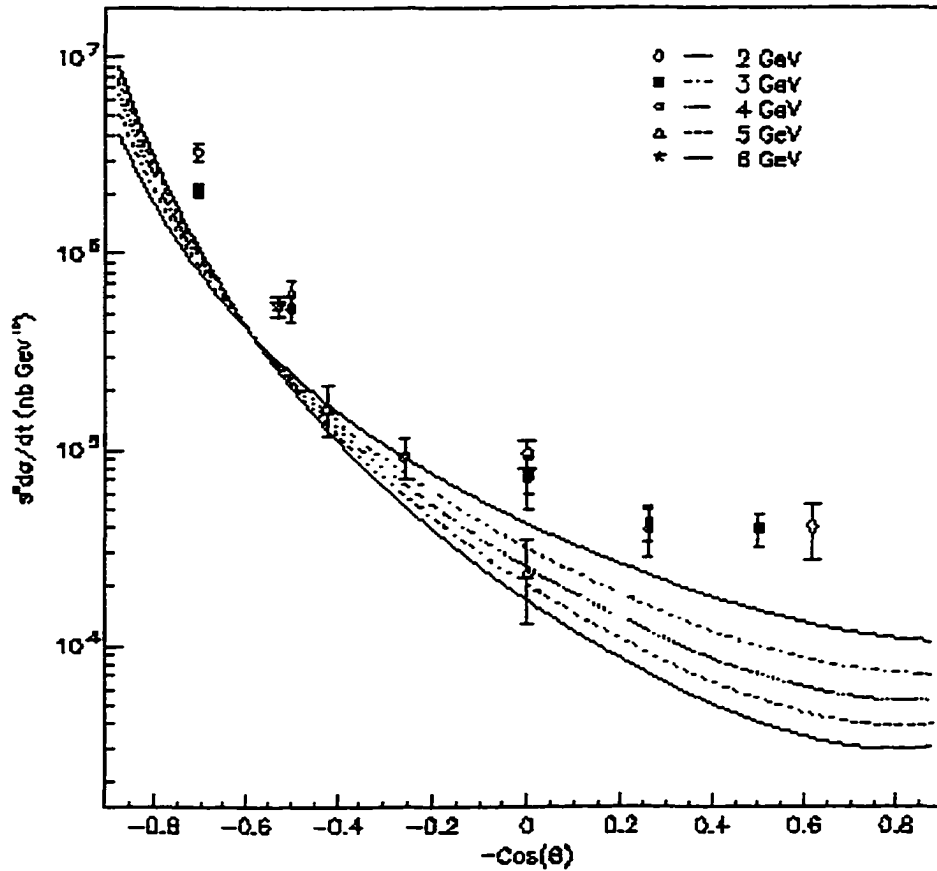


Figure 2.14: Angular dependence of Compton $\gamma p \rightarrow \gamma p$ data. Curves are from a model by Radyushkin [42]. The curves in the figure indicate the calculated angular dependence of the cross section for a given incident photon energy. Figure courtesy of A. Radyushkin [45].

Chapter 3

Experiment

3.1 Overview

Experiment E89-012 was performed in experimental Hall C at the Thomas Jefferson National Accelerator Facility (TJNAF) during three consecutive months in the Spring of 1996 and in short subsequent runs ending in the Fall of 1997. TJNAF (formerly CEBAF) was designed to produce an electron beam of 4.0 GeV with a current of 200 μA and near 100% duty factor. It was also designed to provide beam to three experimental endstations simultaneously. During the first part of E89-012, Hall C was the only endstation in operation and as such received 100% of the beam available in the accelerator. During later phases of the experiment, beam was being supplied to all three experimental halls. Two spectrometers, the High Momentum Spectrometer (HMS) and the Short Orbit Spectrometer (SOS) had been commissioned and were available for use during the experiment. For the measurement of the process $\gamma d \rightarrow d\pi^0$, there was no effort to detect the π^0 or its decay products and the HMS was used, in single arm mode, to detect the deuteron in the final state. In total, the differential cross section for the process $\gamma d \rightarrow d\pi^0$ was measured at incident

electron energies of 0.845 GeV to 4.045 GeV for deuteron center-of-mass scattering angles of $\theta_{cm} = 90^\circ$ and 136° .

3.2 Accelerator

The Continuous Electron Beam Accelerator Facility (CEBAF) at TJNAF utilizes two superconducting radio frequency (RF) linear accelerators (LINACs) in combination with two recirculating arcs as schematically shown in Figure 3.1. The electron beam may be recirculated through the 7/8 of a mile long accelerator loop a maximum of five times. At present the accelerator is capable of delivering up to $200 \mu\text{A}$ of 4.0 GeV beam. The resulting beam may then be separated, with some flexibility for both currents and energies, into any combination of the three experimental halls.

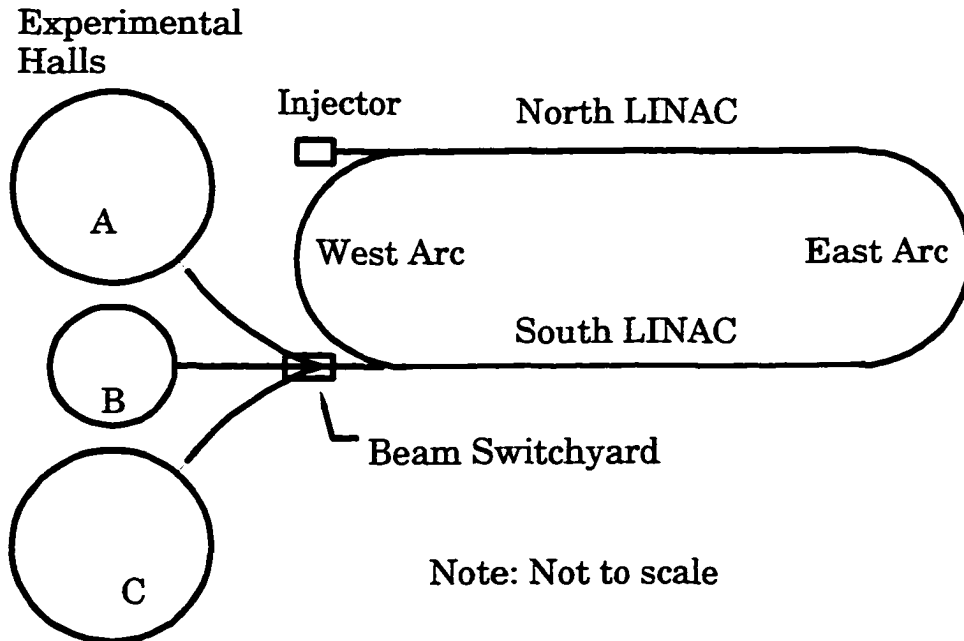


Figure 3.1: Overview of CEBAF showing accelerator and three experimental endstations. The electron beam enters the accelerator at the injector and travels around the accelerator loop in a clockwise direction (if viewed from above).

The electron beam is generated in the injector and enters the accelerator, with an energy of ~ 45 MeV (for the standard tune), at the West end of the North LINAC. With the standard machine tune, each pass through one of the LINACs adds an additional 400 MeV to the beam. A complete circuit of the accelerator adds a total of 800 MeV to the electron beam energy. The recirculated electron beam is placed on top of itself in each of the two LINACs and the resultant beam may be composed of as many as five beams all with different energies. Because the beam (when composed of multiple passes) in the LINAC is not monochromatic, it must be separated into monochromatic components at the entrance to each of the arcs and then recombined at the entrance to each of the LINACs. The entrances to each arc and LINAC have a number of separate magnet strings, one for each possible pass of the beam for separation and recombination of the beam. In the beam switchyard at the end of the South LINAC, the beam may be extracted into each of the experimental halls or a special beam dump line.

Although the duty factor of the accelerator is essentially 100%, the electron beam current is not truly continuous. The beam consists of 1.67 ps long bunches which come at a frequency of 1497 MHz in the accelerator. Each of the experimental halls may receive a fraction (ranging from 0 to 1) of the total accelerator frequency which is dependent on the physics and accelerator program. The energy dispersion of the beam $\Delta E/E \leq 10^{-4}$ and the angular emittance of the beam is less than 2×10^{-9} mrad [46]. The absolute energy of the beam can be determined using the settings of the magnets in the arcs. The current in the injector can be measured in a Faraday cup, and, assuming no losses, the beam in the accelerator and in each experimental hall can then be calculated. Both the current and the energy can be more accurately determined in the Hall C arc and beamline. The method for this is discussed in the following sections.

3.3 Hall C Arc and Beamline

The beam may be extracted in the beam switchyard into the Hall C Arc and Beamline. A schematic overview of the Hall C beamline is shown in Figure 3.2. The beamline from the switchyard to the Hall C dump contains a great deal of instrumentation. In addition to the scattering chamber, target, and dump, there are numerous magnets for steering, focusing, and rastering the beam. There is also a myriad of monitors for measuring the beam current, profile and position. A Møller polarimeter was installed to measure the polarization of the beam for use in later experiments. The bremsstrahlung radiator was installed immediately upstream of the scattering chamber primarily for this experiment and provided the source of real photons for the experiment.

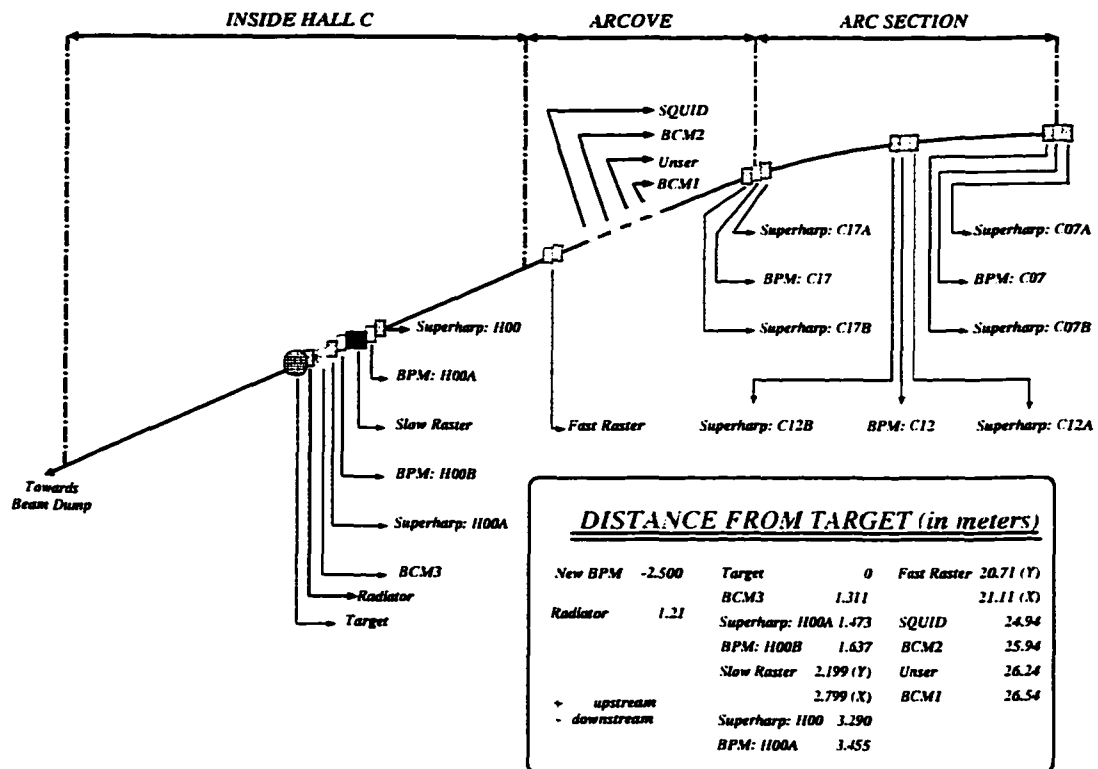


Figure 3.2: Schematic diagram of the Hall C Arc and Beamline with major instrumentation shown. Positions shown are relative to the target center.

3.4 Beam Profile and Position Measurement

Beam profile and position measurements are made using three types of monitors. Beam profile measurements are made using HARPs, which pass a thin set of tungsten wires through the beam. The super-HARPs are similar in design to the HARP and are used to measure both the beam profile and the beam position at various points in the Hall C beam-line, including three critical points in the arc. With these position measurements in the arc, the beam energy can be determined to within 1 part in 1000 (see Section 3.7). Because both the HARP and super HARP actively pass wires through the beam, the beam downstream from the device is not acceptable for most applications when the HARPs are in operation. Due to this disruption of the beam, these instruments cannot be used continuously to monitor the beam. Therefore, beam position is also monitored with cavity type monitors called BPMs (Beam Position Monitor). These monitors have the ability to passively monitor the beam position and are discussed later in this section.

The HARP is used primarily to monitor the beam profile and is shown in Figure 3.3. It does so by passing a thin set of tungsten wires through the beam. This is done remotely by using a DC stepper motor to drive a leadscrew which in turn drives the wires into and out of the beam. While the wires are passing through the beam, the electrical signal induced by the beam striking the wires is read into a CAMAC Aurora 12 Digitizer. The input to the digitizer is gated with the beam-sync to reduce noise. The positions of the wires are determined by measuring the voltage at the center tap of a linear potentiometer [47]. This voltage is read into the same digitizer giving a position measurement better than $\pm 100 \mu\text{m}$. The wire signals are then plotted as functions of their position to give the beam profile. The beam profile measurement was not crucial for the measurement of $\gamma d \rightarrow d\pi^0$ since the electron beam impinged on the radiator well upstream of the target, inducing multiple

scattering and changing the profile of the beam.

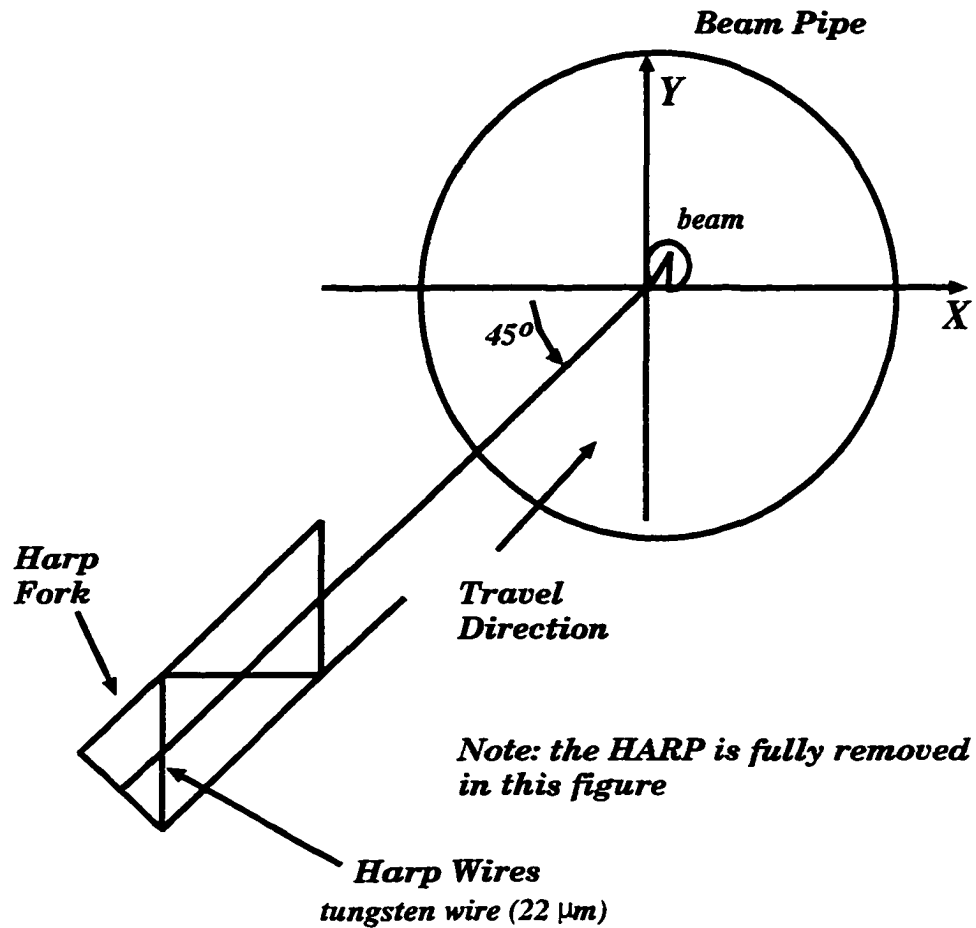


Figure 3.3: Diagram of the HARP beam profile monitor

The super-HARP is used, primarily, to accurately determine the beam position. The super HARP functions in the same manner as the HARP with the exception that the linear potentiometer has been replaced by a rotary shaft encoder to give an absolute position measurement to better than $\pm 10 \mu\text{m}$ [48]. A sample super HARP scan is shown in Figure 3.4.

The BPMs are used to continuously monitor the beam position at various places in the Hall C line and throughout the accelerator. Each BPM consists of a cavity with four

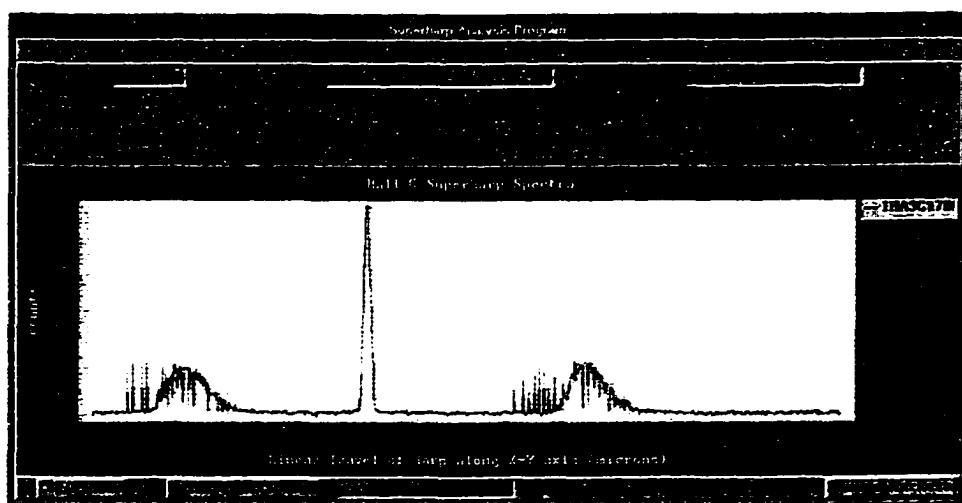


Figure 3.4: Diagram of the HARP beam profile monitor scan. The three peaks come from a pass of each wire through the beam. Note that this scan was taken with improperly tuned beam.

antennae located at $\pm 45^\circ$ with the horizontal and vertical axis as shown in Figure 3.5. These antennae absorb a signal from the fundamental frequency of the beam that is proportional in strength to the distance from the antenna to the beam. Since the position of the beam is determined from the ratio of the signals from opposing antennas, the measurement is essentially independent of the beam current. Any dependence of the position measurement on the beam current comes from nonlinearities in the electronics and is essentially removed with both hardware and software techniques. The monitor is also temperature stabilized to reduce the effects of temperature drifts on the measurement. Since these devices are not intrusive to the beam, they are used to continuously monitor the beam position. The BPM modules in the Hall C Arc were calibrated with the super HARPs. These BPM modules provide an absolute position measurement of ± 1.0 mm and a relative measurement of less than ± 0.2 mm. The BPM modules outside the arc were not calibrated against the super HARPs near them. The position of the beam on the target was verified with a camera during the experiment and after each phase by oxidation marks left on the radiator foils and

the target windows. In all phases of the experiment, the positions of the beam on the target and on the radiator were determined to be suitable and no correction was necessary.

BEAM POSITION MONITOR

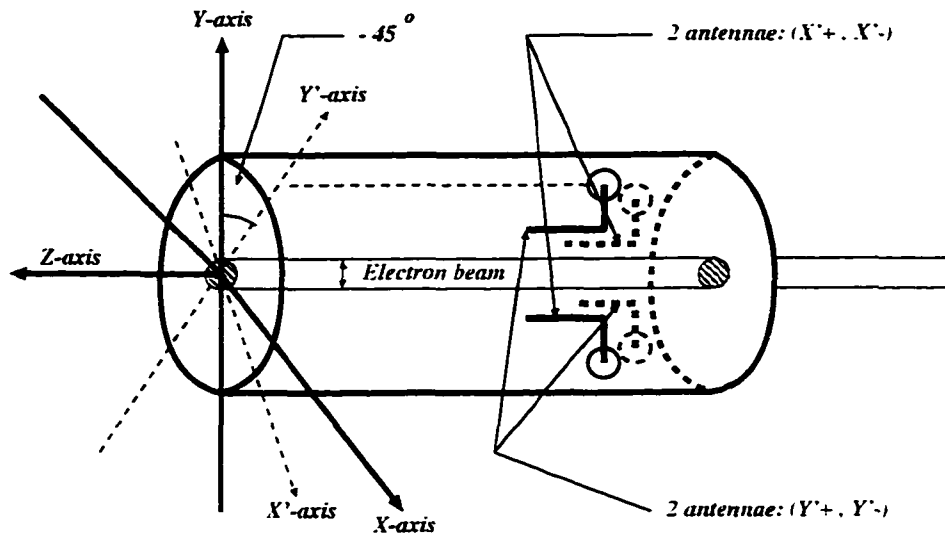


Figure 3.5: Schematic view of a BPM.

3.5 Beam Current Measurement

The beam current is measured on a Faraday cup in the injector and beam loss is monitored throughout the accelerator. If the beam loss, measured by phototubes positioned near the beam pipe, becomes larger than a preset value the beam is tripped off. While this is adequate for accelerator operations it is not accurate enough for most experimental purposes. The use of a Faraday cup in the Hall C dump is not feasible because of the large amount of power contained in a 4 GeV, 100 μ A electron beam. Thus, two other types of current monitors are used in Hall C. The beam cavity monitor (BCM) which is used to determine the integrated beam current on the target in two second increments and a parametric current

transformer (Unser monitor) which is used to calibrate the BCM modules. There are currently three BCM modules, labeled BCM 1, BCM 2 and BCM 3, and one parametric current transformer in use in Hall C.

The BCM module is a cylindrical wave guide mounted in the beamline such that the beam travels on the axis of the guide. The beam passing through the cavity excites resonant modes which are picked up by wire loop antennae. The power in the antenna is proportional to the beam current squared. The materials and dimensions of the cavity can be selected to optimize the performance of the device. The resonant frequencies of a cylindrical cavity are given by

$$f_{lmn} = \frac{\chi_{l,m} c}{2\pi R^2} \sqrt{1 + \frac{n\pi R^2}{L^2 \chi_{l,m}^2}} \quad (3.1)$$

where l, m, n are integers R and L are the radius and length of the cavity and $\chi_{l,m}$ is the l^{th} root of the m^{th} order Bessel function. For the BCMs in Hall C the radius of the cavity is 3.0465 inches [49], thus the resonant frequency $f_{0,1,0}$ is

$$f_{0,1,0} = 1483 \text{ MHz}. \quad (3.2)$$

Much of the difference between this and the fundamental frequency of the accelerator (1497 MHz) can be accounted for with modified apertures and a load antenna.

The quality (Q) factor for a cavity is the ratio of the total stored energy in the cavity to the power dissipated weighted by the frequency,

$$Q = \frac{\omega_0 E_{stored}}{P_{dissipated}}. \quad (3.3)$$

This factor is determined by the material and length of the cavity and relates the sensitivity of the amount of power in the cavity to the temperature (through the dimensions of the

cavity). The cavities were thermally stabilized to reduce the temperature dependence of the current measurement.

To read the signals from BCM 1 and BCM 2 into the data stream, the signal was first mixed down from 1497 MHz to 100 kHz. This signal was then converted by an Analog Devices rms to DC converter (AD637) [50]. The resultant DC level was amplified, shifted, and finally converted to NIM pulses with a Dymec 8410 voltage to frequency converter and TTL to NIM converter. Similar electronics were used for the readout of the parametric DC current transformer. The readback of BCM 3 is slightly different and this monitor is mainly used for accelerator and cryotarget operations.

The parametric DC current transformer or Unser monitor employs an active current transformer and a magnetic parametric amplifier in a common feedback loop as shown in Figure 3.6 [51]. The monitor consists of a toroidal sensor which fits over the vacuum beampipe, a front end electronics box containing associated electronics, and a rack mounted box that conditions the output signals and provides power and remote control to the other components. Since the toroid is sensitive to any current passing through it, a ceramic insulating vacuum nipple must be installed next to the device to insulate it from transient currents traveling through the beampipe. In simplified terms, the electron beam induces a magnetic field in the toroid that is measured by one transformer. The second transformer then drives the total flux in the toroid to zero. This compensation of the magnetic field induced by the beam is done very precisely and is used to determine the beam current passing through the toroid [52].

This device can be used for large frequency and current ranges and is relatively independent of the beam position. The Unser monitor has a very stable gain, but is subject to large drifts in the zero offset. This fact precludes the use of this monitor for experimental beam current measurement and as such, it is only used to calibrate the BCM modules. This

monitor is also thermally stabilized because it is very sensitive to temperature changes.

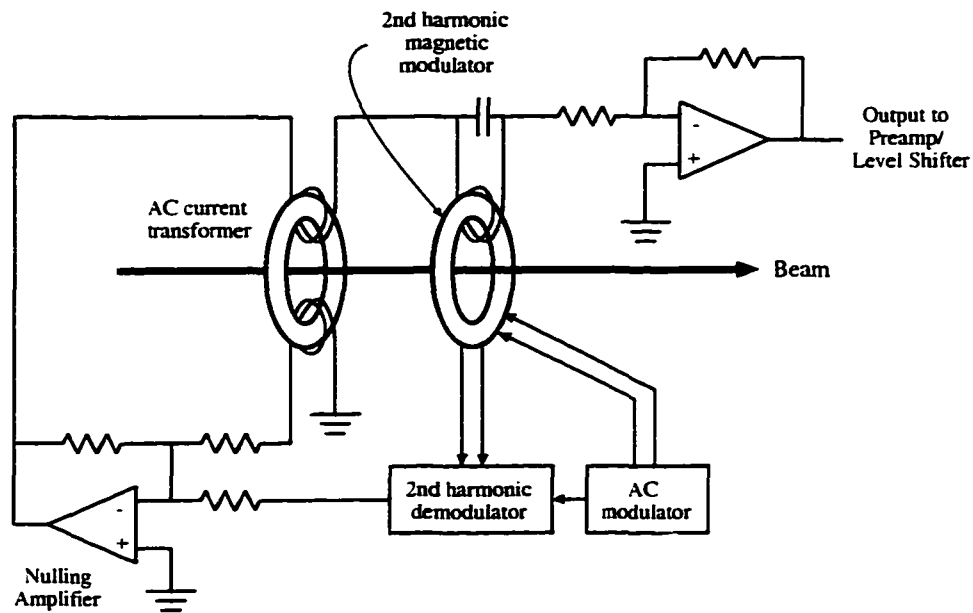


Figure 3.6: Schematic diagram of the Unser beam current monitor. Figure courtesy of C. Armstrong.

The output signal from the standard electronics for the Unser monitor is further conditioned with a preamplifier and level shifter. This shifts the Unser signal, which is nominally of order of a few mV, into a voltage range ~ 5 V. The resultant DC level is then converted to NIM pulses with a Dymec 8410 voltage to frequency converter and a TTL to NIM converter. The voltage to frequency converter is extremely linear in the middle of the 0 to 10 V input range of the device, which is the reason for shifting the DC level of the Unser output. A plot of a linearity test is shown in Figure 3.7. By using these devices for signal processing, high frequency noise is filtered out and the resultant signal is easily read by the scalers in the data acquisition system every two seconds during a run.

The Unser monitor must be absolutely calibrated prior to each experiment to accurately establish the gain of the device. This is done by passing a current on a wire installed next

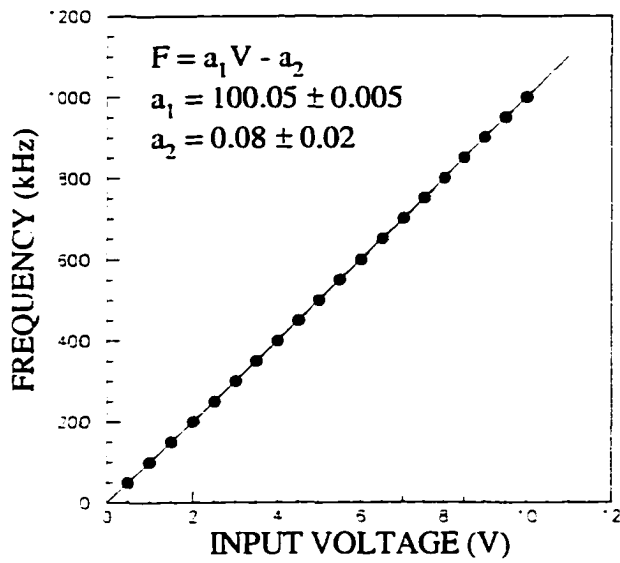


Figure 3.7: V/F linearity test. The line in the figure is a least squares fit to the data.

to the beampipe and through the toroid. Known currents of various magnitude are induced in the wire from a very stable and precise current source. It is the only current monitor that is absolutely calibrated in the Hall C beamline. Calibration of the gain of BCM modules is done by alternately running beam off and beam on through the hall in two minute intervals leaving the data acquisition system on (see Figure 3.8). Zero offsets for the Unser and BCM modules were measured during the beam off periods. During the beam on periods, the gains of the BCM modules were determined by using the known Unser monitor gain. The resulting current measurement is absolutely accurate to better than 2%.

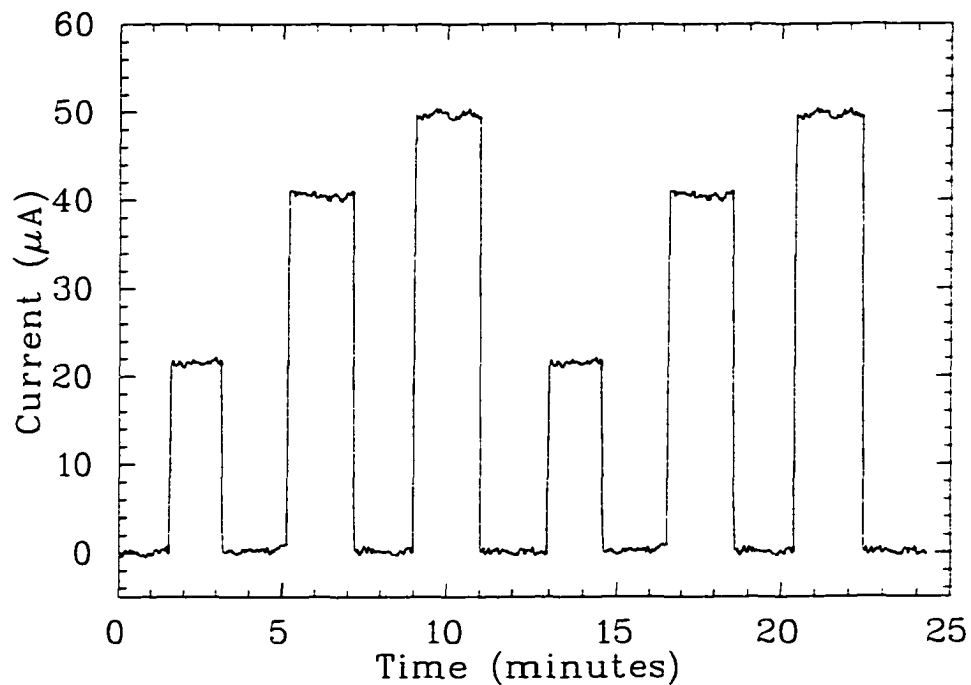


Figure 3.8: Typical beam current monitor calibration run for the Unser monitor.

3.6 Hall C Beam Rastering System

The electron beam incident on the Hall C target and beam dump has an extremely high power density. Average beam currents in Hall C during standard operations can exceed $100\ \mu\text{A}$, while the spot size of the beam entering the hall is typically less than $200\ \mu\text{m}$ in diameter. To protect the targets and dump from damage resulting from these high power densities, the beam is rastered. There are two rasters in Hall C, the fast raster and the slow raster. The slow raster is installed a few meters upstream of the scattering chamber as shown in Figure 3.2. This system was installed to protect the Hall C beam dump and was not needed during any of the running conditions for experiment E89-012; therefore, it was never used. The fast raster was used to keep local boiling of the cryotargets to a minimum and to prevent damage to the bremsstrahlung radiator.

The Hall C fast raster system consists of two sets of bending magnets mounted such that the beam is dispersed in both the horizontal (x) and vertical (y) directions. The current driving the magnets was driven sinusoidally with frequencies selected in the x and y directions such that the raster pattern is not stable (Lissajous pattern) on the target or the radiator. The resulting beam spot is approximately a rectangle with variable x and y dimensions [53]. Since the current is varied sinusoidally, the beam intensity is greatest at the edges of the rectangle. The raster pattern as measured by BPM 3H00A is shown in Figure 3.9. The raster size during all phases of the experiment was chosen to be $\pm 1\ \text{mm}$, but was not crucial since the beam striking the radiator foils was scattered into a larger spot size at the target. This raster size was more than large enough to protect the target and radiator foils from damage during all conditions of E89-012.

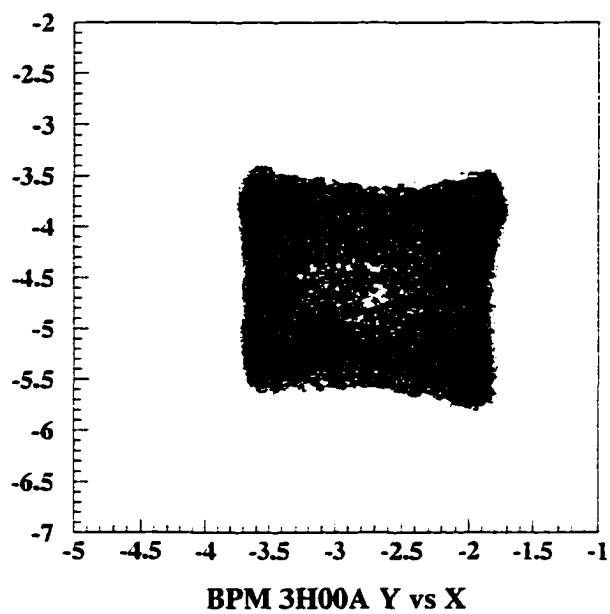


Figure 3.9: Beam raster pattern as seen by BCM 3H00A. Note the increased intensity at the edges and especially the corners of the spot. The pattern is off center (0,0) due to position offsets which have not been accounted for.

3.7 Beam Energy Measurement

Beam energy in the accelerator and the experimental halls is measured in numerous ways at TJNAF. The magnet settings in the East Arc are used to determine the nominal beam energy in each pass. The fields in these magnet strings are well known; however, this measurement is only accurate to $\sim 0.2\%$ due to the large energy acceptance and path length variations of the arc.

The Hall C arc is also used to measure the beam energy. To perform this measurement the focusing elements in the arc are turned off and the beam is directed to follow the central path through the arc. One of the magnets in the Hall C arc has been precisely field mapped. Since the other magnets in the string are the same, their fields are assumed to be similar and, hence, the total field integrated over the path length, $\int_{path} B \cdot dl$, is known to $\sim 0.3\%$. The position and trajectory of the beam is measured at the entrance middle and exit of the arc with three pairs of super HARPS (see Section 3.4). The beam energy can be measured by knowing the field throughout the length of the arc and the properties of the beam at these positions. This technique cannot be used while experimental data are being taken so fluctuations in the beam energy are measured with the BPM modules (see Section 3.4) in the arc. The absolute energy of the beam measured this way is accurate to $\sim 0.3\%$, with existing beam energy drifts of less than 0.1% [54].

In addition to these direct methods, the beam energy for single pass beam was also measured using the differential recoil method. The electron beam was directed at a BeO solid target and scattered electrons were detected using the HMS. The energy of an electron scattered off a Be nucleus is different from that of an electron scattered off an O nucleus.

The difference is given by

$$\Delta E = 2 \left(\frac{E_O}{m_O} - \frac{E_{Be}}{m_{Be}} \right) E_{beam} \sin(\theta/2) \quad (3.4)$$

where E_{beam} is the energy of the electron beam, E_O , E_{Be} are the electron energies after scattering off the O or Be nucleus, and m_O , m_{Be} are the masses of the respective nuclei.

This measurement is discussed in more detail in Reference [55].

A summary of measurements of the beam energy, using each of these techniques, is shown in Table 3.1. As can be seen in the table, the three different methods are consistent. The beam energy measurement is not crucial for experiment E89-012 because the incident photon energy is reconstructed from the recoil deuteron momentum. Errors in beam energy measurement have a negligible effect on the bremsstrahlung yield calculations and a small effect on the determined yield of photo-deuterons (see Section 5.1) therefore, only the standard accelerator tune measurement is used in the analysis.

Method	E_{beam} (MeV)
Standard Accelerator Tune	845 ± 2
Differential Recoil	844.7 ± 1.5
Hall C Arc	845.25 ± 0.7

Table 3.1: Measurements of the beam energy in Hall C using three different techniques for single pass beam.

3.8 Hall C Bremsstrahlung Radiator

To provide a source of real photons for the experiment, the bremsstrahlung radiator was installed 1.21 m upstream from the target. The photon beam was not tagged nor were the electrons bent out of the path of the target, permitting a much greater photon intensity. The

radiator was placed close to the target to allow for accurate calculation of the high energy bremsstrahlung yield (only events with reconstructed photon energy within 100 MeV of the beam energy were considered for the cross section measurement). The opening angle of the high energy bremsstrahlung cone is roughly given by

$$\theta_\gamma \approx m_e/E_{beam}. \quad (3.5)$$

Because this angle is extremely small, it is assumed that all of the high energy photons produced in the radiator pass through the target.

The Hall C bremsstrahlung radiator is described, in detail, in Appendix A. The radiator is essentially a set of thin copper foils which can be placed in the beam remotely. There are five nominal thicknesses 2%, 4%, 6%, 7%, and 8% radiation lengths. Since the photon beam was not tagged, the integrated bremsstrahlung flux was calculated using the techniques of Matthews and Owens [56] (see Appendix B). This method calculates bremsstrahlung produced by electron-electron and electron-nucleus collisions and includes effects from energy loss in the radiator foil and the energy spread of the incident electron beam. The thicknesses of the copper foils are known to better than 0.1% and the calculated bremsstrahlung flux is believed to be accurate to better than 3%. Only the 4% and 6% radiator foils were used in production running while the other thicknesses were used primarily for calibration of the radiator itself and tests of the bremsstrahlung flux calculation.

3.9 Hall C Cryogenic Target

Hydrogen and deuterium targets must be used to perform experiment E89-012, and many others. Gaseous targets do not provide the luminosity necessary to measure small cross

sections, such as those measured in experiment E89-012. The Hall C cryogenic target (cryotarget), capable of maintaining up to three separate cryogenics as target materials, was constructed to provide high luminosity and a large degree of flexibility. The cryotarget consists of three basic subsystems. A gas handling system controls the flow, storage, release, and pressure of the target gases. The mechanical and cryogenic system consists of the vacuum components, heat exchangers, a positioning system for the target cells, and the cells themselves. The remaining subsystem contains all of the instrumentation and controls for the entire target. The operation of a cryogenic target system containing explosive cryogenics (such as hydrogen and deuterium) can be dangerous and therefore each subsystem has its own safety features, which are, in many cases, multiply redundant. Numerous upgrades were performed on the cryotarget between phases of the experiment. A brief description of the cryogenic target is given in this section; a more detailed description of the target can be found in Reference [57]. Figure 3.10 shows the cryotarget in overview.

3.9.1 The Hall C Scattering Chamber

The Hall C scattering chamber is essentially a cylindrical aluminum tank as shown in Figure 3.11. It was designed to accommodate both the cryogenic target and solid target ladder. There are two large openings on either side of the beam entrance and exit. These openings are covered with thin aluminum windows to minimize the amount of material scattered particles must pass through before entering the spectrometers. Each window on the scattering chamber is designed to match the range and acceptance of the related spectrometer. The true opening on the Shot Orbit Spectrometer (SOS) side of the chamber is much larger, vertically, than the actual aluminum window. This is to accommodate the out of plane acceptance of the SOS. Because there is no plan for the SOS to be used out of plane in the

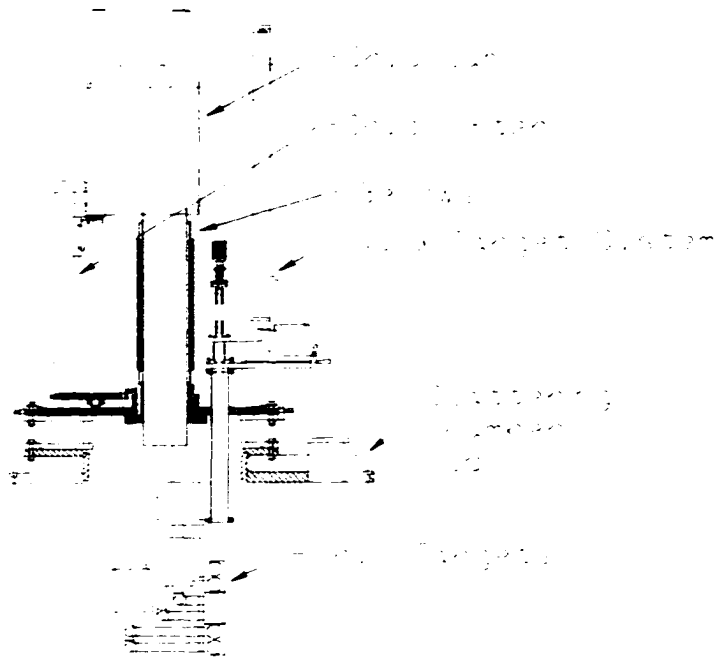


Figure 3.10: Scale drawing of the Hall C cryotarget. The scattering chamber has been removed from the figure for clarity.

near future, much of the opening on the SOS side was covered by a thick aluminum “roll up” with a slot covered by a thin aluminum window, cut out to match the SOS acceptance. The thicknesses of the aluminum windows are given in Table 3.2. Deuterons detected in the experiment are attenuated by these thin windows and a correction for this attenuation (absorption) in the High Momentum Spectrometer (HMS) side window is applied in the analysis (see Section 4.5).



Figure 3.11: Beam view of the Hall C scattering chamber. The Short Orbit Spectrometer and the High Momentum Spectrometer have been abbreviated as SOS and HMS, respectively. The external cryotarget apparatus is mounted on a rotating seal so that the target cells may be removed from the beam.

Inside Diameter	48.50 in
Wall Thickness	2.50 in
Height	53.75 in
HMS Window Thickness	0.016 in
SOS Window Thickness	0.008 in

Table 3.2: Characteristics of the Hall C scattering Chamber.

A vacuum, typically on the order of a few $\times 10^{-6}$ torr, is maintained in the scattering chamber by a TMP-1000 Turbovac turbomolecular pump backed by a Leybold Trivac D65B roughing pump. The vacuum reduces multiple scattering of the beam and minimizes the conductive heat load of any atmosphere surrounding the cryogenic target. The vacuum is measured with a cold cathode gauge connected to a MKS controller. The controller has an analog output that is monitored by the target control system. It also provides a vacuum limit switch that closes a relay when the pressure in the scattering chamber is too high. The relay trips the beam by providing a machine Fast Shut Down (FSD) signal and also closes the gate valve at the entrance of the scattering chamber.

3.9.2 Mechanical Aspects of the Hall C Cryogenic Target

The cryogenic target is designed to maintain up to three separate cryogens in three self contained loops. Under normal operating conditions, the top and bottom loops are filled with liquid hydrogen and liquid deuterium respectively and the middle loop is typically filled with gaseous ^4He . There are four Joules Thompson (JT) valves installed in the system to control the flow of the precooling nitrogen and the coolant helium. Two target cells of different lengths are attached to a cell block installed in each of the loops. The target material in each loop is circulated with a screw type pump through the heat exchanger, where the target fluid is cooled, the cell block and both cells. Cold components of the target are wrapped in super-insulation to reduce the radiative heat load on the target. The target cells are remotely positioned in the beam by the target lifting and rotation system.

Target Loops

A typical target loop is shown in Figure 3.12. Each loop consists of a heat exchanger, a cell block, two cells, two heaters, a pump, and piping. The coolant fluid is piped through fin-tubing enclosed in the heat exchanger as shown in Figure 3.13. The target fluid is directed to flow over these fin tubes so that heat may be removed from the target. The fluid is moved by a screw type pump or fan; the motor for which is immersed in the target fluid. Power for the pump was supplied through vacuum electrical feedthroughs during the first phases of the experiment by a Variac and is presently supplied by a variable frequency drive controller. The temperature in the loop is controlled with the use of two heat-gun style heaters (high power heater and low power heater). Two cells of different lengths are attached to the cell block installed in the lower portion of the loop. The short and long cells were installed to match the extended target acceptance of each of the spectrometers. For this experiment, the extra luminosity provided by the extended cell aids in the measurement of the small cross sections; hence, only the long cell was used. The length of the long cell was initially 15 cm nominally. However, during later phases of the experiment the nominal length of the long cell was 12 cm.

The length of each cell was carefully surveyed both at room temperature and at operating temperature to correct for any thermal contraction. Figure 3.14 shows a close up view of a single cell block used during the later phases of the experiment with a long cell length of 15 cm. Critical dimensions of each cell used during all phases of the experiment are given in Table 3.3. Because the end caps are rounded, the effective length of each target can change with offsets in beam position. For a raster size of ± 2 mm the effective length of a 12 cm cell varies as much as 0.12%. However, during the analysis of the data, cuts are applied to the reconstructed length of the target cell which only include the effective

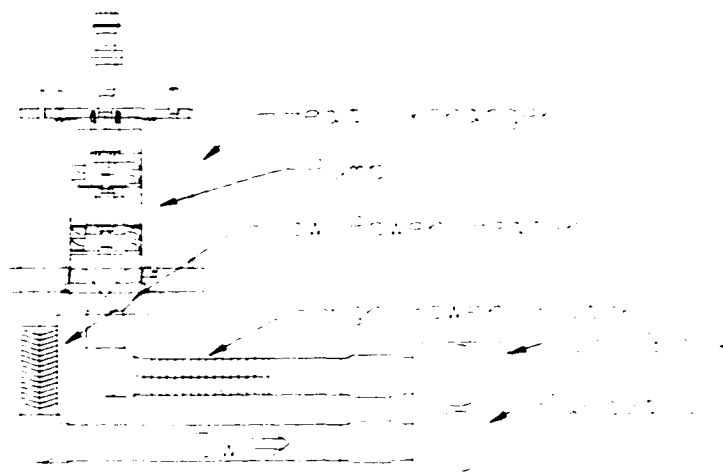


Figure 3.12: Scale drawing of a typical cryotarget loop. Beam is coming out of the picture. Only the longer cell (bottom cell) was used in the experiment.

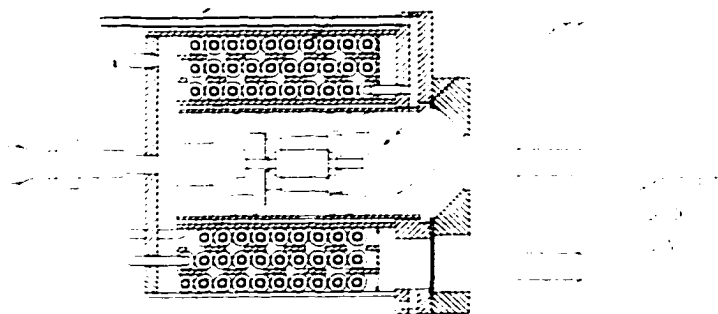


Figure 3.13: Cross sectional view of a typical heat exchanger. Cold helium is piped through the fin-tubing. The target fluid is pumped through the screw type pump and over the outside of the fin-tubing.

length of the cell which is 2 to 3 cm less than the true length. Therefore, physical changes of less than 1% in the length of the cell are negligible. Table 3.3, gives crucial dimensions and offsets for each of the cells used in the experiment. For a more detailed listing of the surveyed dimensions of the cryotargets see References [38] and [58].

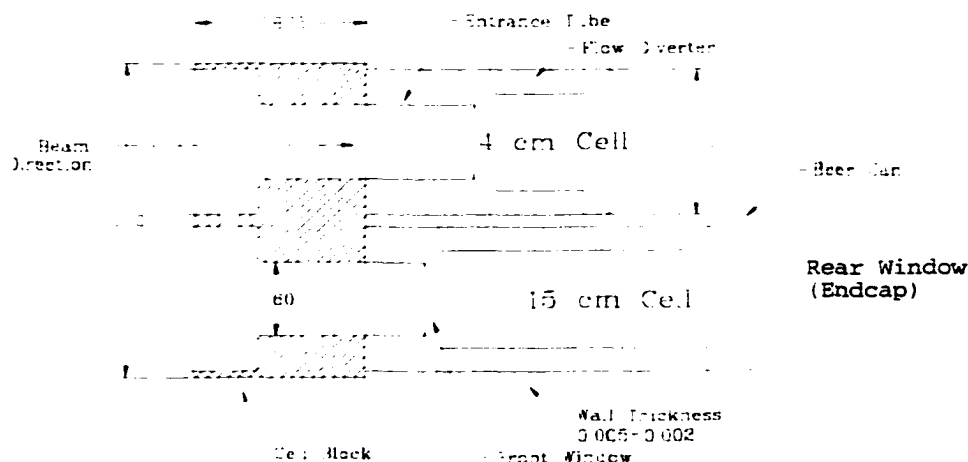


Figure 3.14: Typical cell block and cells shown with the original 15 cm target cell installed on the bottom. The thickness of the front window (on all cells) was $71 \pm 3 \mu\text{m}$. Note that the outer part of the target cell was constructed of a beer can blank supplied by the Coors Brewing Company.

Target	Nominal Length (cm)	Cold Length (cm)	Endcap Thickness (μm)	Z Offset (mm)
H ₂	15	15.34 ± 0.04	119 ± 0.5	3.1 ± 0.06
D ₂	15	15.12 ± 0.04	114 ± 0.5	1.9 ± 0.06
H ₂	12	12.48 ± 0.04	105 ± 0.5	0.9 ± 0.3
D ₂	12	12.46 ± 0.04	114 ± 0.5	0.4 ± 0.3

Table 3.3: Critical dimensions of individual cryotarget cells used in the experiment. The thickness of the front window (on all cells) was $71 \pm 3 \mu\text{m}$.

Joules Thompson Valves and Coolant Supply

There are four JT valves installed in the target system to control the flow of the cooling cryogenics (helium and liquid nitrogen). The liquid nitrogen is used as a pre-cooler and the

valve is typically left mostly open during normal operations. The targets are cooled with ~ 13 K helium supplied by the End Station Refrigerator (ESR). However during the first phase of the experiment, ~ 4 K helium was supplied by the Central Helium Liquefier (CHL).

The main flow of coolant passes through each loop in a serial fashion and is controlled by the main or supply JT valve. With the exception of the middle loop (usually containing helium), each loop has a bypass JT valve that allows as much as $\sim 50\%$ of the coolant to bypass the heat exchanger for each loop. The three helium JT valves are adjusted frequently to change target cells or to change the cooling power available to the target. Control of the JT valve is done through the digital output of the Industry Pack ADIO (analog to digital input/output) card installed in the VME crate. The position of each valve is determined with a LVDT that provides a 0 – 10 V signal corresponding to 0 – 100% open.

Target Motion

As can be seen in Figures 3.15, the cryotarget is a stack of several target cells (including dummy cells). Individual cells were positioned in the beam by the cryotarget lifter. The lifter consists of three lead screw drive nut assemblies attached to carriages mounted in rails. Three sets of rails were positioned vertically at 120 degree intervals about the cryotarget external apparatus. Movement in the vertical direction inside the scattering chamber is allowed by a vacuum bellows constructed by Standard Bellows Inc. The lead screws are driven by three AC servo motors with a 50:1 gear reduction that are controlled by a Koll-Morgan BDS5 system. The controls for two of the motors are slaved to the remaining controller (master controller) to synchronize the motion of all of the motors. The position of the cryostack was determined by a 12-bit resolver attached to the master motor. Home and limit switches were also installed to provide position information and for reasons of

safety.

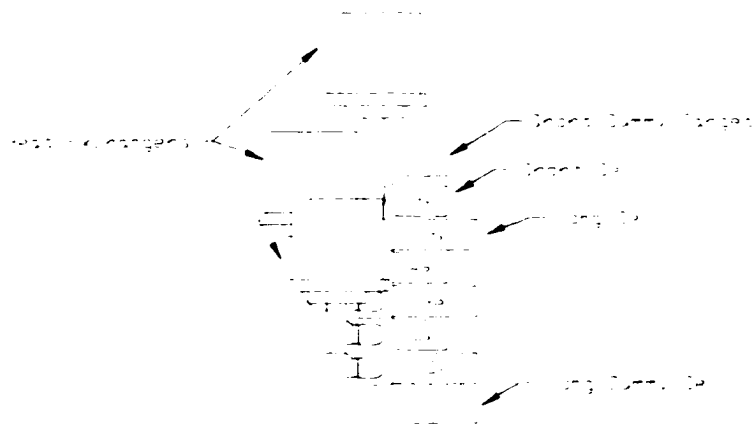


Figure 3.15: Close up view of the Hall C cryotarget target stack. Beam is to the right in the figure.

Because there is not enough room in the vertical direction to install both the solid target ladder and the cryotarget ladder on the same vertical positioning system, the cryotarget can be rotated by 90° to remove it from the beamline. This allows the solid target ladder to be positioned from above. The rotary motion is performed by a single screw driven arm attached to pivots at each end. A DC stepper motor is used to drive this screw and its position is determined by counting steps. The motor is controlled by JK-S5851 stepper motor controller. Home and limit switches were also installed on this system to provide a position reference and for reasons of safety. Rotation in the vacuum is allowed by a rotating seal installed below the vacuum bellows that can be differentially pumped.

3.9.3 Gas Handling System

The gas handling system is crucial to the operation of the cryotarget and consists of three gas panels, one for each target loop, installed on the floor of the hall near the pivot. The gas panel for the hydrogen and deuterium targets are essentially the same, while the helium

gas panel is slightly more simple. There are numerous manual and computer controlled valves in each panel to allow the target to be pumped and purged (cleaning process), filled, and relieved. Filters are installed in the hydrogen and deuterium panels to minimize the contaminants introduced in the system when filling from a vendor-supplied bottle. To aid in the operation of the target and to provide a reservoir for warm target gases to be collected and supplied, 1000 gal tanks were installed in the hydrogen and deuterium loops. Two lines are installed (inlet and outlet) connecting the target loop and the gas panels.

Pressure is measured at several places on each target loop by both manual (dial gauges) and computer controlled pressure transducers. There are four pressure transducers and three manual gauges installed in the hydrogen and deuterium loops. In addition to this instrumentation, a differential pressure gauge was installed to measure the pressure difference on each side of the pump in the target (i.e. the pump head). The helium panel was instrumented with only manual gauges. As a physical safety, relief valves and rupture disks were installed in the gas handling system to ensure that any excess pressure in the loops would be relieved without damaging the cells or releasing explosive gases into the hall. If the relief valves opened or the rupture disks broke, all gases would be released up the vent stack to the top of the hall and eventually to the outside atmosphere above the hall.

3.9.4 Instrumentation and Control

The complete instrumentation of the cryotarget involved the combination of numerous subsystems and two computers, a Motorola MV 162 input output controller (IOC) and a PC, connected to the Hall C LAN (local area network). An EPICS database running on the IOC was constructed to monitor and control almost every aspect of the target system. The IOC was installed in a VME 6u crate located on the floor of the hall near the gas panels. Com-

munication between the IOC and other subsystems was primarily achieved using multiple RS232 serial connections. Industry Packs were installed on the IOC and a separate carrier board to perform digital to analog conversions for output, analog to digital conversions for input (i.e. monitoring heater voltages), and serial communications. A graphical user interface (GUI) was written to interface to the database using TCL/Tk and was executed on a PC running the Linux operating system. To provide additional software safety, an alarm system was implemented that warned the target operator if the database values exceeded set limits in an explicative manner.

Fan Motor Control

Power for the fan motors (pumps) that circulated the cryogenic target fluid, was supplied in two ways. Initially the motors were supplied three phase power from a Variac controlled source. During later phases of the experiment, the fan motors were driven by variable frequency transformers. In both cases, the fan speed was monitored by a tachometer and by readout of the voltage and current drawn by each motor. The tachometer readout was prone to failure; therefore only the voltage and current readings could be depended on to monitor the fan speed. The fan status (on or off) could also be determined from the differential pressure measurement across the pump, which is discussed below.

Pressure and Temperature

Pressure and temperature are the two most important quantities to control in a cryogenic target system. The densities of liquid hydrogen and deuterium are only weakly dependent on the pressure of the fluid. For this and other practical reasons, the pressure was monitored continuously but only controlled within safety margins. Because the densities of the

target fluids are strongly dependent on their temperatures, the temperature in each loop is monitored by a number of different methods. The temperature is also controlled by the high and low power heaters in a proportional, integral differential (pid) control loop with a temperature sensor.

Pressure was measured remotely at four places in the hydrogen and deuterium loops using Sensotec FMA 811 pressure transducers connected to a Sensotec SC200 readout controller. The controller was interfaced to the VME IOC via a serial connection. An Omega PX750-HDI differential pressure transducer connected to an Omega DP41E readout controller was also installed in the hydrogen and deuterium loops to measure the differential pressure across the pump. This measurement provided the system with the pressure difference between the output side and input side of the pump circulating the target fluid. This is also known as the pump head pressure. An acceptable pump head pressure measurement indicates that the pump is working properly. A relay on the SC200 tripped by an over pressure measurement on the same device was used to open a solenoid relief valve to provide another level of safety.

The temperature in each loop is monitored and controlled by smart temperature controllers (Oxford ITC 502). These devices convert the resistance of two Lakeshore Cernox resistors, installed in each loop, into temperature. Communication between these devices and the IOC is achieved through a RS-232 serial connection. Each ITC 502 was capable of controlling the temperature in the loop by adjusting the power it supplied to the low power heater in a PID loop with one of the Cernox resistors. In addition to the PID loop controlling the low power heater, a PID loop operating on the IOC using the same Cernox resistor and the high power heater was also implemented during later phases of the experiment. This was done to compensate for fluctuations in the temperature of the helium coolant supplied by the ESR. Temperature fluctuations were negligible when the beam was stable and,

during periods of instability, the data acquisition system was paused. The temperature in the hydrogen loop was 19 ± 0.05 K and 22 ± 0.05 K in the deuterium loop as measured by the Cernox resistors. These temperatures were more than one degree subcooled for the operating pressures in each loop.

Temperature in each loop was also measured using 270Ω Allen Bradley resistors connected to a single Oxford ITC 501. This measurement was not as accurate as the one performed with the Cernox resistor and, in practice, was only used to measure the level of liquid in each loop. Each loop was also equipped with two hydrogen vapor pressure bulb thermometers. These devices exploit the fact that the hydrogen vapor pressure curve is a well known function of temperature. Thus, by knowing the vapor pressure in each bulb, the temperature can be determined. The pressure in each bulb was measured using a Sensotec TJE pressure transducer connected to a Sensotec SC200. Communication between the SC200 and the IOC was achieved over a RS-232 serial connection. This method of measuring the temperature in each loop proved to be unreliable. The calibration of the TJE pressure transducer was lost after a short time of running in the hall, possibly due to radiation damage to the transducer [59].

3.9.5 Performance of the Hall C Cryogenic Target System

The pressure and temperature of each loop was measured to an accuracy of ± 0.1 psi and ± 0.05 K, respectively. The dependence of the densities of the target fluids (hydrogen and deuterium) on temperature is $\frac{d \ln(\rho)}{dT} \approx -1.25\%/K$ leading to an uncertainty (arising from the uncertainty in the temperature measurement only) of less than 0.1% in overall density. The uncertainty in the pressure measurement led to an uncertainty in the target density of $\frac{d \ln(\rho)}{dP} \approx 0.01\%/psi$ which is negligible. In addition to global changes in density, the target

fluid density can vary locally especially along the beam line. Local changes can result from boiling of the target fluid where the beam passes through the cell. To minimize this effect, flow diverters were installed in the cell in an effort to create a turbulent flow. The beam was also rastered to ± 1 mm to lower the incident power density of the beam for similar reasons (see Section 3.6). The radiator foils also had the effect of reducing the power density of the beam by multiply scattering the electrons to form a wider spot on the target.

To estimate the effect of localized boiling in the target, data were taken on the 15 cm deuterium cell for various currents and raster pattern sizes. The data were and events with suitable electron particle identification and tracking parameters were selected. By examining fluctuations in the yield normalized to beam current, estimates can be made of the magnitude of the effect of localized boiling in the target. A summary of these data is shown in Figure 3.16. As can be inferred from the figure, the density fluctuations present, for a raster amplitude of ± 1 mm and for beam currents less than $50 \mu\text{A}$, are less than 0.5% [60]. A more recent study of the effects of localized boiling found a $\sim 0.04\% / \text{mm} / \mu\text{A}$ drop in target density [61]. This would result in a $\sim 1.5\%$ decrease in the target density for a $50 \mu\text{A}$ beam with a raster size of ± 1 mm. Because this is a small effect and the fact that the electron beam multiple scatters after impinging on the bremsstrahlung radiator (making this an even smaller effect), no correction for localized boiling is made in the analysis.

A chemical analysis of the hydrogen and deuterium target gases was performed by Lawrence Livermore National Laboratory (LLNL). For a detailed description of the collection of samples and results of the test, see Reference [62]. The purity of the hydrogen gas was found to be 99.8% where the largest contaminations were nitrogen and oxygen. These gases should freeze at 19 K and plate to the surfaces in the heat exchanger. Therefore it is assumed that the contamination in target cell is negligible and no correction in density is made. For the deuterium gas, the purity was $\sim 99.5\%$ with the largest contamination

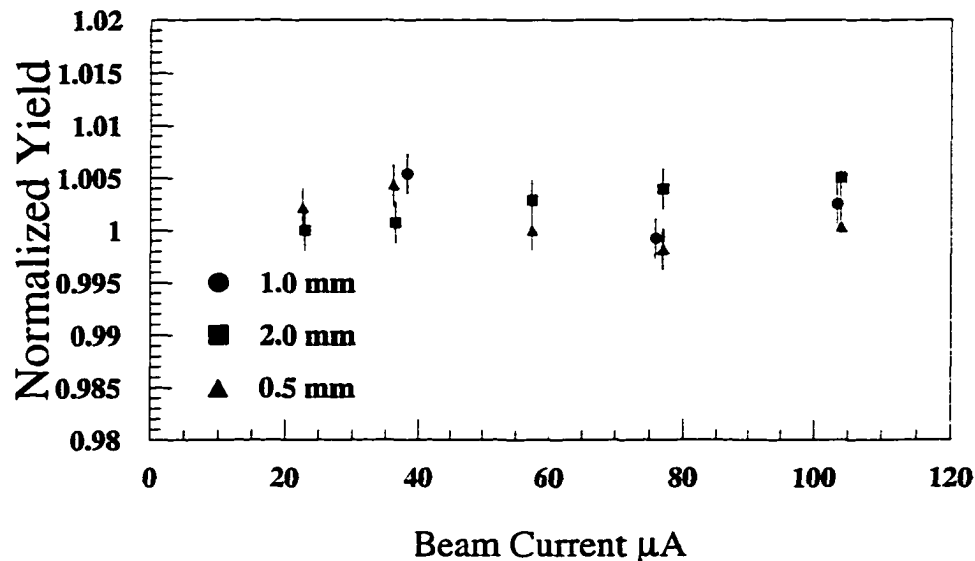


Figure 3.16: Data from the high power test of the 15 cm deuterium cell.

due to hydrogen. Table 3.4 summarizes the results of the gas analysis. Table 3.5 shows the density of liquid para H_2 and ortho D_2 for the operating conditions during all phases of the experiment. Due to uncertainties in target density resulting from uncertainties in temperature, localized boiling, and amounts of ortho D_2 and para H_2 an overall uncertainty of 0.7% is applied to all target densities and, therefore, to the final calculation of the effective target length.

3.10 High Momentum Spectrometer

The High Momentum Spectrometer (HMS) is the largest of the two spectrometers in Hall C. Primarily intended to detect high energy recoil electrons in coincidence with slower moving hadrons in the Short Orbit Spectrometer (SOS), it provided all of the deuteron

Target	Sample	Chemical	Abundance (%)
D ₂	1	D ₂	99.59 ± 0.01
		HD	0.301 ± 0.002
		N ₂	0.070 ± 0.008
		O ₂	0.037 ± 0.04
	2	D ₂	99.54 ± 0.013
		HD	0.220 ± 0.01
		N ₂	0.183 ± 0.008
		O ₂	0.060 ± 0.004
	3	D ₂	99.28 ± 0.01
		HD	0.616 ± 0.003
		N ₂	0.072 ± 0.013
		O ₂	0.037 ± 0.004
H ₂	1	H ₂	99.81 ± 0.01
		N ₂	0.127 ± 0.008
		O ₂	0.061 ± 0.004

Table 3.4: Results of target gas analysis performed at LLNL.

Target Material	Temperature K	Density (g/cm ³)
H ₂	19	0.07230 ± 0.0005
D ₂	22	0.1670 ± 0.00117

Table 3.5: Densities of cryogenic target fluids. Errors reflect the uncertainty in target density from temperature, pressure, and localized boiling and the uncertainty of relative amounts of ortho and para hydrogen. Values in the table are from References [38] and [58].

detection for the experiment. Since the decay photons from the recoil π^0 produced in the process $\gamma d \rightarrow d\pi^0$ cannot be detected in a magnetic spectrometer, the HMS was used in single arm mode only. The spectrometer, shown in Figure 3.17 is composed of two basic parts, a carriage that supports the magnets and a separate carriage supporting the shield house. The two parts are connected, but one can move relative to the other when the entire spectrometer is rotated. To minimize variations in the positions of the detectors relative to the magnets, the detectors were mounted to a frame connected directly to the magnet carriage.

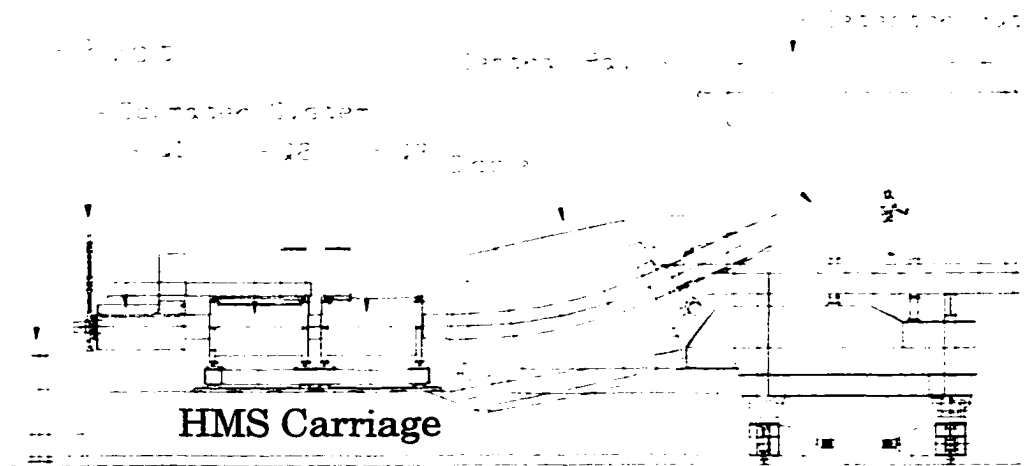


Figure 3.17: Scale drawing of the High Momentum Spectrometer (HMS) showing magnet carriage and detector hut.

3.10.1 HMS Optical System

The HMS optical system consists of four superconducting magnets in a QQQD formation. The spectrometer has a 25° bend in the vertical direction for the central ray. The maximum central momentum setting is over 7.3 GeV, although the largest setting yet obtained is only 4.4 GeV. To aid in the optical study of the spectrometer, a movable collimator system was installed on the front of the first quadrupole, Q1. The central momentum setting,

angle, polarity, and collimator position can be set remotely from the Hall C counting house. An EPICS database containing magnet parameters, spectrometer settings, and cryogenic information was developed to monitor crucial properties of the spectrometer. The magnets were cooled by liquid helium provided initially by the Central Helium Liquefier (CHL) and later by the End Station Refrigerator (ESR).

Current for the quadrupoles was provided by three Danfysik System 8000 power supplies. These supplies are water cooled and are capable of providing 3000 A at 5 V. The dipole was also powered by a series 8000 power supply capable of providing 3000 A at 10 V. A summary of the physical characteristics of the magnets is shown in Table 3.6. The quadrupole magnets have superconducting coils that are surrounded by soft iron to increase the central field while reducing stray fields. Additional windings, for multipole corrections, were installed in each of the quadrupoles; however, these were not energized during any part of the experiment.

Magnet	Length (m)	Effective Length (m)	Focus Direction	Pole Radius (Quad) or Gap (Dipole)
Q1	2.34	1.89	Dispersive	25 cm
Q2	2.60	2.155	non-Dispersive	35 cm
Q3	2.60	2.186	Dispersive	35 cm
D	5.99	5.26	N/A	42 cm

Table 3.6: Summary of the characteristics of the HMS magnets. The Focus directions are given for point-to-point tune only.

Optical axes of the quadrupoles were determined using the Cotton-Mouton procedure and found to vary slightly from the physical axis of the magnets [63]. The quadrupoles were aligned with respect to their optical axes. The fields in the magnets are determined and regulated by monitoring the current in the magnet. The quadrupoles are “degaussed” (placed on consistent hysteresis curves) by raising the current in them to 120% of their 4

GeV values. The magnets move less than 1.0 mm, relative the spectrometer carriage, when the spectrometer is rotated. This motion is reproducible to ~ 0.5 mm. The dipole field was monitored and regulated with an NMR probe. The fields of all the magnets were found to be stable to 1 part in 10^{-4} . A summary of the performance characteristics of the HMS is given in Table 3.7.

Maximum Central Momentum	7.3 GeV
Momentum Acceptance	$\pm 10\%$
Momentum Resolution	0.05%
Solid Angle	8.1 msr
Angular Acceptance (in plane)	± 32 mrad
Angular Reconstruction (in plane)	± 0.5 mrad
Angular Acceptance (out of plane)	± 85 mrad
Angular Reconstruction (out of plane)	± 0.8 mrad
Extended Target Acceptance	~ 10.0 cm

Table 3.7: Summary of HMS performance characteristics [64].

Movable collimator systems were attached to the front of both spectrometers to better understand their optical properties. The collimator systems are constructed of a machinable tungsten alloy, Densimet (90% tungsten 10% CuNi), and are quite similar. Each collimator system contains four positions, large collimator, small collimator, sieve slit and removed. A schematic of the HMS collimator system is shown in Figure 3.18. The sieve slit is an array of holes drilled in a sheet of Densimet with a smaller diameter hole in the center and two “missing” holes on either side of this central hole as shown in the figure. The missing holes provide information on the orientation of the sieve slit during analysis. Optical studies of the HMS were performed using both the sieve slit and the large collimator. Normal production data were taken exclusively with the large collimator. The small collimator was not used during the experiment.

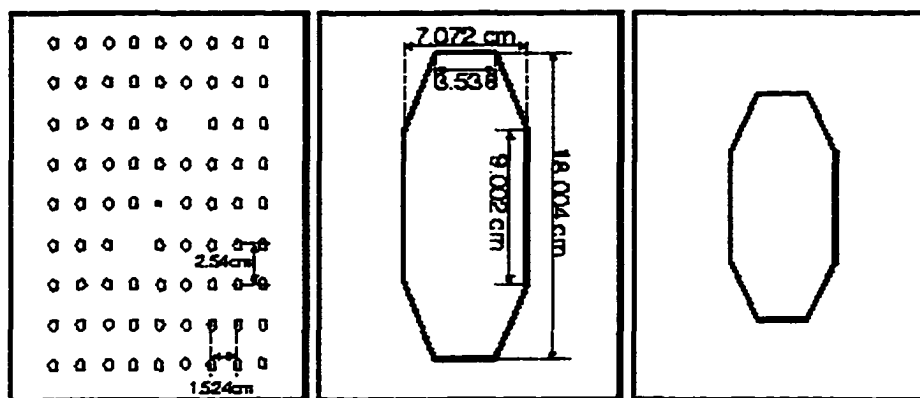


Figure 3.18: Schematic view of the three positions available in the HMS collimator system. From left to right they are the sieve slit, the large collimator, and the small collimator. The thickness of each octagonal collimator is 2.5 inches. The thickness of the sieve slit is 1.0 inch.

3.10.2 Commissioning and Calibrations of the HMS

Both spectrometers in Hall C have complex optical properties. To better understand these instruments and to optimize their performance, various studies were performed. Initial studies of the HMS centered on improving the focus of the spectrometer. Calibration measurements for absolute momentum and angle settings were also taken. Extensive measurements, especially with the sieve slit and slanted target, were made to improve the reconstruction matrix elements for both of the spectrometers. A brief discussion of these measurements and studies for the HMS is given in this section. For a detailed discussion of similar measurements for the SOS, see Reference [65]. The field settings of the magnets in the spectrometer are chosen such that entire magnet string focuses in a certain way or tune. There are several different tunes for the HMS including point-to-point and parallel-to-point. The point-to-point or standard tune for the spectrometer focuses rays from the same point in the target with the same momenta and different angles to a single point on the true focal plane (see below). The standard tune for the HMS was used exclusively for

all of the measurements associated with the experiment. Optical properties described in this section are for the standard tune.

Focal Plane Studies

The initial field settings in the HMS were determined using a COSY Infinity model for the spectrometer. This model incorporated the measured field maps of the quadrupoles and a calculated field map for the dipole. The conversion from current to field was also determined using the field maps. The fields were later fine-tuned to give the best focus at the focal plane. The focus was adjusted in the dispersive (X) direction using Q1 (the first quadrupole) and in the non-dispersive (Y) direction using Q2. Field variations of Q3 had little effect on the focus; therefore, the ratio of Q3 to Q1 predicted initially by the model was left unchanged.

The true focal plane is defined to be the surface where rays from the target with different angles and momenta are focused. This surface is approximated by a plane that makes an angle of $\sim 85^\circ$ with the detector focal plane. The detector focal plane, known simply as the focal plane, is defined to be perpendicular to the central ray of the spectrometer and to intersect it at the same point the true focal plane does (roughly halfway between the two drift chambers which are described in Section 3.10.4). The coordinate system for the focal plane follows the TRANSPORT convention [66]. In this convention, X points vertically down, Z is along the direction of the central ray, and Y points in the non-dispersive direction such that $\hat{Y} = \hat{Z} \times \hat{X}$. The X-focus of the spectrometer is adjusted such that $\delta = ((p - p_{central}) / p_{central}) = 0$ rays are centered at $(0, 0)$ in the focal plane. This was done by first adjusting the field in Q1 to move the X-focus to $X_{fp} = 0$ and then adjusting Q2 to move this focus to $Y_{fp} = 0$. This procedure was then iterated to achieve the best focus at the detector focal plane. Figure 3.19 shows the focus, in X and Y , of the spectrometer

at the focal plane with data from C(e,e').

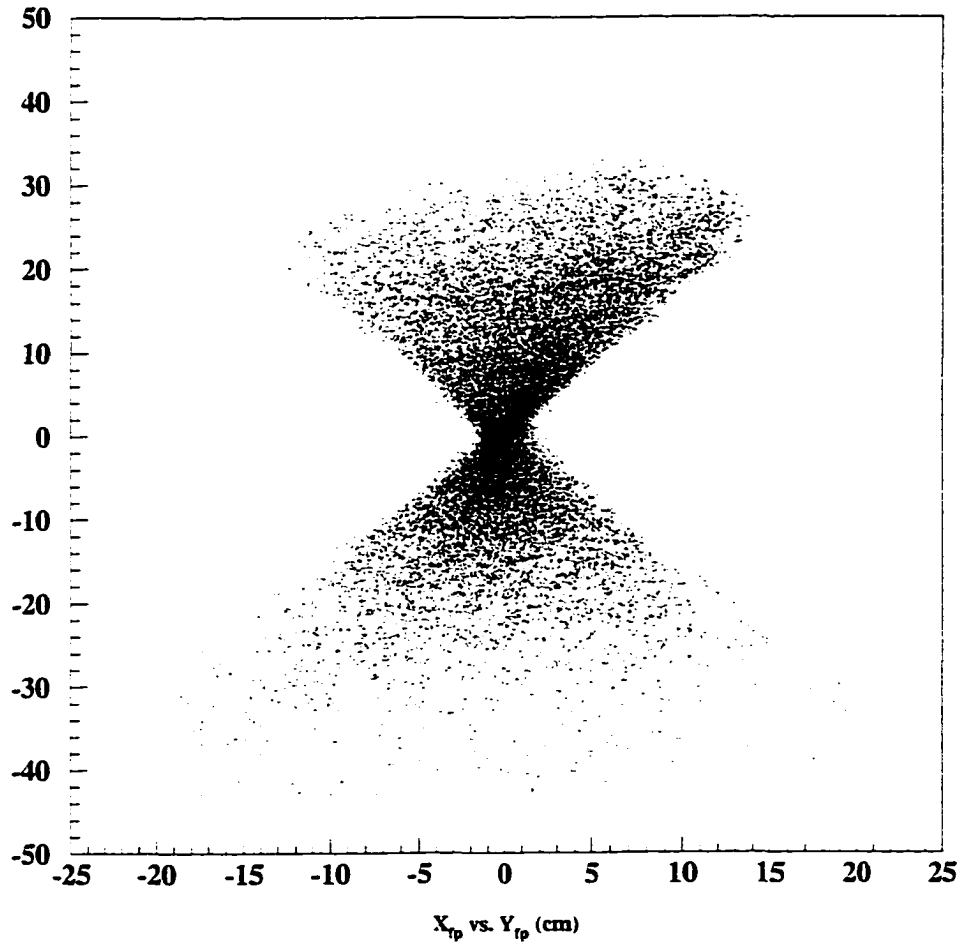


Figure 3.19: Data from C(e,e') scattering showing X vs. Y at the focal plane in the HMS.

HMS Reconstruction

Four focal plane quantities X_{fp} , Y_{fp} , dX_{fp}/dZ (abbreviated (X'_{fp})), and dY_{fp}/dZ (abbreviated (Y'_{fp})) are determined for each track from information provided by the drift chambers (see Section 4.1). Because only four focal plane quantities are determined, only four

target quantities, δ , X'_{tar} , Y'_{tar} , and Y_{tar} , which describe the track at the target before entering the spectrometer, can be reconstructed. Note that the position of the interaction in X and Z at the target cannot be determined for this choice of reconstruction variables. For the calculation of the target quantities, it is assumed that the interaction took place along the axis of the beam ($X_{tar} = 0$). The quantity δ , normally given in percent, is the difference of the reconstructed momentum from the central momentum divided by the central momentum $\delta = ((p - p_{central}) / p_{central})$. The transport convention described above is also used at the target. Let ζ_{target} be the point along the axis of the beam where the ray originates, then Y_{tar} is given by $Y_{tar} = \zeta_{target} \sin(\theta_{HMS})$ where θ_{HMS} is the angle setting of the HMS relative the beam. X'_{tar} and Y'_{tar} are the slopes of the ray in the dispersive and non-dispersive directions, respectfully.

The target quantities are calculated to first order ($N = 1$) using a matrix equation

$$\xi_{tar}^{\alpha} = R_{\beta}^{\alpha} \xi_{fp}^{\beta} \quad (3.6)$$

where the matrix R is known as the reconstruction matrix and a summation over repeated indices is implied. The target and focal plane quantities are given by $\xi_{tar}^{\alpha} = \delta, Y_{tar}, X'_{tar}, Y'_{tar}$ and $\xi_{fp}^{\alpha} = X_{fp}, Y_{fp}, X'_{fp}, Y'_{fp}$, respectively and $\alpha, \beta = 1 \dots 4$. To improve the reconstruction, the matrix elements must be calculated to higher order, $N > 1$, by using a Taylor expansion. However, the simple matrix equation given in Equation 3.6 cannot be used because the target quantities become complex convolutions of the focal plane quantities at higher order. In general, the target quantities are given, to order N by

$$\xi_{tar}^{\alpha} = R_{k,l,m,n}^{\alpha} (X_{fp})^k (Y_{fp})^l (X'_{fp})^m (Y'_{fp})^n \quad (3.7)$$

where $0 \leq k, l, m, n \leq N$, $k + l + m + n \leq N$, and a sum over repeated indices is implied.

Initially, these matrix elements are calculated using a COSY model of the spectrometer. The model simulates the optical properties of the spectrometer by using field maps, effective lengths, and positions of each of the magnets. To improve the spectrometer reconstruction, the matrix elements were fitted from data taken with a number of different sieve slit/collimator settings and target configurations. The fitting procedure is described in more detail in Reference [65]. It involves fitting sieve slit data from point targets placed at known points in the beam to reconstruct both angles and Y_{tar} . The momentum or δ was reconstructed using elastic data as described in Section 3.10.2. Reconstruction matrix elements fitted to 5th order are used in the analysis of all data for the experiment.

Examination of the target quantities projected to the sieve slit (see Figure 3.20) show that the matrix elements give relatively good angular reconstruction. Since the targets used in the experiment are all longer than 12 cm, the Y_{tar} reconstruction must be done correctly so that there is only a minimal dependence of δ on Y_{tar} . The Y_{tar} acceptance of the spectrometers was studied by positioning a slanted carbon target in the beam. The position of the interaction along the beam axis was moved and measured by moving the target vertically in the beam as shown in Figure 3.21. The dependence of δ on Y_{tar} is shown in Figure 3.22 for various positions of the slanted target. As is shown in the figure, for $-5\% \leq \delta \leq 5\%$, δ is relatively independent of Y_{tar} .

HMS Momentum Calibration

Calibrations of the HMS absolute momentum were performed by a number of different methods. One method was to use elastic H(e,e')p scattering scans to directly determine the momentum. This technique requires that the absolute beam energies are well known. The absolute momentum, using this technique, of the HMS was calibrated to 0.3% using

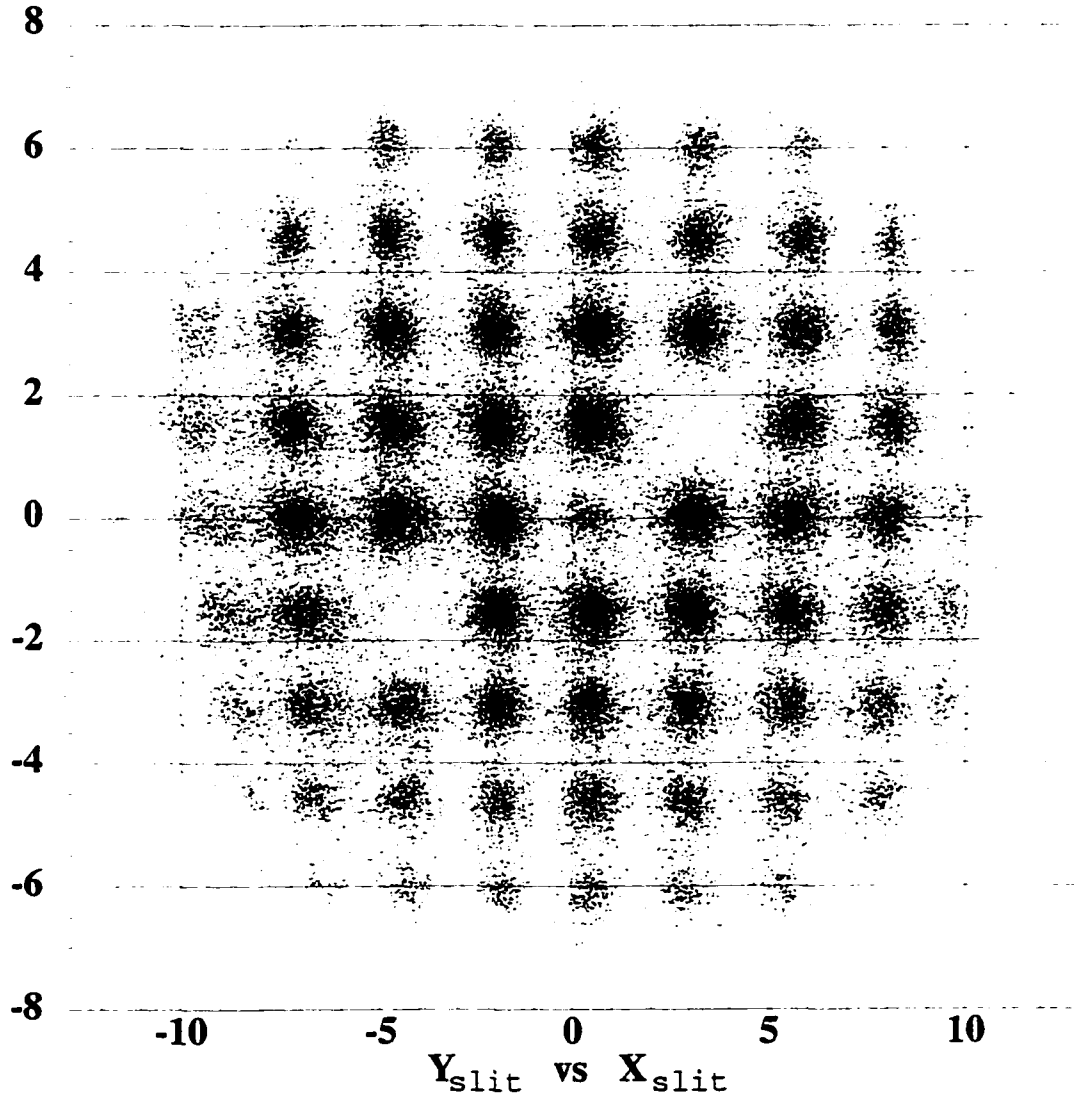


Figure 3.20: HMS sieve slit reconstruction. In this run the sieve slit is not centered on the central ray. This is evident from the ~ 5 mm offset (from 0,0) of the central hole in X_{slit} . The target quantities are projected forwards to the face of the sieve slit. Figure courtesy of G. Niculescu.

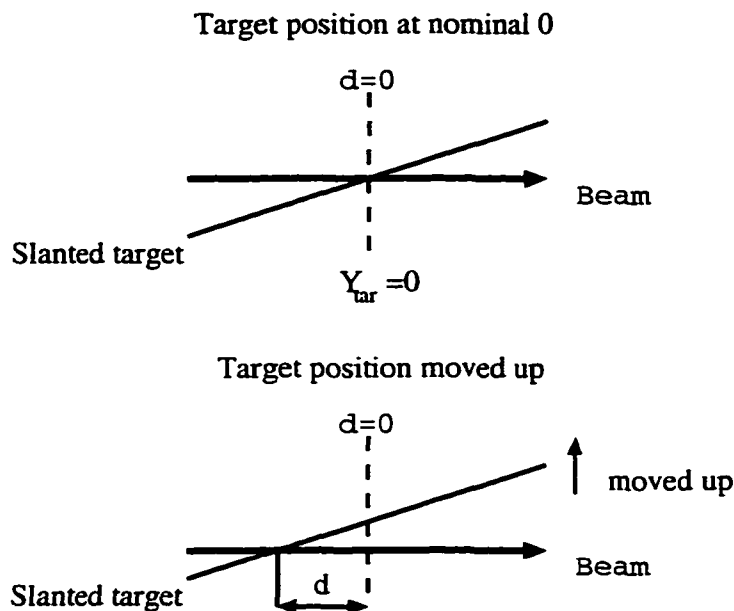


Figure 3.21: Schematic showing the slanted target positioned in the beam line. The position along the axis of the beam is determined from the vertical position of the target.

the beam energy measurement in the Hall C Arc. A second technique involved the use of an angular scan of elastic $H(e, e')p$ data at a constant beam energy, which minimizes any dependence of the calibration on the beam energy. There is however, a slight dependence on the spectrometer angle measurement using this technique. The momentum calibration, using this technique, is better than 0.1% [64]. A 0.1% uncertainty in the spectrometer momentum is therefore used in the analysis on the cross section data.

HMS Angle Calibration

The HMS angle was measured by comparing marks, scribed into the floor of the hall, to a pointer at the back of the spectrometer. The marks on the floor were surveyed into place and allow for positioning of the HMS carriage to better than 0.1 mrad. However, the spectrometer magnets can move during rotation giving angular variations as large as

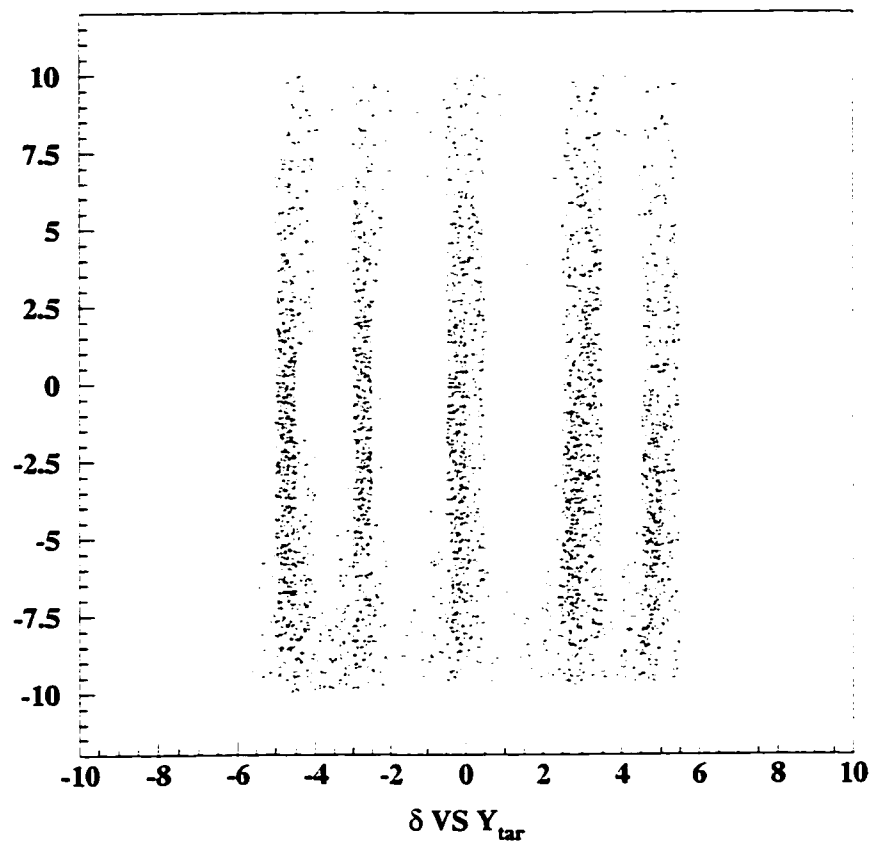


Figure 3.22: HMS δ dependence on Y_{tar} . δ is given in % and Y_{tar} is given in cm.

1.0 mrad. Measurements of $H(e,e',p)$ scattering at numerous kinematics were used to check the momentum and angular offsets of both of the spectrometers. The HMS offsets measured in this fashion have an uncertainty of ± 1.0 mrad. However, they are convoluted with the offsets in the SOS and cannot always be separated. An inclusive scan of $H(e,e')$ scattering was performed using the HMS and was also used to calibrate the angle of the spectrometer. If the momentum is assumed to be well known, then the angular offsets determined by the scan are less than ± 0.5 mrad. Therefore, a rms uncertainty of ± 0.5 mrad for the HMS angle is used in the calculation of error for the cross section.

3.10.3 HMS Acceptance

Each spectrometer in Hall C, for given central settings, can only detect charged particles produced within a specific volume of six-dimensional acceptance space described by six variables δ , X' , Y' , X , Y , and Z , where the TRANSPORT convention has been used (see page 78). The spectrometers can therefore only detect events, which occur at points in this space, over a limited range in these variables. As the separation between the coordinates (in this six dimensional space) of an event and the central settings of the spectrometer increases, the probability that the spectrometer will detect the event decreases. The acceptance of the spectrometer is defined to be the probability that the spectrometer will detect (accept) an event originating from a point (X, Y, Z) with kinematical properties described by δ , X' , and Y' . The acceptance of the spectrometer A is therefore a function of the six variables $A = A(\delta, X', Y', X, Y, Z)$.

The acceptance function for the two spectrometer system involving both the HMS and SOS is a complex convolution of the acceptances of both of the spectrometers. Throughout the experiment however, the HMS was used in single arm mode only, thus, effects from

acceptance of the SOS can be ignored. Consider a process described by the differential cross section $\frac{d\sigma}{d\Omega}$. The number of events detected by the HMS is given by

$$N = \int d\delta dX' dY' d^3\vec{X} \frac{d\sigma}{d\Omega}(\delta, X', Y', \vec{X}) A_6(\delta, X', Y', \vec{X}) \quad (3.8)$$

where A_6 is the six variable acceptance function of the HMS. In most cases, the target material is thin enough that energy loss and multiple scattering of the beam are negligible. In such cases, the cross section is independent of the position and the expression in Equation 3.7 can be simplified by integrating the acceptance over \vec{X}

$$N = \int d\delta dX' dY' \frac{d\sigma}{d\Omega}(\delta, X', Y') A_3(\delta, X', Y') \quad (3.9)$$

where A_3 is the three variable acceptance function for the HMS. The quantity N may also be expressed in terms of θ (the in-plane scattering angle) and ϕ (the azimuthal scattering angle) by using the following

$$\cos(\theta) = \frac{\cos(\theta_{HMS}) + Y' \sin(\theta_{HMS})}{\sqrt{1 + X'^2 + Y'^2}} \quad (3.10)$$

$$\tan(\phi) = \frac{-X'}{\sin(\theta_{HMS}) - Y' \cos(\theta_{HMS})}. \quad (3.11)$$

Equation 3.9 can thus be written

$$N = \int d\delta d\theta d\phi \frac{d\sigma}{d\Omega}(\delta, \theta, \phi) A_3(\delta, \theta, \phi). \quad (3.12)$$

The cross sections measured in the experiment are also independent of the azimuthal angle ϕ . The ϕ integration in Equation 3.12 may thus be performed and a new two variable

acceptance function A_2 may be defined. The number of events detected by the spectrometer is then given by

$$N = \int d\delta d\theta \frac{d\sigma}{d\Omega}(\delta, \theta) A_2(\delta, \theta). \quad (3.13)$$

Thus, in most cases, a two dimensional acceptance function must be determined to extract a measured cross section.

A Monte Carlo model of the HMS (described in more detail later in this section) was developed and is used to calculate the acceptance function in Equation 3.13. Figure 3.23 shows the modeled acceptance of the HMS in δ , θ , ϕ , and Z respectively; note that θ , ϕ , and Z are equivalent to Y' , X' , and Y to a very good approximation. To determine the proper acceptance of the spectrometer, the same cuts applied in the analysis of the data must also be applied in the Monte Carlo calculation. In the analysis of the experimental data, only a small portion of the acceptance near the central settings is used. The figure shows that the acceptance of the HMS is essentially flat over a wide range of the δ , θ , ϕ , and Z which is much larger than the limited range (defined by software cuts) used in the analysis. Because of this, there is no need to determine the acceptance as a function of δ and θ and Equation 3.13 may be further simplified. Hence, the number of events detected by the spectrometer is given

$$N = A \int d\delta d\theta \frac{d\sigma}{d\Omega}(\delta, \theta) \quad (3.14)$$

where A is the total integrated acceptance of the spectrometer. This acceptance is integrated over a region in δ , Y_{tar} , X' , and Y' defined by the cuts applied in the analysis of the data. To calculate the acceptance, the Monte Carlo model of the HMS (`mc_hms_single`) is used incorporating these same cuts. The acceptance of the spectrometer is then given by

$$A = \frac{N_{pass}}{N_{gen}} (20 \text{ msr}) \quad (3.15)$$

where N_{gen} is the number of Monte Carlo events generated, N_{pass} is the number of Monte Carlo events passing all cuts, and 20 msr is the total solid angle generated in θ and ϕ .

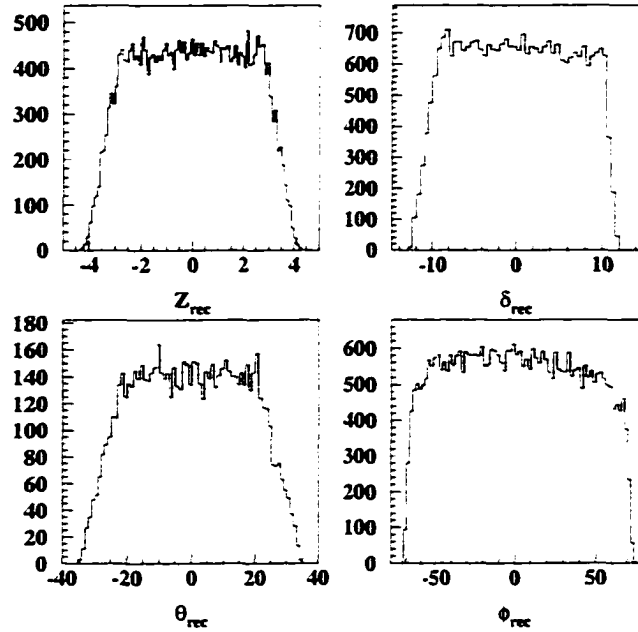


Figure 3.23: Reconstructed quantities as determined from the Monte Carlo model of the HMS for a 12 cm long target with $P_{central} = 4.0 \text{ GeV}$ and $\theta_{HMS} = 60^\circ$. Z_{rec} is given in cm, δ_{rec} is given in percent, and θ_{rec} and ϕ_{rec} are given in mrad.

The Monte Carlo Model of the HMS

The single arm Monte Carlo model of the HMS has three basic parts. Simulated events are created by the event generator in the first part of the Monte Carlo. These events are randomly generated within user defined bounds in target coordinates and transformed to spectrometer TRANSPORT coordinates. Each event is then projected forward to numerous points in the spectrometer. Events which strike apertures, like the collimator and magnet entrances are rejected. Any event that passes through the spectrometer is then projected to

the focal plane. If the event at the focal plane hits at least three out of the four hodoscope (see Section 3.10.4) planes (minimum to form a true trigger), it is finally accepted. All events which are accepted are then reconstructed back to the target and are placed in a n-tuple¹.

Each event is randomly generated in target coordinates $(X, Y, Z, \delta, \theta, \phi)$ where Z points along the axis of the beam and Y points vertically upward. The events are created within user defined bounds that are read from an input file upon initialization. The bounds for the generation of the events are typically defined to match a specific target and spectrometer configuration. For the purposes of calculating the acceptances needed in the experiment, events were generated in a flat distribution for $Z, \delta, \theta,$ and ϕ with bounds matching the cuts used in the analysis. Normal distributions, centered about the axis of the beam, were used to generate X and Y . To complete the event generation process, the coordinates for each event are transformed from the target variables to the spectrometer variables at the target $(X_{tar}, Y_{tar}, X'_{tar}, Y'_{tar}, \delta)$ (where the TRANSPORT convention has been used).

Once the spectrometer coordinates of the event at the target are determined, the event is projected forward to a number of critical points in the spectrometer. This is done by using an equation of the form

$$\xi_{spec}^{\alpha} = F_{i,j,k,l,m}^{\alpha} (X_{tar})^i (Y_{tar})^j (X'_{tar})^k (Y'_{tar})^l (\delta)^m$$

where a sum over repeated indices is implied, $0 \leq i, j, k, l, m \leq N, i+j+k+l+m \leq N, N$ is the highest order of the forward matrix calculation, the subscript *spec* denotes a point in the spectrometer, and $\xi_{spec}^{\alpha} = (X_{spec}, Y_{spec}, X'_{spec}, Y'_{spec})$ denotes the α transport coordinate at the given point in the spectrometer. The forward projecting matrix F may be calculated

¹n-tuples are CERNLIB generated data structures that can be easily analyzed using CERNLIB routines [68].

for any point in the spectrometer between (and including) the target and focal plane. COSY Infinity is used to calculate the forward matrix F by using a list of positions, field strengths, and effective lengths for each of the magnets in the same manner as R in Equation 3.7 is calculated. F is calculated at the front and back of the collimator, the entrance and exit of each magnet, and at other points in the spectrometer including at the focal plane. Events that pass through the walls of the magnets or fail to pass through all of the critical points in the spectrometer defined in the model are rejected. Events that reach the focal plane are checked to ensure that a trigger would have been formed if it had been a true event. Any event passing all of these criteria is accepted.

Finally, events that are accepted are then reconstructed back to the target. These events are used to fill an n -tuple with their initial, focal plane, and reconstructed properties. Desired cuts can then be placed on the generated events in the same manner that cuts are placed on actual data. This enables extensive studies of the optical properties of the spectrometer.

3.10.4 HMS Detector Package

The HMS detector package consists of four separate detector systems as shown in Figure 3.24. The first set of detectors is a pair of drift chambers, which provide all tracking information. The scintillator hodoscope provides both the primary trigger and the time of flight particle identification for heavy particles. The HMS gas Čerenkov detector provides particle identification by separating either electrons from pions or protons from pions. Finally, the lead glass shower calorimeter provides additional electron pion separation. Both the Čerenkov detector and the shower calorimeter can be incorporated into the trigger to reduce or increase the pion to electron ratio as needed by individual experiments. Because the HMS was tuned to detect deuterons for the experiment, there was little useful informa-

tion provided by these two detectors and they could not be incorporated into the trigger or the analysis.

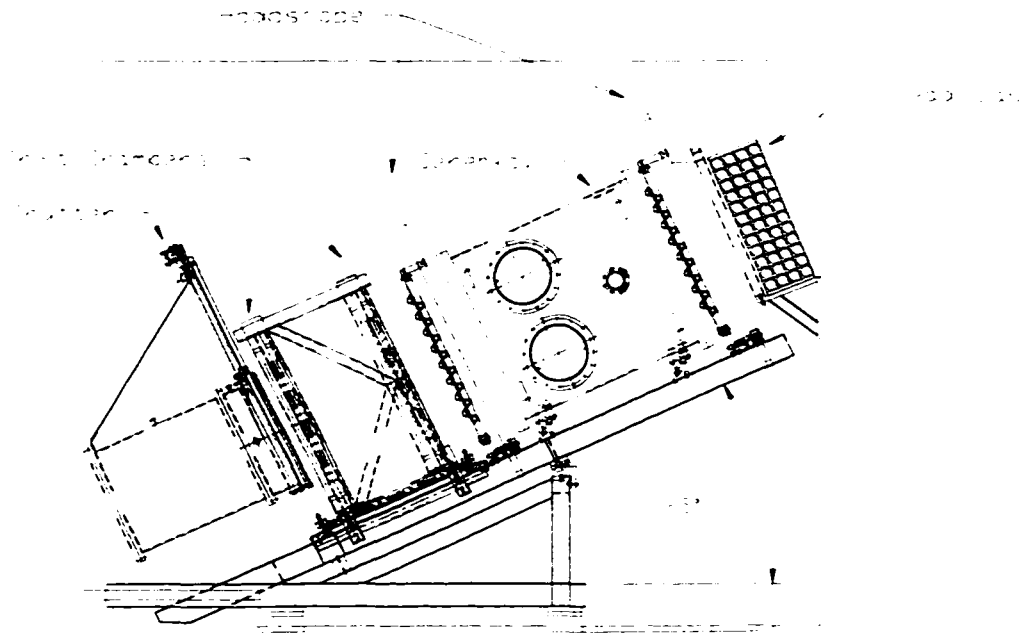


Figure 3.24: Schematic of the HMS detector package as shown from the side. The z positions of the detectors relative to the focal plane are shown below each detector.

The high voltage power for all of the detector systems was supplied by CAEN high voltage power supplies. These supplies have their own serial network (CEANnet) as well as an RS232 serial connection allowing remote operation of the devices. An EPICS database was developed to provide more sophisticated control of the power supplies through a TCL/Tk GUI. These power supplies also have the advantage that they can be custom configured for different applications with the proper selection of removable cards. These cards are inserted into the back of the CAEN mainframe and provide sixteen high voltage channels per card. The CAEN mainframes hold all of the serial communication electronics and can hold up to four individual high voltage cards. The cards used for all wire chamber appli-

cations were CAEN A505s which can provide a maximum of -3000 V and $200\ \mu\text{A}$. The hodoscope and calorimeter phototubes were powered by either an A403 or an A503 card capable of providing -3000 V at $3000\ \mu\text{A}$. Only the four phototubes in the Čerenkov detector required positive high voltage, which was supplied by A503P cards with a maximum output of $+3000\text{ V}$ at $3000\ \mu\text{A}$.

HMS Drift Chambers

The HMS drift chambers were built at TJNAF by the TJNAF-Hampton University wire chamber group. The chambers are mounted directly behind the exit window of the HMS dipole vacuum vessel as shown in Figure 3.24. There are six planes in each chamber (x , y , u , v , y' , x'), each separated by 1.8 cm . The x and x' planes measure position in the dispersive direction, the y and y' planes in the non-dispersive direction and u and v planes at $\pm 15^\circ$ relative to the x planes as shown in Figure 3.25. The chambers themselves were constructed with aluminum frames and have entrance and exit windows constructed of mylar. The $25\ \mu\text{m}$ diameter sense wires are constructed of gold plated tungsten. Schematic diagrams of the HMS drift chambers and a sample cell are shown in Figures 3.25 and 3.26. A detailed description of the HMS drift chambers and their performance is given in Reference [69, 70].

Drift chambers produce a signal when a charged particle passes through the chamber gas, ionizing gas molecules along its path. Electrons freed by this ionization are collected by the sense wire in cells nearest the path of the incident particle. This produces the signal processed by the discriminator electronics. This process is sensitive to the mixture of the gas. Variations in the mixture of the gas can effect the chamber efficiency or render it completely useless for particle tracking measurements. The HMS and SOS chambers were filled with a gas mixture of 50 % argon 50 % ethane by weight, supplied by the Hall C gas

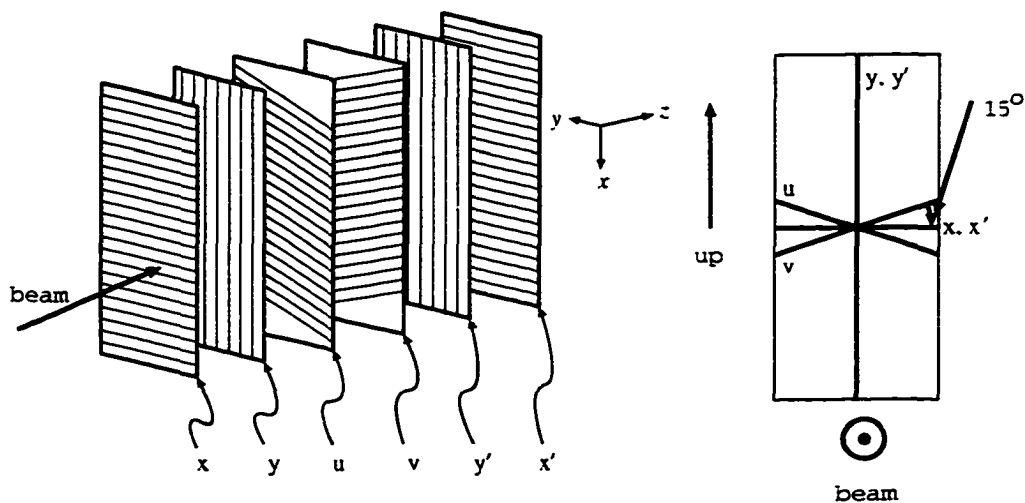


Figure 3.25: Schematic diagram of the wire layout for the HMS drift chambers. Note that X points in the dispersive direction. In the schematic on the right, the lines on the figure indicate the actual wire directions. The position information determined by the wires in a certain plane is perpendicular to that plane. Figure courtesy of C. Armstrong.

handling system. There was a slight contamination of isopropyl alcohol ($< 1\%$) from the temperature controlled bubbler that was used to monitor flow. The gas handling system for the wire chamber gas was contained in a shed outside the counting house. The system was built by the detector group at TJNAF and provides parallel gas flow to all the chambers. It does so by using a MKS 647 four channel gas monitoring system. Using this device, the flow to each chamber may be monitored and separately controlled.

The active planes in each chamber contain alternating field and sense wires and the active planes are separated by planes of field wires. The field wires were held at a negative potential that was determined by the distance to the nearest sense wire. Each sense wire is read by a preamplifier discriminator card (either a LeCroy 2735DC or a Nanometric N-277-1). The low voltage power for operation of these cards was provided by two Acopian low voltage supplies. The discriminator threshold voltage, for all of the cards, was provided by two BK 1600 DC power supplies situated in the counting house, which

**HMS DRIFT CHAMBERS
SINGLE DRIFT CELL**

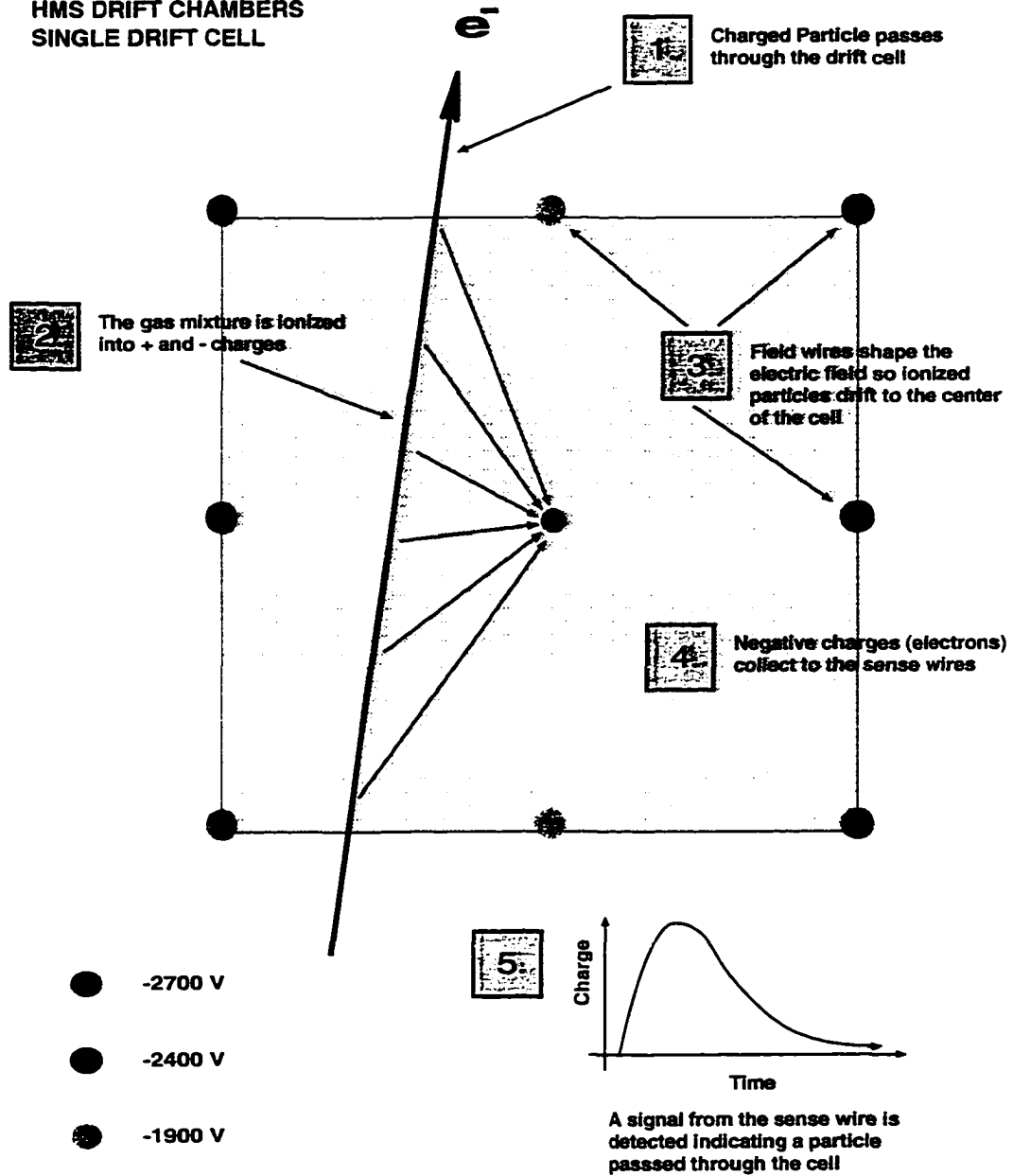


Figure 3.26: Schematic of a HMS drift chamber cell. Note that the sense wire is located in the center of the cell. Figure courtesy of G. Niculescu and D. Abbott.

provided remote control of the threshold level. The outputs from these cards have a 34 pin ECL (emitter coupled logic) header that is connected via twisted pair ribbon cable to LeCroy 1877 multihit FASTBUS TDCs (time to digital converter). These TDCs record up to 16 hits per channel in a timing window that is $32 \mu\text{s}$ long. A detailed description of the software tracking procedure is given in Section 4.1.

The calibration of the HMS drift chambers is manifested in what is known as a time-to-distance map. This map was made for each kinematical setting during all phases of the experiment and only a brief description of the time-to-distance map is given here. Electrons released when a charged particle passes through the chamber take time to reach the sense wire and, hence, produce a signal measured by the wire chamber TDCs known as the drift time (see Figure 3.27). This TDC information together with timing information from the hodoscope is used to determine the distance between the particle track and the sense wire (drift distance). To make the time-to-distance map, which is essential to the drift distance calculation, it is first assumed that the drift distance is flat when averaged over the all of the cells in a given plane. The drift distance is also limited in range from 0.0 cm (at the sense wire in the center of the cell) to 0.5 cm (half of the cell width). The time-to-distance map is generated for a given time T by performing the integral

$$\int_{t_{min}}^T D_{time}(t) dt$$

where t_{min} is the minimum time for the range of the drift time distribution, D_{time} , and is set to -24 ns because timing offsets between the drift chamber and hodoscope TDCs are not removed. In practice, the integral is performed by calculating the running sum of the drift time distribution which is determined from TDC values for the given plane. The drift

distance is then given by

$$d_{drift} = \frac{\text{cell width}}{2} \frac{\int_{t_{min}}^T D_{time}(t) dt}{\int_{t_{min}}^{t_{max}} D_{time}(t) dt}$$

where t_{max} is an upper limit on the range of the drift time distribution which can be large but, in practice is set to 252 ns. The resolution of the HMS drift chambers is better than 300 μm when this calibration is correct.

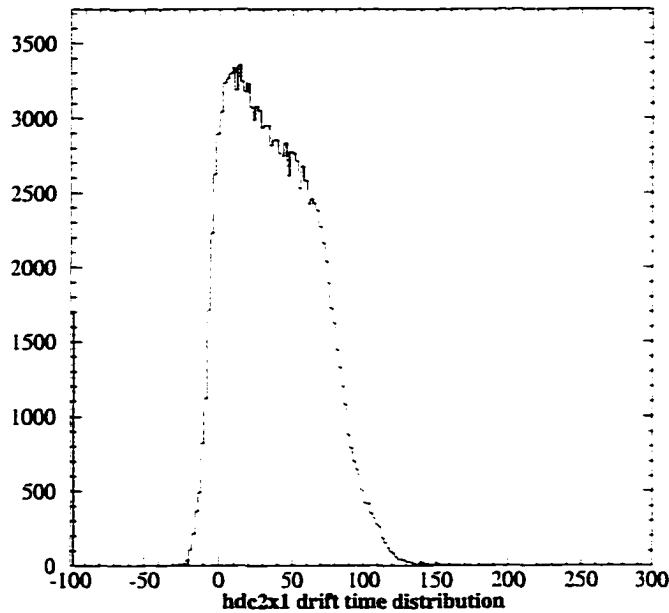


Figure 3.27: Example drift time distribution for one of the planes in the HMS drift chambers. Units on the horizontal axis are in ns.

HMS Hodoscope

The HMS hodoscope was designed and constructed at TJNAF. It was used both to form the trigger (which allows the fast electronics to accept an event) and also to provide particle identification for all parts of the experiment. The detector consists of two pairs of xy

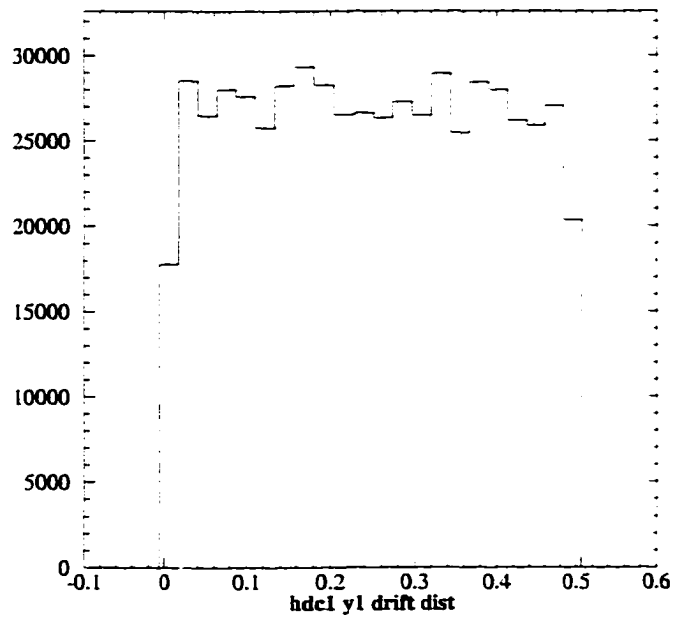


Figure 3.28: Example drift distance for one of the planes in the HMS drift chambers. Units on the horizontal axis are in cm.

planes, made of 2.12 cm thick, 8 cm wide BiCron BC404 plastic scintillators as segments or paddles (see Figure 3.29). The first pair of planes is situated behind the second drift chamber and the second pair is mounted behind the exit of the Čerenkov detector as shown in Figure 3.24. This gives a separation between the two pairs of planes of 2.2 m. The paddles are wrapped with aluminum foil and two layers of Tedlar. Phillips XP2282 B eight stage phototubes are fixed to UVT lucite light guides, which are attached to each end of the paddles. The x planes are made up of 16 paddles that are 120.5 cm long. The y planes are made up of 10 paddles that are 75.5 cm long. The paddles are overlapped by roughly 5 mm to ensure that there are no small gaps in the active area of the detector which is about $120 \times 120 \times 75$ cm. A schematic diagram of a hodoscope pair is shown in Figure 3.29.

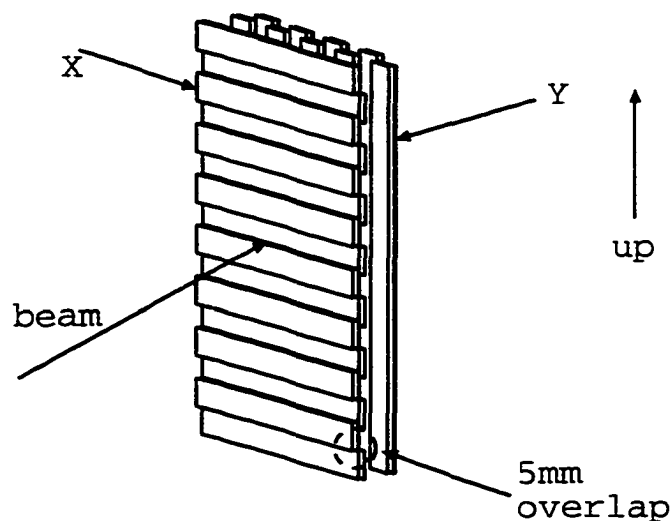


Figure 3.29: Schematic diagram of a HMS hodoscope x, y pair of scintillators planes. Figure courtesy of C. Armstrong.

There are active (zener stabilized) bases attached to each phototube. The phototubes were gain matched using a ^{60}Co source fixed to the center of each paddle. The high voltage on each tube was adjusted until the Compton edge from the gamma rays yielded a

~ 500 mV signal [71]. Corrections from pulse height variations and offsets of individual elements of the hodoscope are determined and applied in software (see Section 4.2). The signals from the phototubes travel through roughly 30 ft of RG58 cable and 450 ft of RG8 air core cable. Upon reaching the counting house patch panel, the signals are split; 1/3 of the amplitude of each signal travels through a 400 ns cable delay to an ADC (analog to digital converter) channel and the other 2/3 of the signal pass to the trigger electronics. The instrumentation of the hodoscope signals is shown in Figure 3.30. The final per plane timing resolution is roughly 100 ps which gives a final particle velocity (β) measurement resolution of 0.02 for a $\beta = 1$ particle. This resolution allowed particle identification of deuterons in the HMS to be done mostly with the time of flight (TOF) measurement (see Sections 4.2 and 4.4).

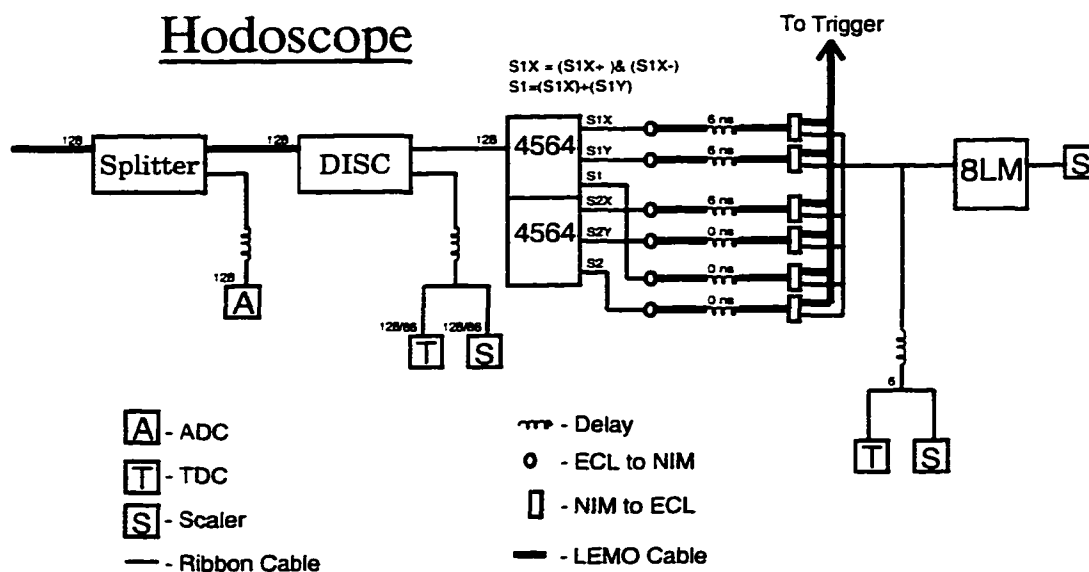


Figure 3.30: Schematic of electronic instrumentation for the HMS hodoscope. Specific electronics are discussed in later sections. Figure courtesy J. Arrington.

HMS Lead Glass Shower Calorimeter

The lead glass shower calorimeter for the HMS was constructed by the Yerevan group. The detector is four layers deep with eleven blocks in each layer and is installed at the back of the detector stack as shown in Figure 3.24. The blocks, with dimensions $10 \times 10 \times 70$ cm, are made of TF1 lead glass and are wrapped in one layer of aluminized mylar and two layers of Tedlar. The light produced in each block is detected by a Phillips XP3462 B phototube mounted on one end of the block. Complete instrumentation of the other end of the blocks, with the same type of phototube, is planned for the future. For light with a wavelength of 400 nm, the attenuation length in the blocks varied from 50 to 100 cm. The high voltage was set to gain match the individual modules to within 20%. Gain matching of all the modules was further refined in software.

The signals from each of the phototubes traveled through ~ 30 ft of RG58 cable and over 450 ft of RG8 air core cable to the counting house. Upon reaching the counting house patch panel, the signals were split with one half of the amplitude of each of the signals passing through a delay to ADC channels and the other half going to the trigger electronics. The first layer of blocks was linearly summed to give the PRSUM signal. An additional signal containing the sum of all the modules, SHSUM, was also formed. These signals provided some measure of particle identification for the trigger. The phototube signals were instrumented as shown in Figure 3.31, with the exception that they were not used as part of the trigger during the experiment. A detailed description of the design and performance of the detector is given in Reference [72]. Since the HMS was tuned to study hadrons throughout the experiment, the shower counter did not provide any useful information and was not used in the formation of the trigger or in the analysis.

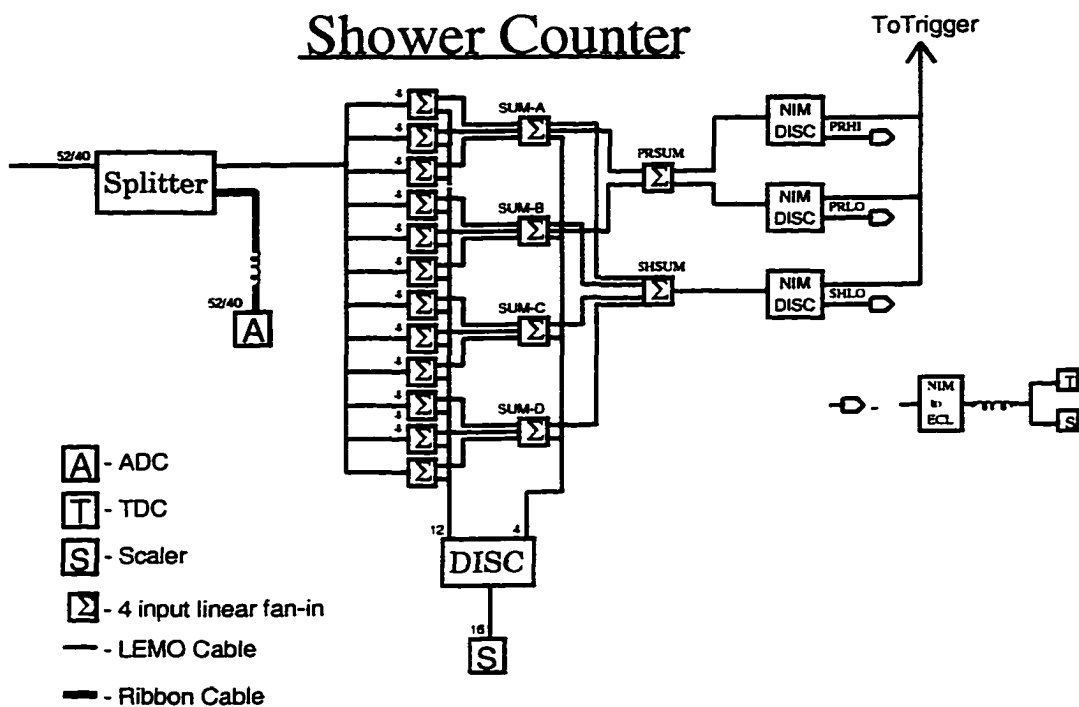


Figure 3.31: Schematic of the HMS lead glass shower calorimeter trigger electronics. The modules labeled NIM DISC are NIM output discriminator modules. The modules labeled with Σ are linear fan ins (signal amplitude adders). Figure courtesy J. Arrington.

HMS Čerenkov Detector

The HMS gas Čerenkov detector was designed and constructed by UVA and TJNAF. It consists of a large aluminum can with multiple ports and large entrance and exit windows. The instrument is installed between the first and second pairs of hodoscope planes as shown in Figure 3.24. The detector is a cylindrical tank with an inner diameter of almost 60 in and a length of roughly 65 in. The tank was designed to handle gas pressures from 7.5 to ~ 45 psia. There are two mirrors at the back of the tank that direct the Čerenkov light onto two Burle 8854 PMTs. The tubes are mounted on the backs of removable flanges directly in the gas. The front face of each of the PMTs was coated with a wavelength shifting film to improve the response of the detector [73]. A schematic diagram of the instrumentation of the HMS Čerenkov detector is shown in Figure 3.32.

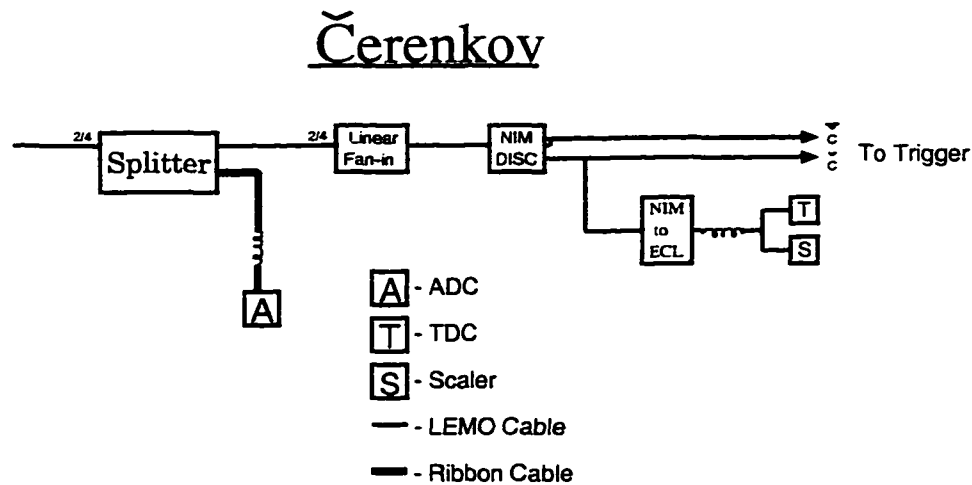


Figure 3.32: Schematic diagram of the HMS Čerenkov detector. Figure courtesy J. Arrington.

To provide another source of particle identification in the trigger, the detector could also be instrumented in the trigger. However, this was not done because the pion rates (when investigating $\gamma d \rightarrow pn$) were much lower than the proton rates. The high voltage on each

PMT was adjusted such that their pulse heights were within 10% of each other. The PMTs were then linearly summed and a threshold was set depending on the particle of interest (if the instrument was used in the trigger). Further refinement of the PMT signals was done in software by analyzing a clean sample of electrons.

To contain gas pressures of both above and below atmospheric pressure, the tank has to have at least two sets of windows; one set must be curved inward for pressures less than 1 atm, and the other set must be curved outwards for pressures above 1 atm. The windows were hydroformed on a special forming jig. During all phases of the experiment, the entrance and exit windows were constructed of 0.040 inch thick aluminum and formed to bow inwards. The gas in the tank during much of the experiment was C_4F_{10} held at a pressure of just under 1 atm. This detector was useful for providing pion-proton separation above ~ 2.5 GeV for the study of the process $\gamma d \rightarrow pn$; it was not used in the trigger or the analysis of the data for the process $\gamma d \rightarrow d\pi^0$.

3.11 Short Orbit Spectrometer

The basic design of the Short Orbit Spectrometer (SOS) was based on the design of the Medium Resolution Spectrometer at LAMPF (see Figure 3.33). The design incorporates one quadrupole magnet QS and two dipole magnets BM01 and BM02 in a $QD\bar{D}$ string. The magnets are non-superconducting and are water cooled by the Low Conductive Water (LCW) system. The main purpose of the SOS is to detect hadrons in coincidence with electrons in the HMS. Since the hadrons are typically slower moving than coincident electrons, the SOS was designed to have a short optical length, a large momentum acceptance, and a medium resolution. The short optical length of the SOS also aids in the detection of short-lived hadrons such as kaons. Although the SOS was not used in the main part of

experiment E89-012, it was used to take backward angle data for the $\gamma d \rightarrow pn$ process and also to collect calibration data to measure quantities such as the attenuation of deuterons in the HMS by studying coincidence ed elastic data. For a detailed description of the SOS see Reference [74].

3.11.1 SOS Optical System

The quadrupole (QS) is closest to the target and focuses in the non-dispersive direction. The first dipole BM01 provides a 33° bend (vertically up), for the central ray, which is then countered by a -15° (vertically down) bend, also for the central ray, in BM02. Both of the dipoles share a common yoke, which makes a compact design. The fields in each of the magnets are monitored by hall probes and current is regulated to maintain the field set point. Power to the magnets is supplied by three Inver Power power supplies mounted on the floor of Hall C. The power supplies are capable of producing up 1000 A; this limits the maximum central momentum setting to 1.75 GeV. Table 3.8 shows the maximum current and voltage available to each of the three magnets. The current output and polarity of the power supplies are controlled remotely.

MAGNET	Max Voltage (V)	Max Current (A)
QS	170	1000
BM01	250	1000
BM02	160	1000

Table 3.8: Maximum power available for the SOS magnets. The maximum of 170 V for QS is only available with the power supply in overdrive.

A movable collimator system was attached to the front of QS to better understand the optics of the spectrometer. The collimator system, shown in Figure 3.34, contains four positions, large collimator, small collimator, sieve slit, and removed. Note the small hole

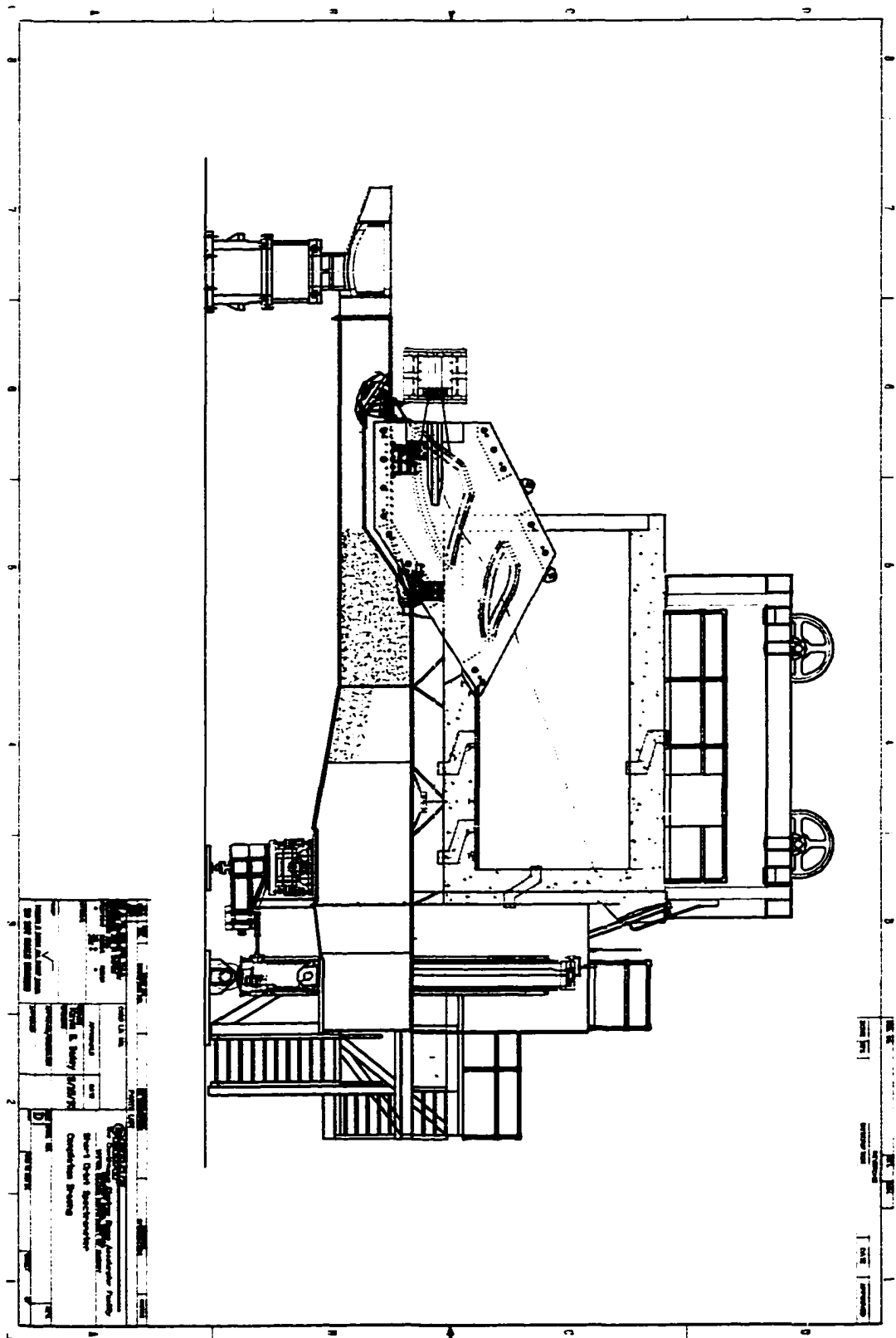


Figure 3.33: Scale drawing of the SOS. Figure 104 shows the central ray as a dot dashed line. Figure courtesy of K. Bailey, Argon National Lab.

in the center of the sieve slit and the 2 “missing” holes on either side of the central hole. The missing holes provided information on the orientation of the sieve slit during analysis. The large collimator was used exclusively for production running of this experiment and the sieve slit was used only to study the optical properties of the spectrometer. The small collimator was not used during the experiment.

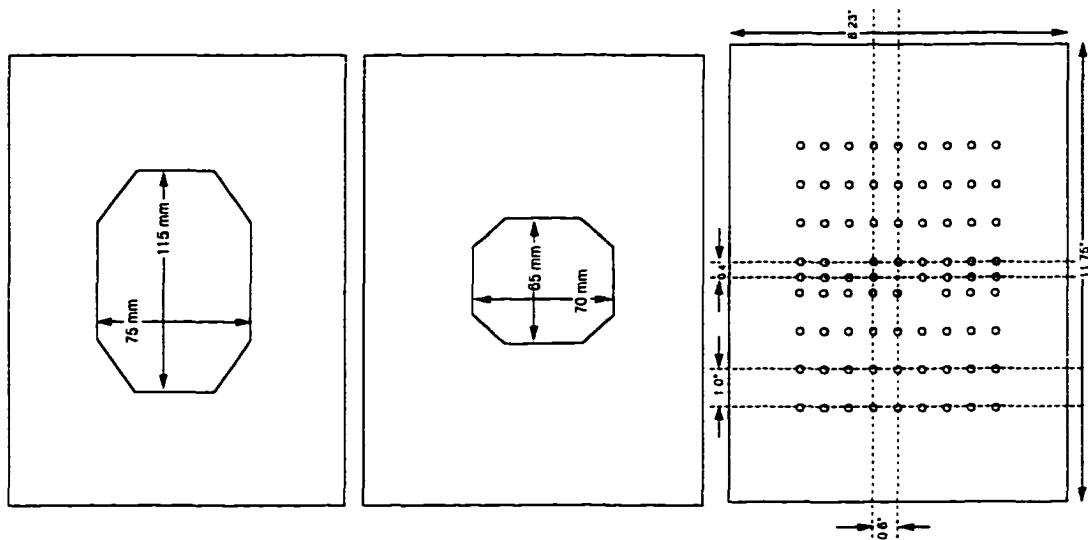


Figure 3.34: Schematic view of the three positions available in the SOS collimator system.

The optical axis for each magnet was surveyed and found to be within 0.1 mm of the physical axis and the SOS magnets were installed and aligned to within 0.2 mm relative to their physical axes. When the spectrometer is rotated, the magnets can move radially up to 2 mm, but these positions are reproducible to better than 0.5 mm. During this experiment, the SOS was operated in the point-to-point standard tune. This tune (as do all others for this spectrometer) gives a small extended target acceptance, but a large momentum acceptance and large solid angle. Both of the dipole fields were mapped and the integral, $\int B \cdot dl$, was determined from this map. The quadrupole field was not mapped and was determined first by using a COSY model [67]. The model was tested using carbon elastic scattering data

taken with the sieve slit. The data showed that the field of the quadrupole was higher than expected by the model for a given current by about 7%; the current was lowered to give the same results as the model. The focal plane of the spectrometer is defined to be 6 cm in front of the first drift chamber and perpendicular to the optical axis (see Figure 3.36). The true focal plane makes an angle of 70° with the detector focal plane (defined focal plane)

The central angle of the SOS was determined in the same manner as the HMS. Scribe marks were surveyed onto the floor of the hall, marking every half degree of the SOS. By comparing a scale positioned at the back of the SOS to these marks on the floor, the central angle of the spectrometer can be measured to within 1.5 mrad when the motion of the SOS magnets is included. The motion of the magnets associated with the rotation of the spectrometer provides the dominant source of uncertainty in determination of the SOS angle. To check this angle measurement, elastic $H(e,e',p)$ data were taken at a number of different kinematics. Although this angular measurement is affected by the beam energy, momentum offsets in both spectrometers and other HMS and SOS offsets which are convoluted and often indistinguishable, the angle offsets for the SOS are less than ± 1 mrad. This is consistent with limits set by the motion in the SOS magnets. An overall uncertainty of 1.5 mrad was applied to all SOS angles.

The spectrometer absolute central momentum calibration may be performed using data from elastic $H(e,e')$ scattering. This technique requires precise knowledge of the beam energy, which is the dominant source of error, and spectrometer angle. To minimize the dependence of the calibration on beam energy, elastic scans were performed at the same beam energy for a number of different spectrometer settings. For central momentum settings below 1.5 GeV, the SOS showed momentum variations of less than 0.2%. For larger central momentum settings, the central momentum is less well known due to a nonlinearity of the magnetic fields. All of the calibration data were collected with a central momentum

setting of less than 1.5 GeV and reflects an uncertainty of 0.2% in absolute momentum.

The SOS reconstruction matrix elements were developed in the same manner as the HMS reconstruction matrix elements (see Section 3.10.2). The final set of matrix elements were calculated to 6th order. Figure 3.35 shows the reconstruction of X' versus Y' at the collimator for elastic $C(e,e')$ data taken with the sieve slit in. A comparison of Figure 3.35 with Figure 3.20 shows that the SOS in-plane angular reconstruction (Y') is not as good as that of the HMS. A summary of the overall performance of the SOS is given in Table 3.9.

Maximum Central Momentum	1.75 GeV
Momentum Acceptance	$\pm 20\%$
Momentum Resolution	0.1%
Solid Angle	10.7 msr
Angular Acceptance (in plane)	± 70 mrad
Angular Reconstruction (in plane)	± 4.0 mrad
Angular Acceptance (out of plane)	± 40 mrad
Angular Reconstruction (out of plane)	± 0.5 mrad
Extended Target Acceptance	3.0 cm

Table 3.9: Summary of SOS performance characteristics [64].

3.11.2 SOS Detector Package

With the exception of the Aerogel Čerenkov, the SOS detector package is very similar to the HMS detector package and is shown in Figure 3.36. The physical design is also more compact, which aids in detecting short lived hadrons. The lead glass shower calorimeter is attached to a rigid mount fixed to the back wall and ceiling of the shield hut. The other detectors are attached to sliding mounts so that individual detectors may be pulled out of the stack and serviced or removed and installed as needed. The instrumentation of the SOS detector package is essentially the same as that of the HMS. All phototube signals are fed into separate ADC, TDC, and scaler channels.

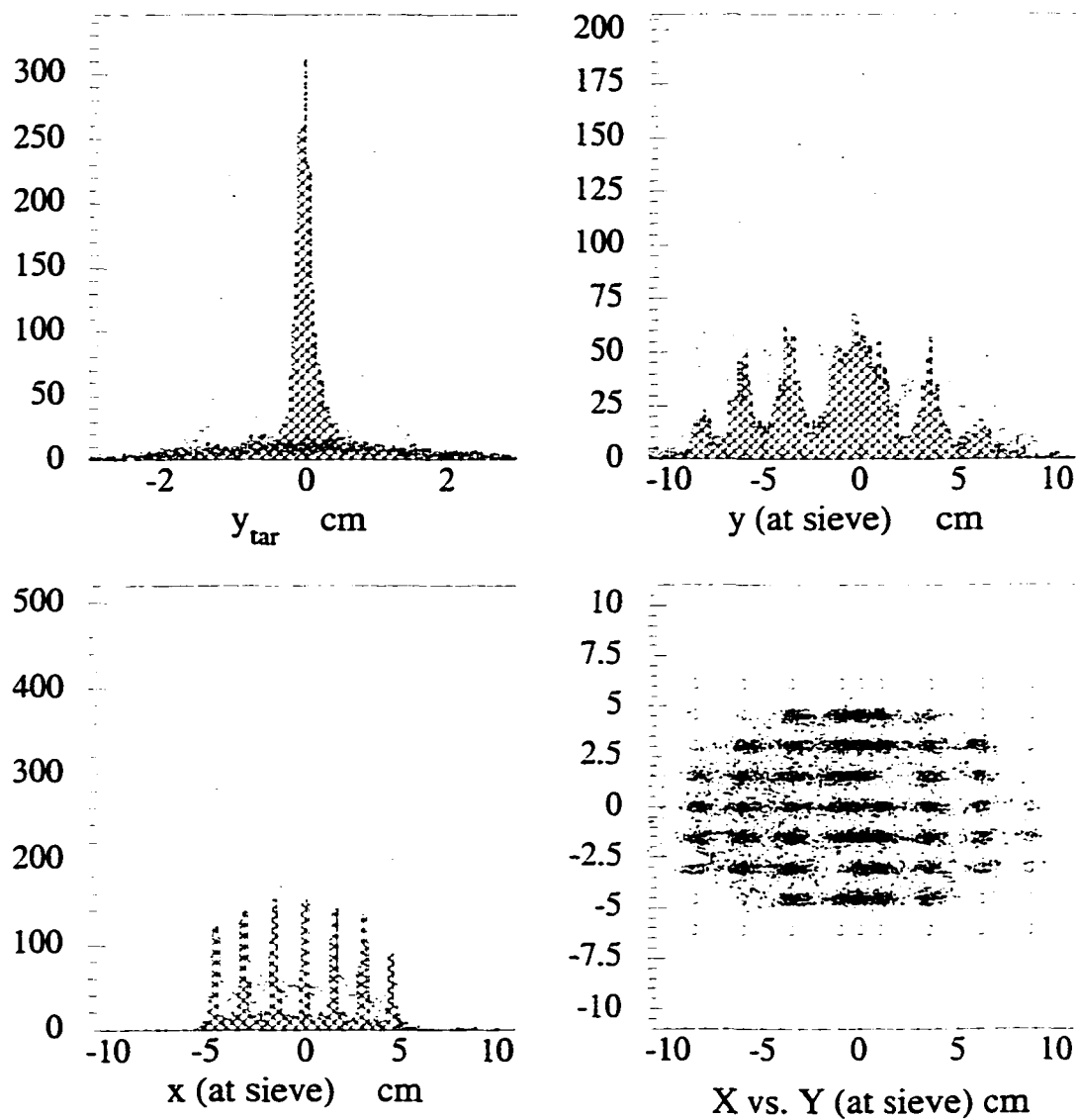


Figure 3.35: Reconstructed Y_{tar} , Y and X at the face of the collimator, and X vs Y at the face of the collimator with the sieve slit in. Data are from $C(e,e')$ scattering. Figure courtesy of C. Armstrong.

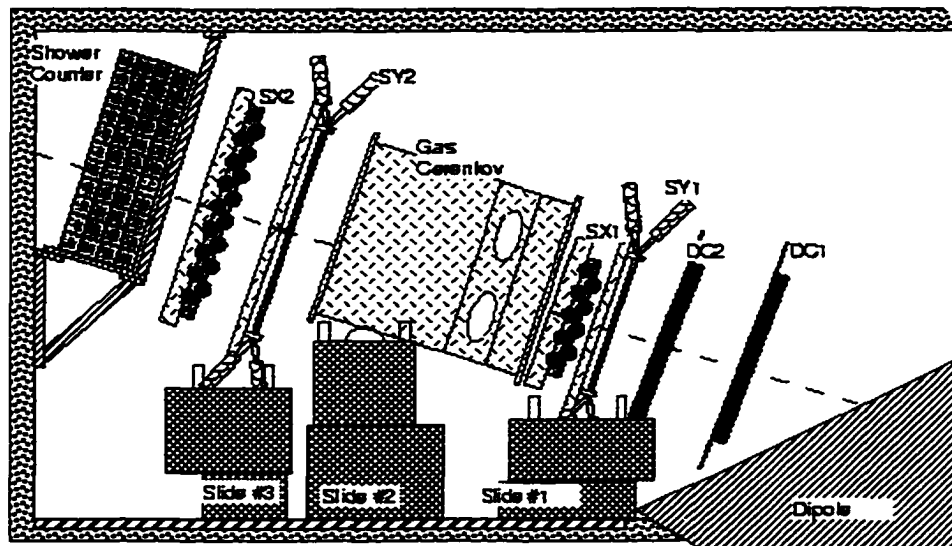


Figure 3.36: Schematic of the SOS detector package. Note that the figure does not show the Aerogel Čerenkov detector which was installed after the first phase of the experiment.

SOS Drift Chambers

The SOS drift chambers were constructed at Brookhaven National Lab and have a different design than those used in the HMS. The basic design is shown in Figure 3.37, and consists of sixteen 0.125 inch G10 plates sandwiched between two 0.50 inch thick aluminum plates, which serve as entrance and exit flanges. Thin mylar (0.0005 inch), coated on both sides with 1200 of copper, serves as entrance and exit windows and as cathode foils which are stacked between the G10 layers. The gold plated tungsten wires, which make up the 1 cm wide drift cells, are embedded between G10 layers and consist of alternating $30\ \mu\text{m}$ sense and $60\ \mu\text{m}$ guard wires. The sense wires are held at ground potential while the guard wires and cathode planes are maintained at a potential of $-1975\ \text{V}$. There are six planes (U, U', X, X', V, V') in each chamber with a 1/2 cell (0.5 cm) offset as shown in Figure 3.38. Figure 3.39 shows the orientation of the wires and the active area of the drift chambers. The X and X' planes give position information in the dispersive direction while the U, U'

(V, V') planes give position information $60^\circ(-60^\circ)$ relative to the X, X' planes.

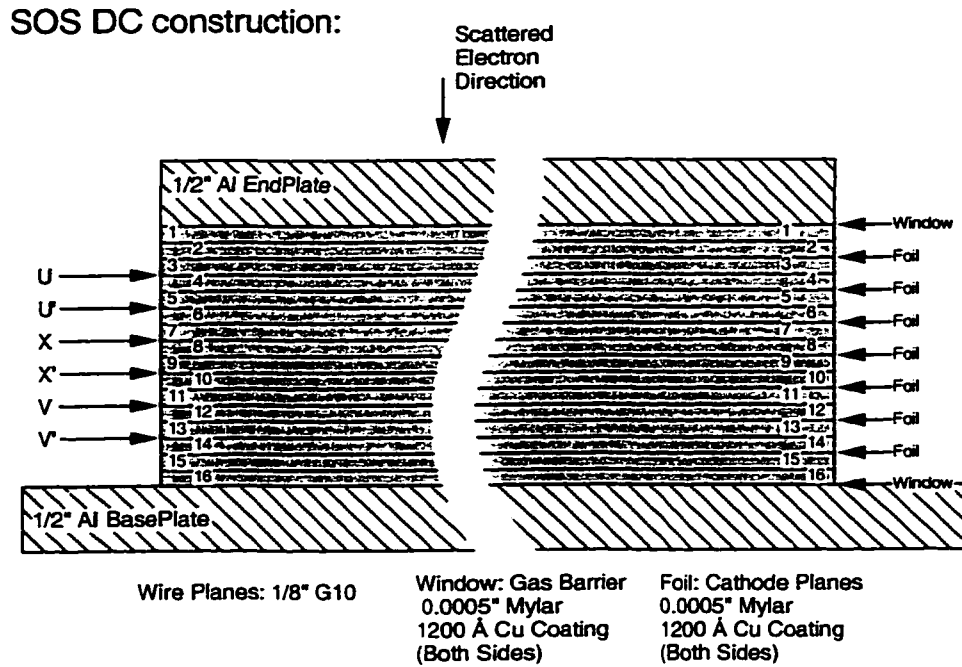


Figure 3.37: Cross sectional view of a SOS drift chamber.

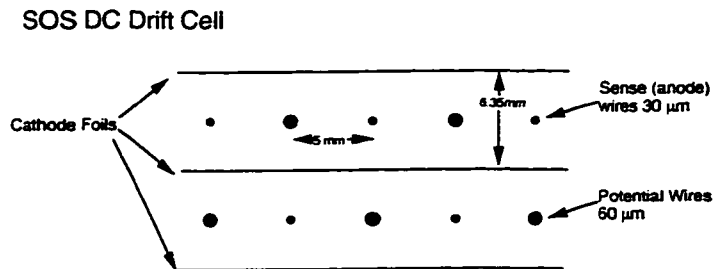


Figure 3.38: Schematic diagram of the wire layout for a pair of planes in the SOS chambers.

The electronic instrumentation associated with the HMS and SOS drift chambers is exactly the same (see Section 3.10.4). The HMS and SOS also use the same gas handling system. The voltage for the thresholds on the discriminator cards are provided by a BK 1600 DC power supply and was normally set to 1.5 V (this was set to 1.5 V for all phases

SOS DC Active Areas

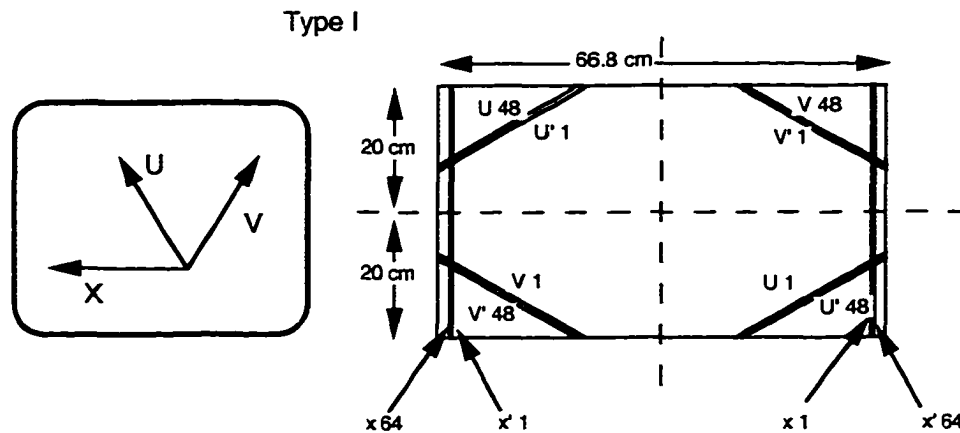


Figure 3.39: Active area of the SOS drift chambers. The figure also shows the orientation of the wires for all planes.

of the experiment). The power supply is located in the Hall C counting house and, therefore, remote changes of the threshold are possible.

The SOS drift chambers have been surveyed relative to the exit of the BM02 dipole. The position of the drift chambers are known to better than 0.5 mm. The position of each wire relative to the center of the chamber is known to $\pm 87 \mu\text{m}$ [77]. The final tracking resolution of the SOS drift chambers was better than 200 μm .

SOS Hodoscope

The SOS hodoscope, designed and constructed at Old Dominion University, is instrumented in the same manner as the HMS hodoscope. It is also constructed out of the same scintillator material as the HMS hodoscope (BiCron BC404) (see Section 3.10.4). As can be seen in Figure 3.36, the hodoscope has four planes that are separated into two pairs of xy planes. One pair of xy planes is situated behind the second drift chamber. The other pair is mounted in front of the lead glass shower counter. The Aerogel Čerenkov was mounted

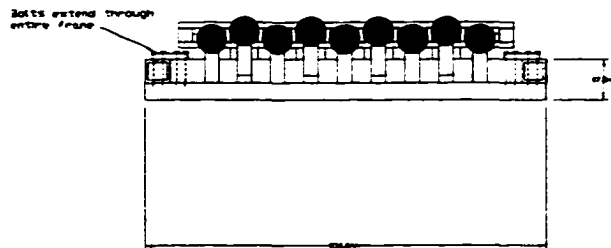
between the x and y planes in the second hodoscope pair during later phases of the experiment. The front planes of the detector are smaller than the rear planes. The paddles are 1.0 cm thick with widths and lengths as shown in Table 3.10. There is also a ~ 5 mm overlap of adjacent scintillators paddles in all planes to ensure that there are no gaps in the active area of the detector which is roughly 113×37 cm. All of the individual paddles are wrapped with aluminized mylar and two layers of Tedlar (PVF) to ensure that they are light tight. Figures 3.40 and 3.41 show the physical characteristics of the SOS hodoscope. The position of the SOS hodoscope was surveyed; however, in practice the position was determined with analyzed tracking information from electron scattering data.

Plane	Number of Elements	Length (cm)	Width (cm)
S1X	9	36.5	7.5
S1Y	9	63.5	4.5
S2X	16	36.5	7.5
S2Y	9	112.5	4.5

Table 3.10: SOS hodoscope physical characteristics.

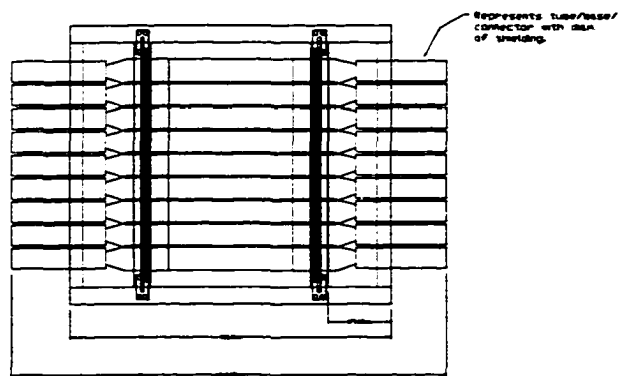
The calibration for the SOS hodoscope PMT high voltage was first done by gain matching the tubes with a ^{60}Co source by setting the voltage such that the pulse height was 500 mV at the tube base. The bases used are the same as the HMS hodoscope bases. Further refinement of the high voltage tune was done by analyzing the ADC spectra for a given set of particles and tracking parameters. Calibration of the hodoscope time of flight measurement is discussed in Section 4.2. The instrumentation for the HMS and SOS hodoscopes are exactly the same and is shown in Figure 3.30.

X1 END VIEW



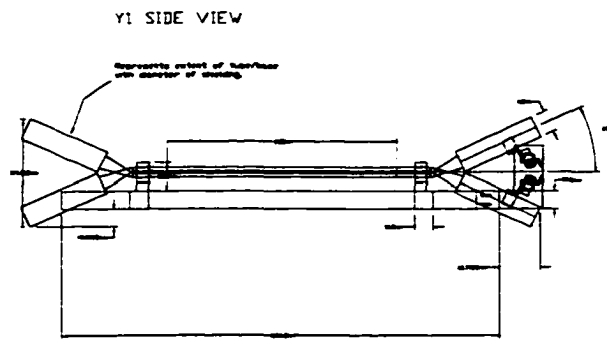
(a) Side view

X1 TOP VIEW

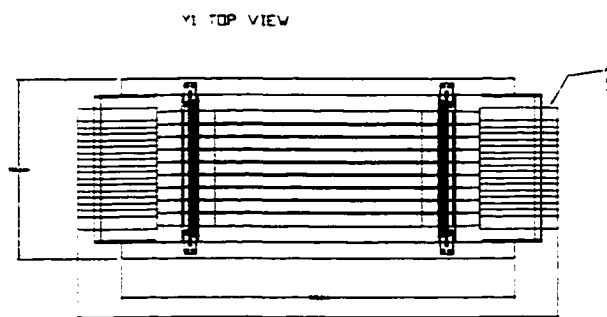


(b) Top view

Figure 3.40: Schematic views of the X planes in the SOS hodoscope.



(a) Side view



(b) Top view

Figure 3.41: Schematic views of the Y planes in the SOS hodoscope.

SOS Čerenkov Detectors

The SOS gas Čerenkov detector was designed and constructed at the University of Colorado, Boulder. It is essentially an aluminum box with entrance and exit windows constructed of 0.254 mm thick Lexan graphic film covered with a 0.0508 mm of Tedlar film. The gas pressure inside the detector must be very near 1 Atm due to the thin window construction. The detector is normally filled with 1 Atm of Freon 12 (CCl_2F_2) which has an index of refraction of 1.00108. This gives an electron detection threshold of 11 MeV and a pion threshold well above the maximum central momentum setting of the SOS.

There are four spherical mirrors mounted at the back of the detector that reflect light into the four PMTs. The four Burle 8854 PMTs are mounted in Winston cones within the gas. The gas pressure is maintained by a gas system that is designed to fill at 0.2 PSI underpressure (below 1 Atm) and relieve at 0.5 PSI overpressure (above 1 Atm) [75]. The system is described in detail in references [74] and [76]. Since the Čerenkov signal is often added to the trigger to give some active particle identification, the output signals from the phototubes had to be matched. This was done by adjusting the high voltage until the pulse height variation was within 10% for all 4 tubes. The high voltage for the tubes varied between 2650 and 2800 V. The power supply for this voltage is of the same type as that used for the HMS Čerenkov. The signals from the phototubes are carried over ~ 30 ft of RG58 and ~ 300 ft of RG8 air core cable. These signals are split, summed and can be instrumented in the trigger as shown in Figure 3.32.

The Aerogel Čerenkov detector was installed to discriminate between pions and other hadrons, such as kaons. It was not needed or used for any part of the experiment and will only be briefly discussed here. A more detailed description of the SOS Aerogel Čerenkov detector is given in Reference [74]. The Aerogel material ($n(\text{SiO}_2) + 2n(\text{H}_2\text{O})$) was orig-

inally developed as a packing material and has an index of refraction of 1.040 ± 0.001 , giving a pion threshold of ~ 0.510 GeV and a kaon threshold of ~ 1.8 GeV. This allows discrimination of pions from Kaons at most spectrometer momenta.

The entire stack of Aerogel material ($100 \times 40 \times 90$ cm) was covered by one layer of 96% reflective Millipore paper and two layers of aluminized mylar on all sides except for the top which was open to the inside of the diffusion box. Fourteen Burle 8854 phototubes are mounted to the diffusion box. There are also two gas feedthroughs attached to the diffusion box which are used to flush dry nitrogen over their Aerogel material. This is done to prevent the Aerogel, which is an exceptionally good dessicant, from absorbing excess moisture from the atmosphere thereby changing the index of refraction. The signals from the phototubes are instrumented as shown in Figure 3.42.

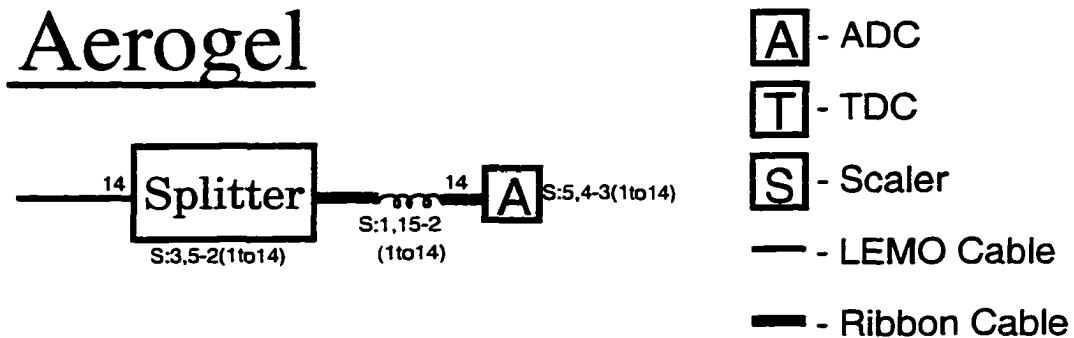


Figure 3.42: SOS Aerogel Čerenkov detector electronic instrumentation schematic. Figure courtesy J. Arrington.

SOS Lead Glass Shower Counter

The SOS lead glass shower calorimeter is exactly the same as the one in the HMS. A detailed description of the lead glass shower calorimeter is given in Section 3.10.4 and more thoroughly in Reference [74]. The instrumentation for the HMS and SOS shower

calorimeters is exactly the same and is shown in Figure 3.31.

3.12 Data Acquisition

Almost all acquisition of physics data at TJNAF is accomplished with the CEBAF Online Data Acquisition (CODA) routines [78]. These routines run on and control a network of front end Input Output Controllers known as Readout Controllers (ROCs) positioned in each data acquisition crate (FASTBUS and VME). The data for each event come as fragments (part of the event comes from each of the ROCs triggered) over the Hall C LAN to the main data acquisition workstation to be processed into a complete event by the event builder. In Hall C, this workstation is a HP 9000/735. In addition to the data from the detectors in the spectrometers, information from beamline sources, scalers, and various databases is collected into the data stream as separate events.

3.12.1 Input Output Controllers

Scaler, ADC, and TDC raw signals are collected in several different VME and FASTBUS crates. Each individual crate has an Input Output Controller (IOC). The IOC is a single board computer, mounted in the individual crate (VME or FASTBUS), that can communicate with each module in the crate as well as over the LAN. Each of the IOCs in Hall C runs an operating system called VxWorks. Routines compiled for VxWorks can be run on these IOCs to control the functions of each module in the crate and determine how the data from each module will be handled.

The ADCs and TDCs are all FASTBUS modules. The hits in the wire chambers in each spectrometer are read by LeCroy LC1876 multihit TDCs. Each of the 96 channels per mod-

ule can store up to 12 hits. The ADC and TDC signals from phototubes are read into LeCroy LC1881M programmable ADCs and LC1872A high resolution TDCs. The LC1881M can be programmed to read only channels with signals above a programmed threshold (set uniquely for each channel). The LC1872A module can also be programmed to sparsify, meaning that channels that did not receive a stop are ignored. These features help keep the raw event size to a minimum number of bytes and improve the data acquisition rate. However, by sparsifying the ADC signals, there is no pedestal information collected during normal data acquisition. To provide a measure of the pedestal for each ADC channel, 1000 events of type PED are taken at the beginning of each run without sparsification. These events are triggered by a gate generator and real triggers are masked out to ensure that only data in the pedestal of the ADC will be collected. The analysis software compares these pedestals with the thresholds programmed into the module. If the thresholds are too low or too high the analysis software warns the user of this problem so that viable data are not lost.

VME crates in the data acquisition system contain a number of different modules that perform various functions. All hardware scalers incorporated into the data stream are VME modules. The VME crates also contain memory modules and FDDI modules to increase the data transfer rate from the FASTBUS to the main computer. A specialized module called the trigger supervisor controls the state of the run and sends all of the gates to the various TDCs and ADCs. Upon receiving a trigger from one spectrometer, the trigger supervisor waits 10 ns for another possible trigger to come in (the other spectrometer will also provide a trigger if the event is a coincidence event). After this time, it determines which of the four physics event types it has just received, PED, HMS, SOS, COIN. A more detailed description of the trigger supervisor is provided in Section 3.13.

3.12.2 CODA Overview

CODA was developed at TJNAF by the TJNAF Data Acquisition Group and consists of a library of routines that can be compiled for various platforms. CODA contains its own programming language, CODA Readout Language (CRL), and a graphical user interface (GUI), Run Control, that enables the user to control the state of the run as well as monitor basic aspects of the data acquisition system [78]. At the beginning of a set of runs, a run type is selected. This defines how the data acquisition hardware and software respond to any given runtime event by selecting which ROCs are to be used and which routines are to be executed on them. These routines are then downloaded to the individual ROCs, having already been compiled for whatever type of CPU the ROC contains. CODA also provides the user with the ability to define various trigger types other than the standard physics event types. Thus, in addition to the physics triggers, an asynchronous trigger to read out the scalers was generated every 2 seconds. CODA also supplied the trigger to read out various slow controls quantities such as target settings and HMS spectrometer magnet settings from various EPICS databases every two minutes.

In the standard configuration, upon receiving a physics trigger from the trigger supervisor, the FASTBUS ROC reads out the proper modules and transfers the data to a VME memory module. From these the data are transferred to the main computer through a FDDI module. In the main computer, the event fragments taken from each ROC are compiled into separate events with proper headers by the event builder (separate software that runs solely on the main computer) and recorded on hard disk. The data is then analyzed by the Hall C analysis software described in Section 3.15.

3.13 Hardware Trigger

The single arm triggers for the HMS and SOS spectrometers are essentially identical. If single arm triggers are registered in both spectrometers within a certain timing window, then the event is classified as a coincidence event (COIN). For a coincidence event, no single arm data are lost and, in analysis, the event may be treated as two single arm events or a coincidence event. In the standard configuration, a single arm trigger, or more properly a single arm pretrigger, is provided by the scintillators. There are two pairs of xy scintillator planes in the hodoscope for a total of four planes. To define a hit in one plane, photomultiplier tubes on both sides (+/-) of a paddle must fire. The user can define the number of planes that must receive a hit (1, 2, 3, or 4) to give a trigger. In addition to the hodoscope trigger, signals from the Čerenkov and lead glass shower calorimeter can be incorporated into the trigger to provide particle identification. This can be done to select electrons, for example, by requiring the sum of the ADC signals from the shower counter to be above a certain threshold. For the purposes of this experiment however, only the hodoscope was used to define a trigger. A schematic of the general Hall C trigger is shown in Figure 3.43.

3.13.1 Hodoscope Trigger

Since the hodoscope was the only element of the detector stack used in the trigger, it is the only trigger type discussed at length here. In the HMS, the individual hodoscope planes are formed with overlapping plastic scintillators bars (see Section 3.10.4). There are 16 paddles in each x plane ($X1$ and $X2$) and 9 paddles in each y plane ($Y1$ and $Y2$). Each of these paddles are read out on both ends (+/-). Signals from all of the tubes on the + (-) side are fed into an OR gate to form $S1+$ ($S1-$). These two signals are then passed to an AND gate to form $S1X$. The procedure is performed for all 4 planes so that there are four signals

General Trigger

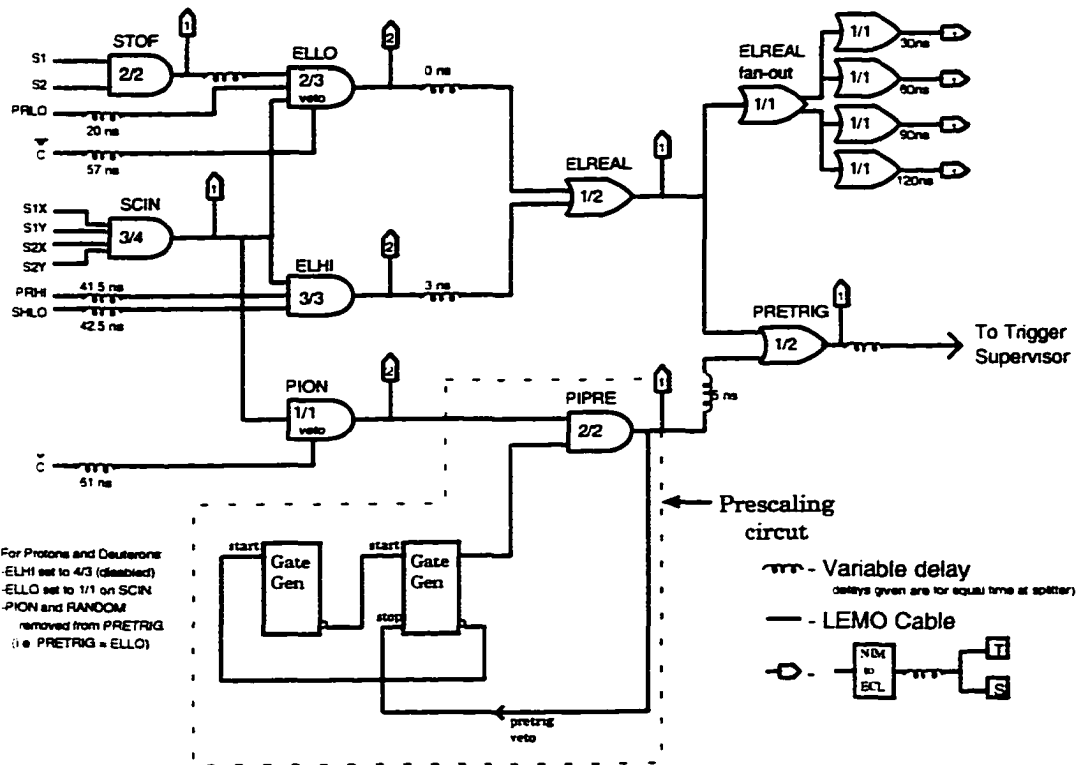


Figure 3.43: Schematic of the General Hall C single arm trigger for the HMS or SOS. Figure courtesy of J. Arrington.

S1X, S1Y, S2X, S2Y. These four signals are passed to a coincidence unit where the user can select the coincidence level from 1/4 to 4/4. Three planes must receive hits to ensure that there is always good timing information. A diagram of the hodoscope trigger is shown in Figure 3.30. During the experiment, most data were taken with a coincidence level of 4/4 (all four planes in the hodoscope must fire) to reduce the rate of accidental triggers. However, at each kinematical setting at least one run was taken with a coincidence level of 3/4 to determine the efficiency of the trigger.

The efficiency of the trigger was determined by examining the individual plane efficiencies with a coincidence level of 3/4. The individual plane efficiencies were determined by counting how many times an individual plane fired and dividing that result by the total number of triggers. In all cases, the efficiency was greater than 99.5%, for each plane. The total efficiency for the trigger is calculated from the individual plane efficiencies and was always greater than 99.5% for the 3/4 coincidence level trigger and greater than 99.1% for the 4/4 coincidence level trigger.

3.13.2 Trigger Supervisor and 8LM

The Trigger Supervisor Module was developed by the TJNAF Data Acquisition Group. This module is mounted in a 9U VME slot and serves as the interface between the data acquisition hardware and software. There are three outputs that determine how individual triggers are processed. Any time a run is in progress, TS GO is enabled. TS EN1 is true during normal data acquisition and TS BUSY is true only when the trigger supervisor is busy processing an event. These signals are accessible through certain addresses in the memory of the trigger supervisor. Thus, by using the IOC installed in the VME crate where the trigger supervisor is located, one can access these addresses and read them or write to

them. By reading/writing to the address for TS EN1, one can read or change the state of the run. In other terms, one can externally pause all the data acquisition by addressing this register. To take advantage of this fact, a set of server routines were compiled for the IOC and a GUI was made so that a run can be paused without having any effect on the quality of the data. This feature was used to pause the run during brief lapses in beam delivery. The trigger supervisor also contains prescale registers for each of the event types. Thus, if the value for the HMS single prescale register is 10, each successive HMS single trigger will decrement a counter and be ignored until the counter reaches 0 at that point the trigger is accepted and the counter reset to 10. Hence, only 1 event in 10 will be accepted.

The operation of the trigger supervisor is rather complicated and a detailed description can be found in the Trigger Supervisor Users Guide [79]; only a brief description is given here. Upon receiving a pretrigger from a single arm, the trigger supervisor waits 10 ns and then latches all enabled triggers that fired. This gives the trigger supervisor a trigger pattern that it then compares with a lookup table to determine which of the four possible types (HMS, SOS, COIN and PED) the trigger is. For example, consider the trigger supervisor receiving a single arm pretrigger from the HMS and 5 ns later it receives a pretrigger from the SOS, the trigger supervisor would then determine that the trigger is a coincidence (COIN) trigger. At this point, the trigger supervisor sends ADC gates and TDC starts to all the appropriate FASTBUS modules. In the case of an HMS single arm trigger, only the FASTBUS modules associated with the HMS and beamline instrumentation will receive gates. For COIN and PED triggers all FASTBUS modules are given gates. Note also that only 1000 PED events are allowed before the TS EN1 becomes true. The gates for each spectrometer are retimed with respect to the single arm trigger. For single arm events, this is not really necessary; however, for coincidence events TDC starts must come at a fixed time relative to the time that the particle passes through the detector in each arm.

The LeCroy LC2365 8LM programable logic module works in some sense in parallel to the trigger supervisor. The pretriggers for HMS, SOS and COIN, are fed into the 8LM, as are the signals TS GO, TS EN1, and TS BUSY from the trigger supervisor. The outputs of the 8LM are four pretriggers and four triggers (see Table 3.11). The triggers occur only when the trigger supervisor is not busy and pretriggers are accepted as fast as the electronic hardware will permit. All the pretriggers and triggers are sent to scalers and are used to determine raw event rates and computer dead times, among other quantities. A schematic diagram of the trigger supervisor electronics is shown in Figure 3.44.

Output	Logic
HMS PRE	$HMS \otimes EN1$
SOS PRE	$SOS \otimes EN1$
COIN PRE	$COIN \otimes EN1$
PED PRE	$PED \otimes GO \otimes \overline{EN1}$
HMS TRIG	$HMS \otimes EN1 \otimes \overline{BUSY}$
SOS TRIG	$SOS \otimes EN1 \otimes \overline{BUSY}$
COIN TRIG	$COIN \otimes EN1 \otimes \overline{BUSY}$
PED TRIG	$PED \otimes GO \otimes \overline{EN1} \otimes \overline{BUSY}$

Table 3.11: 8LM logic table (\otimes implies logical AND and signals with bars on top refer to the logical not of the signal).

3.14 Dead Time Determination

There are two types of dead time for the data acquisition and trigger system. The first type that is discussed in detail here is known as electronic dead time and results from events which are missed because the logic modules in the trigger electronics are busy processing previous events. The second type of dead time is derived from the busy state of the data acquisition system and is called computer dead time. This dead time results from delays due to data transfer over the network, transportation of trigger signals from the counting

Trigger Supervisor

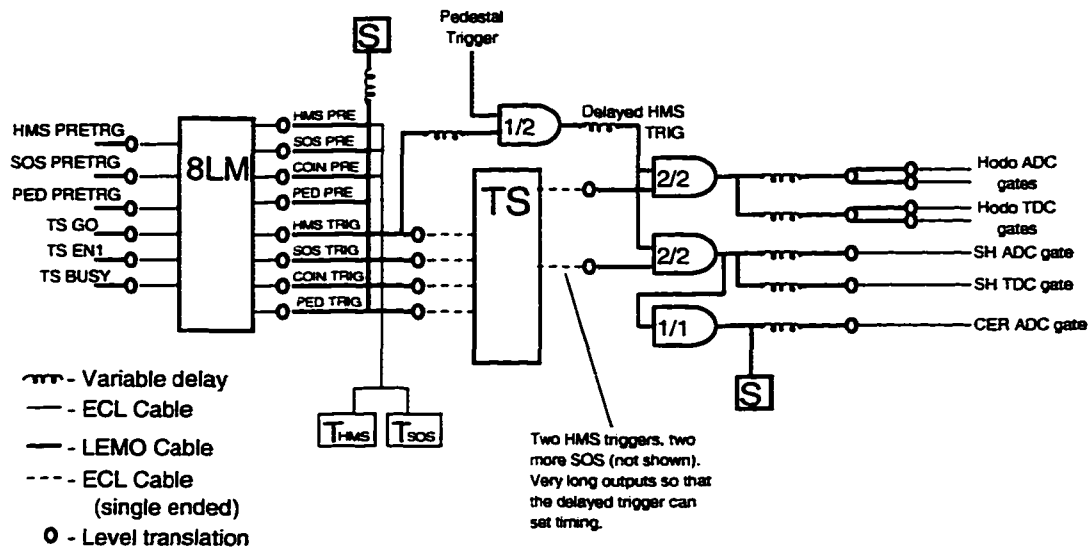


Figure 3.44: Trigger supervisor electronics schematic. Figure courtesy J. Arrington.

house to the hall, and other delays in data transfer from the ADC and TDC modules to the main data acquisition computer. While the first type of dead time typically results in a correction that is almost negligible, the second type of dead time can force corrections to the measured differential cross section of 20 to 30% or more.

3.14.1 Electronic dead time

When a trigger is received, the logic modules produce a level (-0.8 V NIM) for a duration of time called the gate width. The gate width T for the logic modules used in the Hall C trigger is 30 ns. While this level is activated, the logic module ignores any additional incoming triggers and this results in what is called electronic dead time. This dead time is different from the computer dead time discussed later in this section. To understand how a measurement of this dead time is made, first consider the case where the average event rate is roughly a constant over an interval of time and that the occurrence of events is randomly

distributed over the interval. The probability of observing an event in a given time period t is given by

$$P(0, t, \tau) = e^{-t/\tau} \quad (3.16)$$

where τ is the mean time between events. The probability distribution for the time between events is then given by

$$P(t) = \frac{1}{\tau} e^{-t/\tau}. \quad (3.17)$$

It is clear that $R_{true} = 1/\tau$ is the true average event rate. To approximate the fraction of events that will be measured, the probability in Equation 3.17 must be integrated from the gate width of the level, T , to ∞ .

$$f_{live} = \int_T^{\infty} \frac{1}{\tau} e^{-t/\tau} = e^{-T/\tau}. \quad (3.18)$$

For gate widths small compared to τ , Equation 3.18 may be approximated by

$$f_{live} \approx 1 - T/\tau.$$

Thus, the measured event rate R_{meas} is slightly less than the true event rate R_{true} and is given by

$$R_{meas} \approx R_{true}(1 - T \cdot R_{true}) \quad (3.19)$$

where the substitution $R_{true} = 1/\tau$ has been made. To determine the electronic dead time for the trigger, final triggers were generated with gate widths of 30, 60, 90, and 120 ns. This enables a linear extrapolation to $T = 0$ and an approximation of the true event rate. The live time (*live time* = 1 - *dead time*) then becomes a multiplicative correction factor to

the cross section measurement and is given by

$$R_{live} = \frac{R_{true}}{R_{meas}}. \quad (3.20)$$

During the experiment, the electronic dead time was less than 0.5% in all cases and thus R_{live} was very nearly 100% for all running conditions.

3.14.2 Computer Dead Time

Measurement of the computer dead time is significantly more simple than the measurement of the electronic dead time. The computer live time (*live time* = 1 - *dead time*) correction is given simply by the ratio of pretriggers to triggers

$$R_{comp} = \frac{HMSPRE}{HMSTRIG} \quad (3.21)$$

where the ratio is a multiplicative correction to the cross section. This ratio should be the same for all types of triggers (HMS, COIN, and SOS). The dead time is a strong function of the accepted pretrigger rate (prescaled trigger rate). For event rates less than 100 Hz, the dead time is typically less than 1%. For event rates larger than 10 kHz, the dead time is nearly 100%. The dead time is also less if only one spectrometer is accepting triggers, because the dead time for the computer is strongly affected by the amount of data in raw bytes that it is receiving. The dead time correction was determined to be linear, within 1%, up to dead times of more than 99%, and was kept below 30% for the entire experiment.

3.15 Hall C Analysis Software

Event decoding and analysis were done using the standard Hall C analysis software (*Engine*). *Engine* incorporates routines from the CODA and CERN libraries. All events are decoded and run through appropriate analysis loops (i.g., a HMS event is analyzed only by the HMS routines). In addition to physics events, the Hall C *Engine* analyzes all scalers and information from various slow controls databases. Tests and histogram initialization is handled by a special package, the CEBAF Test Package (CTP), developed at TJNAF [80]. The *Engine* routines also support event display and online data analysis (although this last feature was not used for the experiment and will not be discussed). The software also has the additional feature that it is not platform specific and can run on various operating systems including DEC Alpha, HPUNIX, Linux, and Sun OS. The analysis routines in the *Engine* are written in FORTRAN and CTP is written in C. There is also a TCL script that displays run specific information pertinent to the ongoing analysis, such as analysis rate and various tracking efficiencies.

3.15.1 General Event Analysis

For a typical run, the *Engine* starts by reading the main configuration file and various other configuration files containing specific information about spectrometer, target, run, and detector settings, including the reconstruction matrix elements for each spectrometer. The software then initializes all histograms and n-tuples to be used. At this point, it begins looping through the events in the data file. There are basically three event types. Scaler events contain all scaler information for all detector signals and various beam and diagnostic related signals. Information events contain information read from various EPICS data bases and are triggered by the data acquisition software. Physics events are triggers in the

spectrometers that contain signals from the FASTBUS ADCs and TDCs. With the proper event type identification, the event is sent to the various subroutines which are applicable for analyzing the event. For each physics event, reconstruction and various physics quantities are calculated. Finally, the event is booked into various histograms and n-tuples. After the last event is read, *Engine* updates output files and then closes all open files.

3.15.2 HMS Specific Event Analysis

If the event is determined to be a physics event, there are four possibilities. Pedestal events, which have already been discussed in Section 3.12, HMS single events, SOS single events, and COIN (coincidence) events. HMS and SOS events are analyzed by slightly different routines, but in an analogous fashion. COIN events require that both the SOS and HMS analysis routines are called and, with the individual spectrometer data, calculates additional quantities relevant to a coincidence trigger, such as the coincidence time. Because only singles data in the HMS were collected during the experiment (with the exception of some calibration data) only a description of the analysis of an HMS event is described.

At the beginning of each HMS event, the raw quantities from ADCs and TDCs are used to determine pretracked quantities. For example, the time of flight (TOF) between the scintillator planes is determined by timing information in the TDCs and the physical separation between the two sets of planes. This is done without any pathlength corrections and is useful for determining tracking efficiencies among other things. Timing corrections from pulse heights, cable lengths, and signal propagation times are applied prior to the calculation of all timing information. The time measured at the front scintillator plane determines the start time for the HMS drift chambers. Time between the drift chamber start time and a given stop time is converted into path length and, by knowing the properties of the drift

chamber gas, the distance from the hit wire is determined. The tracking algorithm for the drift chambers in both the SOS and HMS is rather detailed and is discussed, at length, in Section 4.1. At this point, the track with the best χ^2 fit is selected. The Čerenkov and lead glass calorimeter ADC signals are recorded and analyzed. Next, path length corrections are applied to all the relevant quantities (i.e. the TOF between the scintillators is corrected for angle and total path length between the paddles which received hits on a given track). Finally, the reconstructed quantities and pertinent physics information are calculated and all information is booked into the appropriate histograms and n-tuples.

Chapter 4

Event Reconstruction

All event reconstruction was performed by the Hall C standard analysis package (*Engine*), which is discussed in detail in Section 3.15 and in Reference [81]. The package incorporates CODA, CERN, and CTP libraries with the Hall C *Engine* FORTRAN routines. Although the analysis software is particularly amenable to customization, the main event analysis remains the same. Events are first decoded from raw data files. Tracks and particle identification information are then generated for events where this is possible (events where this is not possible are discarded). Tracking information is used to generate the reconstructed spectrometer quantities and improve the particle identification. The analyzer also increments both hardware and software scalers. Finally, the standard output is generated in the form of Physics Analysis Workstation (PAW) n-tuples, HBOOK files, and text scaler report files. More in depth physics analysis is done using PAW macros and COMIS as well as with specialized routines written in C. The use of these standard packages allows the execution of the analysis package on many different platforms including HPUX, SUNOS, IBM AIX, and PCs with the Linux operating system.

4.1 Tracking

The two drift chambers in the HMS detector stack were used to provide tracking information. Drift chamber information was gathered for each trigger using multihit FASTBUS TDCs. The standard Hall C analysis software is capable of finding multiple tracks per trigger if the particles producing these tracks are far enough apart. However, only one track, that with the least χ^2 , was selected for each event during the analysis. A brief outline of the tracking procedure in the HMS is presented in this section. The tracking procedure for the SOS is nearly identical and a more detailed description of the general procedure can be found in Reference [82].

When a charged particle passes through the drift chambers, it ionizes the chamber gas, producing electrons. These electrons are collected on the sense wires of each plane, which are some distance away from the real particle track. This distance is determined by first assuming that the particle was incident on the chamber in a nearly perpendicular fashion and by converting the TDC time to distance with the time-to-distance map which is discussed on page 94. The position (in space (x, y)) is approximated by comparing hits in pairs of unlike planes. For example, consider the case of a hit in an x -plane and a hit in a y -plane. These two planes are perpendicular to each other and, therefore, provide a rough set of (x, y) coordinates for the real particle track. The wire chambers have two y -like planes (y, y') , two x -like planes (x, x') , and two u -like planes (u, v) giving a total of six planes. The u (v) planes make angles of $+(-)15^\circ$ with the x planes. Because the angles between the u -like and x -like planes are small, the planes are not considered to be unlike enough to give good position information (give both an x and a y position). However, the angle between the u and v planes is 30° and, as such, the two planes are unlike enough to provide position information with a sufficient resolution.

Many particles which pass through the chambers do not produce hits in all of the six planes. Both x and y information are needed (both are equally important) to properly reconstruct the event, even though there are four x -like planes and only two y -like planes. To ensure that each event will have sufficient y information to form a track, both y planes or one y plane and both the u and v planes must fire. This is guaranteed by requiring at least five out of the six planes in the chamber to fire. This requirement proved to be too strict for the purposes of the experiment and events with hits in four of the six planes were also tracked (for events with two elements of y information only). The four out of six tracking procedure was not used in the production analysis but, it was used to determine the systematic uncertainty related to the tracking efficiency correction (see Section 4.1.1).

Once the approximate positions of the hits are identified, hits that are close to each other are grouped together to form space points. Each space point contains a list of hits with their x and y positions. At this point, it is still uncertain as to whether the particle passed to the right or to the left of each of the hit wires. Because the y and y' planes are close together and staggered by half a cell width (0.5 cm), there is no left-right ambiguity for these planes if they both fire. In all other cases, stubs (short tracks through a given chamber) are fit to all possible left right combinations and the stub with the lowest χ^2 is chosen.

The procedure for finding space points and stubs is performed for each of the two chambers. Having found the best stubs for each chamber, the stubs that are consistent with a corresponding stub in the other chamber are linked together to form tracks by fitting a full track to them. For the stubs to be consistent, they must point to each other or nearly so. This is done for each combination of stubs found; thus, most events with multiple tracks are not lost. In most cases however (> 95%) there is only one track found per event. Finally, the track, which is a fit to consistent stubs in both chambers, with the best χ^2 is chosen for each pair of consistent stubs. The track is recorded as positions in x and y and slopes $\frac{dx}{dz}$

(abbreviated x') and $\frac{dy}{dz}$ (abbreviated y') in focal plane coordinates along with the χ^2 of the fit.

The resolution of the HMS drift chambers is affected by a number of criteria including the accuracy of the survey, the resolution of the TDCs, the performance of the discriminator cards, and the gas mixture. The final per plane resolution of the chambers was determined by comparing the position measurements of the individual planes to the final fitted track. The typical per plane resolution for high energy electrons is better than $300\ \mu\text{m}$. For the same electrons, the overall position resolution is better than $150\ \mu\text{m}$ in x and $200\ \mu\text{m}$ in y . The overall angular resolution is better than $25\ \text{mrad}$ in x' and $35\ \text{mrad}$ in y' . The differences in the x and y resolutions are consistent with the fact that there are four x -like planes and only two y -like planes.

4.1.1 Tracking Efficiency

Typical tracking efficiencies for electrons in the HMS are better than 95% in most cases, and is often better when electrons are detected in coincidence with other particles (detected by the SOS) [83]. Because the HMS was used in single arm mode (the SOS could not be used in coincidence to reject background events) to detect hadrons in the experiment, the tracking efficiency was relatively poor, and in the worst cases was found to be only $\sim 65\%$ – 70% . Since this is such a large correction, the tracking efficiency and the systematic uncertainty associated with it must be well determined. The tracking efficiency was also seriously affected by the HMS gate valve, which was inadvertently left roughly halfway within the HMS acceptance during some of the phases of the experiment (see Section 4.6).

In general, the tracking efficiency is determined by using the HMS hodoscopes and a few calculated scaler quantities. A fiducial cut is placed on the HMS hodoscope paddles

that excludes all paddles which are not close to the center of each plane to form a “sweet spot” as shown in Figure 4.1. By making this cut, only events with particles that produced a trigger and that should have passed through both wire chambers are considered when calculating the efficiency. The tracking efficiency is then determined by taking the ratio of the number of tracks found for this type of event to the total number of these events. Note that this procedure does not exclude all possible accidental triggers.

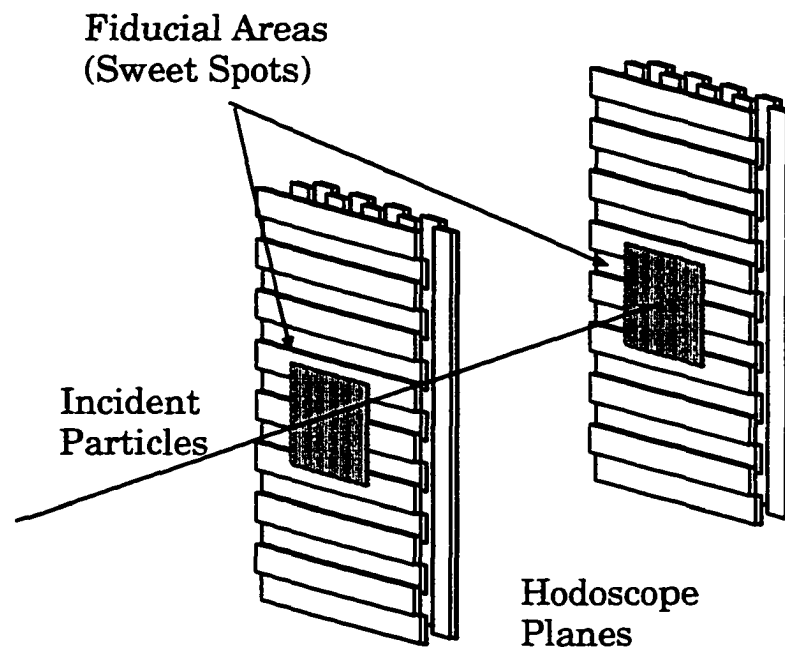


Figure 4.1: Sweet spots in the HMS hodoscope used to determine the tracking efficiency.

To further refine the calculation, an elementary method for particle identification was used. The method was insufficient to be used in the determination of the normalized yields, but it was adequate to study the tracking. To enable proper calculation of the tracking efficiency, all of the analyzed events were booked (not just those with acceptable tracks). Cuts were placed on the TOF-measured β for each particle without any pathlength (tracking) corrections to include only events from the deuteron TOF peak. In this way, the sample of

events used to study the tracking was ensured to be mostly deuterons. At this point, the ratio of the number of events for which a track was found to the total number of events was determined to be the tracking efficiency. The procedure was repeated for both the five out of six and four out of six tracking procedures. The difference in the normalized yield was assumed to be the systematic uncertainty in the tracking efficiency calculation.

The correction for tracking efficiency was calculated for each run. Typical corrections were $\sim 65 - 70\%$ for runs where the gate valve was within the acceptance of the spectrometer and $\sim 85\%$ for runs where the gate valve was fully removed (see Section 4.6). Uncertainties in the tracking efficiency determination resulted in a $< 2\%$ uncertainty in the measured cross section in the worst cases and was typically $< 1.5\%$.

4.2 Time of Flight Measurement

Time of Flight (TOF) is a term that refers to the measurement of the velocity of a particle seen in the detector stack by two detectors that have a large enough physical separation along the path of the particle. The TOF is measured with the hodoscopes in each of the spectrometers and the procedure for making the measurement in the HMS is nearly identical to that in the SOS. As such, only the details of the HMS TOF measurement are given here. When a charged particle passes through one of the scintillator paddles in the hodoscope, light is produced in the paddle. This light travels through the paddle to the photomultiplier tubes (PMT) mounted on each end of the paddle (see Section 3.10.4). PMT signals are then directed to constant level discriminators and eventually to TDCs which provide the critical timing information (see Figure 3.30). There are two pairs of segmented scintillator planes in the HMS. By knowing the difference between the times that a charged particle passes through each of the pairs of planes and the separation between the pairs of

planes, the velocity of the particle can be determined.

The TOF measurement can be improved by making a number of modifications to the hodoscope timing information such as pulse height, cable length, and path length (determined from tracking) corrections. The latter correction is an adjustment to the separation between the hodoscope planes to include the angles of the track and the exclusion of any hits in the scintillators that are inconsistent with the track. Cable length corrections must be applied to account for variations in the lengths of the cables connecting various elements of the detector to the electronic instrumentation. Particles with different velocities and masses create PMT signals with different amplitude. Because the signals from the hodoscope are discriminated with constant level discriminators, the time, measured by the TDC, between the start of the signal and when the signal exceeds the discriminator threshold varies with the signal amplitude. These corrections are recalculated for each kinematical setting following the procedure outlined in Reference [84].

In addition to the corrections mentioned above, the TDC modules themselves must be calibrated. This was done by using an ACL-7120 time interval generator and the RF signal (499 MHz) from the accelerator. A ± 25 ps variation was found between channels on the same TDC module. This variation is negligible when compared to the intrinsic 70 – 100 ps resolution of the individual hodoscope paddles. A TDC module-to-module variation of the order of 100 ps was found and a correction for this variation was applied to the data.

Pulse height corrections were determined using paddles that were crossed (one from an x plane and one from a y plane). The mean time, which is the average of the times measured by both tubes on opposite ends of the scintillator paddle, was used to eliminate any dependence of the pulse height correction on position. By applying a rough pulse height correction to three out of the four PMTs in the crossed pair, the pulse height correction on

the remaining tube can be fit to the form

$$\Delta t = C_{ph} \sqrt{\max\{0, (ADC/C_{off})\}} + t_0$$

where ADC is the raw PMT ADC signal (with the pedestal subtracted), t_0 is an offset, and C_{ph} and C_{off} are parameters that must be fit. This must be done only for particles of interest (i.e. deuterons for this experiment). Therefore a particle identification (PID) cut must be applied to the data before the fit is performed.

Cable length corrections are performed using crossed scintillators in the same manner as pulse height corrections with a different fitting procedure. The average speed of light in the scintillator must also be determined. This is done by comparing the time difference between two PMTs on opposite sides of a scintillator paddle to the longitudinal position of particle tracks through that paddle. The offsets are adjusted so that the final TOF velocity measurement, β_{tof} , matches the velocity determined from the particle momentum. The typical timing resolution (one σ) for electrons in the HMS is ~ 110 ps when the proper fitting has been performed.

4.3 Energy Loss in the scintillators

The ADC signals on the scintillator paddles in the HMS hodoscope were also used to provide useful particle identification information. This can only be done when the difference between the energy loss of the particle of interest is substantially different than that of background particles. The average energy loss in a material can be calculated using the

Bethe-Bloch formula [85] for heavy particles

$$\frac{dE}{dx} = 0.3071 \left(\text{MeV cm}^2/\text{g} \right) z^2 \frac{Z}{A\beta^2} \times \left\{ \ln \left[\frac{1.022\gamma^2\beta^2}{I} \right] - \beta^2 - \frac{\delta}{2} - \frac{C}{Z} \right\} \quad (4.1)$$

where

z is the charge (in units of e) of the incident particle.

Z and A are the atomic number and mass of the absorbing material.

I is the ionization potential (given in MeV).

β and γ are the familiar relativistic quantities for the incoming particle.

δ is the density effect correction.

C is the shell correction.

Figure 4.2 shows the calculated average energy loss for both protons and deuterons in plastic scintillator. As can be seen in the figure, the difference in average energy loss for protons and deuterons with momenta less than 1.8 GeV is large enough to use the scintillators to discriminate between them. Above 2 GeV the average energy loss between protons and deuterons is almost indistinguishable.

Because the energy loss signal is determined from the integrated pulses produced by the PMTs on each end of the scintillator, the raw ADC values (with pedestals subtracted) can be used as a measure of the energy loss of the particle in the paddles. There is no need to convert the raw ADC signal to a calibrated energy loss due to the fact that the information is only being used to discriminate between particles of different types. In practice, only PMTs from the first plane of the hodoscope (X1) were used to determine the energy loss signal dE/dx . To remove any dependence of this signal on position of the hit on the paddles, the geometric means of the PMTs on both ends of the paddle are used to give an energy

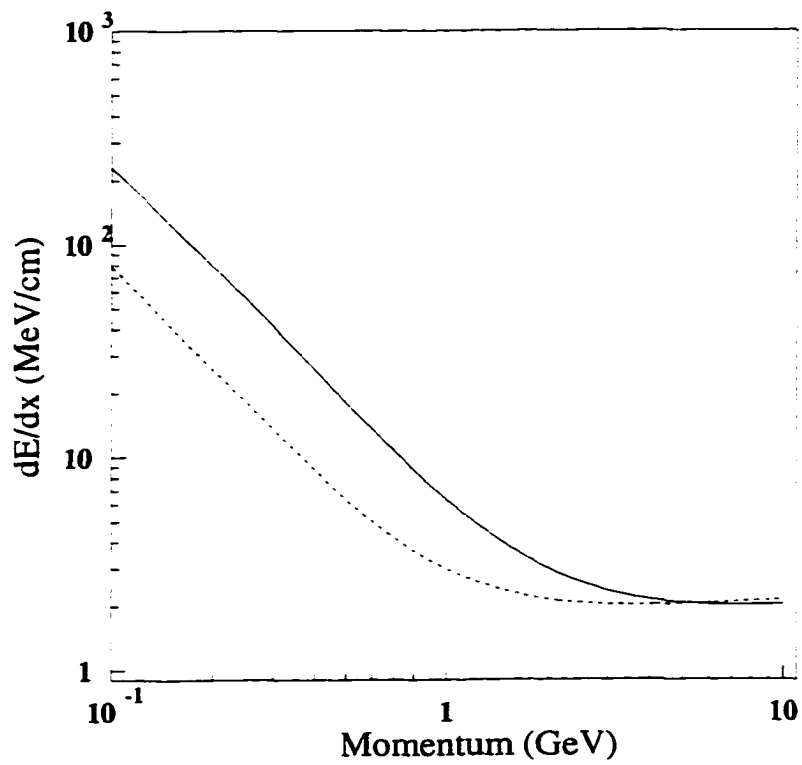


Figure 4.2: Calculated average energy loss, $\frac{dE}{dx}$, for deuterons and protons in a typical plastic scintillator. The solid curve depicts the energy loss of deuterons and the dashed curve is for protons.

loss signal. The average of the geometric means for each of the paddles receiving a hit was taken to account for the possibility that the particle passed through overlapping scintillator paddles. Relative offsets between different paddles were determined by studying the signal $dedx$ as a function of position (in x only) at the face of the scintillator and adjusting them manually for each kinematical setting. Figure 4.3 shows the energy loss signal $dedx$ for a HMS central momentum setting of 0.815 GeV. As can be seen from the figure, there is a clear separation between the proton and deuteron peaks. This signal provided useful particle identification information as described in the next section.

4.4 Particle Identification

Particle identification (PID) was performed using the TOF, energy loss, and reconstructed momentum measurements. As mentioned in the previous section, the energy loss measurement was only useful for separating deuterons from protons at momenta less than ~ 1.8 GeV. Because the TOF β measurement depends on the particle momentum (δ), the δ vs. β spectra for deuterons and protons overlap when projected to the β axis at many of the kinematical settings used in the experiment. To remove this overlap, (and to improve the overall PID resolution) the momentum and TOF β measurements were combined to give the reconstructed mass of the particle seen in the HMS. This can be done simply with the expression

$$M^2 = \frac{p^2 (1 - \beta^2)}{\beta^2} \quad (4.2)$$

where p is the reconstructed momentum of the particle in the HMS (determined from $p = p_{cent}(1 - \delta/100)$ where p_{cent} is the central momentum setting of the HMS) and β

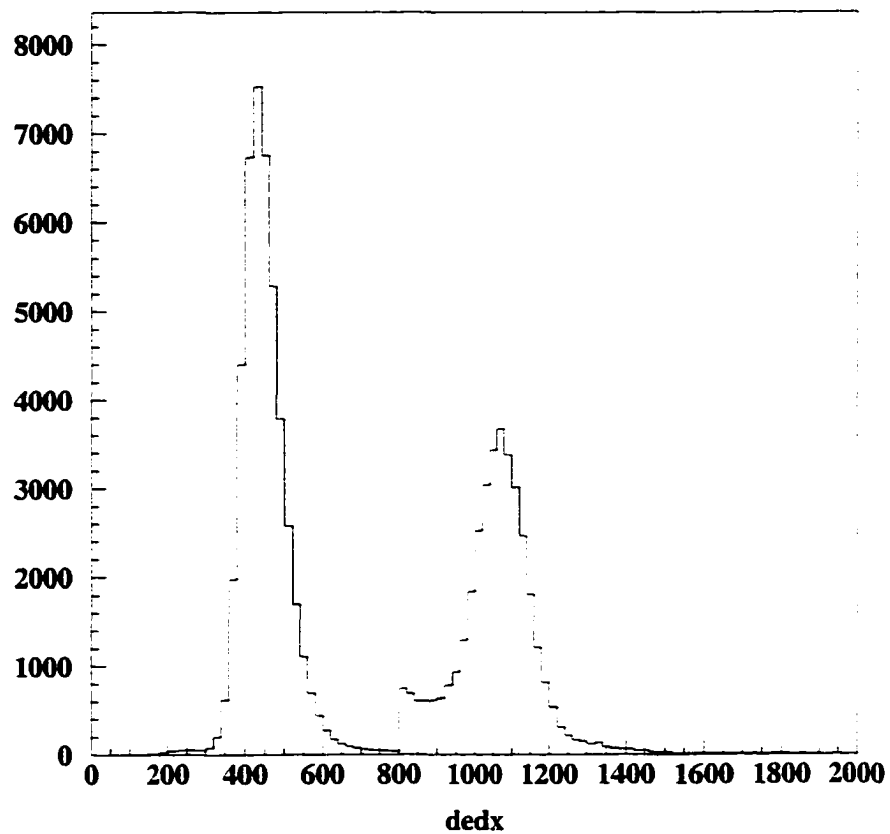


Figure 4.3: Energy loss in the first layer of the HMS scintillators $dedx$ at a momentum setting of 0.815 GeV. The deuteron peak is centered around 1100. For the purpose of clarity, the proton peak, centered ~ 450 with a long tail, has been reduced by a factor of 50.

is measured from TOF. Figure 4.4 shows an example of the reconstructed mass (M^2) as seen in the HMS for single pass (0.845 GeV) beam and $\theta_{cm} = 90^\circ$.

The overall timing resolution of the HMS hodoscope is ~ 150 ps for hadrons, which is typically adequate to separate protons from deuterons using only time of flight. Hadrons, however, can interact with the materials in the detector stack causing them to lose energy and/or undergo strong interactions (possibly producing other particles) in the detector materials. This creates a long hadronic interaction tail in the TOF β spectrum and results in a similar tail in the reconstructed mass spectrum. Because the proton (largely produced by the process $\gamma d \rightarrow pn$) to deuteron ratio was in some cases larger than 1000:1, the proton tail was far more pronounced and extended well beyond the deuteron mass peak as shown in Figure 4.4. Confirmation that this tail is indeed protons, at least at lower momentum settings, is provided by energy loss measurement in the scintillators as shown in Figure 4.5. The proton tail is easily separated using energy loss in the first layer of scintillators for kinematics with lower momentum settings. At higher energies however, where the separation of protons and deuterons with energy loss is not possible, the tail is assumed to be protons. Figure 4.6 shows the reconstructed mass for example runs with incident photon energies ranging between 1.413 and 4.045 GeV at $\theta_{cm} = 90^\circ$ (see Table D.1). As can be seen in the figure, the proton tail becomes more pronounced and the absolute M^2 resolution worsens with increasing momentum. To isolate the deuterons for the determination of the cross section, cuts are placed on the upper and lower edges of the deuteron mass peak. The subtraction of the proton background under this peak is discussed in the following section.

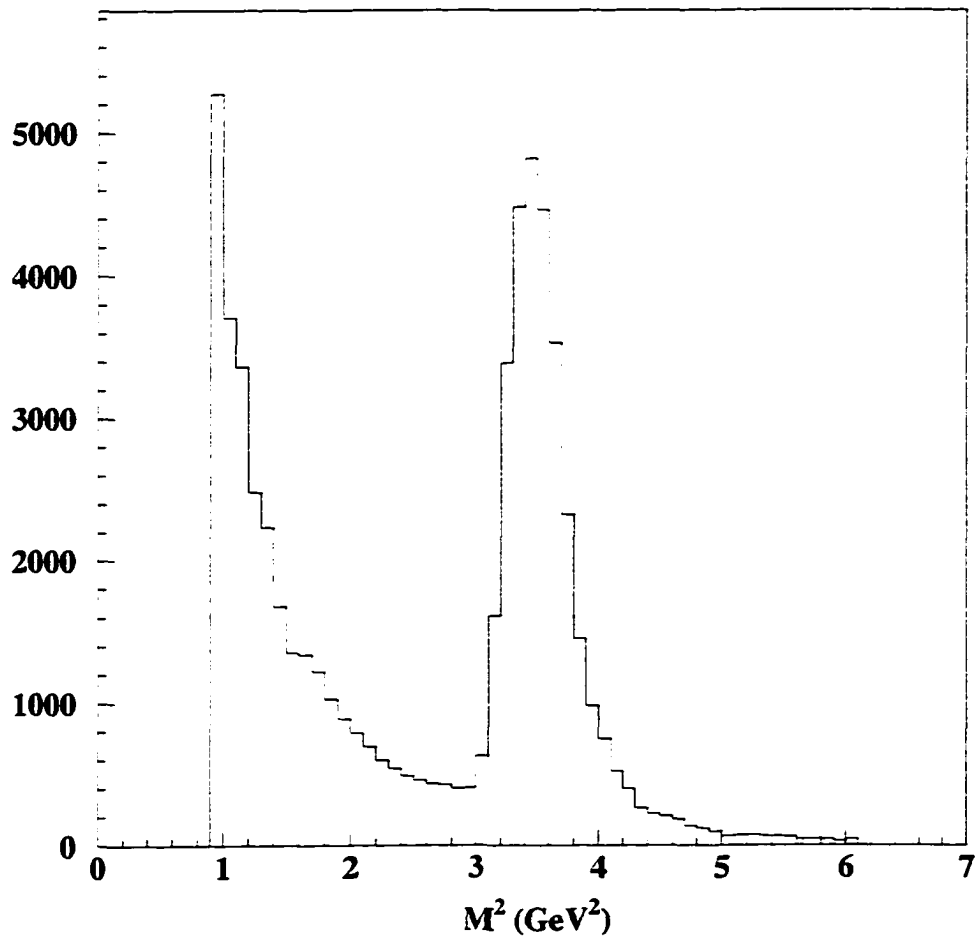


Figure 4.4: Reconstructed mass spectrum for an example run with a beam energy of 0.845 GeV at $\theta_{cm} = 90^\circ$. The bulk proton mass peak has been cut from the figure for clarity.

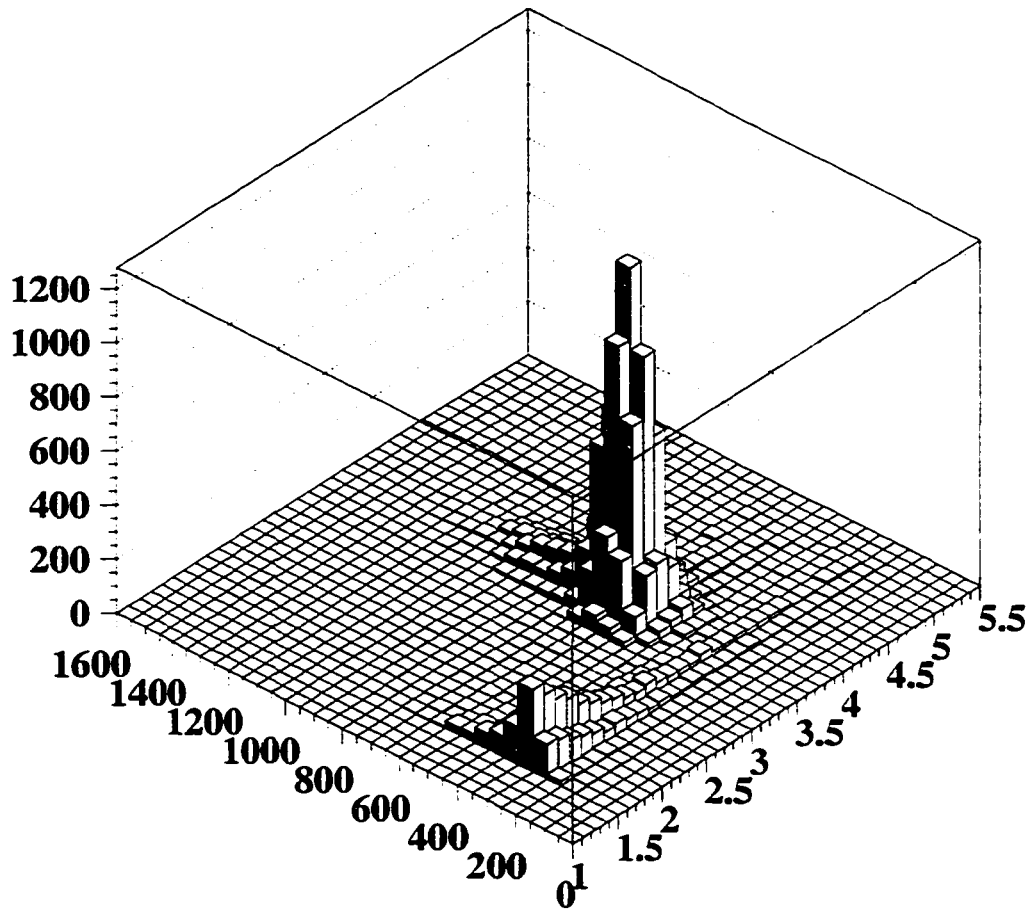


Figure 4.5: Energy loss versus reconstructed mass in the first layer of the hodoscope for $\theta_{cm} = 90^\circ$ and $E_{beam} \approx 1.413$ GeV. Note that there is a clear separation between the proton and deuteron peaks in this phase space.

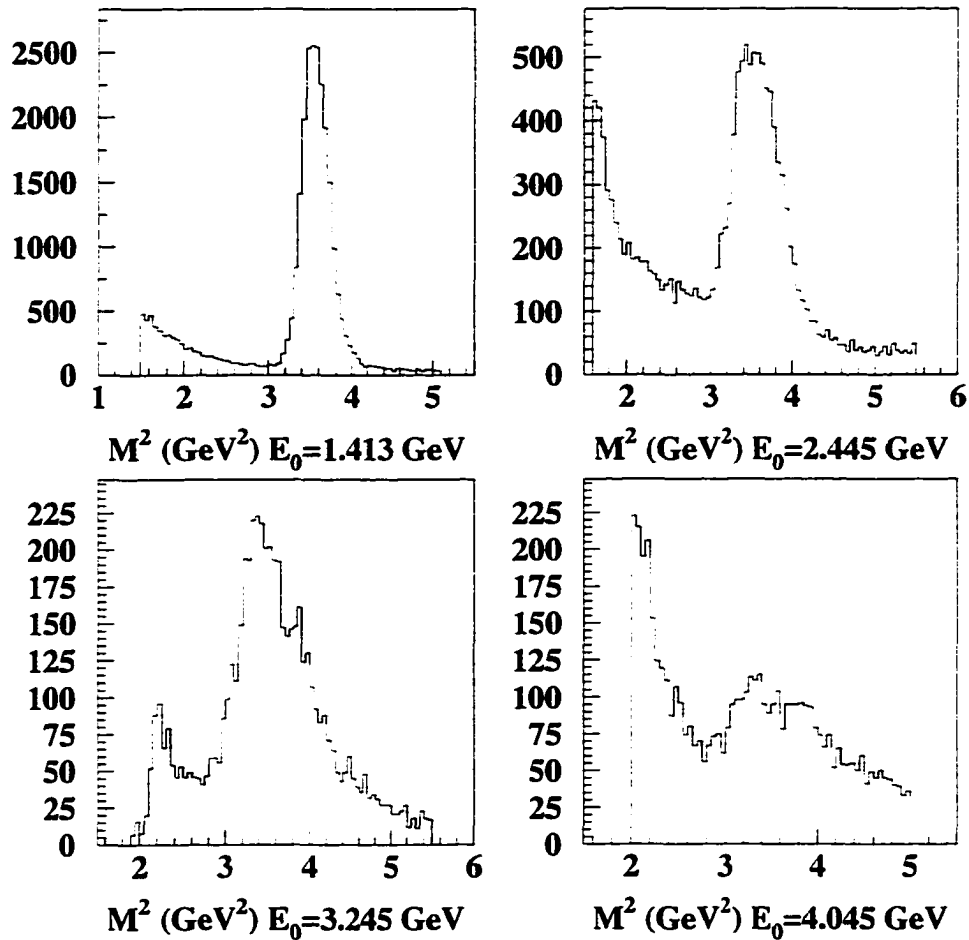


Figure 4.6: Reconstructed mass for $\theta_{cm} = 90^\circ$ at various beam energies (E_0). At higher incident beam energies and spectrometer momenta, the resolution of the reconstructed mass becomes worse. This is clearly indicated in the figure. The proton interaction tail also becomes more pronounced at higher energy.

4.4.1 Background Subtraction

Because the deuteron sample inside the mass peak cuts is contaminated with protons, an estimate and subtraction of this contamination must be performed. This must be performed at every kinematical setting where the energy loss in the scintillators cannot be used to discriminate between protons and deuterons. To estimate this proton background, cuts in the mass spectra with half of the width of the deuteron peak are placed immediately above and below the deuteron peak. An example of this procedure is shown in Figure 4.7. The proton background is estimated as the sum of the shaded areas in the figure. Figure 5.2 shows the effect of the proton subtraction on the endpoint spectrum (the endpoint spectrum is discussed in Section 5.1). The total width along the M^2 axis of the shaded area is thus equal to the total width along the same axis of the deuteron peak. The sum of the yields in the shaded regions is then subtracted from the yield under the deuteron peak on a run by run basis. The widths of all of these cuts were varied to determine the systematic uncertainty for this background subtraction procedure. The uncertainty in the cross section resulting from the background subtraction varied from 1% at the lowest momentum setting to $\sim 20\%$ for the 5 pass ($E_0 = 4.045$ GeV), $\theta_{cm} = 90^\circ$ point. This trend is consistent with the trend shown in Figure 4.6.

4.5 Absorption of Deuterons

To reach the detector stack and therefore produce a trigger, deuterons must pass through a number of different types and thicknesses of material in the target, scattering chamber, spectrometer, and detector stack¹. As the deuterons pass through these materials, they can strongly interact in such a manner that they will not produce a trigger. To form a proper

¹A study of absorption of protons in HMS was performed by D. van Westrum [86].

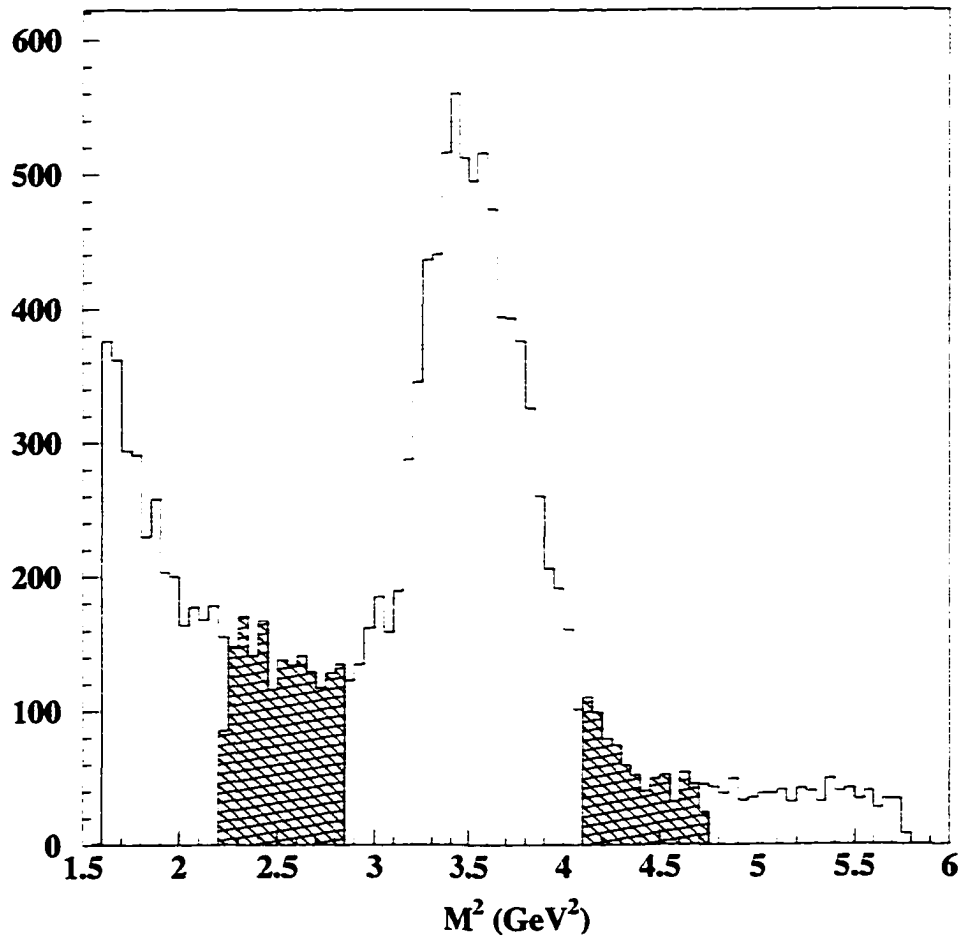


Figure 4.7: Reconstructed mass for $E_0 = 2.245$ GeV beam $\theta_{cm} = 90^\circ$. The background, which is assumed to be protons interacting in the scintillators, under the deuteron mass peak is estimated as the sum of the shaded regions on either side of the peak.

trigger, a hit must be received in all four planes of the hodoscope. Thus, any deuteron reaching the back of the third scintillator plane is likely to provide a trigger. A list of all materials, with their average thicknesses and atomic content up to the last scintillator plane is given in Table 4.1. The probability for transmission of a particle passing through matter is typically calculated with an expression of the form

$$T = \exp\left(-\sum_i \frac{X_i}{\lambda_i}\right) \quad (4.3)$$

where X_i and λ_i are the radiation length and nuclear interaction length of the material i [50]. It was found that this form was not suitable for the experiment; therefore, an alternate form for the transmission of deuterons was developed.

Material		Density (g/cm ³)	Thickness cm	Atomic Mass (amu)
Type	Weight			
D ₂	1	0.167	$\frac{3.366}{\sin(\theta_{HMS})}$	2.01
Al	1	2.70	0.27	26.98
C	0.923	1.03	3.11	12.01
H ₂	0.077	1.03	3.11	1.01
N ₂	0.754	0.0012	292	14.01
O ₂	0.232	0.0012	292	16.00
Ar	0.014	0.0012	292	39.95
C	0.136	0.00493	150	12.01
F	0.864	0.00493	150	19.00

Table 4.1: Summary of various lengths of materials, along the flight path of the recoil deuteron, found in the target and spectrometer. Composite materials have been separated into individual elements with weights other than 1.0. Note that the thickness of the deuterium (found only in the target) varies with the central angle of the HMS.

The transmission probability of deuterons in matter can be calculated by first determining the total cross section for all deuteron interactions. The total deuteron interaction cross section is given approximately as the sum of the total proton-proton (σ_{pp}) and neutron-

proton (σ_{np}) cross sections [87]

$$\sigma_{dA} \approx A^{0.75} (\sigma_{pp} + \sigma_{np}). \quad (4.4)$$

The factor of $A^{0.75}$ is extracted from a fit to the world data for σ_{pp} where A is the atomic mass of the material. The absorption probability is then given as

$$abs \approx \sum_i \frac{\rho_i l_i N_A}{A_i} \sigma_{dA} \quad (4.5)$$

where ρ_i and l_i are the density and length of the material i , and N_A is Avogadro's number. The transmission is then given as $T = 1 - abs$.

To check the validity of this model, measurements of the *ed* elastic cross section were made for two values of q^2 at the same beam energy. Deuterons were collected with the HMS and electrons were detected in coincidence with the SOS. Radiative corrections were applied to the measured cross section to match cuts imposed on the data. The final measured cross section was compared to a parameterization of the world data for the process. The ratio of the measured data to the parameterization was determined to be the deuteron transmission probability; Table 4.2 summarizes the results of the test. Typical deuteron transmissions are between $\sim 75\%$ and $\sim 90\%$. The uncertainty in the calculation is derived from the uncertainty in the measurement of the cross section for the test cases and from the estimated uncertainty in the fit to the σ_{pp} and σ_{np} data. The overall uncertainty in the transmission calculation was determined to be less than 4% at all kinematical settings; therefore, a 4% uncertainty resulting from this calculation was applied to the measured cross section.

P_{HMS}	$\frac{d\sigma}{d\Omega_{meas}}$	$\frac{d\sigma}{d\Omega_{fit}}$	T_{meas}	T_{model}
0.8 GeV	11.8 ± 0.24 pb	15.4 pb	$77 \pm 2\%$	78 %
1.0 GeV	9.2 ± 0.18 pb	11.1 pb	$83.3 \pm 2\%$	83.8 %

Table 4.2: Measured transmission of deuterons in the HMS for two different central momentum settings. The cross sections $\frac{d\sigma}{d\Omega}$ are for the D(e,e'd) reaction one is from a measurement performed using the HMS and SOS without absorption corrections and the other is from a fit to world data. The measured transmission is calculated by taking the ratio of the measured cross section to the cross section determined from the fit.

4.6 HMS Gate Valve

During the first phase of the experiment, the HMS gate valve, mounted on the nose of the spectrometer, was inadvertently left partially in the acceptance of the HMS. This was not discovered until late in the off line analysis. With the exception of the 1.6 GeV setting, all of the $\theta_{cm} = 90^\circ$ data were taken with the gate valve fully removed; the valve was within the acceptance however, during all of the $\theta_{cm} = 136^\circ$ measurements. The gate valve shutter (which was the only piece of the valve in the acceptance) is constructed of stainless steel type 316 and is ~ 14 inches in diameter and 0.525 inches thick. Figure 4.8 shows the reconstructed target quantities projected forward to the face of the gate valve for a run with the valve partially in. The curvature of the gate valve shutter can clearly be seen in the data because particles that pass through the valve have a higher probability of being absorbed or scattered out of the spectrometer acceptance. Reconstruction of the momentum and target quantities for these particles will be corrupted, as well, due to multiple scattering in the valve. For this reason, a cut is applied to remove the left half of the acceptance for all kinematical settings with the valve partially in.

To understand the effect of the valve on the data, the standard Monte Carlo model for the HMS was modified to account for the presence of the valve. The model includes

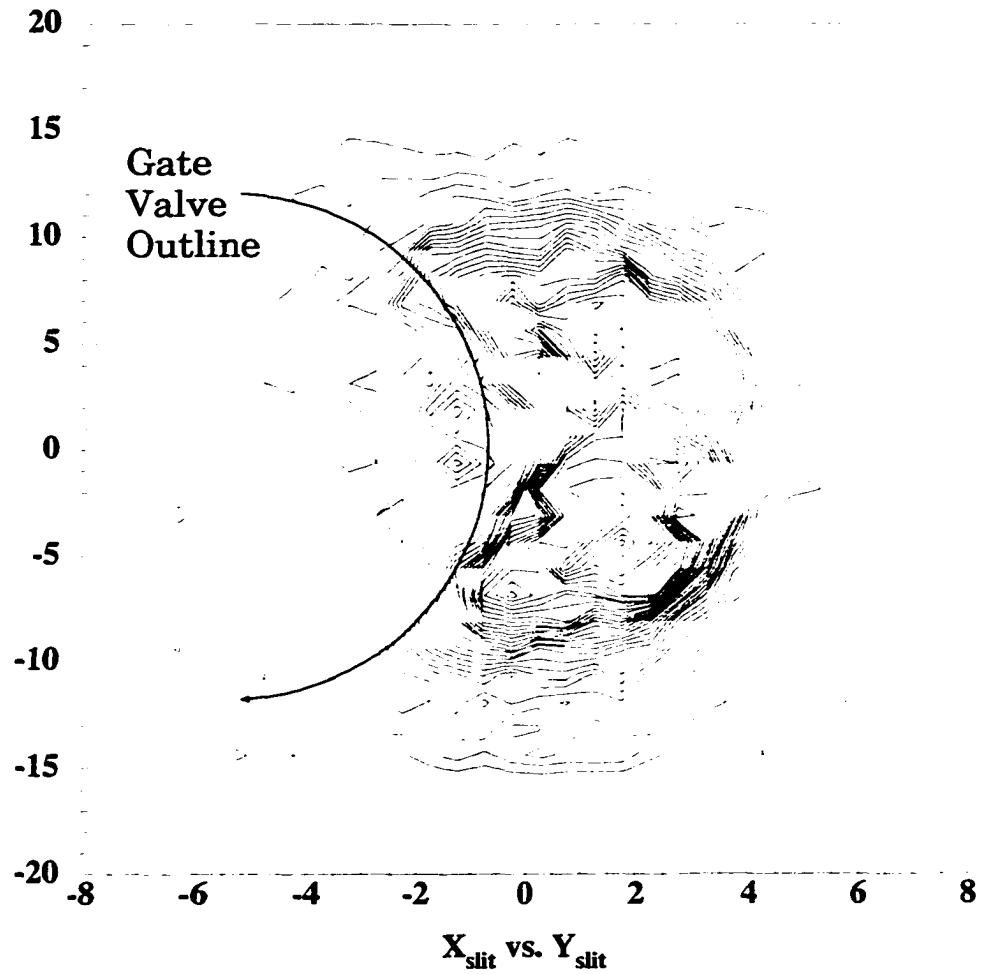


Figure 4.8: Reconstructed target quantities projected forward to the face of the gate valve for a run with the valve present. The solid arc marks the approximate position of the edge of the gate valve. Note the decrease in event density on the left side of the valve.

effects from multiple scattering and energy loss. The energy loss had a negligible effect on the modeled data and caused only a slight smear in the endpoint of the E_γ spectrum (see Section 5.1). However, multiple scattering in the valve shutter did have a profound effect on the results of the model. The first step in modeling of the multiple scattering was to generate an event in the target and project it forward to the face of the valve. A random multiple scattering angle, position offset, and energy loss were generated using a Gaussian approximation for each variable for all events striking the valve. These events were projected back to the target plane where new initial quantities were calculated (see Section 3.10.3). Events with these new initial target quantities were then projected forward through the spectrometer with the standard Monte Carlo model.

Figure 4.9 shows the initial and reconstructed momentum (δ) for deuteron events generated with the Monte Carlo model. The figure clearly demonstrates a smearing of the δ reconstruction for kinematical settings with the gate valve present. A similar affect is also seen in the other reconstructed quantities. The affect of this smearing is reduced by placing cuts rejecting any deuteron whose track reconstructs through the half of the acceptance with the gate valve as shown in Figure 4.10. However, a small percentage of the events which actually did hit the valve are reconstructed to the unobstructed half of the acceptance. An uncertainty of $\sim 3\%$ was applied to the measured cross section, with kinematical settings where the gate valve was within the acceptance of the HMS, to account for these type of events.

4.7 Effective Target Length

Because of poor reconstruction of some events due to multiple scattering in the spectrometer and other processes, there was a large amount of accidental background. The recon-

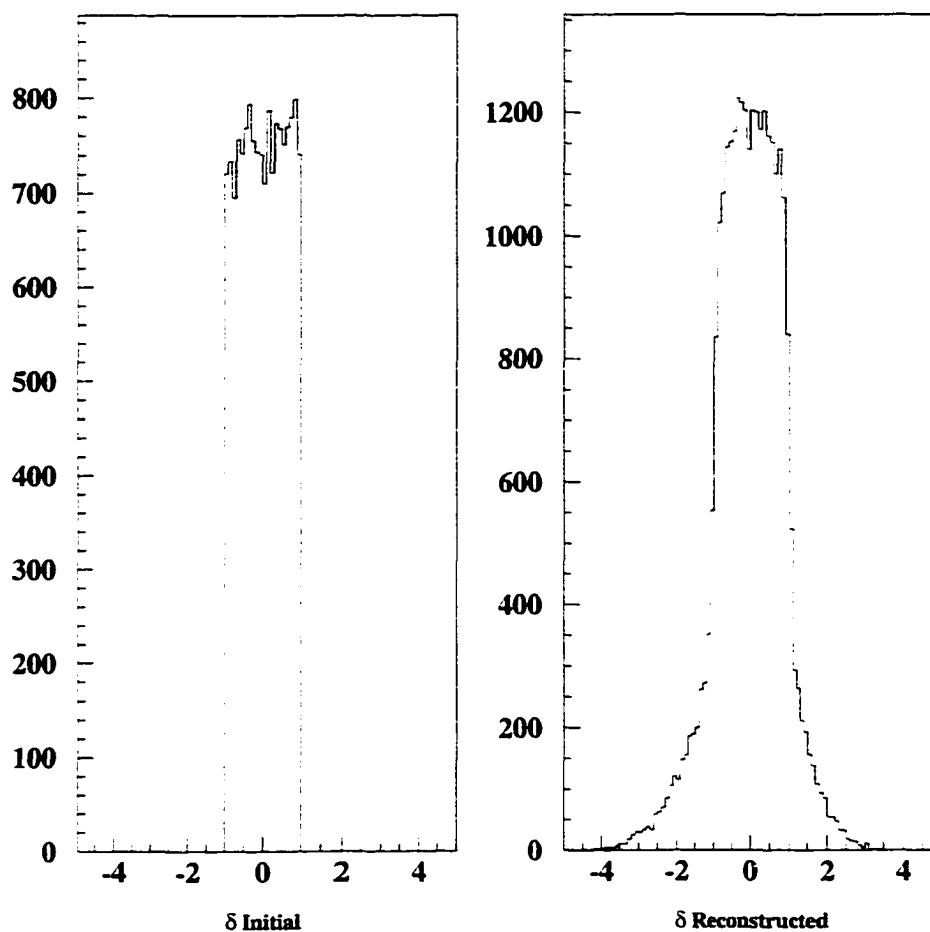


Figure 4.9: Initial (left) and reconstructed (right) momentum from the Monte Carlo simulation including effects from the gate valve for the same kinematics described in Figure 4.8. The broad base of the plot on the right indicates poor momentum reconstruction for events undergoing multiple scattering in the gate valve.

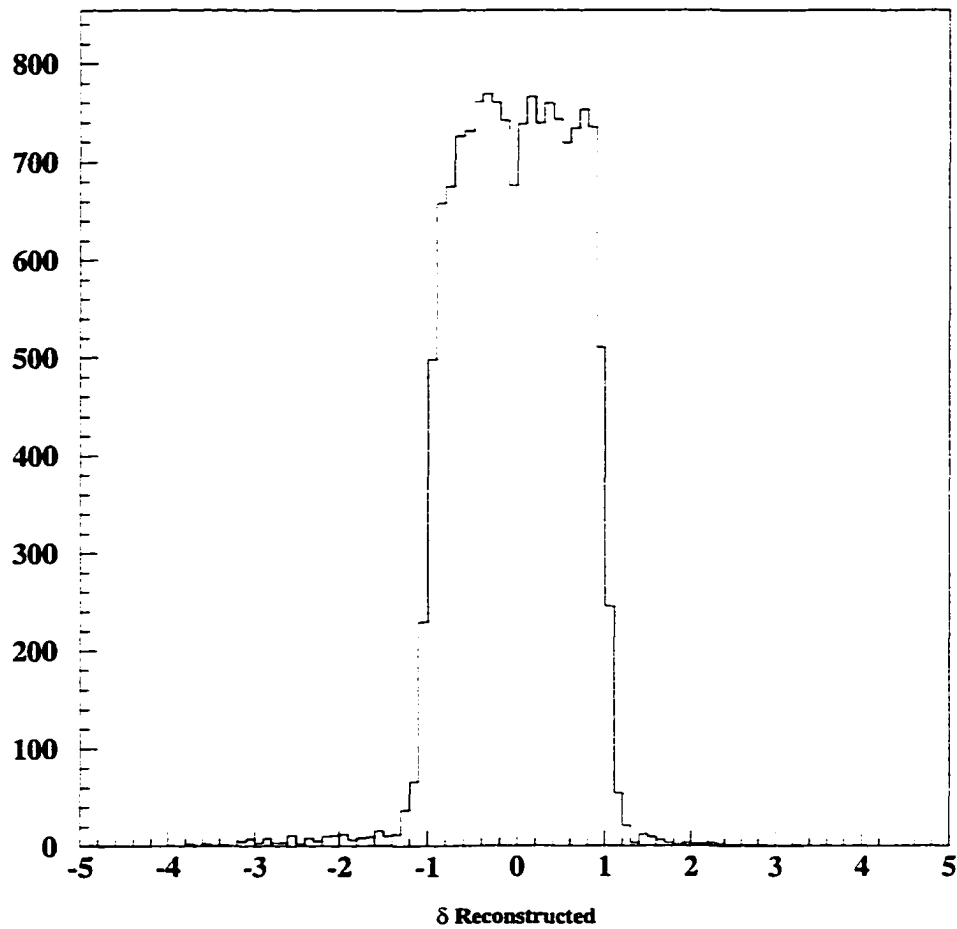


Figure 4.10: Reconstructed momentum for simulated data with the gate valve present. Here cuts on the reconstructed target quantities are made to exclude the part of the acceptance with the valve. As is evident, the cuts are not 100% effective in removing events which passed through the valve.

structed Y_{tar} of events in this background was often calculated to be outside of the physical length of the target cell. Furthermore, a large portion of the events seen in the deuteron mass peak were reconstructed back to the entrance and exit windows of the cell as shown in Figure 4.11. To reduce some of this background, cuts were placed on the reconstructed target length that excluded the entrance and exit windows of the cryogenic cell (see Figure 3.14). The effective length of the target (hence the effective luminosity) was therefore determined by the size of the Y_{tar} cuts. To estimate the precision of this technique, the sizes of these cuts were varied and the normalized yields were compared at all settings. Table 4.3 shows the normalized yields for various Y_{tar} cuts at a sample of various kinematics. As can be seen from the table, the uncertainty in the normalized yield resulting from the Y_{tar} cuts was of the order of 1.5%. Therefore, a systematic uncertainty of 1.5% due to the Y_{tar} cuts was assigned to the measured cross section. Note that the same studies at higher energies were also performed and yielded similar results; however, these tests were less precise due to poor statistics.

Setting	$ Y_{tar} $	Yield
$E_0 = 2.445 \text{ GeV}$ $\theta_{cm} = 90^\circ$	2.0	23.85 ± 0.36
	2.25	23.54 ± 0.35
	2.5	23.53 ± 0.35
	2.75	23.65 ± 0.35
	3.0	24.20 ± 0.36
$E_0 = 1.413 \text{ GeV}$ $\theta_{cm} = 90^\circ$	2.0	72.6 ± 0.7
	2.25	72.0 ± 0.7
	2.5	71.7 ± 0.7
	2.75	71.5 ± 0.6
	3.0	72.0 ± 0.6
	3.25	72.9 ± 0.6

Table 4.3: Normalized yields for various kinematics and Y_{tar} cuts. The data indicate that the uncertainty in the normalized yield resulting from the Y_{tar} cuts is $\sim 1.5\%$. The errors indicated are statistical only.

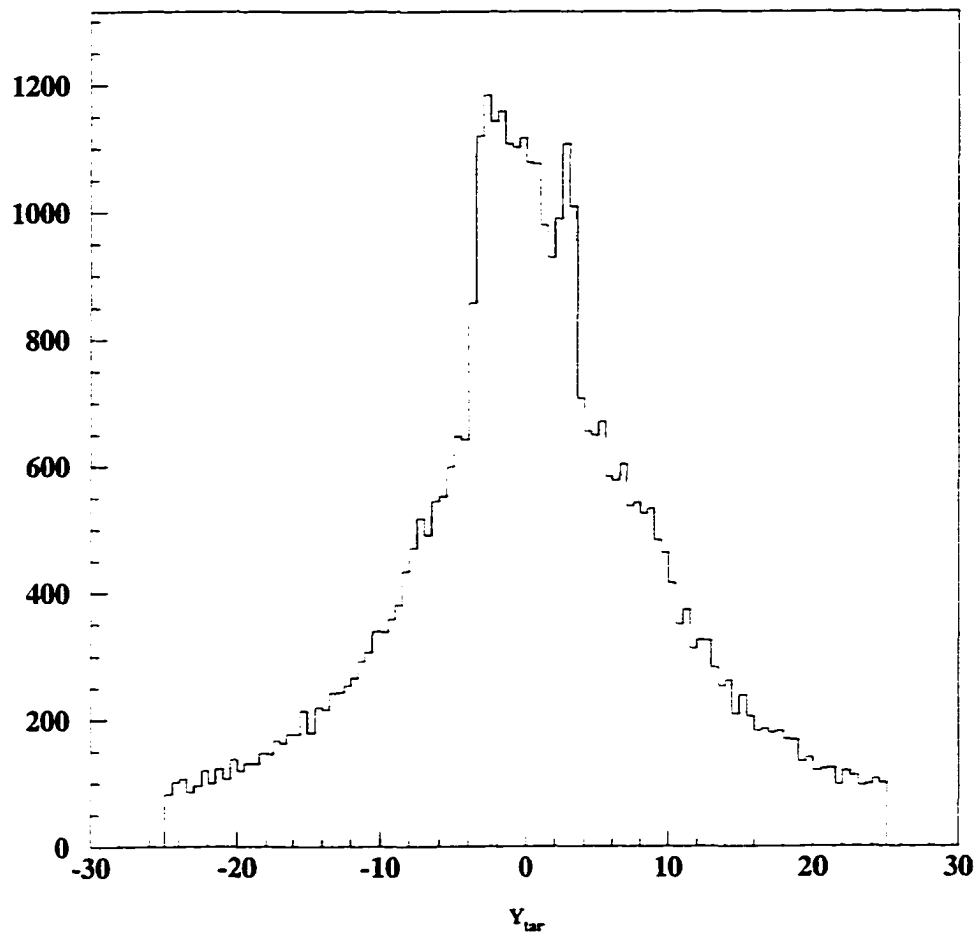


Figure 4.11: Reconstructed Y at the target, Y_{tar} (in cm), for a typical run using a deuterium target with the radiator in and gate valve present. The total length of the target as seen by the spectrometer ranges between $\sim \pm 4$ cm. Note that cuts have been placed on Y_{tar} at ± 25 cm.

Chapter 5

Experimental Cross Section

Once the deuterons have been identified and the proton background under the mass peak has been subtracted, the laboratory experimental cross section, $\frac{d\sigma}{d\Omega}$, may be determined. The determination of this quantity requires the precise knowledge of the bremsstrahlung flux produced in the copper radiator as well as the total deuteron yield and spectrometer acceptance. Backgrounds from other processes, such as $\gamma d \rightarrow d\pi\pi$ and $\gamma d \rightarrow \gamma d$, must also be estimated and subtracted if necessary. Further, contributions to the deuteron yield from electro-processes and interactions with the entrance and exit windows of the cryogenic target must be removed. The techniques for performing these operations on the data are discussed in this chapter.

5.1 Endpoint Spectra

After particle identification has been performed, the data are binned as a function of reconstructed photon energy, E_γ . The reconstructed photon energy is determined by first assuming that the deuteron detected in the HMS was produced by the process $\gamma d \rightarrow d\pi^0$.

By using two-body kinematics and by reconstructing the angle and momentum of the recoil deuteron, the energy of the photon in the process (in the laboratory frame) may be calculated using the following relation

$$E_\gamma = \frac{E_d m_d - (2m_d^2 + m_\pi^2)/2}{m_d - E_d + p_d \cos(\theta_d)} \quad (5.1)$$

where E_d , p_d , and θ_d are the energy, 3-momentum, and angle of the recoil deuteron as measured by the spectrometer. This relation is derived in detail in Section C.3. Because the maximum possible energy of the photons produced in the radiator is slightly less than the beam energy, an endpoint in the E_γ spectrum is expected near the beam energy. To minimize the contribution to the background from two-step and multiple pion processes (see Section 5.1.3), only events near this endpoint are considered. In practice, the electron beam energy is subtracted from E_γ to generalize the analysis. Figure 5.1 shows a typical endpoint spectrum for one run with a deuterium target and a 6.02% copper radiator in the beam without the proton background subtraction. Figure 5.2 shows the same endpoint with the proton background, overlaid in cross hatch, determined by the method discussed in Section 4.4.1.

5.1.1 Subtraction of the Measured Background

The resultant photon beam emerging from the bremsstrahlung radiator is mixed with electrons which on average have lost less than 0.1% of their total energy. These electrons impinge on the target and are capable of producing deuteron events in the HMS via a number of different processes that are indistinguishable (by single arm detection of the recoil deuteron in the HMS) from $\gamma d \rightarrow d\pi^0$ events where the photon is produced in the radiator. Furthermore, photons may interact with the aluminum entrance and exit windows of the

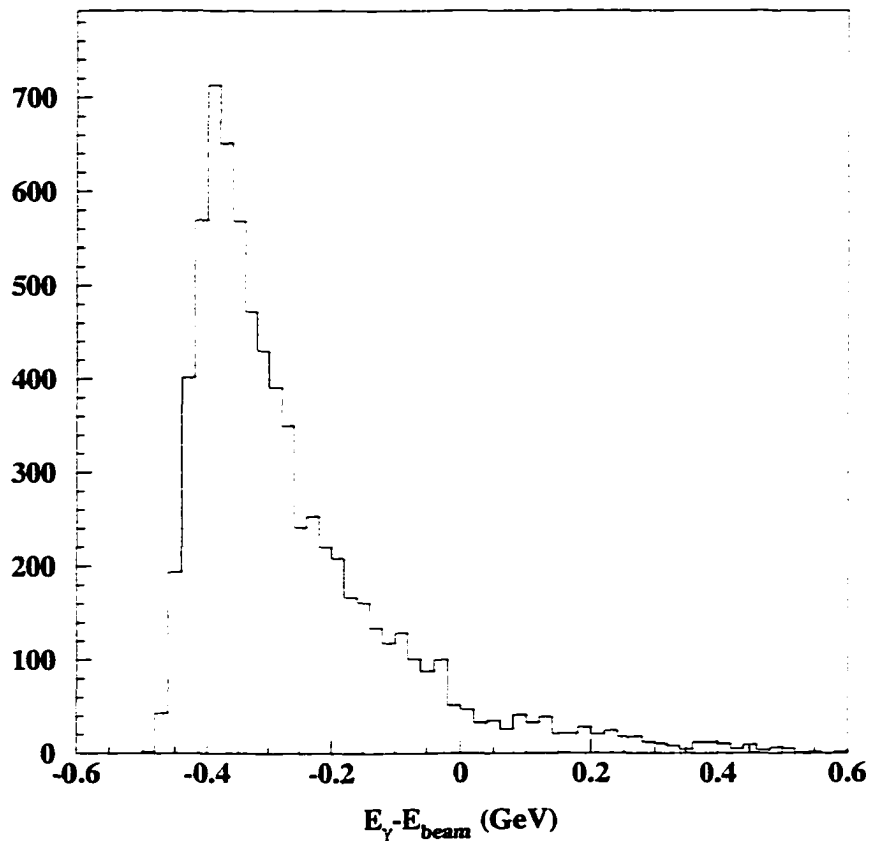


Figure 5.1: Typical endpoint spectrum from a deuterium radiator in run with an incident electron beam energy of 2.445 GeV, $\theta_{cm} = 90^\circ$, and a 6.02% copper radiator. Note that on the horizontal axis the beam energy has been subtracted from the reconstructed photon energy. The events with reconstructed photon energies higher than the endpoint ($E_\gamma - E_{beam} = 0$), which are assumed to be protons, were typically removed by background subtraction methods.

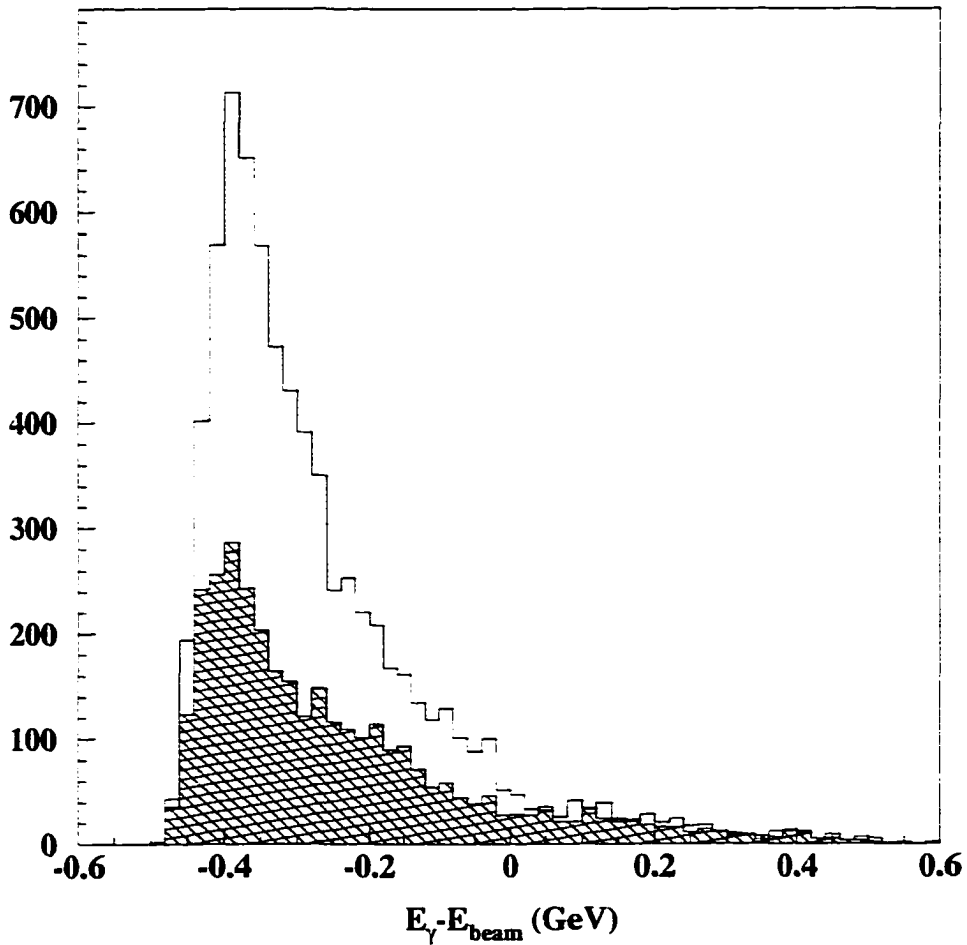


Figure 5.2: The same endpoint spectrum as that shown in Figure 5.1 with the estimated proton background overlaid in cross hatched style. Note that most of the events seen above the photon endpoint are removed by this subtraction.

cryogenic target and produce deuterons via $\text{Al}(\gamma, d)X$ processes.

To measure the electro-produced background, data without the radiator in the beam were collected and also histogrammed in E_γ (the quantity expressed in Equation 5.1). The yield from the deuterium target with the radiator out (Y_{D_2}), normalized by the total integrated electron current, is then subtracted from the yield with the radiator in, $Y_{\text{D}_2}^{(rad)}$, with the equivalent normalization. Thus, contributions from electro-produced deuterons or photo-produced deuterons, where the photon is produced in the target or the aluminum target endcaps, are removed.

To remove contributions to the background from the aluminum windows of the cryogenic target, data using a hydrogen target, with the same physical dimensions, in place of the deuterium target were collected. The effects of multiple scattering of the electron beam and of bremsstrahlung produced in the deuterium target are better approximated by using a hydrogen target instead of an empty cell (with the exception of the 136° data see below which were measured at a time when no hydrogen cell was available). The data are again histogrammed in E_γ and the spectrum $Y_{\text{H}_2}^{(rad)}$ is subtracted from the total yield. To avoid double counting of the electro-produced background from the windows, data from a hydrogen target with the radiator out, Y_{H_2} are subtracted from $Y_{\text{H}_2}^{(rad)}$. The proper subtraction of the hydrogen yields effectively removes any deuterons produced by $\text{Al}(\gamma, d)X$ processes in the windows.

Because of difficulties with the cryogenic target system, measurements of the $\text{Al}(\gamma, d)X$ background could only be made using an empty target cell at all kinematical points where the deuteron center-of-mass angle, θ_{cm} , was 136° and at the $E_0 = 1.645 \text{ GeV}$ $\theta_{cm} = 90^\circ$ point¹. To check that this subtraction was sufficient, measurements of the background were performed using both the hydrogen target and the empty cell for the $E_0 = 0.845 \text{ GeV}$ and

¹The electron beam energy is denoted as E_0 in this document.

$\theta_{cm} = 90^\circ$ point. The difference in the total measured cross section using both methods at this kinematics was determined to be negligible. Therefore, no correction to the background measured with the empty cell was needed. Normalized yields for all four of the run types at the kinematical setting of $E_0 = 3.245$ GeV and $\theta_{cm} = 90^\circ$ are shown in Figure 5.3. As is indicated by the figure, roughly $\frac{2}{3}$ of the deuterium radiator in yield is produced by background processes.

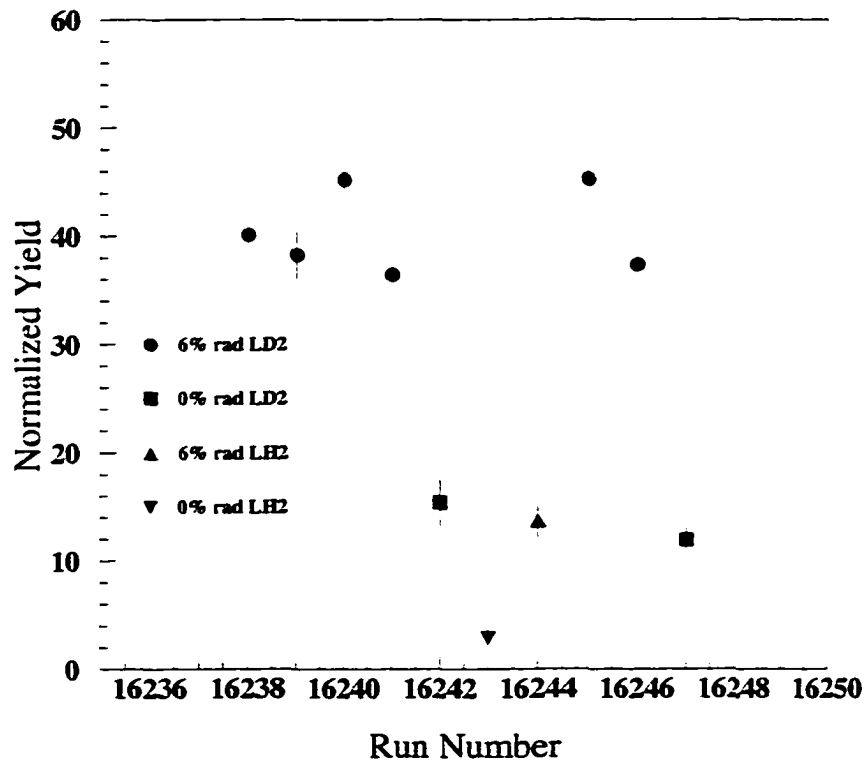


Figure 5.3: Normalized yields from the $E_0 = 3.245$ GeV, $\theta_{cm} = 90^\circ$ setting. The solid circles are for runs with the 6.02% radiator in taken on the deuterium target. The solid squares indicate runs with no radiator taken on the deuterium target. The hydrogen target runs are depicted are triangles upward (downward) pointing for radiator in (out). The Errors shown are statistical only.

5.1.2 Correction to the Radiator Out Spectra

By subtracting the background yields in the proper fashion, the total yield (normalized by the integrated charge) for the process $\gamma d \rightarrow d\pi^0$ is given by

$$Y_{tot} = Y_{D_2}^{(rad)} - Y_{D_2} - (Y_{H_2}^{(rad)} - Y_{H_2}). \quad (5.2)$$

The yields without the radiator are subtracted to remove effects of the electron beam which is mixed with the photon beam produced in the radiator. However, the energy distribution of the electron beam impinging on the target without the radiator in place is not the same as that with the radiator in. The electron beam incident on the radiator experiences both radiative and ionization processes and emerges from the radiator with a vastly different energy distribution. This energy distribution may be calculated using the methods described in Reference [88] and in Section B.1. As an example of the effects of the radiator on the beam energy distribution, the calculated energy loss distribution for an electron beam of incident energy $E_0 = 2.445$ GeV passing through a 6.02% radiation length copper radiator is shown in Figure B.1. The subtraction of the radiator out spectra overcompensates for the effects of the electron beam because the photon energy distribution produced, by electrons, in the target varies with the thickness of the radiator upstream. Thus, the radiator out spectra must be corrected to give an accurate description of the electro-produced background when the radiator is in. This correction is a function of photon energy E_γ and is given by

$$C(E_\gamma) = \frac{N_\gamma^{rad}(E_\gamma)}{N_\gamma(E_\gamma)} \quad (5.3)$$

where $N_\gamma^{rad}(E_\gamma)$ and $N_\gamma(E_\gamma)$ are the calculated bremsstrahlung spectra in the target (not the radiator) with and without the radiator in the beam. Figure B.4 shows the correction

function for a typical kinematical setting. A detailed description of the calculation of this function is described in Section B.2. The total corrected normalized yield is then given by

$$Y_{tot} = Y_{D_2}^{(rad)} - Y_{H_2}^{(rad)} - C(E_\gamma) \cdot (Y_{D_2} - Y_{H_2}). \quad (5.4)$$

A typical spectrum for the total yield using all available data for the $E_0 = 1.413$ GeV and $\theta_{cm} = 90^\circ$ kinematics is shown in Figure 5.4.

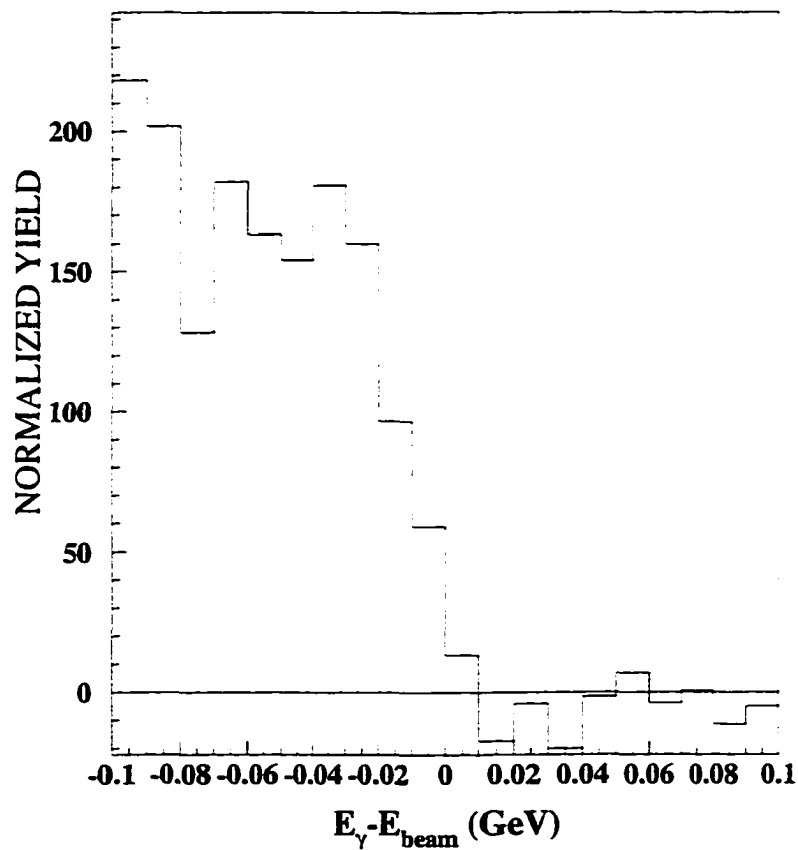


Figure 5.4: Total yield, Y_{tot} , spectrum for $E_0 = 1.413$ GeV and $\theta_{cm} = 90^\circ$ kinematics. The data show a clear endpoint at $E_\gamma - E_{beam} = 0$, where it is expected.

5.1.3 Two Pion Background

As mentioned above, only events where the reconstructed photon energy is near the endpoint are considered in the determination of the final cross section. By using Equation 5.4, it is assumed that the deuteron was produced by the process $\gamma d \rightarrow d\pi_0$. However, if the deuteron was produced by the process $\gamma d \rightarrow d\pi\pi$ then the incident photon energy would be incorrectly reconstructed to be lower than it actually was. The E_γ threshold for two π production processes would then be slightly lower than the endpoint.

To calculate the E_γ threshold for two π production consider the square of the total center-of-mass energy which may be expressed by

$$s = E_{cm}^2 = 2E_\gamma m_{target} + m_{target}^2. \quad (5.5)$$

This may also be expressed in terms of the center-of-mass energies of each of the particles in the final state for the $\gamma d \rightarrow d\pi^0$ process (note that the prime denotes a variable in the center-of-mass)

$$E'_d + 2E'_\pi = E_{cm}. \quad (5.6)$$

Further, note that

$$E'_\pi = \left(\left(\frac{p'_d}{2} \right)^2 + m_\pi^2 \right)^{1/2} \quad (5.7)$$

and by making the proper substitutions the center-of-mass deuteron energy E'_d is given by

$$E'_d = \frac{(E_{cm}^2 + m_d^2 - 4m_\pi^2)}{2E_{cm}}. \quad (5.8)$$

This differs slightly from the expression for the deuteron energy produced by the single pion process ($\gamma d \rightarrow d\pi^0$)

$$E'_d = \frac{(E_{cm}^2 + m_d^2 - m_{\pi^0}^2)}{2E_{cm}}. \quad (5.9)$$

These energies are boosted into the laboratory frame and are used in Equation 5.1 to calculate the threshold, for the two π process which is denoted $E_{2\pi}$, in the E_γ spectrum. Table 5.1 shows the difference between the thresholds for single and double pion production.

E_{beam} (MeV)	θ_{cm}	$E_\pi - E_{2\pi}$ (MeV)
845	90°	64.3
1413		51.2
1645		48.4
2445		42.8
3245		40.0
4045		38.3
845	136°	39.4
1645		28.8
2445		25.3

Table 5.1: Difference between single (E_π) and double pion ($E_{2\pi}$) production thresholds in the reconstructed photon energy, E_γ , at all kinematics. Note as the beam energy and deuteron center-of-mass increase, the difference between the single and double pion production thresholds falls. Thus, at higher energies it becomes more difficult to exclude the double pion production process.

Ideally, events with reconstructed photon energies below the two pion threshold would not be considered in the determination of the differential cross sections. However, because the differences between the single and double pion production thresholds are small, poor statistics precludes such an analysis. Therefore, a comparison between the yields (normalized for bremsstrahlung flux) above and below this threshold was performed at all kinematics where possible. Table 5.2 shows the normalized total yields measured using different regions of the endpoint spectra. Given that the cross section is expected to increase slightly

over the photon energy range with decreasing energy and the statistical precision of the data in the table, there is no evidence of a large contribution from double pion processes. In addition, fits were performed on each endpoint spectrum (see Section 5.1.4) and showed no signature for a large background from the double pion processes.

E_0 (GeV)	E_γ Region		
	1- π	2- π	Full
1.413	500 ± 20	532 ± 17	520 ± 13
2.445	80 ± 20	118 ± 19	111 ± 14
3.245	25 ± 14	35 ± 4	32 ± 4

Table 5.2: Normalized yields from various regions of the endpoint spectra and various kinematical settings at $\theta_{cm} = 90^\circ$ (errors are statistical only). The 2- π region extends from $E_0 - 100$ MeV to the two-pion threshold $E_{2\pi}$ which are given in Table 5.1. The 1- π region extends from $E_{2\pi}$ to $E_0 - 10$ MeV. The full region covers the range $E_0 - 100 \leq E_\gamma \leq E_0 - 10$.

5.1.4 Endpoint Fitting

The endpoint spectra may be fit in a simple fashion by assuming that the dependence of the cross section is small over the angular acceptance of the spectrometer. The bremsstrahlung spectra, calculated using the methods described in Reference [56] and in Appendix B, is weighted by s^{-n+1} where the parameter n is determined later from a fit to the endpoint spectrum. This function is then smeared in E_γ using a Gaussian distribution with a resolution chosen to simulate the limitations from the spectrometer resolution. The fit is thus of the form

$$F_{d(\gamma,d)\pi^0}(E_\gamma) = C_1 \frac{dN_\gamma(E_\gamma)}{dE_\gamma} [s(E_\gamma)]^{-n+1} \quad (5.10)$$

where $dN_\gamma(E_\gamma)/dE_\gamma$ is the calculated bremsstrahlung flux (described in Appendix B) smeared with the Gaussian distribution and the parameters C_1 and n are determined from the fitting procedure. Figures 5.5, 5.6, and 5.7 show fits to the endpoint spectra at various

kinematical settings. The parameter C_1 varied in magnitude at each kinematical setting. The power n in Equation 5.10 was determined to be ~ 9.6 for the 90° data and ~ 13.0 for the 136° data.

These endpoint spectra may also be used to study possible contributions to the background from double pion production processes. Indications that the double pion production processes provide a substantial background would manifest themselves in a sharp rise in the data, of the same form given in Equation 5.10, near the threshold for double pion production. As shown in Figures 5.5, 5.6, and 5.7, no indications of a sizable double pion production background can be seen in the data.

5.2 Determination of the Cross Section

The laboratory differential cross sections, $\frac{d\sigma}{d\Omega_{lab}}$, are determined by integrating the total yield given by Equation 5.4 between lower and upper bounds E_l and E_h such that $E_l \leq E_\gamma \leq E_h$. The bounds were chosen such that $E_l = E_0 - 100$ MeV and $E_h = E_0 - 10$ MeV for all kinematical settings. The upper bound was chosen to avoid problems arising from the lack of knowledge of the bremsstrahlung yield near the endpoint. The lower bound was selected to minimize contributions from background processes (with the exception of double pion production processes) to the total yield. The yield from this integration was normalized by the total accumulated charge (integrated electron current). The laboratory cross section is then given by

$$\frac{d\sigma}{d\Omega_{lab}} = \frac{Y_{tot}}{\Delta\Omega \cdot N_t \cdot N_\gamma \cdot A} \quad (5.11)$$

where $\Delta\Omega$ is the effective solid angle of the spectrometer; N_t is the thickness of the target atoms (g/cm^2); N_γ is the integrated photon flux; and A is a correction factor that accounts

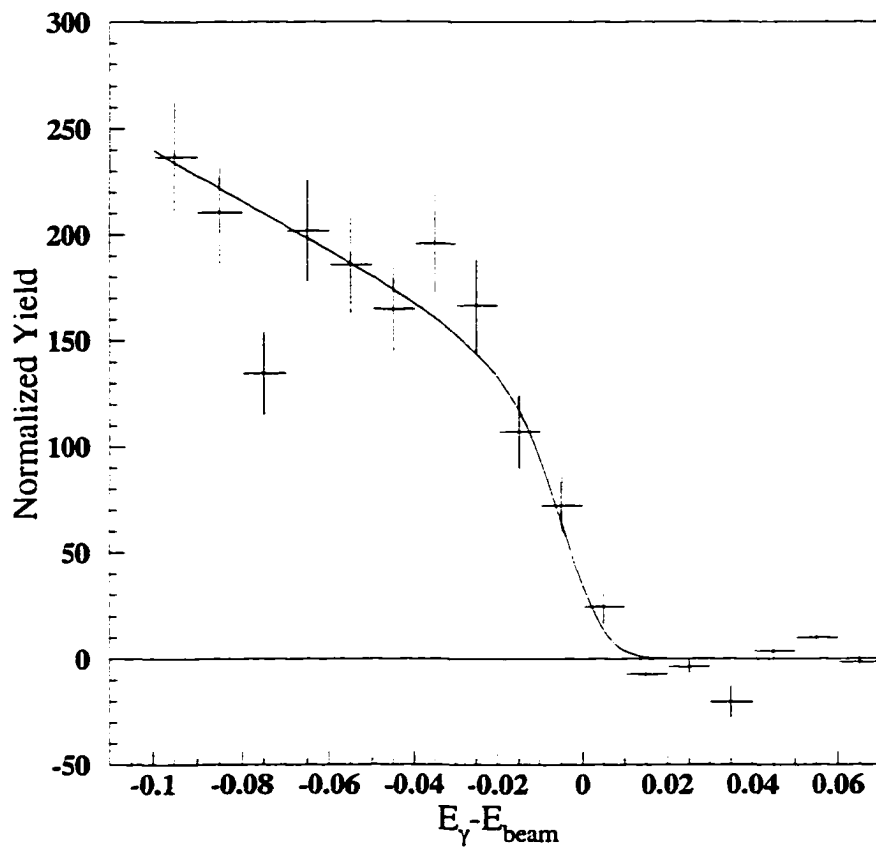


Figure 5.5: Endpoint spectrum for $E_0 = 1.413$ GeV and $\theta_{cm} = 90^\circ$. The solid curve in the figure is from a fit of the form shown in Equation 5.10. Errors shown are statistical only.

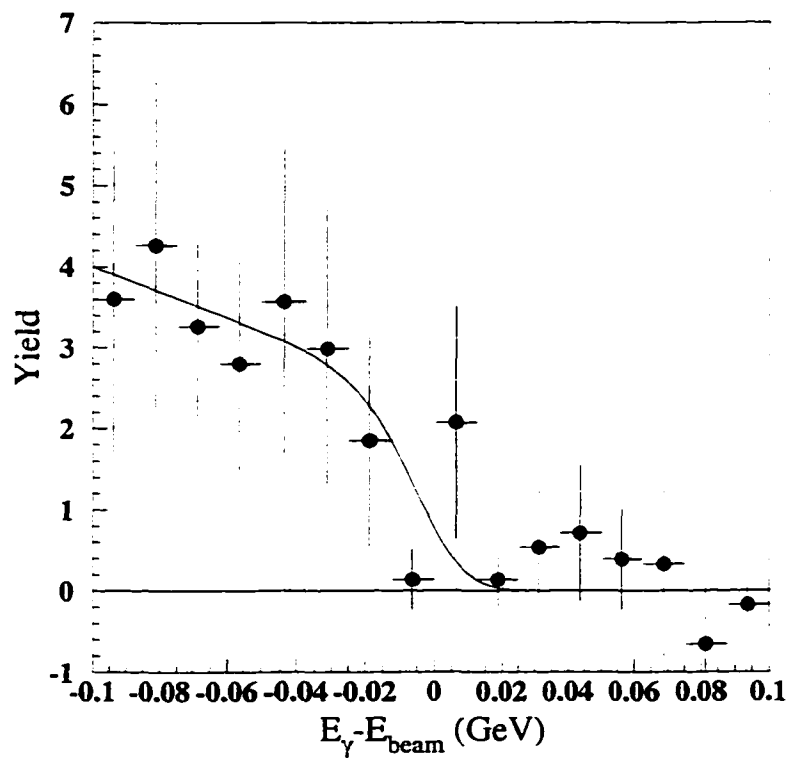


Figure 5.6: Endpoint spectrum for $E_0 = 2.445$ GeV and $\theta_{cm} = 90^\circ$. The solid curve in the figure is from a fit of the form shown in Equation 5.10. Errors shown are statistical only.

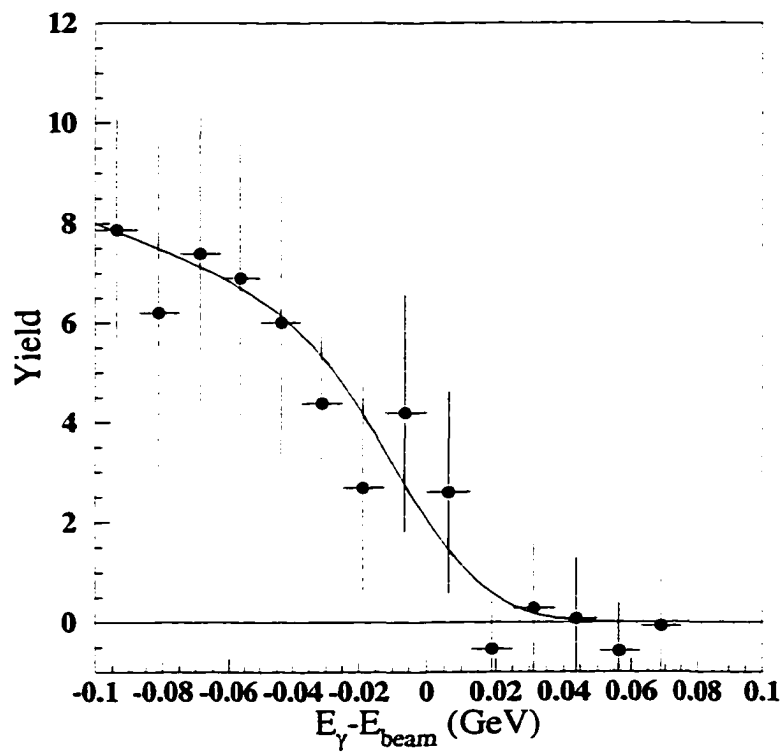


Figure 5.7: Endpoint spectrum for $E_0 = 3.245$ GeV and $\theta_{cm} = 90^\circ$. The solid curve in the figure is from a fit of the form shown in Equation 5.10. Errors shown are statistical only.

for detector and tracking efficiencies and absorption of the recoil deuterons (see Section 4.5).

Because the bremsstrahlung flux is not measured, the quantity N_γ must be determined by integrating the calculated bremsstrahlung spectrum over the same region used in the determination of the normalized yield, Y_{tot} . The bremsstrahlung spectrum is calculated numerically using software code (written in C) described in Appendix B, that incorporates the methods of Matthews and Owens [56]. The calculation includes contributions to the bremsstrahlung flux from both electron-nuclear and electron-electron interactions. It also includes effects from the incident energy spread of the electron beam and for energy loss in the radiator.

The differential cross section in the center-of-mass frame, $\frac{d\sigma}{d\Omega_{cm}}$, is given by

$$\frac{d\sigma}{d\Omega_{cm}} = \frac{d\sigma}{d\Omega_{lab}} \frac{d\Omega_{lab}}{d\Omega_{cm}} \quad (5.12)$$

where the Jacobian $d\Omega_{lab}/d\Omega_{cm}$ is given by

$$\frac{d\Omega_{lab}}{d\Omega_{cm}} = \frac{\sin^2(\theta_{lab})}{\sin^2(\pi - \theta_{cm})} [\cos(\pi - \theta_{cm}) \cos(\theta_{lab}) + \gamma_{cm} \sin(\pi - \theta_{cm}) \sin(\theta_{lab})]. \quad (5.13)$$

The quantities θ_{cm} and θ_{lab} are the center-of-mass and laboratory scattering angles as shown in Figure C.3. γ_{cm} is given by

$$\gamma_{cm} = \frac{E_\gamma + m_d}{E_{cm}} \quad (5.14)$$

where E_{cm} is the total center-of-mass energy. A derivation of the Jacobian in Equation 5.13 is given in Section C.4.

5.3 The Invariant Cross Section $\frac{d\sigma}{dt}$

To convert the center-of-mass cross section to a more useful form for the study of scaling properties, the center-of-mass cross section must be transformed to the invariant cross section $\frac{d\sigma}{dt}$. This is accomplished with the Jacobian $d\Omega_{cm}/dt$ which is discussed in Section 1.2 and is given by

$$\frac{d\Omega_{cm}}{dt} = \frac{\pi}{|\vec{p}_i| |\vec{p}_f|} \quad (5.15)$$

where \vec{p}_i and \vec{p} are the initial and final 3-momenta of the deuteron in the center-of-mass. A derivation of this quantity is given in Section C.1. The invariant cross section is thus given by

$$\frac{d\sigma}{dt} = \frac{d\sigma}{d\Omega_{cm}} \frac{d\Omega_{cm}}{dt}.$$

5.4 Compton Background

In addition to the possible contributions to the background described in Section 5.1.3, there exists another possible source of background. Compton scattering on the deuteron, $\gamma d \rightarrow \gamma d$, can produce recoil deuterons that would be indistinguishable from deuterons produced by $\gamma d \rightarrow d\pi^0$. To estimate this background, the processes of Compton scattering off the proton ($\gamma p \rightarrow \gamma p$) and π^0 photoproduction on the proton ($\gamma p \rightarrow p\pi^0$) are first considered. Both of these processes have been studied by Shupe *et al.* and are discussed in Reference [15]. It is assumed that the differential cross section for the processes obey the following relations

$$\frac{d\sigma_{\gamma p \rightarrow \gamma p}}{dt} \sim \mathcal{F}_1 \frac{d\sigma_{\gamma d \rightarrow \gamma d}}{dt} \quad (5.16)$$

and

$$\frac{d\sigma_{\gamma p \rightarrow p\pi^0}}{dt} \sim \mathcal{F}_2 \frac{d\sigma_{\gamma d \rightarrow d\pi^0}}{dt} \quad (5.17)$$

where \mathcal{F}_1 and \mathcal{F}_2 are form factors that account for the deuteron in the initial and final states. Because the processes are both coherent, it is expected that the form factors in Equations 5.16 and 5.17 are similar. Therefore it is expected that the ratios R_p and R_d , given by

$$R_p = \frac{\frac{d\sigma_{\gamma p \rightarrow \gamma p}}{dt}}{\frac{d\sigma_{\gamma p \rightarrow p\pi^0}}{dt}} \quad (5.18)$$

and

$$R_d = \frac{\frac{d\sigma_{\gamma d \rightarrow \gamma d}}{dt}}{\frac{d\sigma_{\gamma d \rightarrow d\pi^0}}{dt}}, \quad (5.19)$$

will be similar, $R_p \sim R_d$. Figure 5.8 shows the ratio R_p for various values of t . Because $R_p \lesssim 5\%$ over the region $-4.29 \leq t \leq -0.71$ it is expected that $R_d \lesssim 5\%$ over a similar region of t . The range of t for this experiment is $-6.15 \leq t \leq -0.74$. Therefore a possible contribution to the total yield of 3% from $\gamma d \rightarrow \gamma d$ is assumed although no correction is made for this background. A systematic uncertainty resulting from this possible background contamination of 3% is applied to the measured cross sections.

5.5 Summary of Systematic Uncertainties

Systematic uncertainties stemming from limited knowledge of experimental equipment, calculated quantities, and background contributions limit the accuracy of the measured differential cross section. These uncertainties can be loosely categorized into two groups, global uncertainties and point-to-point uncertainties. Global uncertainties are applied equally to all points. Point-to-point uncertainties vary in magnitude over the range of the data. The

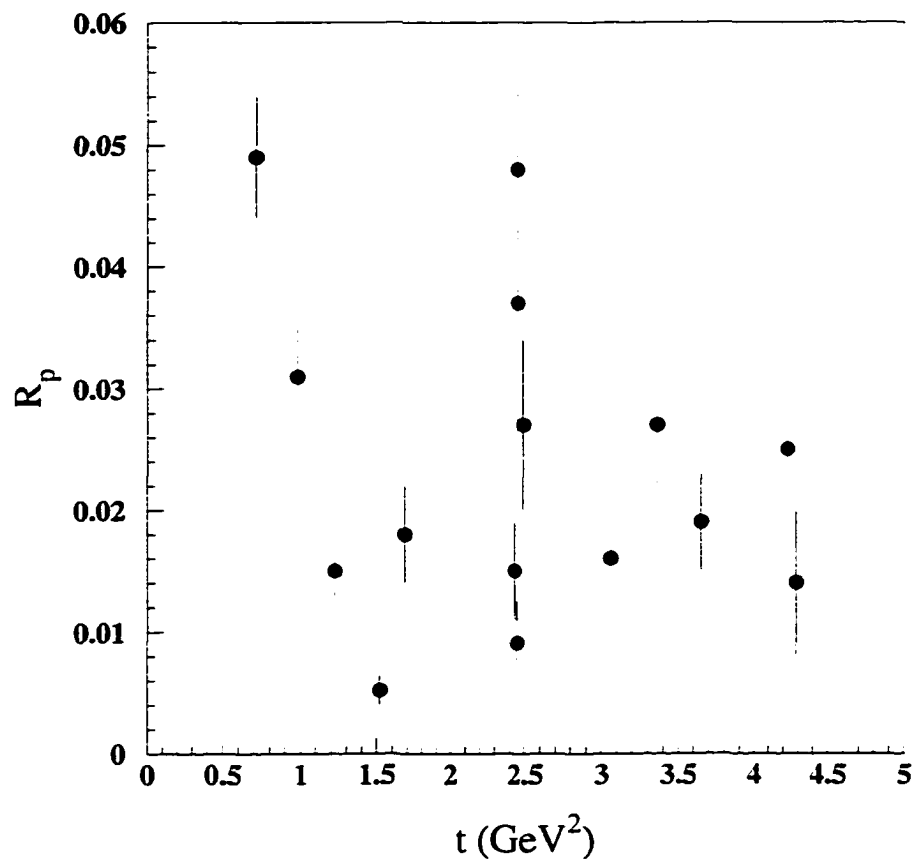


Figure 5.8: The ratio of the differential cross sections for Compton scattering to π^0 production on the proton, R_p . Data are from Reference [15].

systematic uncertainties are summarized in Table 5.3.

A number of uncertainties arise from the accuracy of the measurement of the electron beam current and energy and the calculation of the photon flux. The measurement of the electron beam current is accurate to $\sim 1.5\%$ [89]. It is believed that the uncertainty in the bremsstrahlung flux calculation is of the order of 3% [56]. While the energy of the electron beam has no direct effect on the measured cross section, it does have an effect on the calculated bremsstrahlung spectrum and can also affect the resolution of the E_γ reconstruction, which is discussed in Section 5.1. The normalization of the radiator out spectra $C(E_\gamma)$, which is based on the bremsstrahlung spectra calculations, is estimated to be accurate to roughly 3%. However, the contribution from this uncertainty to the measured cross section is $\sim 1.5\%$ because the measured background is roughly 1/3 of the total yield. The thicknesses of the radiator foils were measured to better than 0.1% and thus had little effect on the calculated bremsstrahlung yield. An overall uncertainty of $\sim 4\%$ was applied to the measured cross section due to inaccuracies in the beam energy and current measurements and the photon flux determination.

Uncertainties in particle identification were primarily due to the determination of the proton background which, at the highest beam energy, dominated all other uncertainties. Errors in the subtraction of the proton background resulted from the placement of cuts about the deuteron mass peak. These cuts were varied slightly to estimate the systematic uncertainty in the proton background subtraction. The total uncertainty in the particle identification is estimated to range between $\sim 3\%$ at the lowest beam energies to $\sim 20\%$ at the $E_0 = 4.045 \text{ GeV}$, $\theta_{cm} = 90^\circ$ point.

The solid angle of the HMS was calculated for each kinematical setting matching the cuts used in the analysis as described in Section 3.10.2. The Monte Carlo model for the calculation of the solid angle used a COSY model with 5th order matrix elements describing

the transformation of the focal plane quantities to the target. The model was determined to be better than 2% accurate by comparing model calculations to measured data when using the full acceptance of the spectrometer [64]. Because software cuts are applied to the acceptance of the spectrometer (on the reconstructed target quantities see Section 3.10.3) a more conservative systematic uncertainty of 3% is applied to the effective solid angle determination. Uncertainties arising from the HMS gate valve are of the order 3%.

The efficiencies of the HMS hodoscope trigger and detector were determined to be very high (nearly 100%). Because these efficiencies were so high and only very small corrections to the data were needed, the uncertainty applied to the cross sections were negligible. The dead time correction, discussed in Section 3.14 was determined to be accurate to within 1%. The uncertainty in the tracking efficiency was determined by comparing yields from various tracking methods to be within 1% as discussed in Section 4.1. Errors resulting from the calculation of the absorption of deuterons are discussed in Section 4.5 and were determined to be less than 3%.

Physical variations in the lengths of the target cells were negligible because the cuts placed on the reconstructed target length were placed well within the limits of the entrance and exit windows. This helped to reduce the accidental background; however, the effective lengths of the target had to be determined from the widths of these cuts. An uncertainty of $\sim 1.5\%$ is applied to the measured cross section to account for the accuracy of the software cut target length. Errors in the density of the target from temperature and pressure measurements and the purity of the target fluid were determined to be less than 1% as discussed in Section 3.9. The uncertainty in the target density resulting from possible localized boiling was estimated to be less than 1% as discussed in the same section.

The various systematic uncertainties are added in quadrature to give the total systematic uncertainty. This uncertainty is then added in quadrature to the statistical uncertainty to

give the total uncertainty in the measured laboratory cross section. Uncertainties in the laboratory cross section transform linearly to the center-of-mass cross section and to the invariant cross section $\frac{d\sigma}{dt}$. Uncertainties arising from and the use of the Jacobians are negligible when compared to the overall systematic errors.

Description	Global Uncertainty	Point-to-Point Uncertainty
Beam Current	<1.5%	
Photon Flux Calc	<3%	
Beam Energy		1-2%
Radiator Thickness	<0.1%	
Solid Angle		3%
Target Density	<1.5%	
Dead Time	<1%	
Tracking Efficiency	1%	
Angular Resolution	0.5%	
Trigger Efficiency	<0.5%	
Y_{tar} Cuts		1.5%
E_γ Cuts		1-5%
Gate Valve		3%
Particle Identification		3-20%
Deuteron Absorption	3%	
$\gamma d \rightarrow \gamma d$ Contamination	3%	

Table 5.3: Summary of systematic uncertainties in the measured cross section.

Chapter 6

Results and Discussion

During the experiment, the differential scattering cross section for the process $\gamma d \rightarrow d\pi^0$ was successfully measured at two center-of-mass angles for a number of incident photon energies. These are the first measurements of a photo-process with a nucleus in both the initial and final states to be performed in this energy range. The measurements also cover a large range of momentum transfer to the deuteron (q) with $0.76 \leq -t \leq 6.15 \text{ GeV}^2$ (note $t = q^2$). Although data for the center-of-mass angle of $\theta_{cm} = 90^\circ$ extend to photon energies of 4.045 GeV, the $\theta_{cm} = 136^\circ$ data only extend to photon energies of 2.445 GeV. This is largely due to limited beam time and difficulties with background identification. Table 6.1 shows the center-of-mass cross sections and various kinematical quantities are shown in Table D.1.

6.1 Asymptotic Scaling Laws

The asymptotic scaling laws (or constituent counting rules) predict that the invariant cross section $\frac{d\sigma}{dt}$ for the process $\gamma d \rightarrow d\pi^0$ should obey the following relation at large center-of-

Beam Energy (GeV)	\bar{E}_γ (GeV)	θ_{cm}	Statistical Uncertainty	Systematic Uncertainty	$\frac{d\sigma}{d\Omega_{cm}} \left(\frac{nb}{sr} \right)$
0.845	0.783	136°	6.8%	5.6%	20.4 ± 1.8
1.645	1.583		7.2%	9.9%	0.372 ± 0.46
2.445	2.383		18%	14.3%	0.0179 ± 0.004
0.845	0.783	90°	7.5%	6.8%	32.8 ± 3.3
1.413	1.368		8%	9%	2.58 ± 0.3
1.645	1.583		8.7%	7.9%	0.96 ± 0.11
2.445	2.390		9%	11.4%	0.079 ± 0.011
3.245	3.190		4.5%	12.6%	0.023 ± 0.003
4.045	3.990		9.4%	21.4%	0.0064 ± 0.002

Table 6.1: Center-of-mass differential cross sections for the process $\gamma d \rightarrow d\pi^0$ measured during Experiment E89-012. The errors given for the cross sections are the sums of the systematic and statistical uncertainties performed in quadrature. The photon energy \bar{E}_γ is used to determine kinematical quantities such as s and t and is obtained from the midpoint of the total photon energy region used in the analysis.

mass energies and angles

$$\frac{d\sigma}{dt} \sim s^{-13} f(\theta_{cm}) \quad (6.1)$$

where the function $f(\theta_{cm})$ depends only on the center-of-mass scattering angle (for $s \sim t \rightarrow \infty$). The data shown as $s^{13} \frac{d\sigma}{dt}$ should then approach a constant value if this is an accurate model for the process at these energies. Figures 6.1 and 6.2 show the invariant cross section multiplied by s^{13} . As can be seen in Figure 6.1 the data at the center-of-mass angle of $\theta_{cm} = 90^\circ$ clearly do not agree with this prediction. The $\theta_{cm} = 136^\circ$ data are however consistent with this model. At $\theta_{cm} = 90^\circ$ the data are in good agreement with previous measurements performed by Imanishi *et al.* [?] for $E_\gamma \approx 0.77$ GeV and those performed at SLAC [?] for $E_\gamma \approx 1.6$ GeV. The data at $\theta_{cm} = 136^\circ$ is also consistent with previous measurements by Imanishi *et al.* at $\theta_{cm} = 130^\circ$ for $E_\gamma = 0.77$ GeV. Further, it should be noted that the range of q^2 covered at both center-of-mass angles are similar (see Table D.1). Because the center-of-mass angles are large, contributions from diffractive scatter-

ing, which can greatly enhance the measured cross section at small center-of-mass angles are expected to be negligible. The data as a whole are inconsistent with the constituent counting rules (CCR) model predictions because the invariant cross section is predicted to obey the scaling law given in Equation 6.1 at all large center-of-mass angles. This implies, perhaps, that the energy region where these scaling predictions would be valid has not yet been reached.

6.2 Reduced Nuclear Amplitudes

As discussed in the previous section, the center-of-mass energies seem to be too low for the predicted constituent counting rule (CCR) behavior to be observed. Because the reduced nuclear amplitude (RNA) analysis accurately describes elastic ed scattering (see Figure 2.10) in a slightly lower energy region where the CCR predictions were not successful and pion photoproduction is a similar process (both having deuterons in the initial and final states), it might be expected that the RNA analysis applied to the $\gamma d \rightarrow d\pi^0$ process would meet with more success. Recent results from TJNAF show that the deuteron electromagnetic form factor ($A(Q)$) is consistent with the RNA prediction and indicate the possible onset of scaling as predicted by the CCR model [32]. As discussed in Section 2.3, the RNA approach is largely an attempt to observe scaling by removing soft wave-function effects responsible for quark binding within the nucleons by factoring the electromagnetic form factors of the nucleons from the scattering amplitude of a given process. Following this model, the cross section for the $\gamma d \rightarrow d\pi^0$ process in the center-of-mass should be given by

$$\frac{d\sigma}{d\Omega_{cm}} = \frac{|\vec{p}_f|}{64\pi^2 s |\vec{p}_i|} p_T^{-6} f^2(\theta_{cm}) [F(Q^2/4)]^4 \quad (6.2)$$

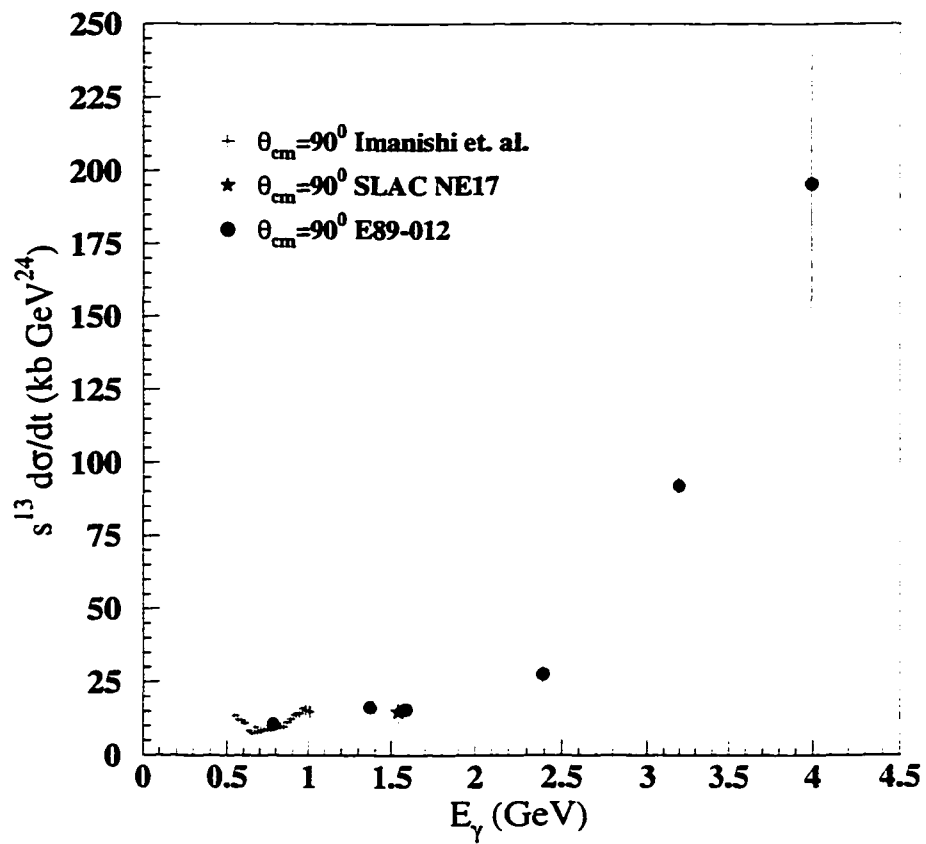


Figure 6.1: Data shown as $s^{13} \frac{d\sigma}{dt}$ for $\theta_{cm} = 90^\circ$. The data are clearly inconsistent with the Constituent Counting Rule predictions. Errors shown include both statistical and systematic uncertainties.

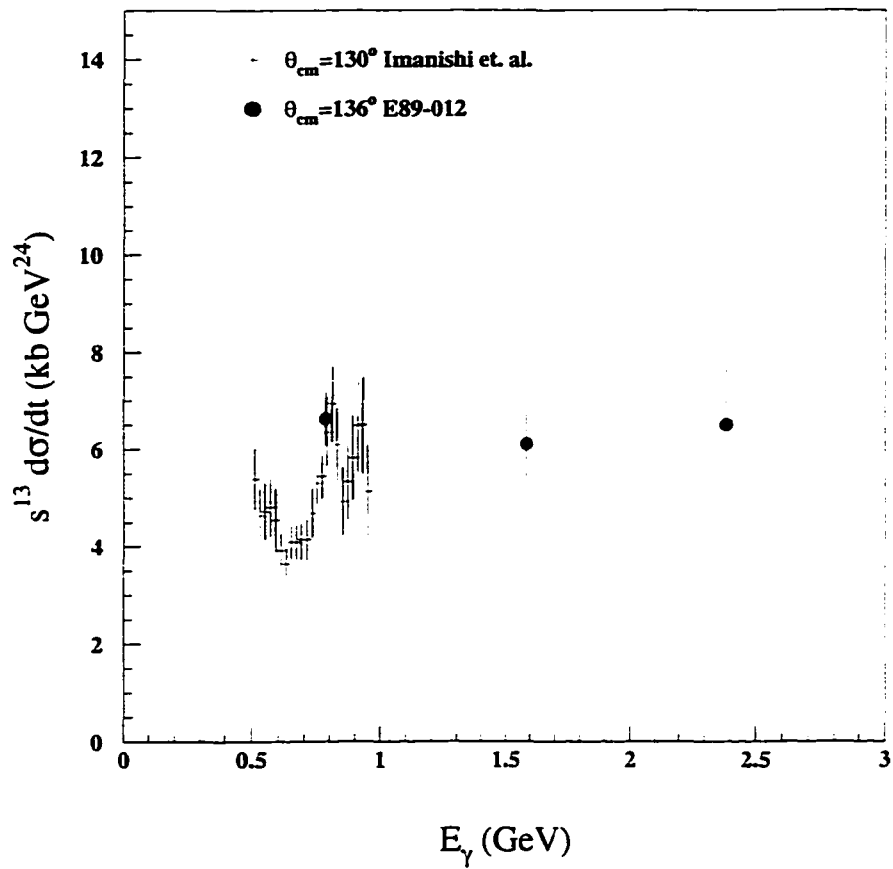


Figure 6.2: Data for $\theta_{cm} = 136^\circ$ shown as $s^{13} \frac{d\sigma}{dt}$. The data are consistent with the Constituent Counting Rule predictions. Errors shown include both statistical and systematic uncertainties.

where $F(Q^2/4)$ is the dipole form factor of the nucleon; $Q^2/4 = -(q/2)^2$ (where $q^\mu/2$ is the approximate 4-momentum transfer to each nucleon); p_T is the transverse momentum of the final state deuteron; \vec{p}_i and \vec{p}_f are the initial and final momentum of the deuteron in the center-of-mass; and $f(\theta_{cm})$ is a function dependent only on the center-of-mass scattering angle (unrelated to the function in Equation 6.1). If this approach were an accurate description of the process, the data, for a given center-of-mass angle shown as $f^2(\theta_{cm})$, would approach a constant. The data shown in Figures 6.3 and 6.4 clearly do not agree with this prediction. This might be surprising given that this model seems to accurately describe elastic electron deuteron scattering at even lower center-of-mass energies and momentum transfer plus both processes are coherent.

Attempts have been made to study the electromagnetic form factor of the deuteron using pion photoproduction on the deuteron [90]. The form factor of a hadron, $F_H(q^2)$, can be thought of as the probability amplitude for the hadron to remain bound after absorbing a momentum transfer of q . Because both ed elastic scattering and π^0 photo-production (on the deuteron) are coherent electromagnetic processes involving a deuteron in the initial and final states (and require that the deuteron remains bound), it might be expected that the process of pion photoproduction behaves in a manner similar to ed elastic scattering (by scaling with the deuteron form factor $A(Q)$). The analysis of Friedman and Kendall [90] in essence, assumes an Impulse Approximation for π^0 photoproduction which may be questionable since the form factor extracted from their data is in some cases more than 20% different from the form factor measured by elastic ed scattering. Regardless, if some type of scaling were to be observed by factoring the π^0 photoproduction data by the deuteron electromagnetic form factor, this would indicate that much of the reaction dynamics for the process $\gamma d \rightarrow d\pi^0$ are contained in the form factor of the deuteron. The data are shown in Figure 6.5 as a function of $-q^2$ ($-q^2 = -t$) where q^μ is the four momentum transferred to

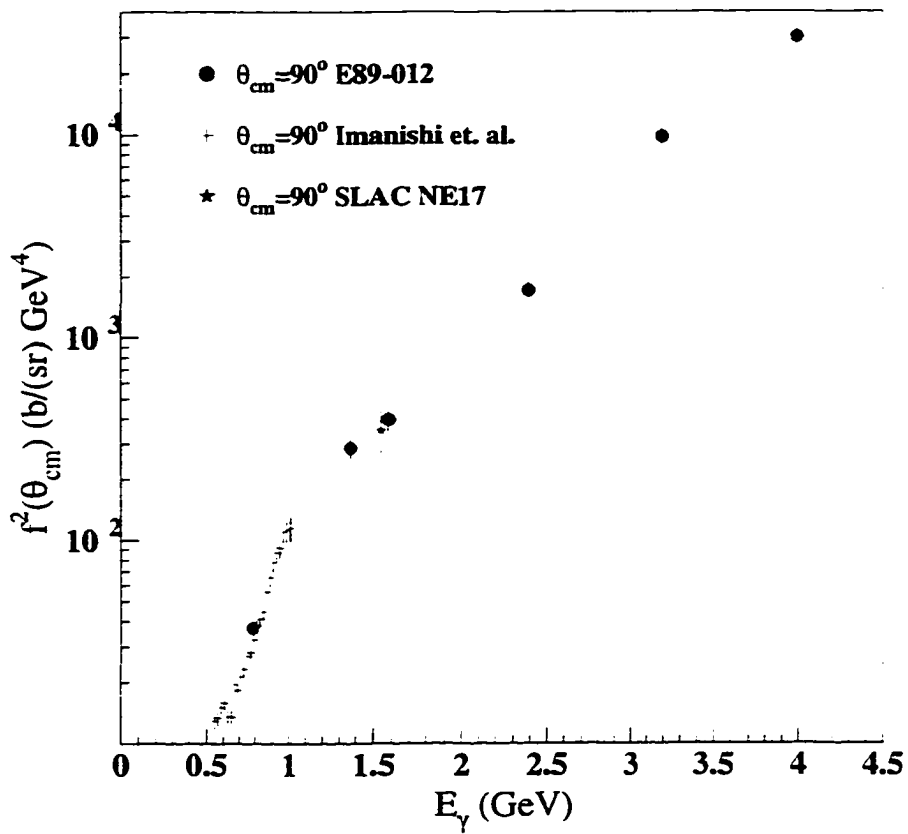


Figure 6.3: Data for the process $\gamma d \rightarrow d\pi^0$ shown as $f^2(\theta_{cm})$, which is described by the RNA analysis above, for $\theta_{cm} = 90^\circ$. Errors shown include both statistical and systematic uncertainties.

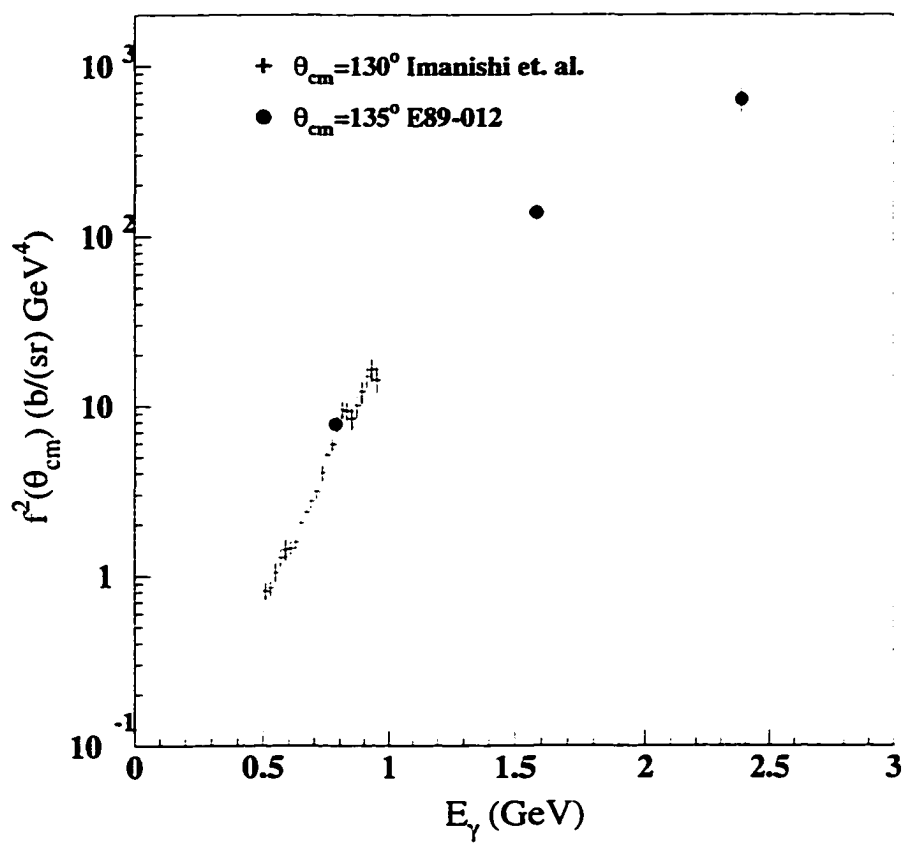


Figure 6.4: Data for the process $\gamma d \rightarrow d\pi^0$ from the present work shown as $f^2(\theta_{cm})$, which is described by the RNA analysis above, for $\theta_{cm} = 136^\circ$. Errors shown include both statistical and systematic uncertainties.

the deuteron, and in Figure 6.6 factored by the deuteron form factor $A(Q)$ and $-t$ (where $Q^2 = -q^2$). In Figure 6.6, the form factor of the deuteron $A(Q)$ was determined from a fit to the world data obtained from References [91, 92, 93, 94] and [95]. There is no striking feature of Figure 6.6 that would indicate that the process $\gamma d \rightarrow d\pi^0$ behaves like the deuteron electromagnetic form factor.

6.3 Comparison with Other Photoreactions

It is clear from Figures 6.1 and 6.2 that the cross section for $\theta_{cm} = 90^\circ$ does not fall as rapidly as s^{-13} and that the cross section for $\theta_{cm} = 136^\circ$ falls at a rate which is consistent with s^{-13} . The CCR model predicts that the invariant cross section should behave as

$$\frac{d\sigma}{dt} \sim s^{-n} f(\theta_{cm})$$

where n is determined as the minimum number of constituents needed to describe the process (see Section 2.2). The power n is, in this model, independent of the center-of-mass scattering angle. It is therefore useful to fit the data obtained in the experiment to the form As^{-n} (where A and n are parameters determined from the fit) at each center-of-mass angle for data with incident photon energies above ~ 1 GeV (which is an arbitrary cutoff) in the case of the 90° data and by using all three points in the case of the 136° data. The power n was determined to be $n = 9.6 \pm 0.4$ for $\theta_{cm} = 90^\circ$, and for $\theta_{cm} = 135^\circ$, $n = 13.1 \pm 0.3$.

The results of these fits yield values for n which are largely different at both deuteron center-of-mass angles. This phenomenon was recently observed by Bochna and Terburg *et al.* [?] for the process $\gamma d \rightarrow pn$. These results prompt a closer inspection of the world data for photo-processes. Table 6.2 shows the results of fits of the form As^{-n} (for similar center-

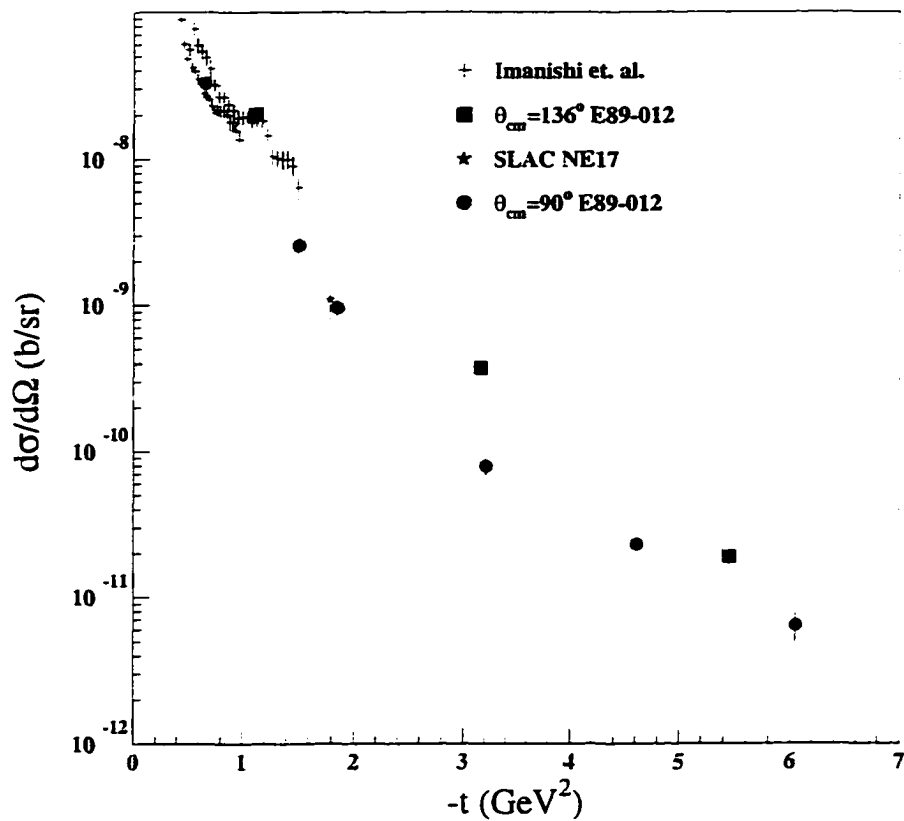


Figure 6.5: Center-of-mass differential cross sections for the process $\gamma d \rightarrow d\pi^0$ at both 136° and 90° shown as a function of t , the momentum transfer to the deuteron. The symbols in this figure have the same meaning as those in Figure 6.3. Errors shown include both statistical and systematic uncertainties.

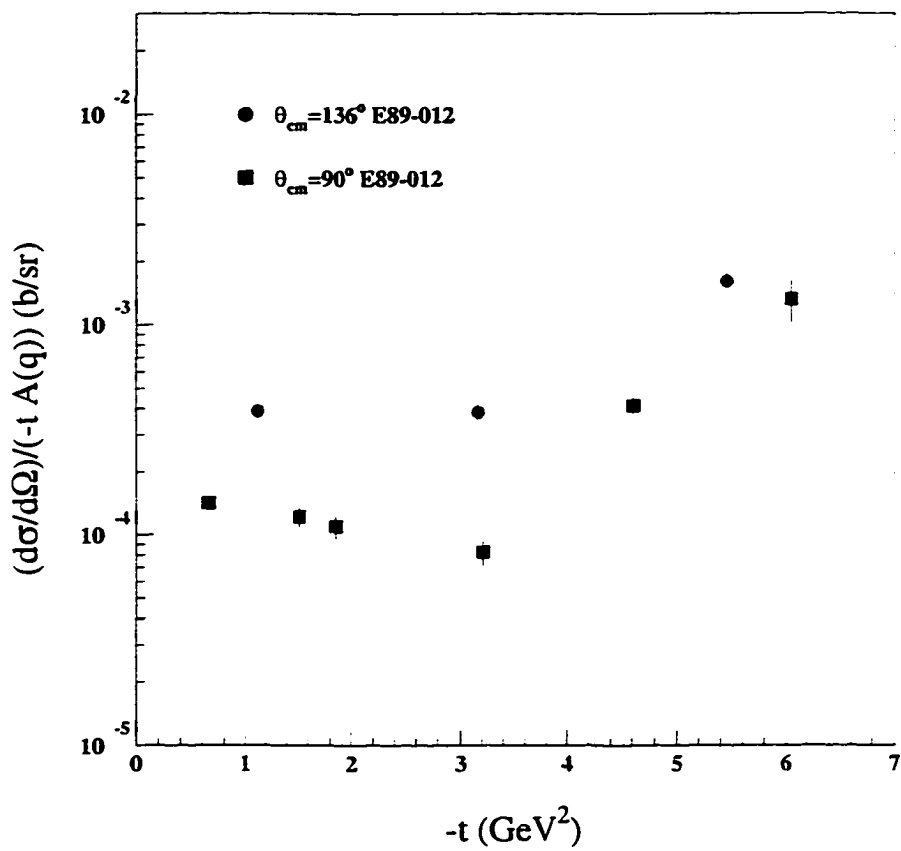


Figure 6.6: Center-of-mass cross sections factored by the deuteron electric form factor $-t A(Q)$. $A(Q)$ was determined from a fit to the world data compiled from References [91, 92, 93, 94] and [95]. Errors shown include both statistical and systematic uncertainties.

of-mass angles) for some of the world data for photo-processes. While for each process, there is at least one center-of-mass angle at which the CCR prediction agrees with the data, there seems to be a definite dependence of the power n on the scattering angle. Note that Anderson *et al.* show the data for the $\gamma p \rightarrow \pi^+ n$ process as an angular distribution [14]. Their figure implies that the data agree with the predicted scaling of s^{-7} for all center-of-mass angles. This is misleading because the data are not taken at (or near) constant center-of-mass angles for each beam energy with the exception of $\theta_{cm} = 90^\circ$. By using the fit of the angular distribution of the data given by the authors, the data may be separated into several θ_{cm} bins. The data analyzed in this fashion are inconsistent with the CCR prediction for angles differing from $\theta_{cm} = 90^\circ$. The data for photoreactions, when viewed in this manner, seem to contradict the Constituent Counting Rule predictions and when considering other possible models such as the model proposed by Radyushkin [42], casts doubts on the application of perturbative QCD for intermediate energy nuclear reactions.

6.4 Conclusions

The data for the process $\gamma d \rightarrow d\pi^0$ collected during Experiment E89-012 and in earlier works are inconsistent with the CCR and RNA predictions. In the case of the former, this is may not be surprising due to the low center-of-mass energies involved in the process for the relevant photon beam energies. While the $\theta_{cm} = 136^\circ$ data are consistent with the s^{-13} scaling behavior of the invariant cross section $\frac{d\sigma}{dt}$ predicted by the Constituent Counting Rules, the data for $\theta_{cm} = 90^\circ$ clearly do not agree with this prediction despite the fact that the data for both angles cover a similar region of momentum transfer. The data for both angles are also in strong disagreement with the RNA analysis. This is somewhat unexpected given the similarities between π^0 photoproduction on the deuteron and elastic ed scatter-

Reaction	Ref	θ_{cm}	n from CCR Model Prediction	n from fit
$\gamma p \rightarrow \gamma p^\dagger$	[15]	45°	6	5.9 ± 0.3
		90°		7.1 ± 0.4
		105°		6.2 ± 1.4
$\gamma p \rightarrow p\pi^0$	[15]	60°	7	5.8 ± 0.3
		90°		7.0 ± 0.3
		105°		6.1 ± 0.5
$\gamma p \rightarrow \pi^+ n$	[14]	90°	7	7.6 ± 0.7
$\gamma d \rightarrow pn^\dagger$	[20]	36°	11	9.6 ± 0.8
		52°		9.6 ± 0.1
		69°		10.8 ± 0.1
		89°		11.1 ± 0.3
$\gamma d \rightarrow d\pi^0$	This Work	136°	13	13.1 ± 0.2
		90°		9.6 ± 0.4

Table 6.2: Overview of some of the world data for real photoprocesses. The invariant cross section $\frac{d\sigma}{dt}$ has been fit to the form $A s^{-n}$ for data with similar center-of-mass angles. The superscript \dagger indicates that the fit was given by the authors of the given reference.

ing (discussed in Section 6.2) and the success of the RNA model in describing elastic ed scattering. However, this should not be a complete surprise because the RNA model fails to describe data from other nuclear processes such as $\gamma d \rightarrow pn$ [96, 97, 20]. Unfortunately, at the present time there are no traditional meson exchange calculations available that are valid in this energy region. The calculations of Imanishi *et al.* [?] were performed using specific amplitudes. A similar calculation using more appropriate amplitudes might be applicable at higher energies [98].

It is evident that the application of perturbative QCD to nuclear processes in the intermediate energy region (few GeV) is highly questionable. It also seems apparent that models using only meson-baryon degrees of freedom are not applicable in this energy region. It is unclear, at this time, how the transition from meson-baryon degrees of freedom to quark-gluon degrees of freedom should be made. One can see that the data collected at the two center-of-mass angles during the experiment have a different s dependence for each angle. A careful inspection of some of the world data on photoreactions indicates that this phenomenon is not unique to the $\gamma d \rightarrow d\pi^0$ process. A recent analysis of the $\gamma p \rightarrow \gamma p$ reaction by A. Radyushkin suggests that the angular dependence of the power law fall off ($s^{-n(\theta_{cm})}$) may be a result of soft wave function effects that should not be ignored [42]; however, the data available for this process are not sufficient to test this model. A recent proposal to study this reaction at TJNAF in a similar energy region has been approved [99], and an attempt to extend this analysis to other photoreactions is being considered. An experiment to investigate the small angle behavior of the $\gamma d \rightarrow pn$ cross section at slightly higher energies also at TJNAF is scheduled for 1999 in an attempt to observe a change in the observed power law s dependence [100]. It is evident from the present data that more theoretical and experimental efforts are needed to understand the observed energy dependence of these photoprocesses.

Appendix A

Bremsstrahlung Radiator

The Hall C Bremsstrahlung Radiator was designed, constructed, and installed as part of this thesis project. This radiator was used for experiment E89-012 and remains installed for future experiments in need of an upstream radiation source [100]. The radiator is positioned roughly 1.2 m upstream from the target center and has five nominal target positions (excluding removed) which can be chosen remotely. For experiment E89-012 the target positions were filled with copper foils with nominal radiation lengths of 2%, 4%, 6%, 7%, and 8%. The 4% and 6% targets were used extensively throughout experiment E89-012.

A.1 Hardware design aspects

Figure A.1 shows a full view of the hardware components of the bremsstrahlung radiator without the vacuum mounting hardware. The radiator target is based on a highly modified HARP design [101]. In addition to the target, there is a self contained water cooling system to prevent damage to the foils during high current operation. The control system is integrated into the Hall C Cryogenic Target control system.

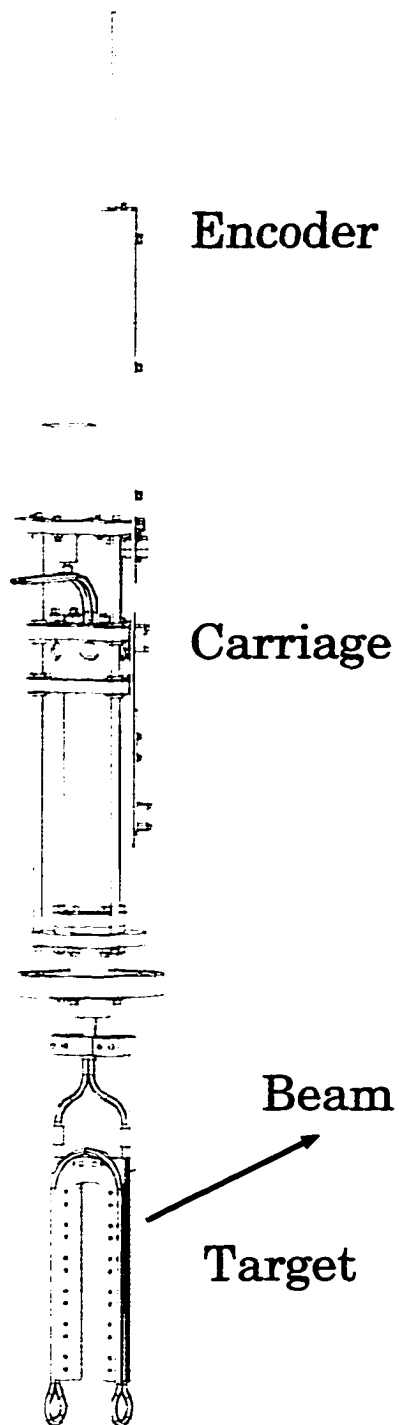


Figure A.1: Hall C bremsstrahlung radiator shown without the vacuum hardware. The target/heat sink, to which the copper foils are attached, and water lines can be seen at the bottom of the figure. The copper foils are not shown.

A.1.1 Radiator foils and target mount

The various radiator thicknesses are made from stacked extruded thin foils copper that were supplied in standard thicknesses of 0.0005, 0.001, 0.010, and 0.025 inches. The thickness of each foil was measured at numerous points to ensure that it was uniform. These thicknesses are constant to within $\pm 3 \mu\text{m}$ over the entire surfaces of the foils. The foils were cut into rectangles with approximate dimensions 1.5 by 0.75 inches. While the intersections of the sides may not be exactly perpendicular, the sides are straight over their entire length to within $\pm 1 \mu\text{m}$. The positions of the corners of the rectangle were recorded on a coordinate measurement instrument with relative errors of $\pm 1 \mu\text{m}$. This allowed the measurement of the area of the entire foil to be calculated simply by separating it into two triangles and using

$$A = \frac{1}{2} \begin{vmatrix} 1 & 1 & 1 \\ x_1 & x_2 & x_3 \\ y_1 & y_2 & y_3 \end{vmatrix} \quad (\text{A.1})$$

where A is the area of one triangle and x_i, y_i are coordinates of each of the three vertices. The mass of each foil is measured to within $\pm 0.1 \text{ mg}$. Table A.1 shows the nominal thickness and actual thickness of each of the five radiator targets. In some cases, as many as three foils were stacked to make up the complete thickness. The thicknesses for each of the foils making up the stack are given for each position.

The foils were clamped to the target mount which served as a heat sink (Figure A.2). A thermal conductive paste with low outgassing properties was applied where contact was made. The temperature of the heat sink was maintained by a closed loop water cooling system which is described in Section A.1.2. The horse shoe shape of the heat sink and the arrangement of the external water line allows the radiator targets to be inserted into the

Nominal Thickness (%)	Mass (g)	Area (cm ²)	Thickness g/(cm ²)	Total Thickness (% radiation length)
2	1.4974	6.978	0.2146	1.847 ± 0.002
	0.1626	7.111	0.0229	
4	1.5380	7.267	0.2117	3.489 ± 0.003
	1.5491	7.214	0.2147	
	0.1620	7.264	0.0223	
6	4.3316	7.260	0.5966	6.021 ± 0.003
	0.6283	7.064	0.0889	
	0.6443	7.264	0.0887	
7	4.3960	7.260	0.6052	7.060 ± 0.003
	1.5102	7.034	0.2147	
	0.6346	7.207	0.0881	
8	4.3380	7.260	0.5975	7.975 ± 0.041
	1.4944	7.076	0.2119	
	1.5421	7.132	0.2162	

Table A.1: Thickness data for copper foils making at given target positions in the radiator. The large error for the 8% foil stack is due to poor surface area data. Individual foils making up the complete stack for a given radiator thickness are separated for clarity.

electron beam without turning the beam off or passing large radiation lengths of material through it. The heat sink and clamps are made of aluminum 6061-T6.

A.1.2 Water cooling system

The temperature of the target/heat sink was maintained at around room temperature to dissipate the heat induced in the foils by the electron beam. This was accomplished with a closed loop water cooling system. The main elements in the loop in addition to the heat sink are the water pump, the heat exchanger, resin filter, and flow/pressure switches. A diagram of the loop is shown in Figure A.3.

The system is similar to a TIG welding torch radiator. The basic pieces of a Bernard model 3500SS welding torch cooler were used. The unit is a self contained heat exchanger

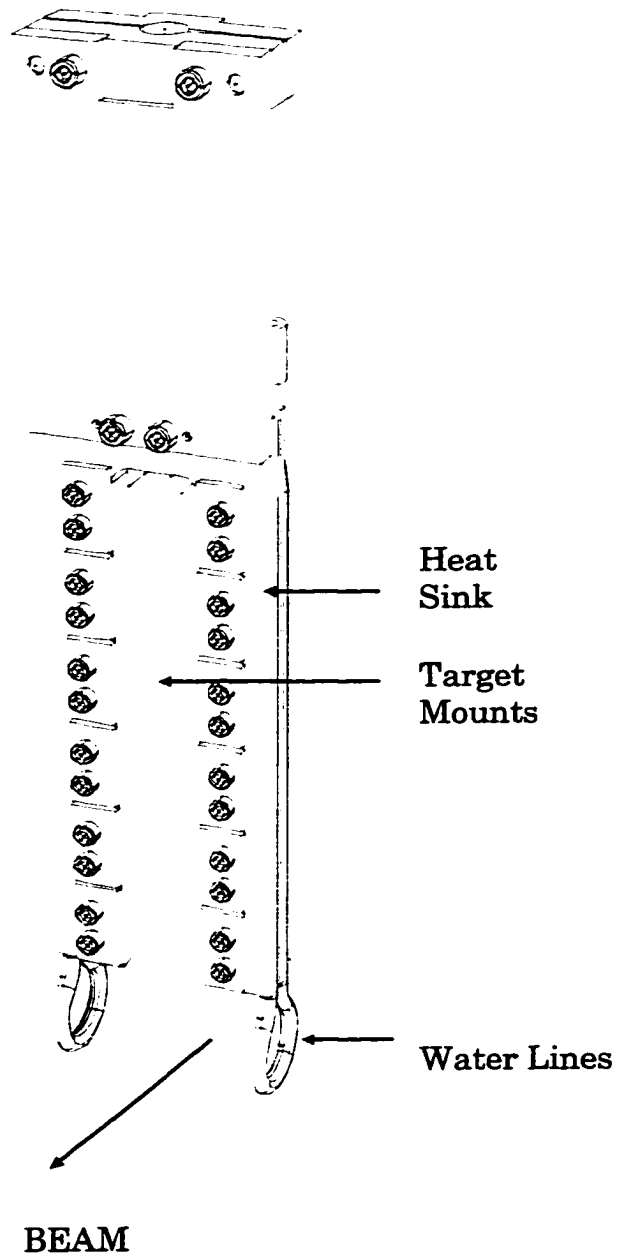


Figure A.2: Downstream view of the bremsstrahlung radiator target mount/heat sink. View shows clamps, heat sink, and waterlines, which wrap around the back (upstream side) of the target.

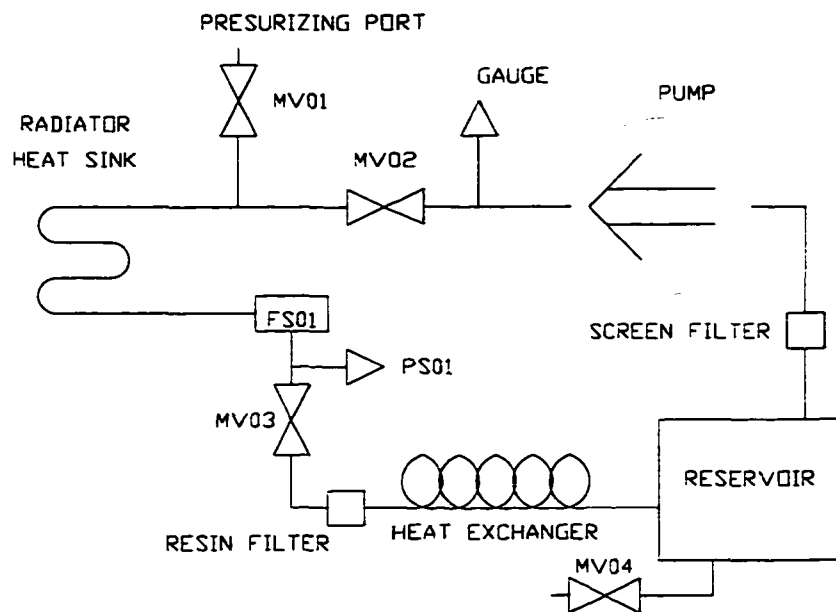


Figure A.3: Flow schematic for radiator water cooling system. Manual valves are denoted with the prefix MV. PS and FS are the symbols for pressure and flow switches.

water pump and reservoir, with the additional features of being a long running, low maintenance device. This combination of features made it highly suitable for the bremsstrahlung radiator. The pump/fan motor was replaced with a slightly more powerful unit as were all nonmetal parts. The final device is a self contained unit with copper, brass, and stainless steel water handling components. An external filter was added to the system to reduce activated contaminants in the cooling water. Various valves are placed throughout the system as are two safety switches that detect flow and pressure. The description and function of each component is given in the following list.

- Reservoir: provides stable water source for the pump.
- Screen filter: removes large particulate contaminants from water to protect the pump.
- Pump: brass rotary vane pump under normal operating conditions supplies roughly 2 gallons of water per minute at 60 psig. The power for the pump is supplied by a 110

V continuous duty fan/pump motor.

- MV02, MV03: manual valves which allow isolation of the cooling pump filters and reservoir.
- MV01: valve serves as a pressurizing port for purging the system of water for maintenance.
- MV04: manual valve used to fill the reservoir.
- Radiator heat sink: radiator target mount/heat sink which is described above and in Figure A.2.
- MV05, MV06: manual valves that allow isolation of the bremsstrahlung radiator.
- FS01, PS01: flow and pressure switches that allow remote sensing of the state of the cooling flow.
- Resin filter: Culligan Micropore sub-micron filter for minimizing contamination of radionuclides produced in the water.
- Pressure gauge and flow meter: elements intended for diagnostic and installation purposes.

The flow rate necessary for dissipating the heat induced in the radiator by the beam was calculated using standard techniques. For an electron beam current of $100 \mu\text{A}$ on a six percent copper foil, the heat load is less than 110 W [102]. Thus, less than 0.1 gallon per minute is needed. This allows an average foil temperature of $\sim 114^\circ$ above the ambient temperature of Hall C. The electron beam was also rastered to reduce the power density induced on the radiator foils and the cryogenic target. The water cooling system was modified for later experiments to provide cooling for the Hall C solid target ladder.

A.1.3 Vacuum and motion components

All vacuum components other than the radiator foils and target mount are stainless steel (SST304 or SST314). Joints between different vacuum components are made with copper gaskets (Conflat or equivalent) giving completely radiation resistant vacuum seals. Cajon VCR fittings are used on the water feedthroughs that are coupled to stainless steel flex lines. Thus, all critical components of the system (vacuum and water containment) are metal and impervious to scattered radiation. The vertical motion of the radiator target ladder is enabled through a welded vacuum bellows, custom made by Standard Bellows. The bellows is constructed of heat treated AM350 SST heat treated segments giving roughly a 50,000 full eight inch cycle lifetime. It is good practice to only use 75% to 80 % of the rated bellows travel, therefore, only six inches (± 3.0 inches from nominal 0) is used. This should extend the cycle lifetime well beyond the specification.

Vertical positioning of the radiator foils is driven by a DC stepper motor (SLO-SYN M063-LS09). The motor shaft is coupled to a lead screw with 1/2-20 threads that passes through a drive nut attached to the carriage assembly (see Figure A.1). This combination gives vertical positioning steps of less than 0.0002 inches and also permits a lower power motor to be used to lift the estimated vacuum load of 100 lbs present in the bellows assembly.

The entire radiator assembly is installed in the Hall C beam line roughly 1.21 m upstream from the target center. Lead shielding is stacked around the entire radiator to reduce background in the hall. The radiator was installed in November of 1995. A leak check was performed on all vacuum components after installation was completed and has functioned without vacuum failure ever since.

A.2 Control subsystem for the Bremsstrahlung Radiator

Remote control of the bremsstrahlung radiator is accomplished with a VME to CAMAC interface. Routines written in C and compiled for the VME input output controller (IOC) use remote CAMAC addressing to communicate with a BiRa 5333B scanning voltage ADC and a Joerger SMC24BPC stepper motor controller. A linear potentiometer (ETI systems LW30-200) with a 10V reference is used to give the absolute position of the radiator target ladder accurate to within ± 0.001 inches. The routines are invoked by the Experimental Physics and Industrial Control System (EPICS) state machine for the Hall C Cryogenic target. The state machine also passes parameters necessary for the proper control and positioning of the radiator.

The general operation of the radiator is handled through the Hall C cryogenic target graphical user interface (GUI). The radiator GUI, shown in Figure A.4, is a subsystem of the main target GUI and allows point and click selection of the standard positions used in experiments and shows the general status of the system updated ever 2 seconds. It also allows more advanced users to view the status of the pump and radiator motor controller and position the radiator anywhere in the beam.

A.3 Performance of the Bremsstrahlung Radiator

The radiator has functioned without failure in any subsystem since it was installed. It was used extensively throughout experiment E89-012 and has been used intermittently since then. Data for the process $\gamma p \rightarrow \pi^+ n$ were taken in the SOS to check the yields from the separate foil stacks. Particle identification for the π^+ is accomplished by time of flight in the scintillators for separations from protons and deuterons, and by the lead glass



Figure A.4: Radiator GUI screen. (Figure is shown in greyscale. The actual GUI is in color.)

shower calorimeter for separation from positrons. The reconstructed photon energy is determined from kinematics and only the data from photons with energy $2.045 \text{ GeV} \leq E_\gamma \leq 2.420 \text{ GeV}$ are considered. These data are summarized in Table A.2, and are shown in Figure A.5. The slight curvature in the data is due to the nonlinearity in the bremsstrahlung yield as the thickness of the radiator increases. To remove this nonlinearity, the yields are normalized to photon flux calculated with the techniques described in Appendix B. The photon flux normalized data are shown in Figure A.6. Because the data in Figure A.6 lie on a flat line, the measurement of the thickness of the radiator foils and calculation of the bremsstrahlung yield for a thick target are consistent.

Nominal Radiator Thickness (%)	Radiator Thickness (%)	Normalized Yield (counts)
0	0.0 ± 0.0	0.0 ± 0.13
2	1.847 ± 0.002	6.89 ± 0.17
4	3.489 ± 0.003	11.92 ± 0.18
6	6.021 ± 0.003	18.61 ± 0.26
7	7.060 ± 0.003	20.92 ± 0.25
8	7.975 ± 0.010	23.00 ± 0.44

Table A.2: Corrected yields for the process $\gamma p \rightarrow \pi^+ n$ for various foil stacks. The yield for 0.0 % thickness has been subtracted from all data points.

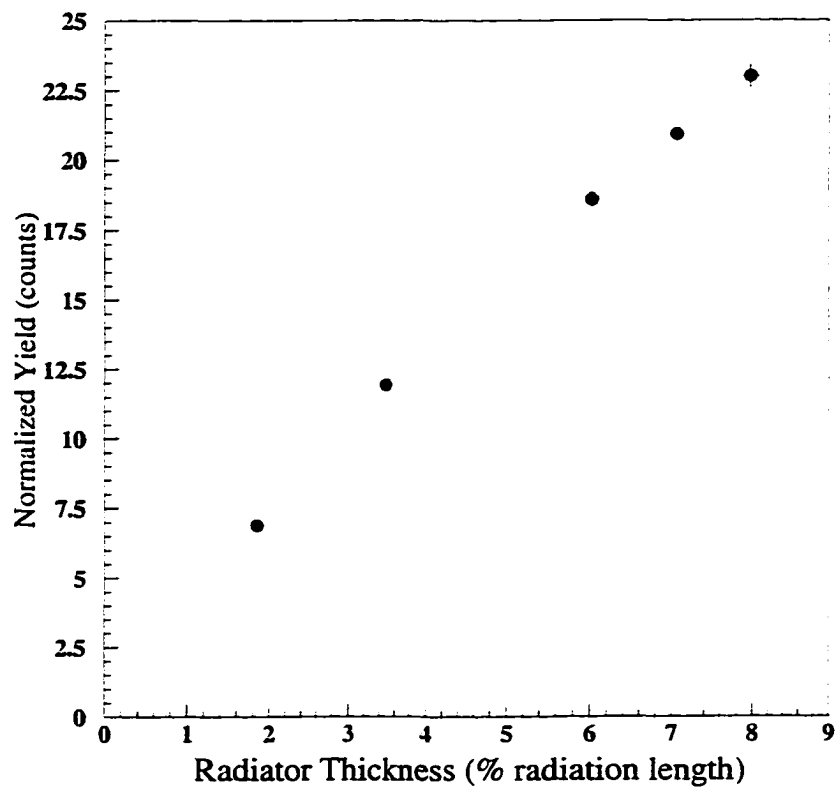


Figure A.5: Data for $\gamma p \rightarrow \pi^+ n$ from radiator linearity test. The data are shown with the normalized yield from the radiator out case subtracted from the normalized yield for each radiator. Error bars are typically smaller than the point and are statistical only. Note that no cross sections were extracted from this data.

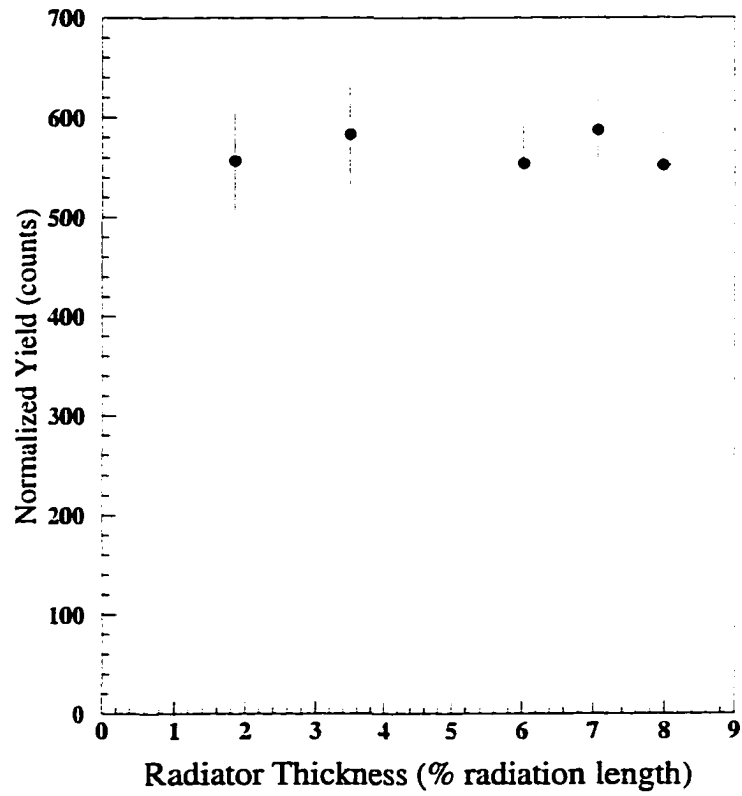


Figure A.6: Data for $\gamma p \rightarrow \pi^+ n$ from the radiator linearity test normalized by the calculated photon flux.

Appendix B

Bremsstrahlung Calculations

The photon yield from the bremsstrahlung radiator has to be calculated because the photon beam is not tagged. Code to do this calculation was developed based on the methods of Matthews and Owens [56]. The general calculation includes bremsstrahlung produced from electron-nucleon and electron-electron interactions and effects from the energy loss of the incident electrons in the radiator and the energy spread of the initial electron beam. The methods outlined in Reference [88] are used to determine the electron energy loss spectra in the radiator foils. The results are compared to a calculation that does not include energy loss effects. The routines are written in C and are compiled using the *gnu* C compiler, *gcc*, with optimization for mathematical speed. The correction function, $C(E_\gamma)$, applied to the “radiator out” spectra is also calculated with the same routines and is discussed here.

B.1 Bremsstrahlung Yield

For high incident electron energies ($E_0 \gg m_e$), the opening angle of the high energy bremsstrahlung cone produced in a radiator is given approximately by

$$\theta_\gamma \approx 2m_e/E_0 \quad (\text{B.1})$$

where E_0 is the incident electron beam energy and m_e is the mass of the electron. The rms multiple scattering angle for the electrons emerging from a radiator is given by

$$\theta_{\text{mult}} \approx \frac{13.6\sqrt{2}}{p} \sqrt{l/l_r} [1 + 0.038 \ln(l/l_r)] \quad (\text{B.2})$$

where p is the momentum of the incident electron in MeV and l/l_r is the thickness of the radiator in radiation lengths. Because these angles are less than a few milliradians (for high energy photons) and the radiator is ~ 1.2 m upstream from the target, the entire high energy bremsstrahlung flux is incident on the target. Therefore, formulae describing the total, integrated over angle, cross section for the bremsstrahlung yield are used in the calculation of the bremsstrahlung flux.

The total cross section (integrated over angle) for the bremsstrahlung yield is given by

$$\frac{d\sigma(E_0, k)}{dk} = \frac{\alpha r_0 Z^2}{k} [\Phi_n(Z, E_0, k) + \Phi_e(Z, E_0, k)] \quad (\text{B.3})$$

where $\alpha = 1/137$, $r_0 = 2.82 \times 10^{-13}$ cm, k is the photon energy, Z is the atomic number of the radiator, and Φ_n and Φ_e are the electron-nuclear and electron-electron bremsstrahlung

spectra respectively. The total bremsstrahlung yield is then given

$$\frac{d^2 n(Z, E_0, k)}{dk dt} = \frac{3.495 \times 10^{-4}}{Ak} [Z^2 \Phi_n + Z \Phi_e] \left(\frac{\text{photons cm}^2}{\text{MeV g}} \right) \quad (\text{B.4})$$

where A is the atomic number of the radiator. The electron-nuclear spectrum is calculated using extremely relativistic Bethe-Heitler theory, includes a Coulomb correction, and accounts for effects from intermediate screening. This is accurate for high photon energies k except very near the endpoint of the bremsstrahlung spectrum, $k < k_{max} \approx E_0 - m_e - 0.02Z \text{ MeV}$, where additional improvements have been made. The electron-electron spectrum is calculated assuming the incident electrons are extremely relativistic compared to the atomic electrons and a small correction has been applied to account for binding of the atomic electrons. The complete spectrum, as described by Equation B.4, does not include effects from the energy spread of the incident beam or for energy loss of the incident electrons in the radiator.

B.1.1 Energy Loss Effects

Electrons traversing the thickness of a radiator can lose energy at any point in the radiator foil. This has a strong effect on the bremsstrahlung yield for radiators with thicknesses larger than $\sim 0.5\%$ radiation lengths. It is possible for the incident electrons to lose energy by radiating bremsstrahlung and by collisions with atomic electrons in the radiator material (ionization). These two energy loss distributions are numerically combined to give a distribution for the total energy loss. The collision loss energy distribution for electrons with incident energy E_0 , traversing a radiator (atomic number Z) of thickness T , emerging with an energy E is given by

$$W_C(E, E_0, Z, T) = \begin{cases} \Phi_B(\lambda) & \text{for } \lambda \leq 8.37 \\ 1.2774/\lambda^2 & \text{for } 8.37 < \lambda \leq 150 \\ 0 & \text{for } \lambda > 150 \end{cases} \quad (\text{B.5})$$

where λ is a dimensionless parameter describing the energy loss. Φ_B is a parameterization (by Blunk and Leisegang [103]) of the Landau distribution for small energy losses (small λ). The $1/\lambda^2$ tail is added to fit the Landau distribution at higher energy losses and, for speed in computation, a cut off (for $\lambda > 150$) has been applied. The radiation loss distribution is calculated using an approximate form for the bremsstrahlung spectrum and is given by

$$W_R(E, E_0, Z, T) = \frac{[\ln(E/E_0)]^{\zeta-1}}{E \Gamma(\zeta)} \quad (\text{B.6})$$

where $\zeta = 1.44 T$ and the thickness of the radiator, T , is given in radiation lengths. In practice, $1/\Gamma(\zeta)$ is calculated numerically using a Padé approximation derived to $\mathcal{O}(5)$ using the methods described in Reference [104]. The radiation and collision loss distributions are folded together to give the complete energy loss distribution

$$W(E, E_0, Z, T) = \int_E^{E_0} W_C(E_0, E', Z, T) \cdot W_R(E', E, Z, T) dE' \quad (\text{B.7})$$

where it has been implicitly assumed that the electrons first lose energy by collision and then by radiation. The calculated energy distribution for an electron beam with incident energy $E_0 = 2445.0$ MeV traversing a copper radiator of thickness 6.02% radiation lengths is shown in Figure B.1.

The energy spectrum of the incident beam, before it impinges on the radiator, is also taken into account. The energy distribution of the beam at CEBAF is extremely narrow (beam dispersion is less than 10^{-3}). Therefore the incident energy distribution is approx-

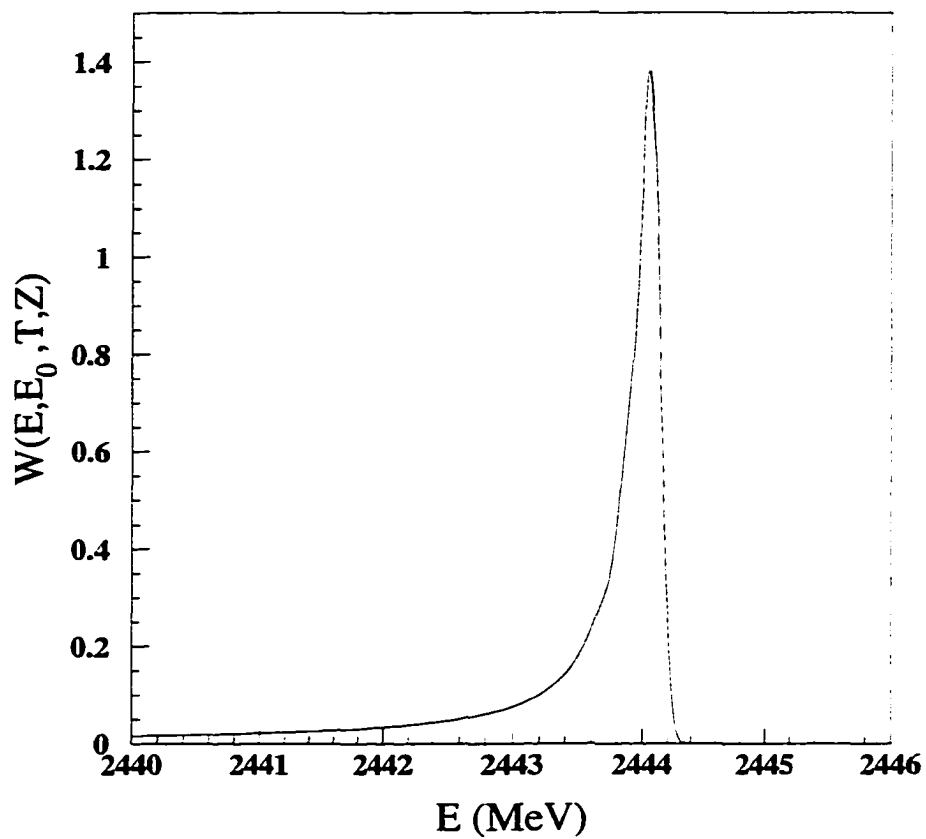


Figure B.1: Calculated electron energy distribution $W(E, E_0, Z, T)$ for a beam with an incident energy of $E_0 = 2445.0$ MeV passing through a copper radiator with a thickness of 6.02% radiation lengths.

imated as a rectangular box with width $\Delta = 5 \times 10^{-4} E_0$ and height $1/\Delta$. The incident energy loss distribution used in the calculation of complete bremsstrahlung spectrum is given by

$$\mathcal{E}(E, E_0) = \begin{cases} 1/\Delta & \text{for } E_0 - \Delta/2 \leq E \leq E_0 + \Delta/2 \\ 0 & \text{otherwise} \end{cases} \quad (\text{B.8})$$

B.1.2 Complete Bremsstrahlung Spectrum

The energy loss and incident energy distributions given by Equations B.8 and B.7 must be folded with Equation B.4 to give the complete bremsstrahlung spectrum (in photons per MeV)

$$\frac{dN(k, E_0, Z, T)}{dk} = \int_{E_0 - \frac{\Delta}{2}}^{E_0 + \frac{\Delta}{2}} \frac{dE}{\Delta} \int_{k_{\min}}^E dE' \frac{d^2n(Z, E', k)}{dk dt} \int_0^T dt W(E', E, Z, t) \quad (\text{B.9})$$

where $\frac{d^2n}{dk dt}$ is the bremsstrahlung flux determined from Equation B.4. Both the energy loss spectrum and bremsstrahlung spectrum given above involve additional integrations. Performing the five integrations (the final integration over k gives the photon yield) with the proper stepsizes to ensure an accurate result involves an inordinate amount of computation time. To make the calculation more tractable, the last two integrations in Equation B.9 are performed only once for a given complete calculation and the resulting distribution I is given by

$$I(E, E', Z, T) = \int_0^T dt \int_{E'}^E dE'' W_C(E, E'', Z, t) W_R(E'', E', Z, t). \quad (\text{B.10})$$

To a very good approximation, the shape of this spectrum does not change for small incident energy changes therefore, the spectrum is only shifted in accordance with shifts in incident energy E . The spectrum $I(E, E', Z, T)$ is shown in Figure B.2 for an incident beam energy

of 1413 MeV and a 6.02% copper radiator.

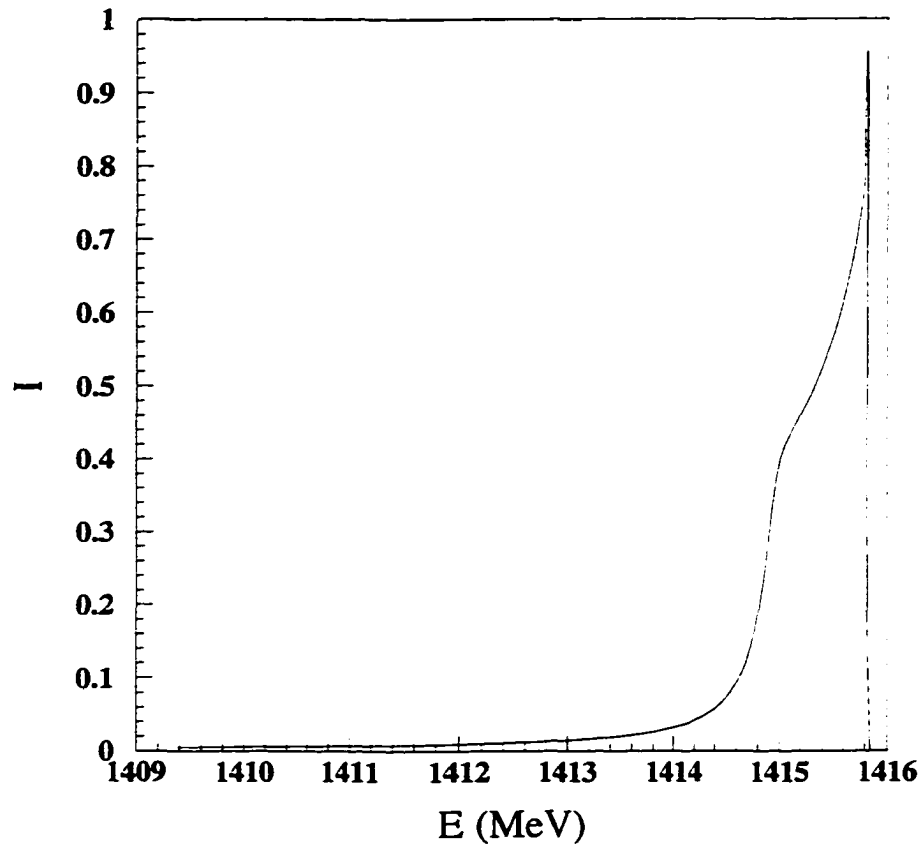


Figure B.2: Calculated distribution $I(E, E', Z, T)$ for an incident beam energy of 1413 MeV a 6.02% copper radiator and a beam energy spread of 0.1%.

There is a 10-15% difference between calculations using Equations B.4 (thin code) and B.9 (thick code) for the calculation bremsstrahlung spectrum for a $\sim 6\%$ copper radiator. The two calculations, for an incident electron energy of 2445 MeV and a 6.02% copper radiator, are shown in Figure B.3. In practice, the bremsstrahlung yield (total number of

photons) is determined from the integration of Equation B.9

$$N_{\gamma}(Z, E_0, T) = \int_{k_{min}}^{k_{max}} dk \frac{dN(k, E_0, Z, T)}{dk} \quad (\text{B.11})$$

was used for all kinematics with integration limits k_{min} and k_{max} chosen to match the E_{γ} cuts used in the analysis (see Section 5.1). The calculation of the bremsstrahlung spectrum is accurate to within 3% except near the tip of the spectrum where the flux is less well known. The results of these calculations agree well with previous work by Belz [19] and Kinney [105] and are consistent with the radiator calibration data shown in Figure A.6.

B.2 Correction Function $C(E_{\gamma})$

To remove the background resulting from electro-produced deuterons in the data, data with the radiator removed were taken on both hydrogen and deuterium targets. A direct subtraction of the normalized yields calculated from these runs would be $\sim 25\%$ inaccurate due to effects from energy loss of the beam in the radiator when the radiator is in place. These raw yields are then an overestimate of the electro-produced deuteron background when the radiator is in place and must be corrected. These spectra are corrected by calculating the bremsstrahlung yield in the target for incident electron beams with and without the radiator in place. Because the target is a thin radiator and this is a $\sim 25\%$ correction to a $\sim 25\%$ background subtraction, the thin code is used in the calculation of this correction function, $C(E_{\gamma})$. The incident electron energy spectrum is calculated using Equation B.7 and folded with the bremsstrahlung yield as given by B.4 to give the radiator in spectrum

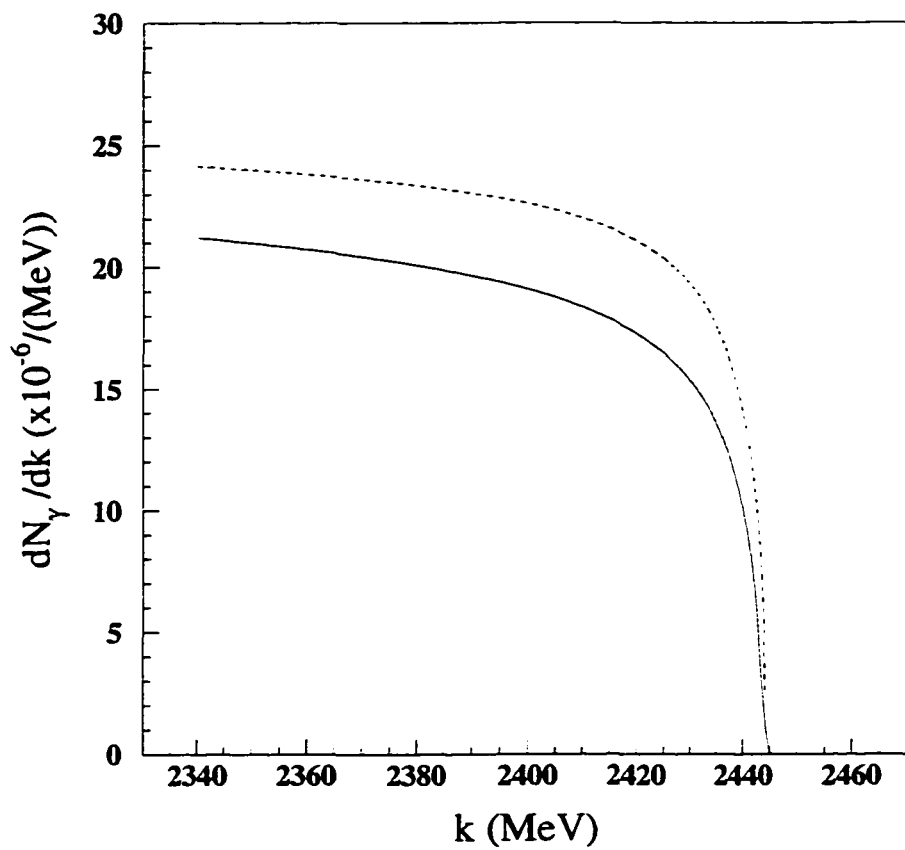


Figure B.3: Calculated bremsstrahlung spectra for an electron beam energy of 2445 MeV and a 6.02% copper radiator. The solid curve is a calculation using the thick code, and a similar calculation using the thin code is shown as the dashed curve.

for bremsstrahlung produced in the target. The correction function is then given by

$$C(E_\gamma) = \frac{N_\gamma^{\text{rad}}(E_\gamma)}{N_\gamma(E_\gamma)} \quad (\text{B.12})$$

where

$$N_\gamma^{\text{rad}}(E_\gamma) = \int dE' \frac{d^2 n(E', k)}{dk dt}$$

and $N_\gamma(E_\gamma)$ is given by Equation B.4 with $Z = 1$. The application of the correction function to the data is discussed in Section 5.1. Figure B.4 shows the correction function for a 15 cm long deuterium target, an incident electron beam energy of 2445 MeV, and a 6.02% copper radiator.

B.3 Calculated Yields

Table B.1 gives a list of the calculated yields used in the analysis. The Full region was chosen to be $-100 \text{ MeV} \leq E_\gamma - E_0 \leq -10 \text{ MeV}$. The $2\text{-}\pi$ region was chosen so that $-100 \text{ MeV} \leq E_\gamma - E_0 \leq E_{2\pi} - E_0$ (see Section 5.1.3). Similarly, the $1\text{-}\pi$ region was chosen such that $E_{2\pi} - E_0 \leq E_\gamma - E_0 \leq -10 \text{ MeV}$.

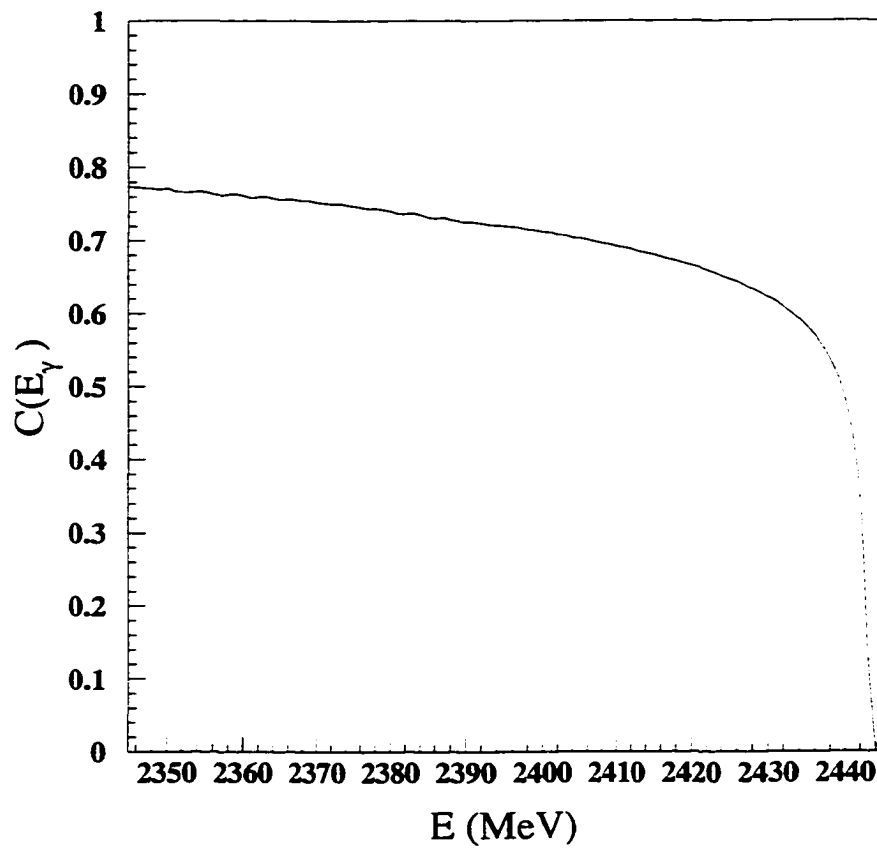


Figure B.4: The correction function $C(E_\gamma)$ for a 15 cm deuterium target, an incident electron beam energy of 2445 MeV, and a 6.02% copper radiator.

Kinematics		$E_0 - E_{2\pi}$ (MeV)	Photon Yield ($\gamma/1000 e^-$)		
E_0 (GeV)	θ_{cm}		2- π	1- π	Full
0.845	136°	39.4	3.81	1.57	5.38
	90°	64.3	2.34	3.04	
1.413	90°	51.2	1.79	1.29	3.08
1.645	136°	28.8	2.17	0.47	2.64
	90°	48.4	1.62	1.01	
2.445	136°	25.3	1.49	0.25	1.73
	90°	42.8	1.17	0.57	
3.245	90°	40.0	0.73	0.29	1.29
4.045	90°	38.3	0.91	0.39	1.02

Table B.1: Calculated photon yields in $\gamma/1000 e^-$. The regions are described in the text above. All calculated yields are accurate to $\sim 3\%$ [56].

Appendix C

Derivation of Useful Expressions

The derivations of important quantities are shown in the following sections and are provided only as a reference. The order in which they appear in this appendix is the same order that they appear in the main text.

C.1 Jacobian $\frac{d\Omega_{cm}}{dt}$

Consider the process $AB \rightarrow CD$ in the center-of-mass as shown in Figure C.1. For consistency, it is assumed that A is the beam particle; B is the target particle; D is the detected particle; and C is the undetected recoil particle. The Mandelstam variable t is given by

$$t = (p_A^\mu - p_D^\mu)^2$$

and $d\Omega_{cm}$ is given by

$$d\Omega_{cm} = 2\pi \sin(\pi - \theta_{cm}) d\theta = -2\pi d(\cos(\pi - \theta_{cm})).$$

The quantity t may be expanded

$$t = p_A^2 + p_D^2 - 2p_A^\mu p_{D\mu}$$

which is equivalent to

$$t = m_A^2 + m_D^2 - 2E_A E_D + 2 |\vec{p}_A| |\vec{p}_D| \cos(\theta_{cm}) .$$

or equivalently

$$t = m_A^2 + m_D^2 - 2E_A E_D - 2 |\vec{p}_A| |\vec{p}_D| \cos(\pi - \theta_{cm}) .$$

The quantity $\frac{dt}{d\Omega_{cm}}$ may then be determined

$$\frac{dt}{d\Omega_{cm}} = \frac{|\vec{p}_A| |\vec{p}_D|}{\pi}$$

which implies that the Jacobian can be given as

$$\frac{d\Omega_{cm}}{dt} = \frac{\pi}{|\vec{p}_A| |\vec{p}_D|}$$

C.2 Center-of-Mass Three Momenta

Consider the process $AB \rightarrow CD$ in the center-of-mass as shown in Figure C.1. The description of the particles is the same as that discussed in the previous section. The square

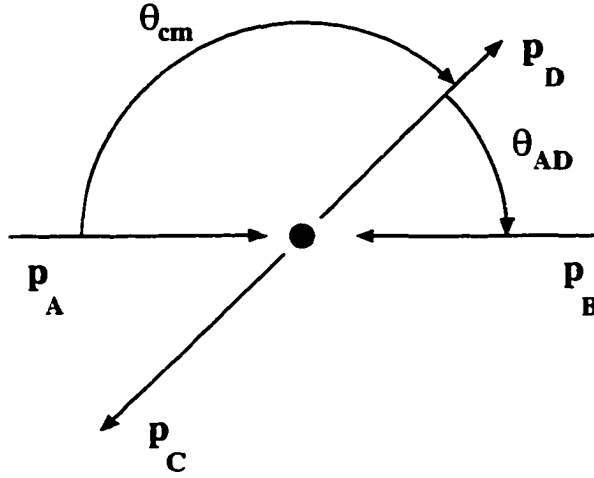


Figure C.1: The two body process $AB \rightarrow CD$ in the center-of -mass. Note that θ_{AD} in the laboratory frame is the angle of the detected particle (d in the experiment) as seen by the spectrometer.

of the center-of-mass energy s may be written as

$$\sqrt{s} = (p_D^2 + m_D^2)^{\frac{1}{2}} + (p_R^2 + m_R^2)^{\frac{1}{2}} .$$

By squaring both sides of the equation and by noting $p_D = p_R = p_f$ this may expressed as

$$s = (p_f^2 + m_D^2) + (p_f^2 + m_R^2) + 2 (p_f^2 + m_D^2)^{\frac{1}{2}} (p_f^2 + m_R^2)^{\frac{1}{2}} .$$

Squaring both sides once again and regrouping terms gives

$$s^2 - 2s (m_R^2 + m_D^2) + (m_D^2 - m_R^2)^2 = 4p_f^2 s .$$

Solving for p_f (the center-of-mass three momenta of each of the outgoing particles C and D) gives

$$p_f^2 = \frac{(s - (m_D - m_R)^2) (s - (m_D + m_R)^2)}{4s} .$$

A similar expression may be obtained for the initial center-of-mass momenta p_i using the masses of particles A and B .

C.3 Reconstructed Photon Energy E_γ

The photon energy is determined by assuming that the recoil deuteron detected in the HMS was produced by the process $\gamma d \rightarrow d\pi^0$. Thus, the energy of the photon involved in the reaction producing the deuteron in the HMS can be determined from the reconstructed deuteron momentum and angle. Consider a general photoprocess $\gamma T \rightarrow DR$ as shown in Figure C.2, where T is the target particle, D is the detected particle, and R is the recoil particle which remains undetected. Let m_i , p_i , and E_i be the mass, momentum, and energy of particle i . The other kinematical quantities are shown in the figure.

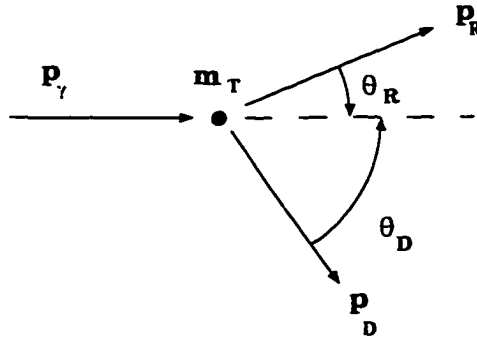


Figure C.2: Kinematics of a general photoprocess in the laboratory frame.

The following relations may be obtained from energy and momentum conservation

$$p_\gamma = p_D \cos(\theta_D) + p_R \cos(\theta_R) ; p_D \sin(\theta_D) = p_R \sin(\theta_R) \quad (\text{C.1})$$

and

$$E_\gamma + m_T = E_D + E_R \quad (C.2)$$

$$E_\gamma + m_T = \sqrt{(p_D^2 + m_D^2)} + \sqrt{(p_R^2 + m_R^2)}.$$

By combining Equations C.1 and C.2 the following expression may be obtained

$$2E_R[E_D - m_T - p_D \cos(\theta_D)] = 2p_D(E_D - m_T) \cos(\theta_D) - m_R^2 - p_D^2 - (E_D - m_T)^2. \quad (C.3)$$

An expression for E_γ using only reconstructed quantities is obtained by noting $E_\gamma = E_D + E_R - m_T$ and making this substitution in Equation C.3

$$E_\gamma = E_D - m_T + \frac{2p_D(E_D - m_T) \cos(\theta_D) - m_R^2 - p_D^2 - (E_D - m_T)^2}{2[E_D - m_T - p_D \cos(\theta_D)]}.$$

This may be reduced to

$$E_\gamma = \frac{E_D m_T - (m_D^2 + m_T^2 - m_R^2) / 2}{m_T - E_D + p_D \cos(\theta_D)}. \quad (C.4)$$

By making the proper substitutions for the particle masses for the process $\gamma d \rightarrow d\pi^0$ an expression for the reconstructed photon energy using only reconstructed quantities is finally obtained

$$E_\gamma = \frac{E_d m_d - (2m_d^2 - m_{\pi^0}^2) / 2}{m_d - E_d + p_d \cos(\theta_d)}.$$

C.4 The Jacobian $\frac{d\Omega_{lab}}{d\Omega_{cm}}$

The Jacobian used to transform the cross section in the laboratory (*lab*) to the center-of-mass (*cm*) is used extensively in experimental nuclear physics. The specific Jacobian for two particles in the initial and final states is discussed here. In this section, primed quan-

titles signify variables in the *cm*. Consider the general process where a beam of particles interacts with a target stationary in the *lab* frame as shown in Figure C.3. Note that the velocity of the *cm* in the *lab* frame is given by

$$\vec{\beta}_{cm} = \frac{\vec{p}_B}{m_T + E_B}$$

which implies that

$$\gamma_{cm} = \frac{E_B + m_T}{E_{cm}}$$

where E_{cm} is the total *cm* energy. The Lorentz transformation of momenta p and energy E from the *lab* to the *cm* is given by

$$\begin{pmatrix} E' \\ p' \cos(\theta') \end{pmatrix} = \begin{pmatrix} \gamma_{cm} & -\gamma_{cm}\beta_{cm} \\ -\gamma_{cm}\beta_{cm} & \gamma_{cm} \end{pmatrix} \begin{pmatrix} E \\ p \cos(\theta) \end{pmatrix}$$

$$p' \sin(\theta') = p \sin(\theta).$$

By using the above relations and noting that energy and momentum are conserved, the following equation may be obtained

$$\gamma_{cm} (p'_D \cos(\theta') + \beta_{cm} E'_D) \tan(\theta) = p'_D \sin(\theta'). \quad (C.5)$$

Note that

$$d\Omega = -2\pi d(\cos(\theta))$$

$$\frac{d(\sin(\theta))}{d\Omega} = \frac{\cos(\theta)}{2\pi \sin(\theta)}$$

and

$$\frac{d(\tan(\theta))}{d\Omega} = \frac{\sec^2(\theta)}{2\pi \sin(\theta)}$$

by differentiating the right hand side of equation C.5 it can be seen that

$$\frac{d}{d\Omega'} (p'_D \sin(\theta')) = p'_D \frac{\cos(\theta')}{2\pi \sin(\theta')} \quad (\text{C.6})$$

and the left hand side of the same equation

$$2\pi \frac{d}{d\Omega'} [\gamma_{cm} (p'_D \cos(\theta') + \beta_{cm} E'_D) \tan(\theta)] = -\gamma_{cm} p'_D \tan(\theta) + \gamma_{cm} (p'_D \cos(\theta') + \beta_{cm} E'_D) \frac{\sec^2(\theta)}{\sin(\theta)} \frac{d\Omega}{d\Omega'}$$

Solving for $\frac{d\Omega}{d\Omega'}$ gives

$$\frac{d\Omega}{d\Omega'} = \frac{\sin^2(\theta)}{\sin^2(\theta')} [\cos(\theta') \cos(\theta) + \gamma_{cm} \sin(\theta') \sin(\theta)]$$

which is the desired result. Note that in this text the center-of-mass angle is the deuteron center-of-mass angle and $\theta' = \pi - \theta_{cm}$.

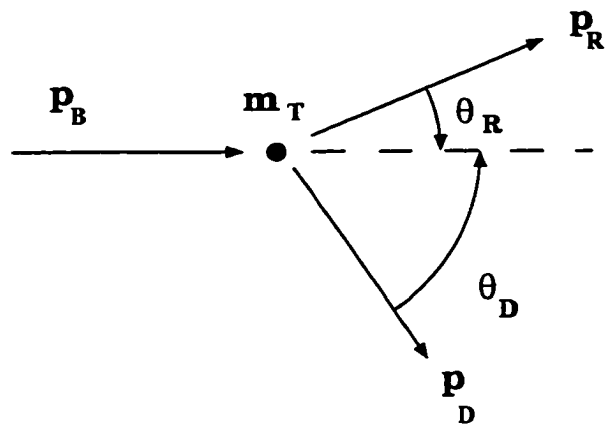


Figure C.3: General laboratory kinematics for a two-body process.

Appendix D

Kinematics

Beam Energy (GeV)	E_γ (GeV)	θ_{cm}	θ_{HMS}	P_{HMS} (GeV)	s GeV ²	$-t$ GeV ²
0.845	0.783	136°	21.42°	1.081	6.46	1.12
0.845	0.783	90°	43.21°	0.815	6.46	0.654
1.413	1.368	90°	42.04°	1.280	8.65	1.51
1.645	1.583	136°	20.20°	1.953	9.46	3.16
1.645	1.583	90°	41.50°	1.438	9.46	1.85
2.445	2.383	136°	18.89°	2.738	12.5	5.46
2.445	2.390	90°	39.58°	1.979	12.5	3.21
3.245	3.190	90°	37.81°	2.476	15.5	4.61
4.045	3.990	90°	36.22°	2.938	18.5	6.05

Table D.1: Table of kinematical settings used during the experiment. The beam energy is the incident electron beam energy. \bar{E}_γ is the central photon energy. θ_{cm} is the center-of-mass angle of the scattered deuteron. θ_{HMS} and P_{HMS} are the angle and momentum settings of the HMS. s and t are the Mandelstam variables where t is the square of the momentum transferred to the deuteron.

Index

- 8LM, 122, 124
- accelerator, 40
- acceptance function, 85
- ADC, 118, 123, 129, 130
- analysis
 - software, 128
- analysis procedure
 - general, 128
 - HMS, 129
- asymptotic scaling laws, 12, 15, 17–25, 180, 192
- background
 - proton, 147, 148
- beam
 - BCM, 47
 - BPM, 44
 - current, 46
 - calibrations, 49
 - energy measurement, 54
 - resolution, 55
 - general, 40, 41
 - position, 43
 - profile, 43
 - raster
 - fast, 52
 - slow, 52
 - UNSER, 48
- Bethe-Bloch formula, 138
- bremsstrahlung
 - flux calculation, 56, 173
 - spectrum, 168, 209
 - yield, 209
 - table, 217
- CEBAF, 40
- center-of-mass scattering angle
 - definition, 5, 8, 9
- Cerenkov, 115, 120, 130
 - Aerogel, 115
- CERN libraries, 128

CODA, 117, 119
 CODA Readout Language, 119
 compton scattering
 deuteron, 174
 proton, 35, 38, 174
 constituent counting rules, 12
 correction function, 164, 215
 cross section
 E89-012 data, 181
 general, 8
 invariant, 15, 181, 183, 184, 188, 191, 192
 cryotarget, 56–67, 72, 203
 cell, 62, 63
 dimensions, 63
 stack, 65
 contamination, 72
 controls, 66
 density, 72
 fan, 67
 fluid pump, 67
 gas analysis, 71
 gas system, 65
 heat exchanger, 62
 lifter, 64
 local boiling, 69
 performance, 69
 pressure, 67
 purity, 70
 software, 66
 temperature, 67
 CTP, 128
 dead time, 124
 computer, 127
 electronic, 125
 deuteron
 absorption, 147
 double pion photoproduction, 158, 166
 electron scattering, 182
 form factor, 24, 26, 28, 185
 reduced form factor, 28
 scattering
 aluminum, 159
 electron, 150
 drift chamber, 129
 calibration, 94
 time to distance map, 94
 electron beam, 40
 See beam, 40

endpoint, 158
 fitting, 168
 energy loss, 138
 electron, 210
 in radiator, 164
 Engine, 128
 EPICS, 66, 74, 90, 119, 128, 203
 FASTBUS, 94, 117–119, 123, 132
 FDDI, 118
 Fock state, 3
 form factor, 21, 31
 deuteron, 185
 hadronic, 185
 nucleon, 31, 185
 Hall C
 Arc, 42
 beamline, 42
 HARP, 43
 high voltage, 90
 HMS, 71
 acceptance, 84, 87
 angle calibration, 82
 collimator, 75
 commisioning, 76
 COSY model, 80
 detector, 89
 drift chamber, 91
 highvoltage, 90
 hodoscope, 95
 shower calorimeter, 99
 detector materials, 149
 detector package, 89
 focal plane, 77
 focus, 77, 78
 gate valve, 151
 magnets, 73
 momentum, 141
 momentum calibration, 80
 Monte Carlo, 151
 optical system, 73
 performance, 75
 reconstruction, 78
 extended target, 80
 matrix elements, 79
 sieve slit, 80
 slanted target, 80
 resolution, 75, 168
 TOF, 136
 true angles, 85

hodoscope, 120, 129, 136, 141
 energy loss, 138
 sweet spot, 134
 timing resolution, 138

IOC, 66, 68, 69, 117, 122, 203
 cryotarget, 66

Jacobian
 invariant cross section, 174, 220
 lab to center-of-mass, 173, 224

JT valve, 64

Landshoff scattering, 13, 19

Linux, 67, 128, 131

live time, 126

Mandelstam variables, 7

meson exchange calculations, 2, 31

momentum
 transfer, 6
 transverse, 8

Monte Carlo, 86, 87

motor
 AC Servo, 64
 stepper, 65, 202

multiple scattering, 153

neutron
 form factor, 24

Oxford ITC 501, 69

Oxford ITC 502, 68

pedestal event, 118

PID, 98, 102, 136, 139, 140, 142, 143
 energy loss, 145
 reconstructed mass, 141, 144–146
 resolution, 143

pion
 form factor, 24

PMT, 97, 99, 101, 113, 114, 116, 137

PQCD
 applicability of, 34
 general, 4
 general hadronic process, 10
 hard scattering, 11
 scaling laws, 15
 scaling laws, 180

proton
 background, 144, 148
 compton scattering, 35, 174
 elastic scattering, 19
 form factor, 18, 24

- pion photon production, 175
 - reconstructed mass, 144, 146
- pulse height correction, 137
- QCD, 3
 - coupling constant, 3
 - sum rules, 35
- radiator, 195–200, 202, 204–207
 - controls, 203
 - cooling, 198
 - design, 195–197, 199, 202
 - foils, 197, 198
 - overview, 55
 - photon flux, 56
- reconstructed photon energy, 158, 223
- reduced nuclear amplitude, 24
- reduced nuclear amplitude, 28, 182
- reduced nuclear amplitude
 - general, 28
- ROC, 117, 119
- SC200, 69
- scaling laws, 15
- scattering
 - deuteron compton, 174
 - elastic ep, 18
 - Landshoff, 4, 14, 17
 - proton compton, 174
 - proton proton, 19
- scattering chamber, 59
- scattering, Landshoff, 17
- shower counter, 116, 120, 130
- SOS, 102
 - angle measurement, 106
 - Cerenkov detector, 115
 - collimator, 103
 - detector
 - highvoltage, 90
 - drift chambers, 109
 - hodoscope, 111
 - magnets, 103
 - optical system, 103
 - performance, 107
 - sieve slit, 108
 - survey information, 111
- Sudakov suppression, 14
- Super HARP, 43
- systematic uncertainties, 175
- target
 - length, 63

determination, 153
effective, 153, 156
solid, 65
TCL/Tk, 67, 90, 128
TDC, 94, 117, 118, 123, 129, 132, 134,
137
time-of-flight, 98, 129, 135, 136, 138, 141
TJNAF, 39
TOF, 136
tracking, 130, 132
efficiency, 134
four out of six, 133
resolution, 134
TRANSPORT, 77, 84
convention, 78
coordinate system, 77
focal plane, 77
trigger, 98, 99, 101, 120, 123, 127, 128
COIN, 118, 120
HMS, 118, 120, 123
SOS, 118, 120
trigger supervisor, 118, 122
UNSER monitor, 48
vacuum, 59, 60
window, 59
VME, 64, 66, 117, 118, 122, 203

References

- [1] R. G. Roberts, *The Structure of the Proton*, Cambridge University Press, Cambridge (1990).
- [2] Stanley J. Brodsky and G. Peter Lepage, *Advanced Series in High Energy Physics, Vol 5, Perturbative Quantum Chromodynamics*, ed. A.H.Mueller, (1989).
- [3] R.J. Holt, Phys. Rev. **C41**, 2400 (1990).
- [4] R. Gilman and R. J. Holt *et al.* CEBAF Proposal PR94-012.
- [5] J. D. Björken and S. D. Drell, *Relativistic Quantum Fields*
- [6] F. Halzen and A. D. Martin, *Quarks and Leptons*, John Wiley and Sons, New York (1984).
- [7] G. Peter Lepage and Stanley J. Brodsky, Phys. Rev. **D22**, 2157 (1980).
- [8] Yu. L. Dokshitzer, V. A. Khoze, A. H. Mueller, and S. I. Troyon, *Basics of Perturbative QCD*, (1991).
- [9] James Botts and George Sterman, Nuc. Phys. **B325**, 62 (1989).
- [10] Michael G. Sotiropoulos and George Sterman Nuc. Phys. **B425**, 489 (1994).

- [11] Stanley J. Brodsky and Glennys R. Farrar, Phys. Rev. Lett. **31**, 1153 (1973).
- [12] V. Matveev, R. Muradyan and A. Tavheliidze, Nuovo Cimento Lett. **7**, 719 (1973)
- [13] Carl E. Carlson, Nuc. Phys **A508**,481c (1990).
- [14] R. L. Anderson *et al.*, Phys Rev. **D14**, 679 (1976).
- [15] M. A. Shupe *et al.*, Phys. Rev. **D19**, 1921 (1979).
- [16] P. V. Landshoff and J. C. Polkinghorn, Phys Lett. **B44**, 293 (1973).
- [17] J. Napolitano, *et al.*, Phys. Rev. Lett. **61**, 2530 (1988).
- [18] J. E. Belz, *et al.*, Phys. Rev. Lett **74**, 646 (1995).
- [19] J. E. Belz, Two Body Photodisintegration of the Deuteron at Intermediate Energy, Ph.D. Thesis, California Institute of Technology, (January 1994) (unpublished).
- [20] C. W. Bochna and B. P. Terburg *et al.*, *submitted to* Phys. Rev. Lett.
- [21] D. G. Crabb *et al.*, Phys. Rev. Lett. **65**, 3241 (1990).
- [22] C. E. Carlson, M. Chachkhunashvili, F. Myhrer, Phys. Rev. **D46**, 2891 (1992).
- [23] D. Potterveld, ANL-Preprint PHY-7057-me-92 (1992).
- [24] A. Imanishi *et al.*, Nuovo Cimento **100A**, 735 (1988).
- [25] A. Imanishi *et al.*, Phys. Rev. Lett. **54**, 2497 (1985).
- [26] Datum extracted from the SLAC NE-17 results by D. Meekins, (unpublished) (1994).
- [27] Nathan Isgur and C H. Llewellyn Smith, Phys. Rev. Let. **52**, 1080 (1984).

- [28] Nathan Isgur and C H. Llewellyn Smith, *Nuc. Phys.* **B317**, 526 (1989).
- [29] Nathan Isgur and C H. Llewellyn Smith, *Phys. Lett.* **B217**, 535 (1989).
- [30] Stanley J. Brodsky and Benson T. Chertok, *Phys. Rev.* **D14**, 3003 (1976).
- [31] S. J. Brodsky and B. T. Chertok, *Phys. Rev. Lett.* **37**, 269 (1976).
- [32] L. C. Alexa *et al.*, submitted to *Phys. Rev. Lett.*
- [33] S. J. Brodsky and J. R. Hiller, *Phys Rev.* **C28**, 475 (1983).
- [34] W. P. Schütz *et al.*, *Phys. Rev. Lett.* **38**, 259 (1977).
- [35] F. Martin *et al.*, *Phys. Rev. Lett* **38**, 1320 (1977).
- [36] J. H. Koch and R. M. Woloshyn, Conference Proceedings, 1976 Meson-nuclear Physics, Pittsburgh, New York (1976).
- [37] S. S. Kamalov, L. Taitor, and C. Bennhold, *Phys. Rev.* **C55**, 98 (1997).
- [38] B. K. Jeon, T. Sato, H. Ohtsubo, *Phys. Lett.* **B228**, 304 (1989).
- [39] H. Garcilazo and E. Moya de Guerra, *Phys Rev.* **C52**, 49 (1995).
- [40] S. I. Nagornyi, YU. A. Kasatkin, I. K. Kirichenko, *Sov. J. Nucl. Phys.* **55**, 189 (1992).
- [41] S. I. Nagornyi, private communication.
- [42] A. Radyushkin HEP Preprint 9803316 v2, (1998).
- [43] A. Radyushkin submitted to *Phys. Rev. D*.
- [44] A. Radyushkin, Private Communication (1998).

- [45] A. Radyushkin, Private Communication (1998).
- [46] C. Sinclair, Private Communication.
- [47] R. Abbott, B. Bowling, and E. Woodworth, HARP User's Manual, CEBAF Tech Note TN92-050 (1992).
- [48] C. Yan et al., Nucl. Instrum. Meth. **A365**, 261 (1995).
- [49] G. Niculescu, Resonant Cavities used as Beam Current Monitors, TJNAF Document, unpublished (1995).
- [50] *Data Converter Reference Manual*, Analog Devices Norwood, Ma. (1992).
- [51] K. Unser, The Parametric Current Transformer, paper presented at the Accelerator Instrumentation Workshop CEBAF, Newport News Va., USA., 1991
- [52] K. B. Unser, *Parametric Current Transformer User Manual*, Bergoz (1991).
- [53] C. Yan, User's Manual of the Hall C Beamline, CEBAF Internal Report (unpublished).
- [54] P. Gueye, M. Tiefenback, and C. Yan, Hall C Beam Energy Measurement, CEBAF Internal Report (unpublished).
- [55] D. Dutta *et al.*, Beam Energy Determination Using Kinematic Methods, CEBAF Internal Document (1995) (unpublished).
- [56] J. L. Matthews and R. O. Owens, NIM **111**, 157 (1973).
- [57] J. Mitchell, Specifications for the Control System of the Hall C Cryogenic Targets, TJNAF Internal Document (unpublished) (1995).

- [38] J. Dunne, Memorandum regarding the survey of the cryotargets pre-t20, CEBAF Internal Document (unpublished) (1996).
- [58] J. Dunne, Memorandum regarding the survey of the cryotarget for t20, CEBAF Internal Document (unpublished) (1997).
- [59] J. P. Chen, Private Communication.
- [60] K. Gustaffson, Cryotarget Density Dependence on Beam Current, TJNAF Internal Report (1996) (unpublished).
- [61] K. Gustaffson, Private Communication. (1998).
- [62] B. Terburg, The Target Gas Analysis Vademecum, CEBAF Internal Document (unpublished) (September 1997).
- [63] J. Cobb and J. Murray, Nucl. Inst. Meth. **46**, 99 (1967).
- [64] R. Ent, Private Communication (1998).
- [65] K. A. Assamagan, D. Dutta, and P. Welch, Hall C Matrix Element Optimization Package, CEBAF Internal Document (unpublished) (1996).
- [66] D. C. Carey, K. L. Brown, and F. Rothacker, TRANSPORT, A Computer Program for Designing Charged Particle Beam Transport Systems, SLAC-R-95-462, (1995).
- [67] M. Berz, COSY Infinity Version 7 User's Guide and Reference Manual, Michigan State University (1996).
- [68] Physics Analysis Workstation Reference Manual, Version 2.03, CERN Program Library Long Writeup Q121 (1993).

- [69] O. K. Baker *et al.*, Nucl. Instrum. Meth. **A367**, 92 (1995).
- [70] G. Niculescu, Ph.D. Thesis, Hamton University (1998) (unpublished).
- [71] C. Armstrong, Procedure used to set the SOS/HMS hodoscope PMT voltages, (1995) CEBAF Internal Document (unpublished).
- [72] H. Mktchyan, CEBAF Internal Document, (unpublished).
- [73] C. Cothran, Private Communication.
- [74] W. J. Cummings, SOS Handbook, (1996) CEBAF Internal Document (unpublished).
- [75] D. van Westrum, Ph.D. Dissertation, University of Colorado, Boulder (1998) (unpublished).
- [76] R. Smythe, CEBAF Hall C Čerenkov Detector Handbook (1995) CEBAF Internal Document (unpublished).
- [77] J. Price., Determination of the wire position in the SOS drift chambers, (1995) CEBAF internal Document. (unpublished).
- [78] CEBAF Online Data Acquisition System Users Manual, TJNAF Internal Document (1993) (unpublished).
- [79] Trigger Supervisor User's Guide. CEBAF Internal Document (unpublished).
- [80] S. A. Wood., CEBAF Test Package Documentation. CEBAF internal Document. (unpublished).
- [81] J. R. Arrington, Inclusive Electron Scattering From Nuclei at $x > 1$ and High Q^2 . Ph.D. Thesis, California Institute of Technology, (1998) (unpublished).

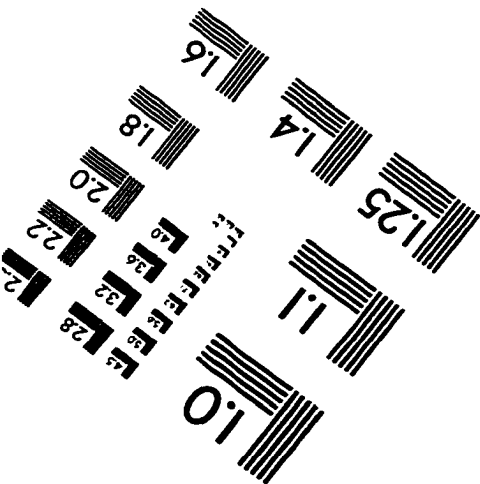
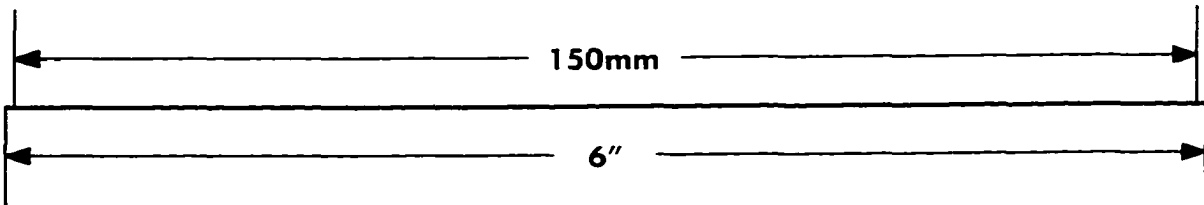
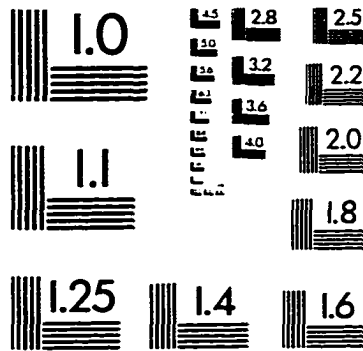
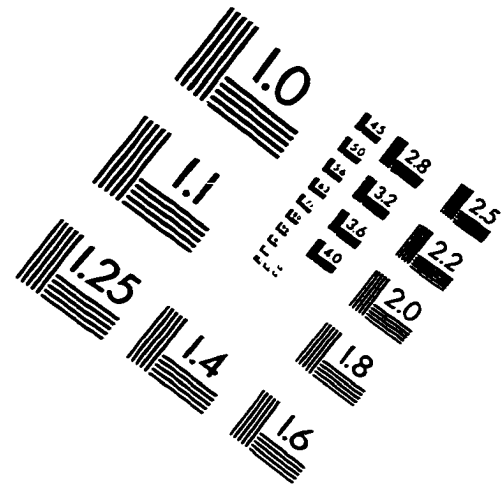
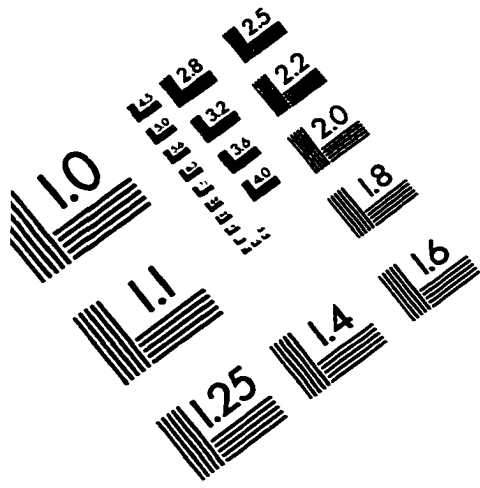
- [82] D. F. Geesman, Tracking in the SOS Spectrometer, CEBAF Internal Document (1993) (unpublished).
- [83] D. van Westrum, Tracking Efficiencies CEBAF Internal Report (unpublished).
- [84] C. A. Armstrong, Hall C Time-of-Flight Fitting Code, CEBAF Internal Document (1995) (unpublished).
- [85] R. W. Leo, Techniques for Nuclear and Particle Physics Experiments, Springer-Verlag, Berlin (1994).
- [86] D. van Westrum, Measurement and Estimate of Proton Absorption in the Hall C Spectrometers, CEBAF Internal Report (1997).
- [50] *Review of Particle Properties*, Phys. Rev. **D50**, 1173 (1994), p. 224.
- [87] P. E. Bosted, et al., Phys. Rev. **C42**, 38 (1990).
- [88] J. L. Matthews, R. O. Owens, and D. J. S. Findlay, NIM 180, **573** (1981).
- [89] C.S. Armstrong, Ph.D. Thesis, College of William and Mary, (unpublished) (1998).
- [90] J. I. Friedman and H. W. Kendall, Phys. Rev. **129**, 2802 (1963).
- [91] S. Platchkov, *et al.*, Nuc. Phys. **A510**, 740 (1990).
- [92] R. G. Arnold *et al.*, Phys. Rev. Lett. **35**, 776 (1975).
- [93] F. Coester *et al.*, Phys. Rev. **C11**, 1836 (1975).
- [94] R. G. Arnold *et al.*, Phys. Rev. **C23**, 363 (1981).
- [95] A. Honegger, Private Communication. (1998).

- [96] B. P. Terburg, Ph. D. Thesis, University of Illinois Urbana Champaign, (unpublished) (1998).
- [97] C. W. Bochna, Ph.D. Thesis, University of Illinois Urbana Champaign, (unpublished) (1998).
- [98] T. S. H. Lee. Private Communication (1998).
- [99] B. Wojtsehowski, *et al.*, TJNAF Proposal PR97-108 (1997).
- [100] R. J. Holt *et al.*, TJNAF Proposal PR96-003 (1997) (unpublished).
- [101] J. E. Feldel Private Communication.
- [102] D. Meekins, Necessary Flow Rates of Cooling Water in the Bremsstrahlung Radiator, TJNAF Internal Document (unpublished) (1994).
- [103] O. Blunk and S. Leisegang, *Z. Physik* **128**, 500 (1950).
- [104] C. M. Bender and S. A. Orszag, *Advanced Mathematical Methods for Scientists and Engineers*, Mc Graw Hill, New York (1978).
- [105] D. Potterveld, Private Communication, (1996).

Vita

The Author was born in Alexandria, Virginia, June 21, 1968. He graduated from Anandale High School in June 1986. He received a B.S. in physics and math from James Madison University in May of 1990. He started graduate school at the College of William and Mary in Virginia in 1990 and received a M. S. in physics in 1992. He has completed the requirements for the degree of Ph. D. from the College of William and Mary in Virginia December of 1998.

IMAGE EVALUATION TEST TARGET (QA-3)



APPLIED IMAGE, Inc
1653 East Main Street
Rochester, NY 14609 USA
Phone: 716/482-0300
Fax: 716/288-5989

© 1993, Applied Image, Inc., All Rights Reserved

